Use of hyphenated analytical techniques to isolate and characterise antiviral compounds against SARS-CoV-2 from South African medicinal plants

by

Luke Invernizzi

16006692

Supervisor: Prof Vinesh J. Maharaj

Co-supervisor: Dr Phanankosi Moyo

Submitted in fulfilment of the requirements for the degree

PHILOSOPHIAE DOCTOR CHEMISTRY

In the Faculty of Natural and Agricultural Sciences

UNIVERSITY OF PRETORIA

April 2023

Declaration

I, **Luke Invernizzi**, hereby declare that the thesis, which I hereby submit for the degree ***Philosophiae Doctor*** at the University of Pretoria, is my own work and has not previously been submitted by me for a degree at this or any other tertiary institution.

Signature: 

Date: 11th April 2023

Plagiarism Declaration

Full names of student	Luke Invernizzi
Student number	16006692
Title of work	Use of hyphenated analytical techniques to isolate and characterise antiviral compounds against SARS-CoV-2 from South African medicinal plants

Declaration

1. I understand what plagiarism is and am aware of the University's policy in this regard.
2. I declare that this thesis is my own original work. Where other people's work has been used (either from a printed source, internet, or any other source), this has been properly acknowledged and referenced in accordance with the requirements as stated in the University's plagiarism prevention policy.
3. I have not used another student's past written work to hand in as my own.
4. I have not allowed, and will not allow anyone to copy my work with the intention of passing it off as his or her own work.

Signature:  Date: 11th April 2023

Acknowledgements

I want to express my sincere gratitude to my supervisors Prof VJ. Maharaj and Dr P. Moyo, for their continuous support, guidance, and scientific contribution to this research project. Additionally, for their guidance in subjects surpassing the project and for teaching me to think like a true scientist, far beyond mere 'proof-of-concept'.

I also want to thank our collaborator, Prof I. Tietjen (Wistar Institute, USA), for the exciting and ongoing collaboration and for the screening of the samples. A special thanks to the collaborators in Switzerland (University of Basel), Prof T. Klimkait and Ms L. Urda for their exceptional hospitality and training provided on the SARS-CoV-2 plaque-based bioassays and additionally for their willingness to screen the samples.

I want to acknowledge the Department of Science and Innovation (DSI) consortium members and Mr FJ Isaacs whose contributions made the project possible. Additional thanks are offered to Dr J. van der Westhuizen for the molecular docking training and assistance. Similarly, thanks are offered to Mr J. Sampson, for assisting with collecting plant material from the University of Pretoria gardens and to Ms M. Nel (H.G.W.J. Schweickerdt Herbarium) for identifying the plants. Thanks are offered to Mr N. van Vuuren for all the assistance and advice. Special thanks are expressed to Dr M. Wooding for all her reassurance, advice and, most importantly, guidance on how to remain sane and analytically grounded in the midst of a storm. I want to thank Dr J. Pretorius for the constant help, support, advice, and fascinating physical chemistry conversations – despite being far, your emails always kept you near. I express my gratitude for the support received from the group members of the Biodiscovery Center (University of Pretoria), with a special thanks to Mr PM. Mc Millan, Mr WJ. Rudolph and Ms I. Sefoka for all the assistance, encouragement and perpetual thought-provoking conversations.

This work would not have been possible without funding from the DSI and the National Research Foundation (NRF). The CHPC is similarly acknowledged for the use of its facilities.

And finally, words cannot express my gratitude for the love, support, and encouragement I received from my friends and family as a whole. My deepest gratitude is especially expressed to my parents (Arline and Stephan), sister (Jessie), grandparents (BF/BE Vincent) and to my great-aunt Irene, whose guidance, support, intellectual and pharmacological conversations kindled my love for science and scratched my metaphorical medical itch. I needed you all.

My knowledge of this life is small, the eye of faith is dim; But 'tis enough that Christ knows all, And I shall be with Him…

-Richard Baxter (1681)

Summary

As new SARS-CoV-2 cases continue to be reported worldwide and more subvariants are discovered, developing antivirals capable of complementing vaccine strategies remains an important research avenue. Natural products are a valuable resource in drug discovery and provide good starting points for the development of new therapeutic chemotypes. With most research focusing on *in silico* drug discovery methods against COVID-19, this work goes beyond *in silico* approaches and uses hyphenated analytical techniques and *in vitro*-based bioassays to identify the bioactive compounds present in three South African medicinal plants.

A literature survey and score-based criterion were used for the selection of plants. Firstly, a database query using keywords relevant to the study was utilised to identify South African plants with potential antiviral activity against the SARS-CoV-2 virus. Thereafter, plants identified from the database were ranked based on a logical scoring system. The criteria used to select species for the study included consideration of the plant's traditional use, toxicity, plant part used, published information and reported use for symptoms associated with COVID-19. A total of 19 plants were subsequently prioritised and selected based on their assigned score.

Different parts of the selected plants were collected, dried and ground to a powder prior to extraction. A small portion of the plant material was used for extraction using in-house developed extraction vessels where a sequential ultrasonicator-mediated extraction method was utilised using, primarily, DCM and MeOH as the extraction solvents. A subset of the resulting extracts was fractionated using a robotic liquid handler and a C8 SPE cartridge to generate 7 semi-purified fractions of each extract, ranging from highly polar to moderately non-polar in nature. The resulting 30 extracts and 147 fractions (originating from selective fractionation of a subset of fractions) were screened *in vitro* in AlphaScreens to assess the sample's potential spike receptor-binding domain/angiotensin converting enzyme-2 (RBD/ACE2) antagonistic activity. Further *in vitro* pharmacological evaluation was carried out against the SARS-CoV-2 main protease (M^{pro}) enzyme. From the 30 extracts that were evaluated (originating from 19 different plant species) in the spike RBD/ACE2 assay, 14 had a measured IC_{50} of < 30 µg/mL, and only 3 showed >80% inhibition at 10 µg/mL in M^{pro} inhibition bioassays. Of the 147 plant fractions screened, 37 (25.2% hit rate) were found to have an IC_{50} < 30 µg/mL in spike RBD/ACE2 inhibition assays and only 7 (4.8 % hit rate), which showed >80% inhibition at 10 µg/mL in the M^{pro} inhibition bioassays. Amongst these,

samples originating from *Gunnera perpensa* L., *Siphonochilus aethiopicus* and *Podocarpus henkelii* were found to display potent antiviral activity in either the M^{pro} or spike RBD/ACE2 inhibition assays and hence prioritised for further analyses.

Of particular note, the *G. perpensa* extract and subsequent purified fractions were found to have an IC_{50} < 0.001 µg/mL in the spike RBD/ACE2 inhibition screens. UPLC-IMS-HRMS analysis was carried out on the bioactive *G. perpensa* extract and fractions in order to tentatively identify the compounds contributing to the observed bioactivity. The compounds α/β-punicalagin **(18)**, punicalin **(23)** and (Z)-lespedezic acid **(17)** were tentatively identified and hypothesised to be key bioactive compounds. A bioassay-guided fractionation scheme was followed to test the hypothesis and ensure an unbiased screening approach, which utilised a robotic liquid handler, a Buchi Flash system and an HPLC-PDA-MS instrument to purify the bioactive compounds further. Through the use of analytical reference standards and UPLC-IMS-HRMS analysis, α/β-punicalagin **(18)** and punicalin's **(23)** identities were confirmed. 1D and 2D NMR analysis and UPLC-IMS-HRMS analysis were used to identify (Z)-lespedezic acid **(17).**

Having had confirmed the identities of compounds **18** and **23**, the next step was to measure the quantities of the two most potent compounds, viz., compound **18** and **23**, in the DCM:MeOH extract. To do this quantification, a UPLC-IMS-HRMS method, partially validated according to the International Council for Harmonisation of Technical Requirements for Registration of Pharmaceuticals for Human Use (ICH) guidelines, was utilised. The quantities of punicalin **(23)** and α/β-punicalagin **(18)** were determined in the DCM:MeOH extract and found to be 2.12 ± 0.15% and 1.51 ± 0.15% (% w/w), respectively. Furthermore, the concentration of the ellagitannins in the dried plant material was found to be 0.19 ± 0.01% and 0.14 ± 0.01% (% w/w) for punicalin **(23)** and α/β-punicalagin **(18)**, respectively. Both these compounds, **18** and **23**, were rescreened in both the enzyme- and whole-cell plaque-based bioassays. In the spike RBD/ACE2 inhibition assays, the IC_{50} value of punicalin **(23)** was found to range between 9.5 nM and 35.4 nM against the various variants of concern. Similarly, the IC_{50} value of α/β-punicalagin **(18)** was found to range between 6.6 nM (Beta) and 13.3 nM (Omicron). The IC_{50} value of (Z)-lespedezic acid **(17)** was found to be 90.91 µg/mL (265.59 µM) against the SARS-CoV-2 M^{pro} and in the spike RBD/ACE2 inhibition assay, was found to be IC_{50} = 0.0404 ± 0.0056 µg/mL (0.1180 ± 0.0164 µM).

In the whole-cell plaque-based bioassays, punicalin **(23)** was found to inhibit the formation of virus-driven cytopathic changes, against the Wuhan strain (Wild type), Beta, Delta and

Omicron variants of SARS-CoV-2. The IC_{50} values for punicalin **(23)** were found to range between 1.210 μM (Omicron variant) and 13.52 μM (Delta variant) with minimal cytotoxicity. Similarly, in the whole-cell plaque-based bioassays, α/β-punicalagin **(18)** was found to inhibit the formation of virus-driven cytopathic changes against the Wuhan strain (Wild type), Beta, Delta and Omicron variants of SARS-CoV-2. The IC_{50} value of α/β-Punicalagin **(18)** was found to range between 1.210 μM (Omicron Variant) and 13.52 μM (Delta variant) with minimal cytotoxicity. Additionally, (Z)-lespedezic acid **(17)** was also found to inhibit the formation of virus-driven cytopathic effects against the Wuhan strain (Wild type), Beta and Delta variants of SARS-CoV-2 in the plaque-based bioassays. Its IC_{50} value was found to be 10.41 μM (Wuhan variant), 40.49 μM (Beta variant) and 24.07 μM (Delta variant), with minor cytotoxicity observed in healthy Vero E6 cells.

To assess for either additive or synergistic activity, various combinations of the ellagitannins were prepared and tested in viral CPE quantitative assays. Interestingly, the punicalin:α/β-punicalagin (10:1) and punicalin:α/β-punicalagin (3:1) combinations had the lowest EC_{50} value in the spike RBD/ACE2 inhibition assays against the Wuhan variant. Their IC_{50} values were found to be 5.0 μM and 8.4 μM, respectively, for the 10:1 and 3:1 ratios, indicating >2 fold increase in activity relative to the separate punicalin **(23)** and α/β-punicalagin **(18)** solutions. Synergism was determined based on a $p < 0.05$ paired Student's t-test, as determined by the Bliss Independence model.

In order to try and understand the mechanism of action of the two active compounds, we used *in silico* molecular docking. The mechanism of action of punicalin **(23)**, α/β-punicalagin **(18)** and (Z)-lespedezic acid **(17)** was hypothesised to be by the inhibition of viral entry by antagonising the spike RBD/ACE2 interaction. The three compounds were found to make extensive interactions with spike RBD. A comparison of the compound's docking scores found β-punicalagin to have the best docking score, namely -9.217 kcal/mol. Additionally, α-punicalagin, punicalin (**23**) and (Z)-lespedezic acid (**17**) similarly also had good docking scores of -8.686 kcal/mol, -7.891 kcal/mol and -7.917 kcal/mol, respectively. Hydrogen interactions were found to be the key interaction occurring between the compounds and the enzyme. These interactions were found to occur between functional groups of the compounds and a few key amino acid residues required for viral attachment.

Initial biological screening of extracts and major compounds from *S. aethiopicus*, a widely used traditional plant, showed that the hydroxylated lactone of siphonochilone **(25)** (HLS) possessed good antiviral activity against the SARS-CoV-2 virus in whole cell assays. Due to

this observation, HLS **(25)** was isolated and identified following targeted isolation. Additional biological screening of the compound showed that it could inhibit the SARS-CoV-2 virus in a dose-dependent manner in plaque-based bioassays. The compound was found to have an IC_{50} value which ranged between 8.0 µM and 16.0 µM against the Wuhan, Beta and Delta SARS-CoV-2 variants of concern. Notably, the compound exhibited a high selectivity index with minimal cytotoxicity observed against healthy Vero E6 cells. *In silico* molecular dynamic simulations, studies led to the formulation of a hypothesis that the mechanism of action of HLS is by inhibiting the PLpro enzyme of the virus. A semi-synthetic method, utilising methylene blue, a photosensitiser, was developed to produce (stereoselectively) HLS **(25)** from the toxic and inactive precursor compound present in the plant, viz., siphonochilone **(24)**. *In silico* ADME work was conducted, predicting HLS **(25)** to show good druglike qualities important for oral drugs. 2D NMR spectroscopy and SCXRD analysis of the crystals obtained for HLS **(25)** allowed for the determination of the previously undescribed absolute configuration (Flack parameter of 0.01) of the molecule. Notably, the stereochemistry at the 4 chiral centres (C-5, C-4a, C-8a and C-9a) were found to be of the (*S*) and (*R*) configuration for positions C-5 and C-4a, respectively and similarly, (*S*) and (*R*) for stereocenters C-8a and C-9a, respectively. Additionally, the compound was found to crystallise in an orthorhombic space group, facilitated by an intermolecular hydrogen bond between 9a-OH and the carbonyl oxygen of C-8.

Initial biological screening of extracts and fractions of *P. henkelii*, one of South Africa's endangered yellowwood species, showed both the extract and fractions to have potent antagonistic activity against the spike RBD/ACE2 interaction. Of note, the extract and Primary Fraction 4 were found to have an IC_{50} value of 0.56 µg/mL and 0.194 µg/mL, respectively. A bioassay-guided fractionation scheme was employed, which consisted of 2 purification steps. The first purification step relied on a C8 SPE cartridge and a robotic handler to produce semi-purified fractions rich in compounds of a similar polarity. This was done by using a step-wise elution gradient. The second purification step utilised a C18 semi-prep HPLC-PDA-MS instrument where Fraction 4 and Fraction 6 were further processed to isolate 2 compounds found to possess antiviral activity in subsequent biological assays. By using UPLC-HRMS, NMR and SCXRD analysis, the compounds were successfully characterised and identified as inumakilactone B **(52)** and sandaracopimaric acid **(53)**. Of note, inumakilactone B **(52)** was found to crystallise in an orthorhombic space group facilitated by intermolecular hydrogen bonds between C3-O-H and O7. Similarly, sandaracopimaric acid **(53)** was also found to crystallise in an orthorhombic space group facilitated by 2 intermolecular hydrogen bonds between the O18 and H18 atoms of each molecule (via bridging H).

Both compounds were found to have antiviral activity in the enzyme-based and whole-cell bioassays. Of particular interest, inumakilactone B **(52)** was found to inhibit the SARS-CoV-2 virus in a dose-dependent manner in plaque-based bioassays, where the compound was found to have an IC_{50} value ranging from 0.285 µg/mL to 0.35 µg/mL against the Omicron and Beta variants respectively. The compound's bioactivity compared well with those observed for the positive control, remdesivir, for which the IC_{50} value ranged between 0.263 µg/mL to 0.355 µg/mL. The compound exhibited a high selectivity index, with cytotoxicity observed only at high concentrations in healthy Vero E6 cells. Sandaracopimaric acid **(53)** acted selectively against the spike RBD/ACE2 interaction and the M^{pro} enzyme. Its IC_{50} value was found to be 4.143 ± 0.699 µg/mL in the spike RBD/ACE2 interaction screens against the WT(USA-WA1/2020) and 5.4 ± 0.3 µg/mL against the main protease enzyme of the same virus. SCXRD analysis of the crystals obtained for inumakilactone B **(52)** allowed for the determination of the compound's absolute configuration, which was previously undescribed.

In conclusion, 6 antiviral compounds against the SARS-CoV-2 virus were successfully identified from three South African medicinal plants using hyphenated analytical techniques and *in vitro* and *in silico* biological approaches. Further studies are planned to evaluate further the compounds for potential commercial use, of which key studies include *in vivo* efficacy and *in vivo* toxicity studies.

Additional outputs based on this work

Published Papers

- L. Invernizzi; P. Moyo; J. Cassel; C. J. Isaacs; J. M. Salvino; L. J. Montaner, T. Tietjen, V. J. Maharaj. "Use of hyphenated analytical techniques to identify the bioactive constituents of *Gunnera perpensa* L., a South African medicinal plant, which potently inhibit SARS-CoV-2 spike glycoprotein – host ACE2 binding". *Analytical and Bioanalytical Chemistry*, (2022).

Conference Proceeding

- L. Invernizzi, P. Moyo, I. Tietjen, T. Klimkait, V. Maharaj. "*In vitro* screening of South African medicinal plants in the pursuit of anti-viral agents against SARS-CoV-2". GA 69th Annual Meeting, *Planta Medica*, (2021).

Oral Presentations

- L. Invernizzi, P. Moyo, I. Tietjen, T. Klimkait, V. Maharaj. "*In vitro* screening of South African medicinal plants in the pursuit of anti-viral agents against SARS-CoV-2". *GA 69th Annual Meeting*, (2021).
- L. Invernizzi, P. Moyo, I. Tietjen, T. Klimkait, V. Maharaj. "*In vitro* screening of South African medicinal plants in the pursuit of anti-viral agents against SARS-CoV-2". *ChromSA Postgraduate Students Workshop*, (2021).
- L. Invernizzi, P. Moyo, I. Tietjen, T. Klimkait, V. Maharaj. "African medicinal plants as a panacea to the continent's health challenge: Insights on a collaborative endeavour exploring this resource in search of Covid-19 treatment regimens." *ARUA*, (2021).
- L. Invernizzi, P. Moyo, I. Tietjen, J. Cassel, E. T. Register, F. Keeney, J. M. Salvino, F. J. Isaacs, L. J. Montaner, T. Klimkait, L. Urda, V. Maharaj. "High throughput in-vitro screening of South African medicinal plants in the search for novel anti-viral agents against SARS-CoV-2" *National Young Chemists' Symposium*, (2022).
- L. Invernizzi, P. Moyo, I. Tietjen, J. Cassel, E. T. Register, F. Keeney , E. F. Marondedze, K. K. Govender, P. P. Govender, J. M. Salvino, F. J. Isaacs, L. J. Montaner, T. Klimkait, L. Urda, V. Maharaj. "High-throughput screening of South

African medicinal plants in the search for novel anti-viral drug leads against SARS-CoV-2" *SACI*, (2023).

Poster Presentation

- L. Invernizzi, P. Moyo, I. Tietjen, J. Cassel, E. T. Register, F. Keeney , E. F. Marondedze, K. K. Govender, P. P. Govender, J. M. Salvino, F. J. Isaacs, L. J. Montaner, T. Klimkait, L. Urda, V. Maharaj. "In-vitro screening of South African medicinal plants in the search for novel anti-viral agents against SARS-CoV-2." *Ethnopharmacology*, (2022).
- L. Invernizzi, P. Moyo, I. Tietjen, J. Cassel, E. T. Register, F. Keeney , E. F. Marondedze, K. K. Govender, P. P. Govender, J. M. Salvino, F. J. Isaacs, L. J. Montaner, T. Klimkait, L. Urda, V. Maharaj. "High-throughput screening of South African medicinal plants in the search for novel anti-viral drug leads against SARS-CoV-2" *H3D*, (2022).
- I. Tietjen, L. Invernizzi, P. Moyo, J. Cassel, E. T. Register, F. Keeney, J. M. Salvino, F. J. Isaacs, V. Maharaj, L. J. Montaner. "Gunnera perpensa ellagitannins synergistically inhibit multiple SARS-CoV-2 variants" *CROI*, (2021).

Patent

- V. Maharaj, L. Invernizzi, P. Moyo, South African Patent No. PA177413/P. SYNTHESIS OF DERIVATIVES OF SIPHONOCHILONE AND THERAPEUTIC USE THEREOF, (2022).

Table of Contents

List of Figures

Chapter 1

Chapter 2

Chapter 3

Chapter 5

List of Tables

Chapter 2

Chapter 3

Chapter 4

Chapter 5

List of Abbreviations

Abbreviation	Expansion
$(CD_3)_2CO$	Deuterated acetone
µL	Microlitre
µM	Micromolar
µm	Micrometer
^{13}C NMR	Carbon 13 nuclear magnetic resonance
^{1}H NMR	Proton nuclear magnetic resonance
3CLpro	3-chymotrypsin-like cysteine protease
Å	Ångström
ACE2	Angiotensin-converting enzyme 2
ACN	Acetonitrile
ADME	Absorption, distribution, metabolism, and excretion of drugs
AI	Artificial Intelligence
ARC	Agricultural Research Council
AU	Absorbance units
BPI	Base peak ion
BSL-3	Biosafety level 3
CC_{50}	Median cytotoxic concentration
CCDC	Cambridge Crystallographic Data Centre
CCS	Collisional cross-section
CD_2Cl_2	Deuterated dichloromethane
$CDCl_3$	Deuterated chloroform
CHAPS	3-[(3-cholamidopropyl)-dimethylammonio]-1-propanesulfonate
COSY	Correlation spectroscopy
CoV	Coronavirus
CSIR	Council for Scientific and Industrial Research
Da	Daltons
DCM	Dichloromethane
DEPT	Distortionless enhancement by polarisation transfer
dH_2O	De-ionised water
DIA	Data-independent acquisition
DMEM	Dulbecco's Modified Eagle Medium

DMSO	Dimethyl sulfoxide
DNA	Deoxyribonucleic acid
dsDNA	Double Stranded DNA
dsRNA	Double Stranded RNA
DTT	Dithiothreitol
EC_{50}	Median effective concentration
EDTA	Ethylenediaminetetraacetic acid
ER	Endoplasmic reticulum
ESI	Electrospray ionisation
EtOAc	Ethyl acetate
EtOH	Ethanol
eV	Electronvolt
FA	Formic acid
FBS	Fetal bovine serum
Fc	Fragment crystallizable region of an antibody
fs	Femtosecond
g	Gram
G. perpensa	*Gunnera perpensa*
GC	Gas chromatography
GC-MS	Gas chromatography-mass spectrometry
h	Hour
H_{ax}	Axial proton
HEPES	4-(2-hydroxyethyl)-1-piperazineethanesulphonic acid
H_{eq}	Equatorial proton
His-tag	polyhistidine-tag
HLS	Hydroxylated lactone of siphonochilone
HMBC	Heteronuclear multiple bond correlation
HPLC	High-performance (pressure) liquid chromatography
HRMS	High-resolution mass spectrometry
HSQC	Heteronuclear single quantum correlation
HTS	High throughput screening
Hz	Hertz
IC_{50}	Half maximal inhibitory concentration
ICH	International Council for Harmonisation of Technical Requirements for Registration of Pharmaceuticals for Human Use
IK	Indigenous Knowledge

IM-MS	Ion mobility-mass spectrometry
IMS	Ion mobility spectrometry
K	Kelvin
L	Litre
LC	Liquid chromatography
LC_{50}	Median lethal concentration
LC-MS	Liquid chromatography-mass spectrometry
LC-SPE	Liquid chromatography-solid phase extraction
LD_{50}	Median lethal dose
m/z	Mass-to-charge
mDa	Millidaltons
Me	Methyl
MeOD	Deuterated methanol
MeOH	Methanol
mg	Milligram
MIC	Minimum inhibitory concentrations
min	Minute
MIT	Minimum intensity threshold
mL	Millilitre
mM	Milimolar
MOA	Mechanism of Action
M^{pro}	Main Protease (SARS-CoV-2)
mRNA	Messenger RNA
MS	Mass spectrometry
n-Hex	n-Hexane
nM	Nanomolar
nm	Nanometer
NMR	Nuclear magnetic resonance
NOE	Nuclear Overhauser effect
NOESY	Nuclear Overhauser effect spectrometry
ns	Nanosecond
Nsp	Non-structural proteins
°C	Degree Celsius
P. henkelii	*Podocarpus henkelii*
PBS	Phosphate buffered-saline

PDA	Photodiode array detector
PFU	Plaque-forming units
PLpro	Papain-like protease
ppm	Parts per million
prep HPLC-PDA-MS	Preparatory high-performance liquid chromatography photodiode array detection mass spectrometry
PXRD	Powder X-ray diffraction
QTOF-MS	Quadrupole tandem time-of-flight mass spectrometer
RBD	Receptor Binding Domain
RdRp	RNA-dependent RNA polymerase
RNA	Ribonucleic acid
RSD	Relative standard deviation
RT	Retention time
S. aethiopicus	*Siphonochilus aethiopicus*
SARS-CoV-2	Severe acute respiratory syndrome coronavirus 2
SCXRD	Single Crystal X-ray diffraction
SD	Standard deviation
SEM	Standard error of mean
SI	Selectivity index
SIR	Single Ion Recording
SPE	Solid-phase extraction
TC_{50}	Median toxic dose
TCEP	Tris(2-carboxyethyl)phosphine
$TCID_{50}$	Median tissue culture infectious dose
TI	Therapeutic index
TLC	Thin-layer chromatography
TMPRSS2	Transmembrane serine protease 2
UPLC	Ultra-high performance (pressure) liquid chromatography
UPLC-HRMS	Ultra-high-performance liquid chromatography-high resolution mass spectrometry
UPLC-IMS-HRMS	Ultra-high-performance liquid chromatography-ion mobility separation-high resolution mass spectrometry
UV	Ultraviolet
V	Volts
var.	Variant
WHO	World Health Organisation
WT	Wild Type

XRD	X-ray diffraction
λ_{max}	Lambda max

Supplementary Data

Chapter 3

Chapter 4

Chapter 5

Chapter 1

General Introduction

1.1 Natural products and their value in drug discovery

Natural products have historically been relied on for the treatment of many illnesses. They have proven to be an essential source of bioactive compounds, with their use dating back to 2600 BC [1]. Natural products form an extensive reservoir of diverse chemical compounds with novel biological targets and mechanism-of-action (MOA). They still provide an essential resource in the development of new drugs and therapeutics. Their incredible diversity and chemical qualities have made them a vital component of the global pharmaceutical arsenal, with roughly half of the commercially available medicinal drugs being either derived from a natural source or being inspired by them [2–4]. Numerous clinically approved drugs for the treatment of either bacterial, fungal or parasitic diseases originated from natural product chemical scaffolds of either plant or microbial origin. A few well-known examples include the anti-inflammatory drug acetylsalicylic acid **(1),** derived from salicylic acid **(2**) obtained from the bark of the willow tree *Salix alba* L.; the opioid analgesics like morphine **(3)**, codeine **(4)**, thebaine **(5)**, noscapine **(6)**, and papaverine **(7)** from *Papaver somniferum*; digoxin **(8)** used for heart failure, from the *Digitalis lanata* flower; the anticancer drug paclitaxel **(9)** from *Taxus brevifolia*; the muscarinic antagonist and muscarinic agonist, atropine **(10)** and pilocarpine **(11)** isolated from the root of *Datura sp*. and *Pilocarpus jaborandi,* respectively and even the antimalaria drugs artemisinin **(12)** and quinine **(13)**, isolated from *Artemisia annua* and *Cinchona sp*. respectively (Figure 1.1) [1,5–8].

The list of natural product-inspired drugs is similarly long, where natural products' unique chemical scaffolds have inspired the development of many synthetic derivates, with the natural product-inspired antiviral drug remdesivir **(14)** being a key example (Figure 1.1) [9].

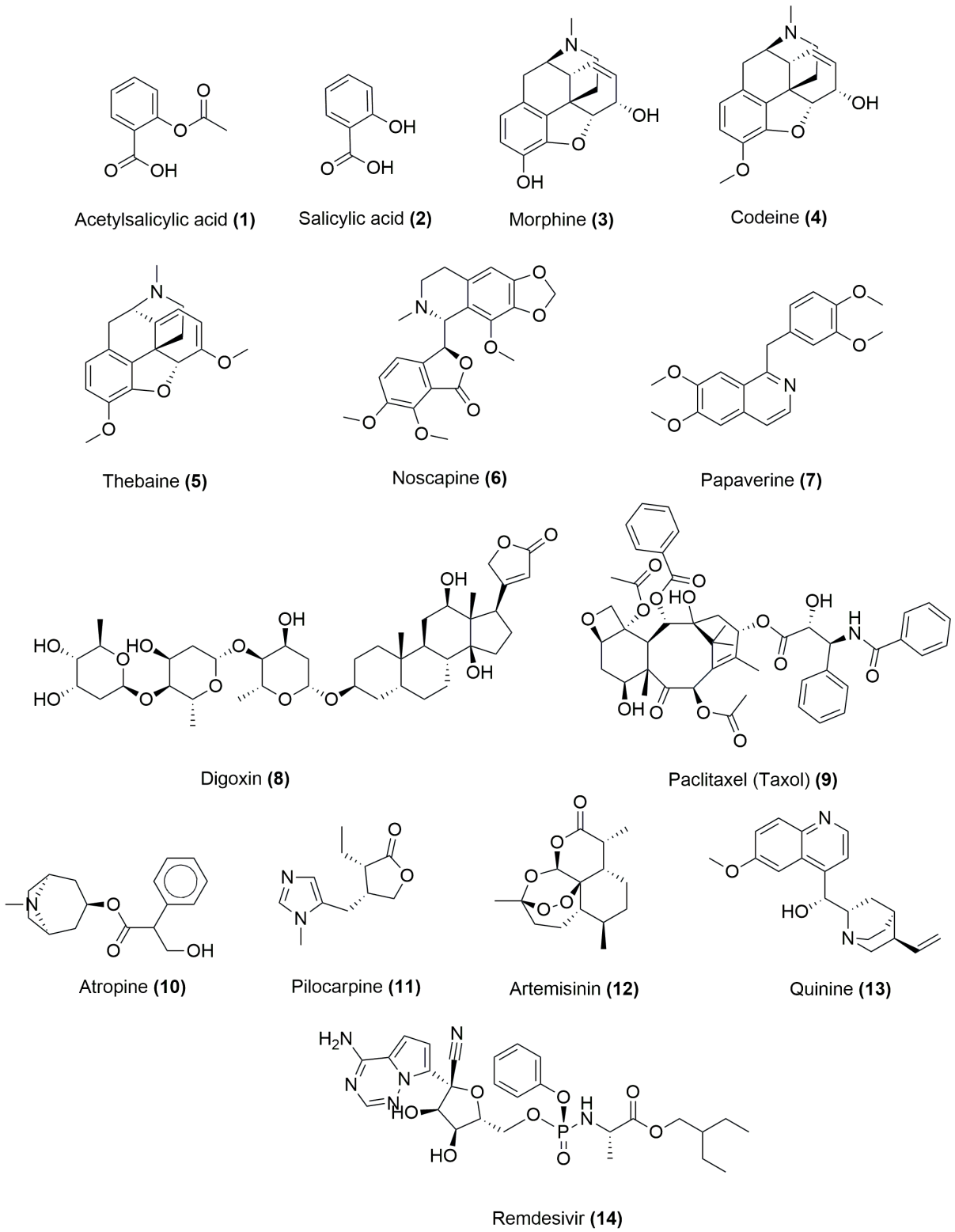

Figure 1.1: Chemical structures of acetylsalicylic acid **(1)**, salicylic acid **(2)**, morphine **(3)**, codeine **(4)**, thebaine **(5)**, noscapine **(6)**, and papaverine **(7)**, digoxin **(8)**, paclitaxel (Taxol) **(9)**, atropine **(10)**, pilocarpine **(11)**, artemisinin **(12)**, quinine **(13)** and remdesivir **(14)**.

Despite the existence of various drug discovery methods like *in silico*-based methods, drug repurposing, hybrid molecule design and structure-based approaches, to name a few, natural product-based drug discovery remains the most enticing route [10].

1.2 Screening libraries and recent advances in technology used in natural product chemistry research

Advances in drug discovery approaches have accelerated in recent years, with great strides taken to overcome the inherent challenges associated with natural product chemistry and drug discovery, ranging from low hit rates to compound purification and characterisation [11].

One of the more significant advances relates to a shift in screening methodology in an attempt to increase the low hit rate in natural product drug discovery. Natural product libraries are being developed to assist in overcoming this problem. Traditionally, bioassay-guided fractionation and purification were among the most popular natural product drug discovery approaches, which relied heavily on the initial screening of crude extracts to determine viable pursuits [12]. However, this approach often takes considerable time and resources with the ever-present possibility of false positives and false negatives arising from initial plant extract screening [13]. A shift towards the pre-fractionation of extracts and the subsequent storage of the fractions in “plant libraries” allows for the high throughput screening of samples against a variety of different biological targets. In this manner, the samples can be stored for an extended period and screened at short notice, being particularly valuable in the event of the discovery of new diseases and the development of pandemics.

A few well-known libraries exist worldwide which hold natural product samples from many biological sources, including marine organisms, plants, fungi and samples of microbial origins. Although these organisations often have their own fractionation method, the overall principle remains the same. A few good examples include AnalytiCon Discovery, Axxam/IMAX Discovery, BioAustralis, Biosortia Microbiomics, NatureBank, Griffith Institute for Drug Discovery, Griffith University and Developmental Therapeutics Program, the National Cancer Institute Natural Products Repository and National Institutes of Health [14].

Despite the adoption and creation of natural product libraries, many other challenges still exist in natural product chemistry, but these are being reduced with the development of newer technologies and practices. Good examples include the advancement of analytical instrumentation like hyphenated techniques including ion-mobility coupled mass spectrometry and the development of ion-mobility libraries to assist in compound identification [15].

Similarly, advances in artificial intelligence (AI) technology to assist with metabolite identification using various libraries and *in silico* fragmentation patterns, like the Waters UNIFI® software [16]; advances in separatory science with newer chromatographic instruments for high throughput compound isolation and advances in the structure elucidation stages with the utilisation of NMR libraries and elucidation software packages. The miniaturisation of equipment like NMR spectrometers with increased sensitivity also reduces bottlenecks. Other advances include genome mining and engineering, which allows the manipulation of genomes to identify genes likely to govern the biosynthesis of select scaffold structures for prioritisation [11].

1.3 Background on COVID-19

1.3.1 SARS-CoV-2 virus and life cycle

The recently discovered severe acute respiratory syndrome coronavirus 2 (SARS-CoV-2) belongs to the *Coronaviridae* family of viruses and falls within the *Coronavirinae* subfamily. The virus is an enveloped, positive-sense single-stranded RNA virus (+ssRNA viruses) with a large genome (27-32 kb) [17]. The genome codes for four structural proteins, namely, the nucleocapsid protein (N), spike protein (S), membrane protein (M) and envelope protein (E), as well as sixteen non-structural proteins (Figure 1.2). The shell of the protein known as the capsid, which encapsulates the nucleocapsid protein, forms a coat over the viral RNA, and has a part in replication and transcription. Additionally, the membrane protein is considered the main organiser for assembling the coronavirus and is found predominantly and most abundantly on the surface of the virus. The spike protein is also integrated into the virus's surface and mediates attachment, fusion and entry into the host cell. The spike protein is a transmembrane glycoprotein which forms homotrimers that protrude from the viral surface. The S-protein consists of two functional subunits, viz., the S1 and S2 subunits which play major roles in the binding via the receptor-binding domain (RBD) (S1) and fusion of the virus (S2) (Figure 1.2). Additionally, the envelope protein also plays an imperative role in assembling the virus, ensuring permeability of the host cell membranes and interaction between the virus and the host cell. The virus's genetic material is encapsulated by a lipid envelope [18,19].

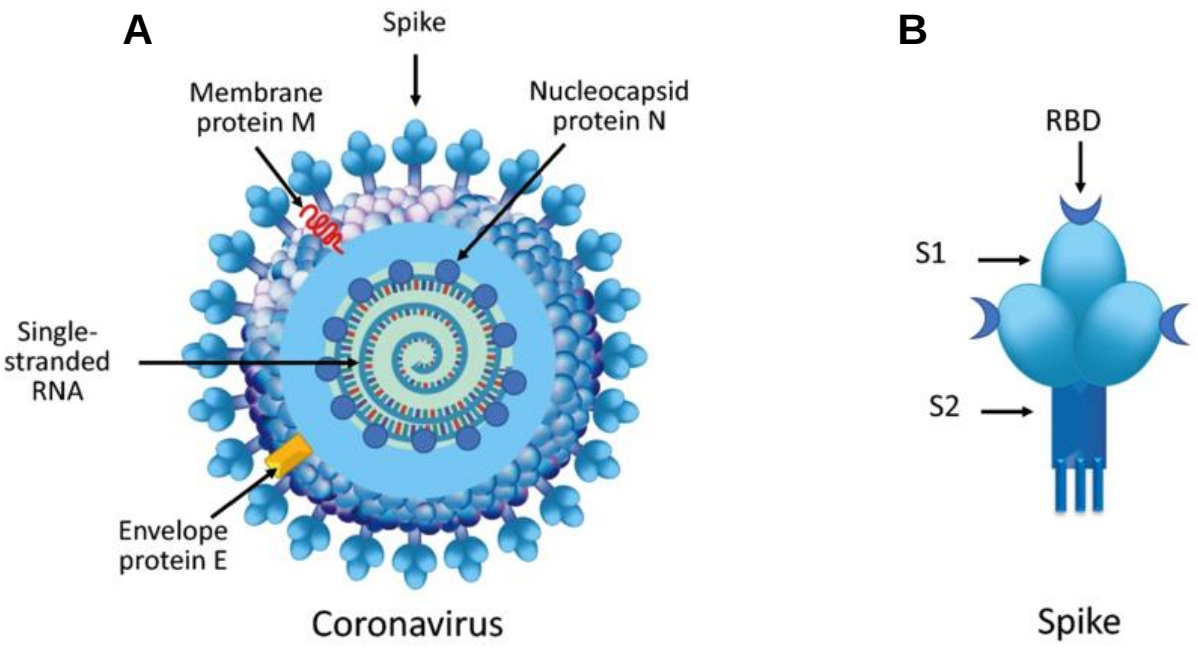

Figure 1.2: (**A**) Illustration of the coronavirus (SARS-CoV-2) structure with the ssRNA, envelope, membrane, spike and nucleocapsid protein highlighted. (**B**) Structure of the spike protein which consists of the S1, S2 and receptor binding domain (RBD). Image by Rossi et al. (2020), licensed under CC BY 4.0 [89].

The non-structural proteins (Nsp1 to Nsp16) are involved in various stages of the life cycle and play an integral role in RNA processing/replication, modification of the endoplasmic reticulum (ER) membranes, polyprotein processing, ssRNA-binding, cap methylation, RNA-dependent RNA polymerase (RdRp) replication/transcription, and even proofreading (Nsp14) [19].

Of the various non-structural proteins, the main protease (M^{pro}), helicase and papain-like protease (PLpro) are among the most commonly reported. The M^{pro} enzyme (Nsp 5) plays a fundamental role in mediating viral replication and transcription of the viral genes. The enzyme forms a homodimer (protomer A and B), with each protomer consisting of three subdomains, two of which form the substrate binding pocket. It functions by hydrolysing the polypeptide at >11 highly conserved sites [20].

The helicase protein (Nsp 13) plays a critical role in viral replication. It consists of 5 domains: a Zinc binding domain, a “stalk” domain, a beta-barrel 1B domain and two “RecA-like” subdomains. These two subdomains play an essential role in nucleotide binding and hydrolysis. The protein utilises energy from the hydrolysis of NTP for the unwinding of the

dsRNA during replication and formation of the viral 5′ mRNA cap. The protein also interacts with RdRp and cooperates with the replication-transcription complex, where the interaction stimulates its function [21].

The viral PLpro (domain of Nsp 3) is required for viral polyprotein processing and is used to generate a functional replicase complex. The protein also functions as an evasion mechanism against host immune responses, where it acts by cleaving post-translational modifications on the host proteins [22]. The protein has an N-terminal ubiquitin-like (UBL) domain and a C-terminal ubiquitin-specific protease (USP) domain, which function catalytically by cleaving ubiquitin (Ub) or ISG15 modifications from host proteins [23].

In reference to the virus' pathogenicity, the virus is spread mainly through the air in droplets from infected people or through indirect contact with contaminated surfaces [24–26]. The life cycle of the virus subsequently begins by gaining entry into the host's epithelial cells through interaction and binding with the cell surface protein angiotensin-converting enzyme 2 (ACE2) through the Receptor Binding Domain (RBD) of its spike (S) protein. The priming of this binding and entry is facilitated through the virus' cellular transmembrane serine protease 2 protein (TMPRSS2) [27]. The priming of this binding results in the subsequent fusion of the viral and cellular membranes. In the absence of TMPRSS2 on the host cell, the virus can still gain entry via endocytosis, and endosomal maturation [28]. After fusion, the viral RNA is released into the host cell cytoplasm for subsequent uncoating and replication [29]. Thereafter, viral RNA is translated into structural and non-structural proteins prior to RNA replication, budding, assembly and subsequent release of virions by exocytosis and host cell apoptosis and lysis (Figure 1.3) [30,31].

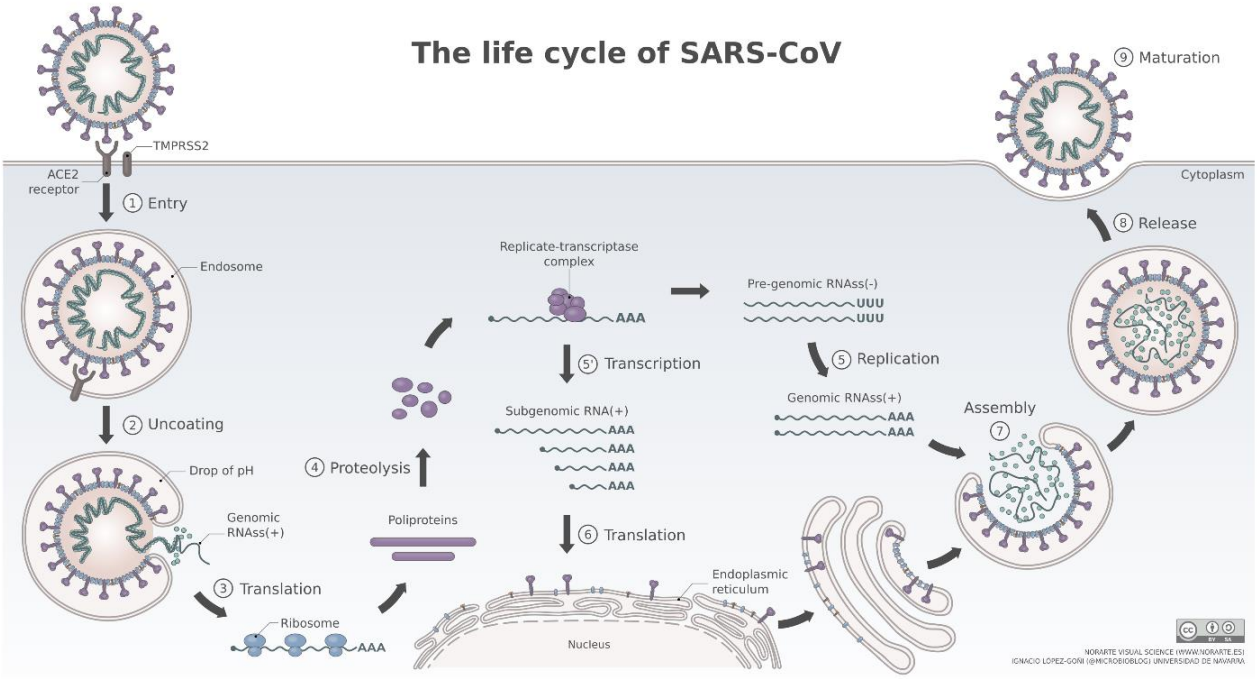

Figure 1.3: Life cycle of the SARS-CoV-2 virus, published by Asensio V. (2020) under CC BY-SA 4.0.

Symptoms of the disease resemble those of colds and flu, and the symptoms experienced previously with MERS and SARS cases. The symptoms are broad and range considerably amongst the population, but fever (≥ 38.0 °C), myalgia or fatigue, cough, sore throat, dyspnea, headache, loss of smell and taste, and diarrhoea remain the most commonly reported [32–34]. Symptoms of COVID-19 range in severity from non-existent (asymptomatic) to severe, where hospitalisation and possible ventilation are required, and the risk of death is high. The exact cause of these significant variations in symptoms and signs is still being researched, but certain risk factors are considered leading causes of severe COVID-19. Risk factors include age, where an increase in age correlates to an increase in severe COVID-19 risk; inactivity and underlying medical conditions, especially those that affect the pulmonary, renal, cardiovascular and immune systems (like cancer, smoking, obesity, diabetes and hypertension) and recently, vaccination status [35,36].

Since the emergence of the first COVID-19 variant in 2019, the virus has spread worldwide, unselectively, with only a few countries unaffected [37]. Since the first case, numerous variants of the virus have emerged, with a select few being of particular concern due to their severe health-affecting properties. According to the WHO, these “variants of concern” are classified

based on their ability to: “Increase in transmissibility or detrimental change in COVID-19 epidemiology; OR increase in virulence or change in clinical disease presentation; OR decrease in effectiveness of public health and social measures or available diagnostics, vaccines, therapeutics” [38].

Since the onset, five variants have been characterised as “variants of concern” by the WHO. These are the Alpha (B.1.1.7), Beta (B.1.351), Gamma (P.1), Delta (B.1.617.2) and the only current circulating variants of concern, Omicron (B.1.1.529) [38]. Collectively, these variants have driven the devastating waves of the pandemic, which currently (December 2022) stand at ca. 651.9 million cases and ca. 6.6 million deaths globally. Of these, ca. 4.05 million cases and ca. 102 550 deaths originated from South Africa [39].

1.3.2 Drug targets and current treatment for COVID-19

The SARS-CoV-2 virus relies heavily on multiple proteins and enzymes to successfully replicate and propagate the virus. These heavily regulated processes require crucial enzymes and proteins, which can, theoretically, all be targets of inhibition by potential anti-CoV drugs [40]. Naturally, some viral host processes can also be objects of inhibition, but only virus-based targets are discussed for brevity and relevance.

Of the various druggable targets, both the structural and non-structural proteins can be druggable targets, although structural proteins tend to be less genetically conserved and more prone to mutations and, as such, lead to low efficacy in drugs.

Of the structural proteins, the S-protein (and specifically the RBD, due to its essential role in viral entry), remains a target of interest and especially for prophylactic treatment. Here, drugs are sought to prevent or disrupt the initial binding of the viral spike protein and the host ACE2 receptor with the S1 subunit [41]. Despite the spike protein being subject to major mutations in the various variants, some drugs have been shown to maintain selectivity and activity against the various COVID-19 variants, where antibodies (both monoclonal and endogenous) fail [42]. Although no pharmaceutical drug currently exists that targets the viral S-protein or prevents the highly preserved interaction of the spike and the ACE2 receptor, vaccine and monoclonal antibodies function in this way. These, however, are prone to reduced activity against the different variants [43].

Of the 16 highly conserved nsps, and those well-researched with known essential functions, like the viral M^{pro}, PLpro, RdRp and helicase, present possible targets for antiviral drugs [30].

In general, proteases are investigated as drug targets which have resulted in several approved antiviral drugs against HIV and even hepatitis C [44].

The SARS-CoV-2 M^{pro} plays an essential role in viral replication and shares many similarities (96%) with the original SARS-CoV-1 virus. The protein does not have a closely related homologue in humans but plays a pivotal role in the life cycle of the virus, making it an ideal drug target with a lower risk of non-selective activity and toxicity to humans [45]. Interestingly, the commercial drug, Paxlovid, is a known M^{pro} inhibitor [46]. As with the M^{pro}, PLpro shares many similarities with the initial SARS-CoV-1 virus (83%) and also functions in viral replication and dysregulation of signalling cascades in infected cells [22]. Due to its vital function in the virus' life cycle, PLpro may also be a feasible pharmaceutical target.

The RdRp also presents a viable target for inhibition. The enzyme is crucial to the coronavirus' life cycle and is well-conserved among other viruses with RNA-based genomes [47]. The RdRp forms a complex with cofactors nsp7 and nsp8 for the stimulation of the protease function [48]. This complex also forms a complex with other nsp's for polymerisation, proofreading and cap-modifying activity and shares 96% similarity in the genome relative to SARS-CoV-1 [49]. Interestingly, the FDA-approved drugs remdesivir and molnupiravir both function as RdRp inhibitors [50]. As with M^{pro}, the RdRp has no homologue in humans, which makes it a viable antiviral target with high selectivity toward the virus.

Finally, viral helicase also has an essential function in the virus' life cycle and forms part of the replication-transcription complex of various coronaviruses and also catalyses the separation of dsRNA by hydrolysis of NTPs [51]. The protein is well conserved in iridoviruses, and inhibition of protein would result in the inability to unwrap dsRNA and hence, the inability to replicate the genome [52].

With the considerable genetic similarities of the nsps in SARS-CoV-2 and other coronaviruses, and the fact that many of their crystal structures have been published, the chances of finding and developing an inhibitor and antiviral drug against these targets increase considerably. Naturally, based on the high similarity in the genome between the SARS-CoV-2 and SARS-CoV-1 virus, some research focuses on the rescreening of antiviral agents previously active against SARS-CoV-1 [53].

Vaccination efforts are still ongoing, with the four current FDA-approved vaccines (for emergency use) being [54]: BNT162b2 (Pfizer-BioNTech COVID-19 vaccine) (monovalent and bivalent mRNA-based vaccine), mRNA-1273 (Moderna COVID-19 vaccine) (monovalent and bivalent mRNA based vaccine), NVX-CoV2373 (Novavax COVID-19 vaccine)

(monovalent adjuvanted recombinant protein vaccine) and Ad26.COV2.S (Janssen/Johnson & Johnson COVID-19 vaccine) (monovalent adenoviral vector vaccine).

In terms of COVID-19 treatment, due to the large variations in symptoms among the population, the management of COVID-19 remains largely symptomatic for mild and moderate cases of the disease and the low-risk population. Here, treatment comprises primarily of drugs for symptomatic relief. For severe cases of the illness, which occur predominantly in the population with risk factors and chronic diseases (especially those affecting vascular endothelium of different organs), treatment typically includes one or more of the following: antiviral drugs like molnupiravir (RdRp inhibitor), Paxlovid (M^{pro} inhibitor) and remdesivir, monoclonal antibodies like bamlanivimab/etesevimab, casirivimab/imdevimab, sotrovimab and bebtelovimab, anti-inflammatory drugs like dexamethasone and immunoregulator drugs like baricitinib, tocilizumab [55,56]. The above treatments are currently FDA-approved for emergency use [57].

1.4 Plants traditionally used for treating respiratory illnesses

From a traditional medicine perspective, numerous plant remedies have for centuries served as a source of primary health care for the treatment of numerous diseases [58]. Much like other low-income 3rd world countries, South Africa relies, and has relied, on traditional medicine for centuries. Due to the high costs of western medicine and its scant availability in rural settings, traditional medicine is still used by a vast majority of people in South Africa [59]. It is, then, not unusual that traditional medicine is also used for the treatment of respiratory diseases, viruses and their associated symptoms.

The most prominent plant families used medicinally in South Africa include members from the Fabaceae, Asteraceae, and Rubiaceae families [60]. From these families, active compounds that have been isolated include flavonoids, polyphenols and alkaloids. The reported mechanism of action is either the inhibition of proliferation of the respiratory virus or alleviating of the associated symptoms by, for example, suppressing the innate inflammatory response [61,62].

An ethnobotanical survey has reported that ca. 3000 South African plants are used traditionally, and over 250 of these are used for treating respiratory illnesses [63,64].

Other countries also rely on medicinal plants for the treatment of respiratory illnesses. Pakistan, for example, has 384 species of plants belonging to 84 families with documented use in respiratory illnesses [61]. Interviews with local health healers in India reported that at

least 82 plant species are used to treat seven types of respiratory diseases like influenza, asthma, tuberculosis, bronchitis, pneumonia, lung disorder and cough and cold [65].

This study, however, focuses on medicinal plant species from South Africa, for which a record exists describing the traditional use in the treatment of respiratory illnesses, colds and flu and its associated symptoms.

1.5 Natural products as a potential source of antiviral drugs

1.5.1 History of natural antiviral products against respiratory illnesses

Natural products provide interesting sources of antiviral activity against numerous respiratory disease-causing viruses. Against the influenza virus, the activity of some Chinese herbal products has been proven in randomised, double-blind, placebo-controlled clinical trials with plants improving patients' recovery time by 17% and significantly reducing the severity of the illness [66]. Beyond seasonal influenza infections, plant remedies have proven their competence against some of the most virulent influenza strains, including the H1N1 Influenza A virus, which caused the calamitous 'Spanish flu' in 1918. For example, the fatality rate amongst patients treated with herbal products was 0.6%, significantly lower than for those who did not use these remedies (reported to be 3%). This success rate was reported to have been replicated in an earlier influenza pandemic between 1889 and 1890 [67].

Natural products have also been used as a source of regimens for treating other respiratory infections caused by the SARS coronavirus. Since their discovery in 2003, the SARS coronavirus families sparked many studies aimed at providing remedies for the treatment of the two most profound pandemics they caused, namely SARS in 2003 and the Middle East Respiratory Syndrome (MERS) in 2012. Natural products emerged as a potential remedy with some plant species, e.g. *Lycoris radiata* (Amaryllidaceae) and *Artemisia annua* (Asteraceae), demonstrating *in vitro* antiviral activity against SARS-CoV-1 in a phenotypic screen [68]. Apart from phenotypic screening, some extracts have demonstrated activity against key enzymes in the SARS-CoV-1 virus, such as the 3C-like protease (3CLpro) and the RdRp [69]. A number of small natural molecules were screened against SARS-CoV-1 and demonstrated exceptional activity in nM to submicromolar scale potency; as an example, the alkaloid compound lycorine isolated from *L. radiata* had an IC_{50} of 15.7 nM against SARS-CoV-1, with a selectivity index of >900 in Vero and HepG2 cell lines [68]. Antiviral activity of more natural product compounds like terpenoids, sesquiterpene lactones, alkaloids and lignoids have also been demonstrated in numerous studies [70–72]. On the other hand, some compounds,

including the flavonoid luteolin and tetra-O-galloyl-β-d-glucose were shown to inhibit entry of SARS-CoV-1 into host cells by binding with the surface spike protein of SARS-CoV-1 [73]. Similarly, three Chinese herbal products and the compound emodin were shown to inhibit SARS coronavirus spike protein and ACE2 interaction, with emodin also blocking the infectivity of S protein-pseudotyped retrovirus to Vero E6 cells [74]. Beyond these *in vitro* and *in vivo* experiments, herbal drugs such as Lianhua Qingwen capsules and Radix isatidis granules were used clinically for the treatment of SARS in 2003 and MERS in 2012 [75].

1.5.2 Natural products as a source of treatment for COVID-19

Prior successes of natural products in antiviral drug research and against previous coronaviruses have provided optimism for the current use of natural products in drug discovery against the novel SARS-CoV-2 virus. Both extracts and pure natural product compounds have shown activity against the virus.

One species that has generated high interest is the herb *A. annua,* along with the herbal product called Covid-Organics 9a herbal product made of *A. annua*. Recently, ArtemiLife screened *A. annua* along with Covid-Organics and *A. afra* against SARS-CoV-2 *in vitro* with data from their study demonstrating these products block viral replication albeit only at high concentrations (IC_{50} ranging between 0.65 mg/ml to 7.73 mg/ml while displaying selectivity index of between 5 to 20) [76]. In contrast to this study, Nair et al. (2021) [77], showed *A. annua* to be more potent against not just the wild-type SARS-CoV-2, but also against the variants B1.1.7 and B1.351 (501Y.V2), which emerged from the United Kingdom and South Africa, respectively.

One of the most advanced studies of natural products as anti-SARS-CoV-2 is that undertaken by the Austrian-based company MGC Pharmaceuticals Ltd. It recently successfully completed phase II clinical trials of its product ArtemiC™, which consists of curcumin, artemisinin, vitamin C, and *Boswellia serrata* (Burseraceae) extract. The company completed the phase II double-blinded trials on 50 infected patients across three independent hospital sites in Israel and India; 50 patients were recruited to the trial, 33 in the treatment group and 17 in the placebo group. The full results demonstrated it to improve the health status, shortened durations of abnormal SpO2 levels, oxygen supplementation and fever of COVID-19 patients delivering a National Early Warning Score (NEWS) of less than or equal to 2. None of the patients in the treatment group required mechanical ventilation or admission to intensive care, whereas all of these events were reported in the placebo group [78].

Recent research has also shown some pure natural product compounds to have potent antiviral activity against the SARS-CoV-2 virus. Of particular note, the natural stilbenoid

(-)-Hopeaphenol was found to inhibit various COVID-19 variants with an EC_{50} of between 10.2-23.4 μM in CPE bioassays [42]. Tylophorine isolated from the medicinal plant *Cynanchum komarovii* AL. which was found to have an EC_{50} = 0.030 μM in Vero E6 cells, Gallinamide A from the marine cyanobacteria *Schizothrix* genus, which has an EC_{50} = 0.028 μM in cathepsin L-mediated endosomal entry assays, cordycepin from the traditional medicine *Cordyceps militaris* Link with an EC_{50} = 2.01 μM in Vero E6 cells, Homofascaplysin A from the marine sponge *Fascaplysinopsis reticulata* with an EC_{50} = 1.1 μM in Calu-3 cells, Licorice-saponin A3 isolated from the medicinal plant *Glycyrrhiza uralensis* Fisch. with an EC_{50} = 0.075 μM in Vero E6 cells and bufotalin, a cardiotoxic bufanolide steroid, cardiac glycoside secreted by a number of toad species was found to have an IC_{50} = 0.016-0.019 μM in Vero E6 cells [79].

1.6 Problem statement and justification

Despite the highly commendable introduction of several SARS-CoV-2 vaccines, the emergence of more transmissible variants is already undermining their efficacy [80]. Most concerning is the fact that some of the new variants have mutations that may render them less sensitive to vaccine-elicited antibodies.

In addition to the emerging threat of more transmissible and virulent variants, another matter of great concern surrounding vaccines (particularly within the first year of availability of the first vaccine) was the fact that low-income countries struggled to access significant quantities of vaccines and, indeed, vaccinate the people, particularly in rural areas [81,82]. Vaccine availability is not the only issue contributing to low vaccination rates in some low-income countries, but internal distribution and vaccine hesitancy could also be possible contributing factors. For example, in South Africa, research conducted by Engelbrecht et al. (2022), found that three out of five participants were unvaccinated, with 44.6% claiming vaccine hesitancy as the cause. The same research found race, interactive-critical vaccine literacy, flu vaccination status, the governmental ability to successfully roll out the vaccines and vaccine risk perception to be other leading causes [83].

In the absence of a widely accepted vaccine, the development and discovery of anti-SARS-CoV-2 small molecules represent a viable complementary strategy to treat and prevent COVID-19. Currently, there are only a few FDA-approved antiviral drugs for the treatment of COVID-19, these being tocilizumab, remdesivir and baricitinib. Paxlovid and molnupiravir remain under the FDA's EUA-authorised list. The drugs tocilizumab, remdesivir and baricitinib remain exclusively for hospitalised patients with oxygen supplementation or on ventilators [84].

Despite the existence of these antiviral drugs, drug costs and availability to low-income countries remain a considerable concern. Consequently, there remains an urgent need to discover and develop a cheaper, more efficacious treatment regimen (which ideally can be self-administered either orally or by inhalation).

In these unprecedented times, all possible avenues should be probed for possible drug leads. Toward addressing these issues, natural products represent an extensive reservoir of diverse molecules with novel biological targets and MOA. These qualities have made them a significant component of the global pharmaceutical arsenal, with over half of medicinal drugs commercially available today having been derived either from natural products or inspired by them [2–4]. From an alternative medicine perspective, plant-based traditional medicines (PTMs) have been documented in ethnobotanical studies for their use in the treatment of many diseases, including those affecting the respiratory system. Over 70% of South Africans use traditional medicines to meet their primary healthcare needs [85]. Considering this statistic, it is only logical to assume that a significant component of the South African population (and indeed a large portion of the Sub-Saharan African region population) who get infected with COVID-19 and develop symptoms will most likely visit their local healer for healthcare. Given the urgent need to find COVID-19 therapies in this environment, it is imperative that we identify which medicinal plants might be the most efficacious against SARS-CoV-2.

Due to the broader bioactivity and specificity of antivirals compared to vaccines, antiviral drugs have an increased chance of remaining effective against different strains of viruses that emerge each season. From a traditional medicine perspective, numerous plant-based herbal remedies have for centuries served as a source of primary health care for the treatment of respiratory diseases and their associated symptoms [86,87]. Plant extracts do have the added advantage in that they may have multiple antiviral compounds present that target multiple viral processes, thus reducing the risk of viral resistance over time.

In light of the challenging environment in which South Africa, Africa and the rest of the world find themselves, the current proposed study seeks to provide complementary avenues to supplement current drugs and vaccine effects in the global COVID-19 challenge. This was achieved by exploring the South African Indigenous Knowledge Systems and flora in search of readily available, affordable and highly efficacious herbal preparations and natural compounds against SARS-CoV-2. This was done by using hyphenated analytical techniques and HTS methodology to identify candidates ready for pre-clinical and clinical research for ultimate upscale and commercialisation, well beyond the typical mainstream *in silico* and enzymatic-based bioassays.

1.7 Study aims and objectives

1.7.1 Aim

The aims of the study were:

a. To contribute to the setup of a South African natural product repository by investigating a selected subset of plants for use against SARS-CoV-2.

b. To isolate and identify antiviral compounds against SARS-CoV-2 from traditionally used South African plants by employing hyphenated analytical techniques.

1.7.2 Objectives

The overall objectives of the study were:

- The selection of a subset of plants with antiviral potential against SARS-CoV-2 using online electronic databases like Google Scholar, Scopus, Scifinder and Zulu Medicinal Plants: An Inventory by Anne Hutchings [88] and literature by using keywords and a scoring criterion.
- The collection, high-throughput extraction and fractionation of the selected plants.
- The identification and purification of bioactive compounds from plant extracts using chromatography-based methods like UPLC-HRMS, flash chromatography, and preparative HPLC-PDA-MS.
- Biological screening of extracts, fractions and pure compounds in enzyme-based bioassays against the SARS-CoV-2 spike RBD/ACE2 interaction and M^{pro} enzyme and in whole cell plaque-based bioassays.
- Structure elucidation of pure bioactive compounds using spectroscopic analytical techniques such as NMR, MS, UV and SCXRD analyses.
- *In silico* molecular docking and molecular dynamic simulation of select bioactive compounds to determine their possible mechanisms of action.

Chapter 2 objectives:

- Literature survey and plant selection.
- SARS-CoV-2 Bioassays background and methodology
- Collection of plant material, extraction and fractionation for subsequent HTS against SARS-CoV-2.

- Bioassay screening of extracts and fractions against SARS-CoV-2 M^{pro} enzyme and spike RBD/ACE2 interaction (AlphaScreen) for biological hit identification.
- Selection of biological “hits” for further investigation.

Chapter 3 objectives:

- UPLC-HRMS analysis of *Siphonochilus aethiopicus* rhizome samples.
- Extraction of *S. aethiopicus* rhizomes and mass-directed isolation of the hydroxylated lactone of siphonochilone (HLS).
- 2D NMR, SCXRD and MS analysis of HLS for absolute structure determination.
- Biological assays of HLS in SARS-CoV-2 enzyme-based and plaque-based bioassays.
- Cytotoxicity analysis of HLS in Vero E6 cells.
- Semi-synthetic conversion of siphonochilone to HLS.
- Molecular docking and molecular dynamic simulations of HLS against the SARS-CoV-2 helicase and PLpro enzyme.
- *In silico* ADME analysis of HLS.

Chapter 4 objectives:

- Extraction and fractionation of *Gunnera perpensa* L.
- Biological screening of *G. perpensa* extract and fractions in SARS-CoV-2 enzyme-based and plaque-based bioassays.
- UPLC-IMS-HRMS analysis of the bioactive fraction of *G. perpensa* to identify the potential bioactive compounds.
- UV- and Mass-directed isolation of α/β-punicalagin using flash chromatography and HPLC-PDA-MS.
- Bioactive compound identification and structure elucidation using NMR, UPLC-IMS-HRMS and analytical reference standards.
- Biological assays of the isolated pure compounds and analytical standards against the SARS-CoV-2 spike RBD/ACE2 interaction and M^{pro} enzyme and in plaque-based bioassays, including cytotoxicity studies in Vero E6 cells.
- *In silico* molecular docking of bioactive compounds against the SARS-CoV-2 spike protein.

Chapter 5 objectives:

- Collection, extraction and fractionation of *Podocarpus henkelii* fruit.

- Biological screening of *P. henkelii* samples against the SARS-CoV-2 Spike RBD/ACE2 interaction, M^{pro} enzyme and in plaque-based bioassays of SARS-CoV-2.
- UPLC-HRMS analysis of the bioactive fractions and samples.
- Mass-directed purification of select compounds, namely inumakilactone B and sandaracopimaric acid.
- Structure elucidation of inumakilactone B using mass spectrometry and SCXRD analysis.
- Structure elucidation of sandaracopimaric acid using NMR, HRMS and SCXRD analysis.
- Biological testing of the isolated compounds against the SARS-CoV-2 spike RBD/ACE2 interaction, the M^{pro} enzyme and plaque-based bioassays in Vero E6 cells
- Cytotoxicity studies of bioactive compounds in Vero E6 cells.

Chapter 6 provides a general conclusion of the study.

1.8 References

1 D. A. Dias, S. Urban and U. Roessner, A Historical overview of natural products in drug discovery, *Metabolites*, 2012, **2**, 303–336.

2 S. Mathur and C. Hoskins, Drug development: Lessons from nature (Review), *Biomed Rep*, 2017, **6**, 612–614.

3 E. C. Barnes, R. Kumar and R. A. Davis, The use of isolated natural products as scaffolds for the generation of chemically diverse screening libraries for drug discovery, *Nat. Prod. Rep.*, 2016, **33**, 372–381.

4 E. Lautié, O. Russo, P. Ducrot and J. A. Boutin, Unraveling plant natural chemical diversity for drug discovery purposes, *Front. Pharmacol.*, 2020, **11**, 397

5 S. Mathur and C. Hoskins, Drug development: Lessons from nature., *Biomed. reports*, 2017, **6**, 612–614.

6 D. I. Macht, A contribution to the chemical-pharmacodynamic relationships of atropine and homatropine, *J. Am. Pharm. Assoc.*, 1922, **11**, 882–897.

7 K. M. O'Shaughnessy, eds. P. N. Bennett, M. J. Brown and P. B. T.-C. P. (Eleventh E. Sharma, Churchill Livingstone, Oxford, 2012, 372–381.

8 P. F. Uzor, V. D. Prasasty and C. O. Agubata, Natural products as sources of antimalarial drugs, *Evidence-Based Complement. Altern. Med.*, 2020, 9385125.

9 A. M. Hamoda, B. Fayed, N. S. Ashmawy, A.-N. A. El-Shorbagi, R. Hamdy and S. S. M. Soliman, Marine sponge is a promising natural source of anti-SARS-CoV-2 scaffold, *Front. Pharmacol.*, 2021, **12**, 666664

10 M. Lopez, M. Leroy, C. Etievant, F. Ausseil, A. Gagnon and P. Arimondo, eds. G. Egger and P. B. T.-D. D. in C. E. Arimondo, Academic Press, Boston, 2016, pp. 63–95.

11 A. G. Atanasov, S. B. Zotchev, V. M. Dirsch, I. E. Orhan, M. Banach, J. M. Rollinger, D. Barreca, W. Weckwerth, R. Bauer, E. A. Bayer, M. Majeed, A. Bishayee, V. Bochkov, G. K. Bonn, N. Braidy, F. Bucar, A. Cifuentes, G. D'Onofrio, M. Bodkin, M. Diederich, A. T. Dinkova-Kostova, T. Efferth, K. El Bairi, N. Arkells, T.-P. Fan, B. L. Fiebich, M. Freissmuth, M. I. Georgiev, S. Gibbons, K. M. Godfrey, C. W. Gruber, J. Heer, L. A. Huber, E. Ibanez, A. Kijjoa, A. K. Kiss, A. Lu, F. A. Macias, M. J. S. Miller, A. Mocan, R. Müller, F. Nicoletti, G. Perry, V. Pittalà, L. Rastrelli, M. Ristow, G. L. Russo, A. S. Silva, D. Schuster, H. Sheridan, K. Skalicka-Woźniak, L. Skaltsounis, E. Sobarzo-Sánchez, D. S. Bredt, H. Stuppner, A. Sureda, N. T. Tzvetkov, R. A. Vacca, B. B. Aggarwal, M. Battino, F. Giampieri, M. Wink, J.-L. Wolfender, J. Xiao, A. W. K. Yeung, G. Lizard, M. A. Popp, M. Heinrich, I. Berindan-Neagoe, M. Stadler, M. Daglia, R. Verpoorte, C. T. Supuran and the I. N. P. S. Taskforce, Natural products in drug discovery: advances and opportunities, *Nat. Rev. Drug Discov.*, 2021, **20**, 200–216.

12 G. R. Eldridge, H. C. Vervoort, C. M. Lee, P. A. Cremin, C. T. Williams, S. M. Hart, M. G. Goering, M. O'Neil-Johnso and L. Zeng, High-throughput method for the production and analysis of large natural product libraries for drug discovery, *Anal. Chem.*, 2002, **74**, 3963–3971.

13 A. Fallarero, L. Hanski and P. Vuorela, How to translate a bioassay into a screening assay for natural products: general considerations and implementation of antimicrobial screens, *Planta Med.*, 2014, **80**, 1182–1199.

14 Natural Product Libraries | NCCIH, https://www.nccih.nih.gov/grants/natural-product-libraries, (accessed 24 December 2022).

15 J. Goshawk, G. Barknowitz and M. Mccullagh, The development of a natural products library using ion - mobility enabled mass spectrometry, 2019.

16 L. Deng, A.-M. Shi, H.-Z. Liu, N. Meruva, L. Liu, H. Hu, Y. Yang, C. Huang, P. Li and Q. Wang, Identification of chemical ingredients of peanut stems and leaves extracts using UPLC-QTOF-MS coupled with novel informatics UNIFI platform, *J. Mass Spectrom.*, 2016, **51**, 1157–1167.

17 M. Pal, G. Berhanu, C. Desalegn and V. Kandi, Severe Acute Respiratory Syndrome

Coronavirus-2 (SARS-CoV-2): An update, *Cureus*, 2020, **12**, e7423.
18 M. Y. Wang, R. Zhao, L. J. Gao, X. F. Gao, D. P. Wang and J. M. Cao, SARS-CoV-2: Structure, biology, and structure-based therapeutics development, *Front. Cell. Infect. Microbiol.*, 2020, **10**, 1–17.
19 S. Boopathi, A. B. Poma and P. Kolandaivel, Novel 2019 coronavirus structure, mechanism of action, antiviral drug promises and rule out against its treatment, *J. Biomol. Struct. Dyn.*, 2021, **39**, 3409–3418.
20 J. Lee, L. J. Worrall, M. Vuckovic, F. I. Rosell, F. Gentile, A.-T. Ton, N. A. Caveney, F. Ban, A. Cherkasov, M. Paetzel and N. C. J. Strynadka, Crystallographic structure of wild-type SARS-CoV-2 main protease acyl-enzyme intermediate with physiological C-terminal autoprocessing site, *Nat. Commun.*, 2020, **11**, 5877.
21 J. A. Newman, A. Douangamath, S. Yadzani, Y. Yosaatmadja, A. Aimon, J. Brandão-Neto, L. Dunnett, T. Gorrie-stone, R. Skyner, D. Fearon, M. Schapira, F. von Delft and O. Gileadi, Structure, mechanism and crystallographic fragment screening of the SARS-CoV-2 NSP13 helicase, *Nat. Commun.*, 2021, **12**, 4848.
22 D. Shin, R. Mukherjee, D. Grewe, D. Bojkova, K. Baek, A. Bhattacharya, L. Schulz, M. Widera, A. R. Mehdipour, G. Tascher, P. P. Geurink, A. Wilhelm, G. J. van der Heden van Noort, H. Ovaa, S. Müller, K.-P. Knobeloch, K. Rajalingam, B. A. Schulman, J. Cinatl, G. Hummer, S. Ciesek and I. Dikic, Papain-like protease regulates SARS-CoV-2 viral spread and innate immunity, *Nature*, 2020, **587**, 657–662.
23 Z. Fu, B. Huang, J. Tang, S. Liu, M. Liu, Y. Ye, Z. Liu, Y. Xiong, W. Zhu, D. Cao, J. Li, X. Niu, H. Zhou, Y. J. Zhao, G. Zhang and H. Huang, The complex structure of GRL0617 and SARS-CoV-2 PLpro reveals a hot spot for antiviral drug discovery, *Nat. Commun.*, 2021, **12**, 488.
24 R. Mittal, R. Ni and J.-H. Seo, The flow physics of COVID-19, *J. Fluid Mech.*, 2020, **894**, F2.
25 T. L. R. Medicine, COVID-19 transmission—up in the air, *Lancet. Respir. Med.*, 2020, **8**, 1159.
26 W. H. Organization, *Getting your workplace ready for COVID-19: how COVID-19 spreads, 19 March 2020*, World Health Organization, 2020.
27 I. P. Trougakos, K. Stamatelopoulos, E. Terpos, O. E. Tsitsilonis, E. Aivalioti, D. Paraskevis, E. Kastritis, G. N. Pavlakis and M. A. Dimopoulos, Insights to SARS-CoV-2 life cycle, pathophysiology, and rationalized treatments that target COVID-19 clinical complications, *J. Biomed. Sci.*, 2021, **28**, 9.
28 J. Y. Y. Kwan, L.-T. Lin, R. Bell, J. P. Bruce, C. Richardson, T. J. Pugh and F.-F. Liu, Elevation in viral entry genes and innate immunity compromise underlying increased infectivity and severity of COVID-19 in cancer patients, *Sci. Rep.*, 2021, **11**, 4533.
29 C. B. Jackson, M. Farzan, B. Chen and H. Choe, Mechanisms of SARS-CoV-2 entry into cells, *Nat. Rev. Mol. Cell Biol.*, 2022, **23**, 3–20.
30 C. Gil, T. Ginex, I. Maestro, V. Nozal, L. Barrado-Gil, M. Á. Cuesta-Geijo, J. Urquiza, D. Ramírez, C. Alonso, N. E. Campillo and A. Martinez, COVID-19: Drug targets and potential treatments, *J. Med. Chem.*, 2020, **63**, 12359–12386.
31 N. Chams, S. Chams, R. Badran, A. Shams, A. Araji, M. Raad, S. Mukhopadhyay, E. Stroberg, E. J. Duval, L. M. Barton and I. Hajj Hussein, COVID-19: A multidisciplinary review, *Front. Public Heal.*, 2020, **8**, 1–20.
32 M. Marshall, COVID and smell loss: answers begin to emerge, *Nature*, 2022, **606**, 631–632.
33 A. Printza, M. Katotomichelakis, S. Metallidis, P. Panagopoulos, A. Sarafidou, V. Petrakis and J. Constantinidis, The clinical course of smell and taste loss in COVID-19 hospitalized patients., *Hippokratia*, 2020, **24**, 66–71.
34 Z. Zhu, X. Lian, X. Su, W. Wu, G. A. Marraro and Y. Zeng, From SARS and MERS to COVID-19: a brief summary and comparison of severe acute respiratory infections caused by three highly pathogenic human coronaviruses, *Respir. Res.*, 2020, **21**, 224.

35 R. Sallis, D. R. Young, S. Y. Tartof, J. F. Sallis, J. Sall, Q. Li, G. N. Smith and D. A. Cohen, Physical inactivity is associated with a higher risk for severe COVID-19 outcomes: A study in 48 440 adult patients, *Br. J. Sports Med.*, 2021, **55**, 1099–1105.

36 L. Kim, S. Garg, A. O'Halloran, M. Whitaker, H. Pham, E. J. Anderson, I. Armistead, N. M. Bennett, L. Billing, K. Como-Sabetti, M. Hill, S. Kim, M. L. Monroe, A. Muse, A. L. Reingold, W. Schaffner, M. Sutton, H. K. Talbot, S. M. Torres, K. Yousey-Hindes, R. Holstein, C. Cummings, L. Brammer, A. J. Hall, A. M. Fry and G. E. Langley, Risk factors for intensive care unit admission and in-hospital mortality among hospitalized adults identified through the US Coronavirus Disease 2019 (COVID-19)-associated hospitalization surveillance network (COVID-NET), *Clin. Infect. Dis.*, 2021, **72**, e206–e214.

37 Worldometer, Coronavirus graphs: worldwide cases and deaths, https://www.worldometers.info/coronavirus/worldwide-graphs/, (accessed 24 December 2022).

38 WHO, Tracking SARS-CoV-2 variants, https://www.who.int/activities/tracking-SARS-CoV-2-variants, (accessed 24 December 2022).

39 WHO, South Africa: WHO Coronavirus disease (COVID-19) dashboard with vaccination data | WHO Coronavirus (COVID-19) dashboard with vaccination data, https://covid19.who.int/region/afro/country/za, (accessed 24 December 2022).

40 C. Gil, T. Ginex, I. Maestro, V. Nozal, L. Barrado-Gil, M. Á. Cuesta-Geijo, J. Urquiza, D. Ramírez, C. Alonso, N. E. Campillo and A. Martinez, COVID-19: Drug targets and potential treatments, *J. Med. Chem.*, 2020, **63**, 12359–12386.

41 C. Wu, Y. Liu, Y. Yang, P. Zhang, W. Zhong, Y. Wang, Q. Wang, Y. Xu, M. Li, X. Li, M. Zheng, L. Chen and H. Li, Analysis of therapeutic targets for SARS-CoV-2 and discovery of potential drugs by computational methods, *Acta Pharm. Sin. B*, 2020, **10**, 766–788.

42 I. Tietjen, J. Cassel, E. T. Register, X. Y. Zhou, T. E. Messick, F. Keeney, L. D. Lu, K. D. Beattie, T. Rali, P. Tebas, H. C. J. Ertl, J. M. Salvino, R. A. Davis and L. J. Montaner, The natural stilbenoid (–)-hopeaphenol inhibits cellular entry of SARS-CoV-2 USA-WA1/2020, B.1.1.7, and B.1.351 variants, *Antimicrob. Agents Chemother.*, 2021, **65**, e0077221.

43 M. Cox, T. P. Peacock, W. T. Harvey, J. Hughes, D. W. Wright, B. J. Willett, E. Thomson, R. K. Gupta, S. J. Peacock, D. L. Robertson, A. M. Carabelli and C.-19 G. U. K. (COG-U. Consortium, SARS-CoV-2 variant evasion of monoclonal antibodies based on *in vitro* studies, *Nat. Rev. Microbiol.*, 2023, **21**, 112–124.

44 W. Zhu, M. Xu, C. Z. Chen, H. Guo, M. Shen, X. Hu, P. Shinn, C. Klumpp-Thomas, S. G. Michael and W. Zheng, Identification of SARS-CoV-2 3CL protease inhibitors by a quantitative high-throughput screening, *ACS Pharmacol. Transl. Sci.*, 2020, **3**, 1008–1016.

45 S. S. Issa, S. V. Sokornova, R. R. Zhidkin and T. V. Matveeva, The main protease of SARS-CoV-2 as a target for phytochemicals against coronavirus, *Plants*, 2022, **11**, 1862.

46 M. Marzi, M. K. Vakil, M. Bahmanyar and E. Zarenezhad, Paxlovid: mechanism of action, synthesis, and *in silico* study., *Biomed Res. Int.*, 2022, 7341493.

47 A. A. Elfiky, SARS-CoV-2 RNA dependent RNA polymerase (RdRp) targeting: an *in silico* perspective , *J. Biomol. Struct. Dyn.*, 2020, **0**, 1–9.

48 H. S. Hillen, Structure and function of SARS-CoV-2 polymerase, *Curr. Opin. Virol.*, 2021, **48**, 82–90.

49 W. Yan, Y. Zheng, X. Zeng, B. He and W. Cheng, Structural biology of SARS-CoV-2: open the door for novel therapies, *Signal Transduct. Target. Ther.*, 2022, **7**, 26.

50 S. M. R. Hashemian, M. H. Pourhanifeh, M. R. Hamblin, M. K. Shahrzad and H. Mirzaei, RdRp inhibitors and COVID-19: Is molnupiravir a good option?, *Biomed. Pharmacother.*, 2022, **146**, 112517.

51 J. A. Newman, A. Douangamath, S. Yadzani, Y. Yosaatmadja, A. Aimon, J. Brandão-Neto, L. Dunnett, T. Gorrie-stone, R. Skyner, D. Fearon, M. Schapira, F. von Delft and O. Gileadi, Structure, mechanism and crystallographic fragment screening of the SARS-CoV-2 NSP13 helicase, *Nat. Commun.*, 2021, **12**, 1–11.
52 A. Yasuo, Host cellular RNA helicases regulate SARS-CoV-2 infection, *J. Virol.*, 2022, **96**, e00002-22.
53 S. Aherfi, B. Pradines, C. Devaux, S. Honore, P. Colson, B. La Scola and D. Raoult, Drug repurposing against SARS-CoV-1, SARS-CoV-2 and MERS-CoV, *Future Microbiol.*, 2021, **16**, 1341–1370.
54 FDA, COVID-19 Vaccines, https://www.fda.gov/emergency-preparedness-and-response/coronavirus-disease-2019-covid-19/covid-19-vaccines, (accessed 23 December 2022).
55 A. J. W. Yip, Z. Y. Low, V. T. K. Chow and S. K. Lal, Repurposing molnupiravir for COVID-19: The mechanisms of antiviral activity, *Viruses*, 2022, **14**, 1–13.
56 C. Alteri, V. Fox, R. Scutari, G. J. Burastero, S. Volpi, M. Faltoni, V. Fini, A. Granaglia, S. Esperti, A. Gallerani, V. Costabile, B. Fontana, E. Franceschini, M. Meschiari, A. Campana, S. Bernardi, A. Villani, P. Bernaschi, C. Russo, G. Guaraldi, C. Mussini and C. F. Perno, A proof-of-concept study on the genomic evolution of Sars-Cov-2 in molnupiravir-treated, paxlovid-treated and drug-naïve patients, *Commun. Biol.*, 2022, **5**, 1376.
57 M. Cascella, M. Rajnik, A. Aleem, S. C. Dulebohn and R. Di Napoli, Features, evaluation, and treatment of Coronavirus (COVID-19), Treasure Island (FL), 2022.
58 B. B. Petrovska, Historical review of medicinal plants' usage, *Pharmacogn. Rev.*, 2012, **6**, 1–5.
59 M. E. Mothibe and M. Sibanda, African traditional medicine: South African perspective ed. C. Mordeniz, IntechOpen, Rijeka, 2019, p. Ch. 3.
60 A. O. Aremu and S. C. Pendota, Medicinal plants for mitigating pain and inflammatory-related conditions: an appraisal of ethnobotanical uses and patterns in South Africa, *Front. Pharmacol.*, 2021, **12**, 758583.
61 Alamgeer, W. Younis, H. Asif, A. Sharif, H. Riaz, I. A. Bukhari and A. M. Assiri, Traditional medicinal plants used for respiratory disorders in Pakistan: a review of the ethno-medicinal and pharmacological evidence, *Chin. Med.*, 2018, **13**, 48.
62 X. Wang, W. Jia, A. Zhao and X. Wang, Anti-influenza agents from plants and traditional Chinese medicine, *Phyther. Res.*, 2006, **20**, 335–341.
63 D. Twilley, S. Rademan and N. Lall, A review on traditionally used South African medicinal plants, their secondary metabolites and their potential development into anticancer agents., *J. Ethnopharmacol.*, 2020, **261**, 113101.
64 I. E. Cock and S. F. Van Vuuren, The traditional use of southern African medicinal plants in the treatment of viral respiratory diseases: A review of the ethnobotany and scientific evaluations, *J. Ethnopharmacol.*, 2020, **262**, 113194.
65 C. P. Kala, Medicinal plants used for the treatment of respiratory diseases in Uttarakhand state of India, *Stud. Ethno-Medicine*, 2020, **14**, 1–8.
66 L. Wang, R.-M. Zhang, G.-Y. Liu, B.-L. Wei, Y. Wang, H.-Y. Cai, F.-S. Li, Y.-L. Xu, S.-P. Zheng and G. Wang, Chinese herbs in treatment of influenza: A randomized, double-blind, placebo-controlled trial, *Respir. Med.*, 2010, **104**, 1362–1369.
67 K. Abascal and E. Yarnell, Herbal treatments for pandemic influenza: learning from the Eclectics' experience, *Altern. Complement. Ther.*, 2006, **12**, 214–221.
68 S.-Y. Li, C. Chen, H.-Q. Zhang, H.-Y. Guo, H. Wang, L. Wang, X. Zhang, S.-N. Hua, J. Yu, P.-G. Xiao, R.-S. Li and X. Tan, Identification of natural compounds with antiviral activities against SARS-associated coronavirus., *Antiviral Res.*, 2005, **67**, 18–23.
69 K.-M. Lau, K.-M. Lee, C.-M. Koon, C. S.-F. Cheung, C.-P. Lau, H.-M. Ho, M. Y.-H. Lee, S. W.-N. Au, C. H.-K. Cheng, C. B.-S. Lau, S. K.-W. Tsui, D. C.-C. Wan, M. M.-Y. Waye, K.-B. Wong, C.-K. Wong, C. W.-K. Lam, P.-C. Leung and K.-P. Fung,

Immunomodulatory and anti-SARS activities of *Houttuynia cordata*, *J. Ethnopharmacol.*, 2008, **118**, 79–85.

70 C.-C. Wen, Y.-H. Kuo, J.-T. Jan, P.-H. Liang, S.-Y. Wang, H.-G. Liu, C.-K. Lee, S.-T. Chang, C.-J. Kuo, S.-S. Lee, C.-C. Hou, P.-W. Hsiao, S.-C. Chien, L.-F. Shyur and N.-S. Yang, Specific plant terpenoids and lignoids possess potent antiviral activities against Severe Acute Respiratory Syndrome Coronavirus, *J. Med. Chem.*, 2007, **50**, 4087–4095.

71 C.-Y. Wu, J.-T. Jan, S.-H. Ma, C.-J. Kuo, H.-F. Juan, Y.-S. E. Cheng, H.-H. Hsu, H.-C. Huang, D. Wu, A. Brik, F.-S. Liang, R.-S. Liu, J.-M. Fang, S.-T. Chen, P.-H. Liang and C.-H. Wong, Small molecules targeting severe acute respiratory syndrome human coronavirus, *Proc. Natl. Acad. Sci.*, 2004, **101**, 10012–10017.

72 M. T. Islam, C. Sarkar, D. M. El-Kersh, S. Jamaddar, S. J. Uddin, J. A. Shilpi and M. S. Mubarak, Natural products and their derivatives against coronavirus: A review of the non-clinical and pre-clinical data, *Phyther. Res.*, 2020, **34**, 2471–2492.

73 L. Yi, Z. Li, K. Yuan, X. Qu, J. Chen, G. Wang, H. Zhang, H. Luo, L. Zhu, P. Jiang, L. Chen, Y. Shen, M. Luo, G. Zuo, J. Hu, D. Duan, Y. Nie, X. Shi, W. Wang, Y. Han, T. Li, Y. Liu, M. Ding, H. Deng and X. Xu, Small molecules blocking the entry of severe acute respiratory syndrome coronavirus into host cells, *J. Virol.*, 2004, **78**, 11334–11339.

74 T.-Y. Ho, S.-L. Wu, J.-C. Chen, C.-C. Li and C.-Y. Hsiang, Emodin blocks the SARS coronavirus spike protein and angiotensin-converting enzyme 2 interaction, *Antiviral Res.*, 2007, **74**, 92–101.

75 [Anonymous], Redeploying plant defences, *Nat. Plants*, 2020, **6**, 177.

76 C. Nie, J. Trimpert, S. Moon, R. Haag, K. Gilmore, B. B. Kaufer and P. H. Seeberger, *In vitro* efficacy of *Artemisia* extracts against SARS-CoV-2, *Virol. J.*, 2021, **18**, 182.

77 M. S. Nair, Y. Huang, D. A. Fidock, S. J. Polyak, J. Wagoner, M. J. Towler and P. J. Weathers, *Artemisia annua* L. extracts inhibit the *in vitro* replication of SARS-CoV-2 and two of its variants, *J. Ethnopharmacol.*, 2021, **274**, 114016.

78 E. Hellou, J. Mohsin, A. Elemy, F. Hakim, M. Mustafa-Hellou and S. Hamoud, Effect of ArtemiC in patients with COVID-19: A Phase II prospective study., *J. Cell. Mol. Med.*, 2022, **26**, 3281–3289.

79 Z. Wang, N. Wang, L. Yang and X. Q. Song, Bioactive natural products in COVID-19 therapy, *Front. Pharmacol.*, 2022, **13**, 926507.

80 A. Fontanet, B. Autran, B. Lina, M. P. Kieny, S. S. A. Karim and D. Sridhar, SARS-CoV-2 variants and ending the COVID-19 pandemic, *Lancet*, 2021, **397**, 952–954.

81 R. Saelee, E. Zell, B. P. Murthy, P. Castro-Roman, H. Fast, L. Meng, L. Shaw, L. Gibbs-Scharf, T. Chorba, L. T. Q. Harris and N. Murthy, Disparities in COVID-19 vaccination coverage between urban and rural counties — United States, December 14, 2020–January 31, 2022, *MMWR Recomm. Reports*, 2022, **71**, 335–340.

82 T. V. Padma, COVID vaccines to reach poorest countries in 2023 — despite recent pledges, *Nature*, 2021, 595, 342–343.

83 M. Engelbrecht, C. Heunis and G. Kigozi, COVID-19 Vaccine hesitancy in South Africa: lessons for future pandemics, *Int. J. Environ. Res. Public Health*, 2022, 19.

84 Coronavirus (COVID-19) | Drugs | FDA, https://www.fda.gov/drugs/emergency-preparedness-drugs/coronavirus-covid-19-drugs, (accessed 28 December 2022).

85 E. P. Springfield, P. K. F. Eagles and G. Scott, Quality assessment of South African herbal medicines by means of HPLC fingerprinting., *J. Ethnopharmacol.*, 2005, **101**, 75–83.

86 I. E. Cock and S. F. Van Vuuren, The traditional use of southern African medicinal plants for the treatment of bacterial respiratory diseases: A review of the ethnobotany and scientific evaluations, *J. Ethnopharmacol.*, 2020, **263**, 113204.

87 N. Papp, S. Bartha, G. Boris and L. Balogh, Traditional uses of medicinal plants for respiratory diseases in Transylvania, *Nat. Prod. Commun.*, 2011, **6**, 1459–1460.

88 A. Hutchings and A. B. Scott, Alan Haxton. Lewis, Gillian. Bunningham, *Zulu medicinal*

plants : an inventory, University of Natal Press, Pietermaritzburg, South Africa, 1996.

89 G. A. Rossi, O. Sacco, E. Mancino, L. Cristiani and F. Midulla, Differences and similarities between SARS-CoV and SARS-CoV-2: spike receptor-binding domain recognition and host cell infection with support of cellular serine proteases, *Infection*, 2020, **48**, 665–669.

Chapter 2

Plant selection, high throughput screening methodology and biological results

2.1 Introduction

2.1.1 South African plants in drug discovery and as antiviral drug leads

Due to its geographical position, and biome diversity, South Africa is reportedly the third most biodiverse country in the world [1]. Approximately 10% of the world's known plant species are found in South Africa, with over 50% being endemic to South Africa [2]. There is ample evidence motivating the interrogation of natural product resources in search of the urgently needed treatment regimens for COVID-19; as the vast South African biodiversity remains untapped in this endeavour, including its well-documented history of the use of medicinal plants in the treatment of a myriad of diseases, including respiratory infections [3]. There is little published data on the anti-coronavirus properties of unique South African plant species; hence, this vast, unique, and readily available natural resource remains an untapped reservoir that could provide complementary COVID-19 treatment regimens.

Paradoxically, despite South Africa's rich biodiversity, only a few commercial health products have originated from South Africa with *Pelargonium sidoides* (Umckaloabo®), *Aloe ferox* Mill., *Centella asiatica* (L.) Urb., *Hoodia gordonii*, *Cyclopia genistoides* (L.) Vent. and *Harpagophytum procumbens* (Burch.) DC. being some of the most well-known [4–6]. Although other literature reports describing the antiviral activity of some South African plants, arguably one of the most well-known and well-documented South African plant-derived products with antiviral properties is the *P. sidoides* commercial product, Umckaloabo®. The product has been shown to possess antiviral activity *in vitro* with selective bioactivity against enveloped viruses implicated in respiratory infections like the herpes simplex virus type 1 (HSV-1) and type 2 (HSV-2), seasonal influenza A virus strains (H1N1, H3N2), respiratory syncytial virus, human coronavirus and parainfluenza virus [7]. It should be noted that the bioactive antiviral compound/s in Umckaloabo® has not been identified, and the overall activity could very likely be due to the particular combination of compounds. The above provides considerable hope for investigating South African plants in the pursuit of novel antiviral compounds, focusing mainly on COVID-19 drugs, in light of the current pandemic.

2.1.2 Strategies for prioritising plants for drug discovery

Given South Africa's extensive plant biodiversity, prioritising a short list of plants for biological screening remains a complex and essential task. The selection of plants must be made meticulously to increase the chances of successfully finding agents with biological efficacy. Although various other approaches exist, two of the most valuable include an ethnobotanical approach and a scoring system/criteria approach, typically used in combination.

2.1.2.1 Ethnobotany

In broad terms, 'Ethnobotany' refers to the scientific study of humankind's interactions with the plant kingdom and typically encompasses anything from the use of plants for food and medicine to its use in music and rituals [8]. In this context, however, it refers to the exploration of traditionally used plants for potential biological and pharmaceutical promise. Here, ethnobotany guides the selection of the plants for further study, with the choice of plants typically aligning with its traditional reported uses. Various traditional medical systems exist worldwide, like the traditional Chinese, Ayurvedic, Unani and African Traditional medicine (ATM) medical systems which are frequently used for plant selection.

2.1.2.2 Scoring systems

A scoring system provides the researcher with a non-biased and quantifiable way to prioritise a list of plants with particular characteristics of interest to the study. The plants are given a score based on how well their characteristics match a particular set of attributes deemed relevant to the study. These characteristics can include plant toxicity, plant availability, plant part used, previous research conducted, and information on the plant's phytochemistry. This scoring approach can even be combined with the ethnobotanical approach, where traditionally used plants can be prioritised based on their related uses. Notably, the scores can be amended to suit the research focus; for example, if the focus is on commercialising a plant extract fit for human consumption, plants with known toxicity will be scored significantly lower. Alternatively, should the focus indeed be on toxic plants with the hope of identifying a novel antineoplastic agent, plants with reported toxicity would be scored significantly higher.

The same can be applied to all the qualifying characteristics. The plant is scored for each category/characteristic based on the extent to which the plant's particular characteristic matches the set of scoring conditions. The approach often utilises a large variety of published resources like Pubmed, Google Scholar, SciFinder and other published books to gather sufficient information for an unbiased assessment.

The combined ethnobotany/scoring approach has already been successfully used in multiple research projects where various drug leads were identified. Of particular relevance, work conducted by Clarkson et al. (2004), utilised this approach to score 623 plants from a particular taxon in the hope of identifying antimalarial agents [9]. From the list, 134 plants were collected and tested for activity against the D10 strain of *Plasmodium falciparum*. Of these, 66 species were found to have promising activity (IC_{50} < 10 µg/mL), of which 23 species (17%) were considered highly active (IC_{50} < 5 µg/mL). This work identified several bioactive compounds against malaria [9].

In another study, conducted by van de Venter et al. (2008), the same methodology (and weighted criteria, i.e., scoring system) was used in which 28 taxa were scored. Of these, eleven plants were prioritised and screened for antidiabetic activity. The work identified several antidiabetic plants and the authors found that the scoring system increased the likelihood of identifying drug candidates and aided in data interpretation [10].

Recently, the same methodology was successfully used in research conducted by Thakur et al. (2019) to identify agents targeting the reduction of Aβ42 protein as a potential treatment of Alzheimer's disease. In this work, 20 traditionally used plants were selected using the scoring system and screened in Aβ42 reduction assays. Of the 33 plants, 10 (30.3%) were active in reducing Aβ42 production [11].

The utilisation of the scoring system in the various diverse research projects highlights this approach's benefit in natural product drug discovery.

2.1.3 Need for new antivirals against COVID-19

The threats posed by viral pandemics are now an everyday, and not unfounded, reality. There are currently over 250 known zoonotic disease-causing viruses, with an additional ca. 1.67 million undescribed thought to exist in birds and mammals, half of which are predicted to have zoonotic potential [12]. The current COVID-19 pandemic is a stark reminder of how ill-prepared humanity is to deal with the emergence of new viruses and those with high mutating abilities. Considering the COVID-19 pandemic alone, over 649 million cases were reported, with over 6.6 million deaths (as of December 2022) within three years. Of the reported cases, 4 million cases originated in South Africa alone, with this number predicted to be significantly underestimated [13,14]. With the risk in variants and subvariants, the chances of infections are an ever-present fear, with some countries still imposing harsh lockdowns. These statistics, understandably, highlight future outbreaks as a severe threat from both a public health and an economic standpoint. Not only the inherent threat of infection alone with its associated health

implications and risks, but also the post-infection and long-term effects like so-called “long-COVID”, which affects >40% of people up to 18 months after their initial infection (in a study conducted on >31 000 participants in Scotland) [15].

Although the key focus is on disease prevention, at times of a severe outbreak, the threat must be confronted and handled using a multifaceted approach, with prevention and concurrent treatment being the ideal response.

From a global perspective, the need for new antiviral drugs is ever-present. Unlike many other microorganisms, viruses have very high mutation rates [16]. Due to their relatively small genome size, small mutations in their genetic makeup can significantly affect their chances of survival. RNA viruses, unlike DNA viruses, have significantly higher mutation rates which correlate with enhanced virulence, evolvability and traits [16]. This is due to 2 main differences in their phenotype, i.e., the inherent instability of RNA (single-stranded) compared to DNA (double-stranded) and the common lack of proofreading enzymes involved in the replication of the virus in RNA viruses [17]. Coronaviruses are unique in that they are RNA viruses and possess enzymes with error-checking abilities called Nsp14-ExoN with cofactor nsp10, which perform proofreading activities [18]. Due to this high mutation rate, the emergence of new viruses and subvariants is an existential problem, and in order to leverage the playing field, the constant development of new antiviral agents is required.

Like many undeveloped countries, South Africa lacks adequate health facilities, partly due to a severely stretched workforce and especially in rural areas where traditional medicine is the most prominent source of healthcare [19]. South Africa’s current economic standpoint shows that future lockdowns are significantly unfavourable. Based on this, the treatment should ideally be something that can be self-administered and not only restricted to hospital use. The current FDA-approved drugs, viz., remdesivir and baricitinib are restricted to severe cases and hospital use. The EUA-authorised antiviral drugs, Paxlovid and molnupiravir, freely available in other countries, are currently scarce and predicted to be costly in South Africa [20]. Due to this, developing new treatments with high availability in South Africa is highly important, especially in regions with limited healthcare access.

2.1.4 SARS-CoV-2 biological assays

Global efforts are focused on studying the SARS-CoV-2 virus to better understand topics like its structure, virulence, virology, transmission, pathogenesis, pathogenicity and pathophysiology, to name a few. Much research has been undertaken to develop potential therapies against the SARS-CoV-2 virus, like vaccines to prevent and lower the risk of future

infections, monoclonal antibodies and recombinant proteins, and therapeutics (drugs) for the treatment of the disease. Additionally, extensive research has similarly been conducted on diagnostic and research tools to study the characteristics mentioned above of the virus [21]. Despite lower attention, diagnostic and research tools like biological assays, which often rely heavily on chemistry principles, play a fundamental role in detecting disease (testing) and screening potential therapeutics for use against the virus.

With COVID-19 being a newly discovered virus, with much research still needed, a limited number of bioassays exist, enabling researchers to test new potential pharmaceuticals for possible biological activity. Amongst these, the following are widely used and amongst the most popular for evaluating candidate therapeutics: protein-protein interaction bioassays, like AlphaScreens; enzymatic assays, like the FRET-based M^{pro} inhibition bioassay and the whole cell plaque-based bioassay [22]. Although pseudovirus bioassays and virus yield reduction assays are also widely used, for the sake of relevance and applicability to the research conducted in the study, only the three appropriate bioassays are described.

1. Protein-protein interaction assays (Protein and antigen binding affinity) e.g., AlphaScreen/AlphaLISA, enzyme-linked immunosorbent assay (ELISA) and homogeneous time-resolved fluorescence (HTRF). Although slight differences exist in the group, the assays rely on proximity for subsequent fluorescence/luminescence, indicating protein-protein or protein-antigen interaction. The newly developed AlphaScreen technology for SARS-CoV-2 Spike-RBD/ACE2 (also used for the PD-1/PD-L1 activity) interaction evaluation described by Tietjen et al. (2021) [23], is used for explanation purposes. In the assay, the SARS-CoV-2 spike-RBD is linked to a nickel chelate donor bead through a His-tag and similarly, the ACE2-Fc protein conjugated to a Protein A Acceptor bead. Protein A is a 42-KDa protein found in the cell wall of *Staphylococcus aureus*, with an inherent affinity towards the Fc region of immunoglobulins [24]. The setup utilises UV absorption and subsequent emission to evaluate the successful binding of the two complementary proteins (Spike-RBD and ACE2 receptor) with high affinity for each other and, understandably, the success of potential drugs to prevent this interaction. Here, the system (consisting of the two bead-linked proteins and potential drug (test substance)) is irradiated with a 680 nm UV light where, should a binding event between the spike RBD and ACE2 receptor exist, a transfer of a singlet oxygen will occur from the Nickel Chelate donor bead to the Acceptor bead (in close proximity due to the Spike-RBD/ACE2 link) and result in luminescence at 615 nm. This will get detected by a spectrophotometer. Evidently, should a potential drug/structure prevent the interaction between the spike-RBD and ACE2 receptor, a singlet oxygen species will still be

produced by the Ni chelate donor bead but decay prior to reacting with the Acceptor bead and thus produce a low/no luminescence.

The acceptor and donor bead are chemically unique, making their interaction attractive. Chemically speaking, the donor bead acts as a photosensitiser upon illumination at 680 nm and converts molecular (ground state oxygen) into the high-energy singlet oxygen species. The acceptor bead contains a thioxene derivative susceptible to reactions with singlet oxygen and generates chemiluminescence at 370 nm. Subsequent energy transfer to fluorophores within the same bead shifts the emission wavelength to 520-620 nm. Due to the instability of the singlet oxygen species, its diffusion (200 nm) and half-life are very short. In the absence of a close Acceptor bead, the singlet oxygen decays and goes undetected (Figure 2.1) [25,26]. Due to the assay's unique characteristics, i.e., versatility to allow modification for various protein-protein interactions, sensitivity and homogeneity, AlphaScreen technology is well suited for high throughput systems and screens.

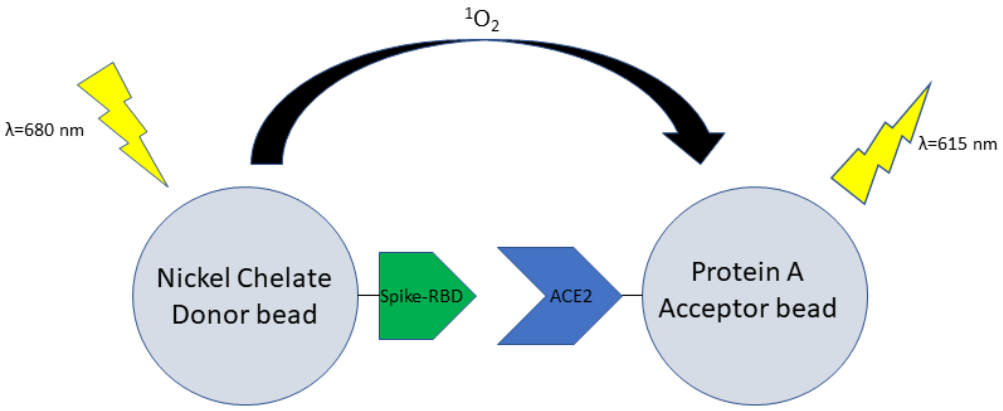

Figure 2.1: Spike RBD/ACE2 (AlphaScreen) protein-protein interaction diagram.

2. Enzyme-based bioassay, e.g., SARS-CoV-2 M^{pro} or PLpro. As with the AlphaScreen's principle of action, enzyme-based bioassays like the SARS-CoV-2 M^{pro} inhibition bioassays utilised in this work rely on the enzyme's intrinsic function and a FRET-based method of activity detection, as described in Tietjen et al. (2022) [23]. In the M^{pro} (or $3CL^{pro}$) enzymatic bioassays, a self-quenched fluorogenic peptide substrate is used for high throughput screening of enzyme inhibitors. The assay utilises a (FRET)-based fluorogenic peptide with an 11 or 14 amino acid sequence (capable of cleavage by SARS-CoV-2 M^{pro}) conjugated at the N- and C- terminals with an Edans donor molecular and Dabcyl quencher molecular respectively. In the absence of the functional protease (or the presence of a protease inhibitor), the amino acid sequence remains unbroken,

maintaining the donor-quencher connection. In this state, irradiation of the donor bead (Edans) with 355 nm wavelength of light results in little to no fluorescence due to the conjugation and absorbance of energy by the attached quencher molecule, *viz.*, Dabcyl.

Conversely, in the presence of a functional M^{pro} enzyme (or inactive drug), the protease cleaves the amino acid sequence at a specific location (between the Gln and Ser amino acid), resulting in a non-fluorescent fragment (containing the Dabcyl bead/molecule) and a highly fluorescent fragment (containing the Edans donor bead). Without the conjugated quencher bead, the donor bead fluoresces and emits light with a specific wavelength (in this case, at 460 nm) (Figure 2.2) [27]. Monitoring the selective wavelength enables the researcher to measure the M^{pro} inhibitory activity of a compound against the enzyme. Based on the substrate's robustness, the protease's continuous activity and the assay's homogeneity, it is ideal for HTS research [28].

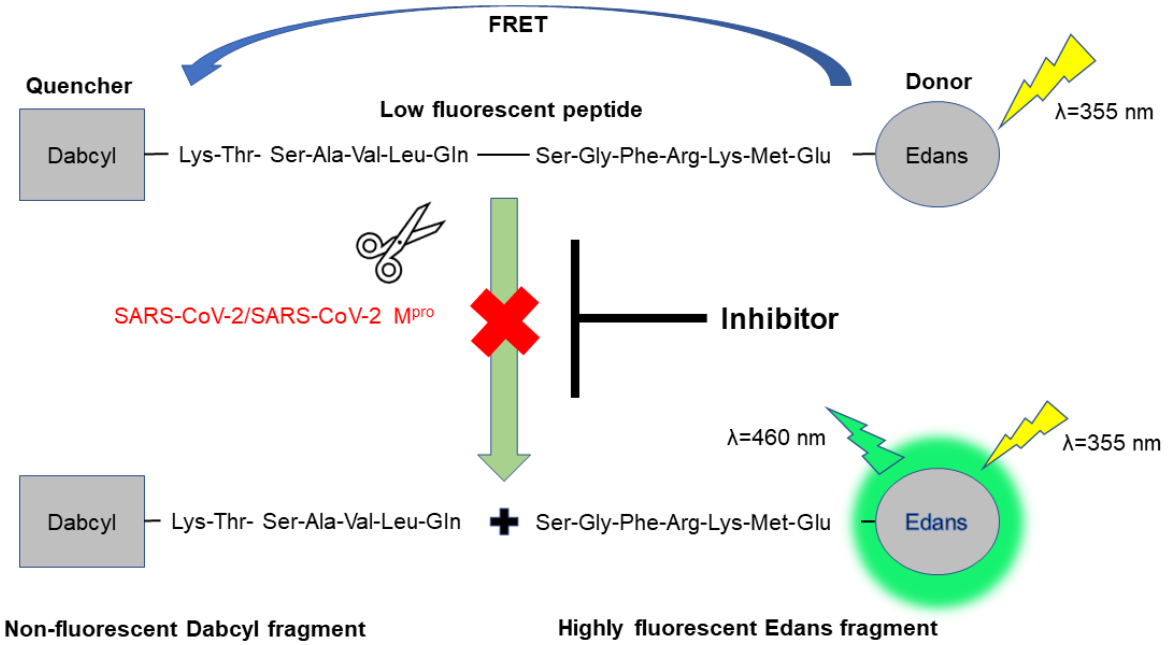

Figure 2.2: Schematic representation of the M^{pro} fluorogenic SARS-CoV-2 enzymatic protease bioassay, adapted from Zhu et al., 2020 [27].

3. Whole-cell bioassay, e.g., SARS-CoV-2 CPE/Plaque-based bioassays. These bioassays are used to enumerate viruses that cause lysing of the host cells by directly measuring their effect. These assays remain the gold standard and most accurate methods for quantifying viable infectious virions and viral neutralisation tests [29,30]. Although other bioassays exist for viral quantification, like AlphaScreen and FRET-based bioassays, these fail to quantify replication-competent virions. Taking the SARS-CoV-2 CPE/Plaque based bioassays as an example, and as described by Urda et al. (2022) and principles

described by Chaurasiya et al. (2016), live SARS-CoV-2 viruses are added to permissive Vero E6, which have been seeded and allowed to grow into a confluent monolayer. The virus is subsequently incubated with the virus-susceptible cells, allowing infection to occur. A nutrient-rich medium is subsequently added, which forms a gel. The viruses that infect cells replicate within the cell before releasing the progeny virions through cell-lysis. The newly released viruses are restricted from spreading too far by the nutrient-rich medium and only infect closely neighbouring cells. The lysed cells detach from the walls of the container and form an area in the monolayer devoid of cells. This area without cells is referred to as the “plaque”. Once the plaques have grown sufficiently, the cells are fixed, and the viruses are killed with formaldehyde. For contrast, cellular strains like crystal violet are used to observe the cells and plaques where cells are selectively stained and plaques unstained. Due to the well-defined contrast, the plaques can be counted, either manually using a bright-field microscope or, recently, using spectrophotometric analyses (Figure 2.3) [30–32].

Additionally, the plaque morphology, like size, shape and border definition, can provide further information on the pathogenesis of the pathogen.

By using these bioassays, the bioactivity of therapeutics can be tested against the virus. Although the MOA of the potential compound is often not clearly observed, the direct effect on the virus’ lifecycle can be evaluated, i.e., from initial infection to cell death.

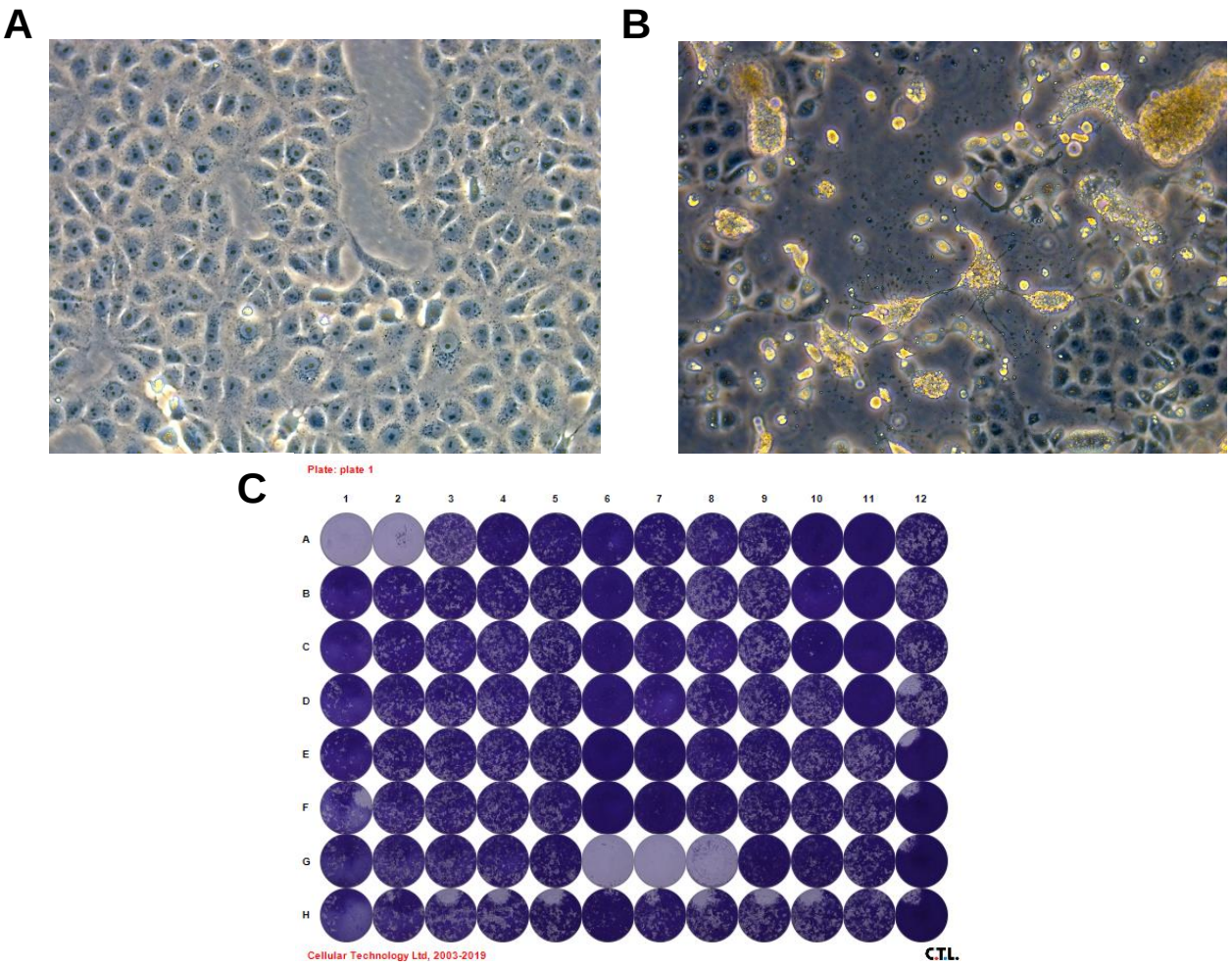

Figure 2.3: (**A**) Early stages of SARS-CoV-2 plaque formation amongst a confluent monolayer of Vero E6 cells. (**B**) Late stages of SARS-COV-2 infection and plaque formation with a clump of dead cells detaching from the well. (**C**) A fixed and stained 96-well plate illustrating the observable plaques due to viral cytopathic effects. Wells stained blue represent healthy Vero E6 cells where wells with white 'polka dots' represent Vero E6 cells with viral plaques (viral CPE). Wells with no visible cells is a characteristic and typical presentation of compound cytotoxicity.

2.2 Materials and Methodology

2.2.1 Chemistry reagents and standards

The analytical reagent grade (AR) dichloromethane (DCM) and methanol (MeOH) extraction solvents were purchased from Merck, South Africa (Merck, Darmstadt, Germany). The solvents used in the fractionation, *viz.*, the super purity HPLC grade MeOH and acetonitrile (ACN), were purchased from Romil-SpS™, Microsep, South Africa (Waterbeach, Cambridge, UK) and the ethyl acetate (EtOAc) from Sigma-Aldrich (Merck, Darmstadt, Germany).

2.2.2 Selection of plants

A subset of plants was selected by the "IK-BASED COVID-19 RESEARCH CONSORTIUM" formed by the South African Department of Science and Innovation (DSI). A further selection of plants was adapted from a method described by Thakur et al. (2019) [11], where a literature review was undertaken at the time of study commencement (March 2020), using a combination of Google Scholar, Scopus, SciFinder^{n} and Zulu Medicinal Plants: An Inventory by Anne Hutchings [33] for the selection of plants. The following keywords were used: "South African medicinal plants" and "traditionally used plants": in combination with the following keywords: "natural products", "SARS", "COVID", "CoV", "SARS-CoV-2", "respiratory virus", "influenza", "plants", "African plants", "natural compounds", "respiratory", "virus", "anti-virus", "*in vitro*", "*in silico*", "cough", "chest complaints", "fever", "colds and flu" and "antiviral". A criteria-based scoring system was used to score and rank the identified potential plants for prioritisation. For completeness, the plants selected by the IK-based COVID-19 research consortium were similarly scored. A numerical-based scoring system was utilised using "1","2", and "3" as qualifiers, where "1" represented weak, "2" medium and "3" strong.

The criteria used for scoring were as follows (Figure 2.4):

1. Degree reported to which the plant is used traditionally to treat symptoms of a viral infection, e.g. reported to be used for colds and flu in combination with a cough, sore throat and/or a fever. The score assigned refers to the degree to which the plant's reported uses matched the statement (symptom). In this case, plants which did not match the statement, i.e. were not used for cold/flu-like symptoms, received a "1", plants which partially aligned with the statement received a "2", and plant's use aligned well with the statement and were used for colds/flu symptoms, received a "3".

2. The degree to which the plant had already been published, either in terms of bioactivity of the extract against SARS-CoV-1, SARS-CoV-2 or other viruses like colds/flu or the phytochemistry work. Plants previously unresearched or with published reported activity against related viruses like the SARS-CoV-1 or influenza, with the active compounds not identified, were given a score a "3". Plants previously researched for antiviral activity, with the actives already identified, were scored a "2".

3. Reported toxicity: Plants with no/little reported toxicity were scored a "3". Plants with moderate/mild toxicity (or unreported) were scored a "2", and plants with high toxicity were given a score of "1".

4. Plant part utilised: If the leaves/fruit were used, implying minimal plant destruction, a score of “3” was given. If stems were used, a score of “2” was given, and if roots (or the entire plant) was used, a score of “1” was given.

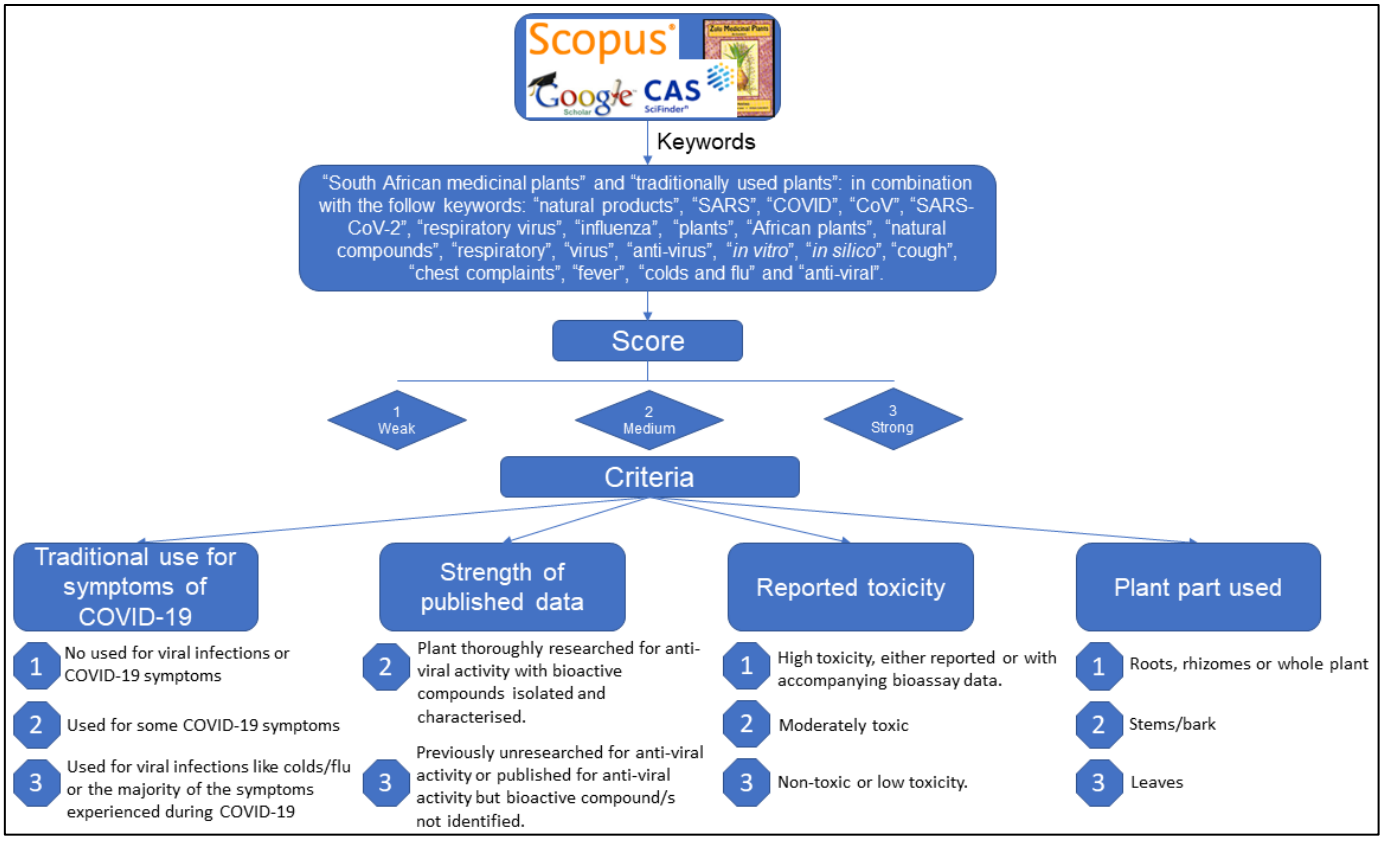

Figure 2.4: Scoring criteria used for the selection of the plant species.

2.2.3 Collection of plants

The selected plants were obtained from various sources based on their availability. A subset of plants was harvested from the Maine van der Schijff Botanical Garden at the University of Pretoria, South Africa, with the help of the Curator, Jason Sampson. Subsequent plant identification was performed at the H.G.W.J. Schweickerdt Plant Herbarium at the University of Pretoria. Other plants were obtained from the University of Pretoria’s plant repository, the Agricultural Research Council (ARC), Pure Organics (from Mr FJ Isaacs), Percival Pty Ltd and the Council for Scientific and Industrial Research (CSIR), Pretoria.

2.2.4 Plant processing, extraction and fractionation

The freshly harvested and unprocessed plants, viz., collected from the Maine van der Schijff Botanical Garden and the plants obtained from the ARC, were processed as follows: The wet plant material was weighed before washing three times with tap water and once with deionised

water. Thereafter, the plant material was oven dried at 60 °C for 3-5 days until sufficiently dry. The dry plant material was ground, using a hammer mill, into a coarse powder before weighing and storing at ambient temperature.

Extraction of all plant material was conducted using ultrasound-assisted micro-extraction. The extraction was performed on 10-12 g of the dried and ground plant material in custom-made glass extraction vessels designed with a fused sintered glass filter (porosity 3) and a Teflon stopcock to assist in fluid retention and expulsion (Figure 2.5). The extraction was performed by placing the entire vessel containing the plant material in the ultrasound bath. A method blank was prepared similarly to the test samples but without any plant material.

Figure 2.5: In-house developed glass extraction vessel fitted with a Teflon stopcock and sintered glass filter (po.3).

Each plant sample (including the method blank) underwent two rounds of extraction in the ultrasonic bath (power—005, frequency—high, time—1 h). The first extraction was performed using a 50 mL 1:1 DCM:MeOH mixture before draining and performing a subsequent extraction step for 1 h, with 50 mL MeOH. The solution was drained from the extraction vessel and combined with the DCM:MeOH solution. A 96%, 60% ethanol extract and a Hexane:MeOH (1:1) extract were also prepared from select plants. In these instances, fresh plant material was used for the separate types of extract, and the plant sample underwent two rounds of extraction (using fresh solvent of the same type) before concentrating on a rotary evaporator and drying to completion using an SP Genevac HT6 (Genevac Ltd., Ipswich, UK) to yield a dried extract. The yields were noted, and the samples were stored in the fridge at 4 °C.

Fractionation of all DCM:MeOH extracts and other selected extracts, including the method blank, took place as described by Invernizzi et al. (2022), a method adapted from Thornburg et al. (2018) [34] using a HypeSep C8 SPE cartridge (2 g/6 mL). In order to fractionate the extract into 7 fractions, a Gilson GX-241 ASPEC® liquid handler fitted with a Verity® 4060 pump controlled with TRILUTION® software was utilised (Figure 2.6).

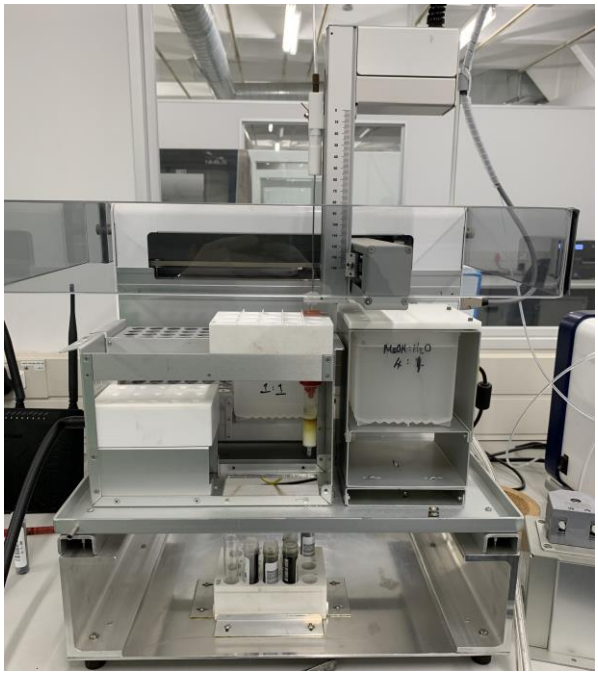

Figure 2.6: Gilson GX-241 ASPEC® liquid handler fitted with a Verity® 4060 pump and a custom-made solvent reservoir.

A 200-250 mg portion of the DCM:MeOH extract of the individual plants was dissolved in a 5 mL solution of MeOH:EtOAc (3:2) before allowing the solution to absorb into a 3 cm x 1 cm dental cottonwool roll in a test tube. Thereafter, the cottonwool containing the extract was dried in an SP Genevac HT6 before being transferred into an empty 10 mL SPE cartridge.

The C8 SPE cartridge was prepared for fractionation by washing it with 3-column volumes of MeOH prior to the conditioning step, where 3-column volumes of the first eluent system, namely H_2O:MeOH (95:5) were passed through. Fractionation was conducted by placing the empty SPE cartridge containing the dried cottonwool-extract in series above the washed and conditioned C8 SPE cartridge (Figure 2.7). The elution was done via positive pressure exerted by the Gilson pumps and performed in a stepwise gradient fashion using 8 mL of the 7 different eluent systems viz., 95:5 (H_2O:MeOH); 80:20 (H_2O:MeOH); 60:40 (H_2O:MeOH); 40:60 (H_2O:MeOH); 20:80 (H_2O:MeOH); 100 % MeOH and 1:1 (ACN:MeOH), as summarised in Figure 2.8.

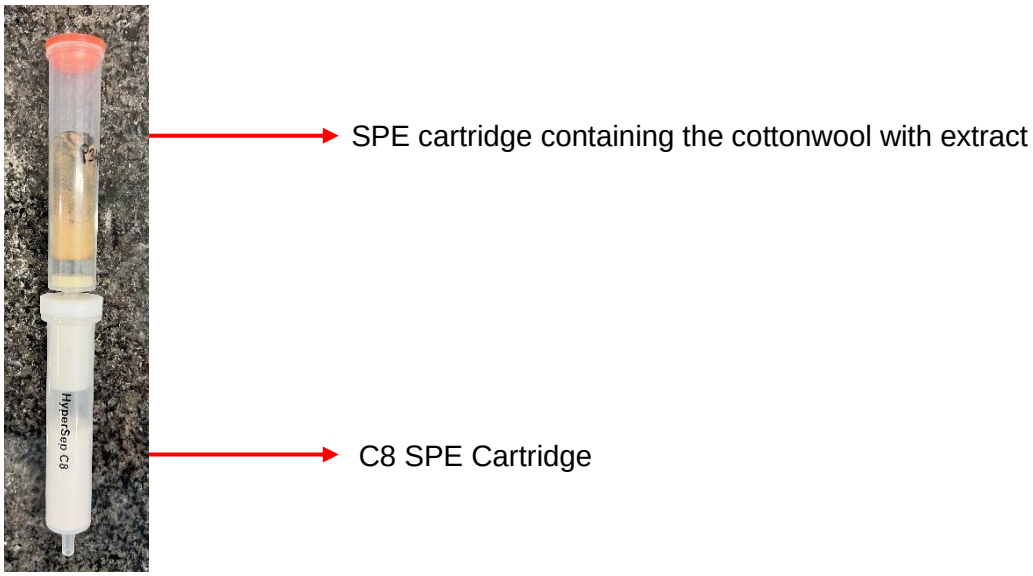

Figure 2.7: Fractionation of plant extract absorbed onto a cottonwool roll placed in series above a C8 SPE cartridge.

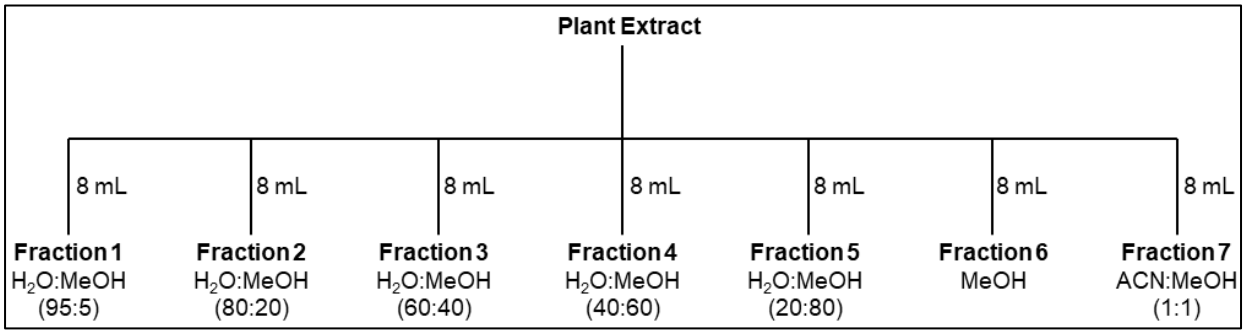

Figure 2.8: Extract fractionation schematic.

The seven fractions generated, one for each eluent system, were collected in separate collection vessels on a volume-based collection method. The fractions were dried in individually pre-weighed polytops using an SP Genevac HT6, their yields recorded, and samples stored at 4 °C until analysis was conducted.

2.3 Biological assays

2.3.1 Biological assays conducted at The Wistar Institute, USA

These bioassays were conducted and made possible by the generous support of colleagues at The Wistar Institute, Philadelphia, USA, under the leadership of Professor Ian Tietjen. The assays were performed as previously published by Tietjen et al. (2021) [23], and described comprehensively in Supplementary Data, Section S2.1.

2.3.1.1 AlphaScreen protein-protein interaction assay

The AlphaScreen bioassays were conducted by incubating ACE2-Fc with a His-tagged SARS-CoV-2 spike-RBD with CHAPS nickel chelate donor beads in 384-low volume plates. Samples were diluted to a final concentration and ready for testing. The ACE2-Fc/protein A acceptor beads were added to the microtiter plate before the addition of the test samples before the addition of the CoV-Spike-RBD-HIS/nickel chelate donor beads. The samples were incubated before measuring the AlphaScreeen fluorescent signals.

To assess selectivity to the SARS-CoV-2 spike-ACE2 RBD interaction, programmed cell death protein 1/ programmed death-ligand 1 (PD-1/PD-L1), an unrelated host pair was used as a comparison. This interaction, too, was assessed using AlphaScreen technology. Two biological repeats were conducted, with each experiment repeated in duplicate to ensure valid results and the data normalised to represent percentage inhibition.

2.3.1.2 Generation of Mpro protein and Mpro enzymatic assays

The specific codon-optimised gene from the BetaCoV/Wuhan/WIV04/2019 strain was acquired to generate the main protease (M^{pro}) enzyme. An expression vector was used to clone the gene before transformation into BL21(DE3). Thereafter, the fusion protein *viz*. HIS-SUMO-M^{pro} was expressed by employing the autoinduction method [35]. After lysation and centrifugation, a column was used to purify the fusion protein, and after subsequent incubation with SUMO protease, the HIS-SUMO was released and the protein purified by using, amongst others, a HIS-TRAP Ni-NTA column.

The M^{pro} enzymatic assays were then performed with the protease activity measured using the quenched fluorogenic substrate {DABCYL}-Lys-Thr-Ser-Ala-Val-Leu-Gln-Ser-Gly-Phe-Arg-Lys-Met-Glu-(EDANS)-NH2 where the M^{pro} enzyme together with the diluted test samples was added to a black low-volume 384-well plates. The assays were initiated by adding the fluorogenic substrate, with fluorescence, particularly at 355 nm (excitation) and 460 nm (emission), monitored continuously. A linear regression model was used to determine the substrate cleavage rate, and the gradients of the curves were normalised to the controls.

2.3.1.3 Viral CPE scoring-based and quantitative assay

For the comprehensive methodology on virus generation, refer to Supplementary Data, Section S2.1.4. Briefly, viral CPE scoring-based assays were conducted by plating healthy Vero E6 cells and incubating them for 24 h. Thereafter, the test compounds were added to the

cells at various concentrations and allowed to incubate for 2 h before adding 50x $TCID_{50}$ of the virus. As controls, each 96-well plate contained uninfected Vero E6 cells and infected (untreated) Vero E6 cells. Following four days of incubation, the wells were scored for viral CPE.

Cell viability restoration was similarly assessed using CPE scoring-based assays but with the addition of 150x $TCID_{50}$ of the virus, added after the 2 h compound incubation period with the test compounds. As before, the cells were incubated to allow the formation of CPE before treatment with resazurin. The cells were fixed and analysed for fluorescence. The normalised data was recorded, and the subsequent EC_{50} values were calculated using non-linear regression analysis.

2.3.2 Biological assays conducted at The University of Basel, Basel, Switzerland

Training and the subsequent bioassays described in Section 2.3.2 were conducted personally (L. Invernizzi) and made possible by the generous support of the Department of Biomedicine, University of Basel (UNIBAS), Switzerland, under the leadership and supervision of Professor Thomas Klimkait.

In vitro screening of compounds was conducted in plaque-forming assays performed against the isolates of the SARS-CoV-2 virus available in the lab, viz., Wuhan, Beta (B.1.351), Delta (B.1.617.2) and Omicron (B.1.1.529) strains. Additionally, cytotoxicity assays were performed in Vero E6 cell lines to determine the cytotoxicity potential of the isolated and purchased compounds. The methods used were adapted from those previously described by Urda et al. (2022) [31].

Plaque assays are valuable for the quantification of infectious viruses. This assay can only be used for viruses that present a cytopathogenic effect (CPE) to the cells during infection.

2.3.2.1 Samples, cells, viruses, and reagents

Dulbecco's Modified Eagle's Medium–high glucose (DMEM) with stable Glutamine (1-26F50-I), Dulbecco's PBS without Ca^{2+}/Mg^{2+} (3-05F29-I), Trypsin-EDTA PBS 1:250 without Ca^{2+}/Mg^{2+} with phenol red (5-51F00-H) and penicillin-streptomycin solution (4-01F00-H) were purchased from BioConcept. Trypan Blue Cell viability reagent (SV30084.0) was purchased from Thermo Scientific. Fetal Bovine Serum (FBS) (10270) was purchased from Gibco. Formaldehyde 37% (33220) and Crystal Violet stain (C6158) were purchased from Sigma-Aldrich and Sigma (Merck), respectively. Lastly, the ethanol used for analysis was purchased

from Huberlab. Remdesivir (>98% purity), used as a positive control, was purchased from Adipogen AG, Liestal, Switzerland. Vero E6 cells were used in the bioassays and provided by V. Thiel, Berne, Switzerland. Cultivation of the cells took place in DMEM, high glucose media.

All samples were carefully prepared as accurately weighed out dry powder samples. The samples were prepared for bioassays by dissolving them in DMSO to prepare a known concentration before dilution to achieve the required test concentrations, typically 50 µg/mL and a set of samples obtained by serial dilution with growth media (Dulbecco's Modified Eagle Medium (DMEM), 2% Fetal bovine serum (FBS), 1% penicillin-streptomycin (PS)). A 500 µM stock solution of remdesivir, the positive control, was prepared prior to further dilution with assay buffer, to create working dilutions of desired concentration, viz., 0.002-50 µM. Due to the intrinsic cytotoxicity of DMSO, its concentration did not exceed 0.5% in any cellular experiment.

Vero E6 cells used in the bioassays were obtained from a group of V. Thiel, Berne, Switzerland. Cell-cultivation occurred in DMEM, high-glucose media (Gibco, Thermofisher AG, Allschwil, CH, Switzerland) supplemented with pen/strep antibiotic (1%, Bioconcept, Allschwil, CH, Switzerland). Cultivation occurred in a humidified environment, at 37 ^{o}C, with a 5% CO_2 atmosphere.

Virus stocks used in the bioassays were obtained from G. Kochs, University of Freiburg, D, (SARS-CoV_FR-3) and by EVAglobal virus archive (SARS-CoV-2 strain/NL/2020—AMS).

2.3.2.2 Viral Reconstitution

Viral propagation occurred in a BSL3 facility where Vero E6 cells were used as the viral host at a multiplicity of 0.1. The virus (supernatant) was harvested on day 3 after infection. Viruses within the supernatant, i.e., cell-free, were quantified by Reverse-transcriptase polymerase chain reaction (RT-PCR) of the viral S-gene RBD and additionally by plaque titration. Plaque assays using Vero E6 cells were used to determine the viral titer.

2.3.2.3 Plaque assay protocol

One day prior to viral infection, Vero E6 cells were seeded at a density of ca. 3 x 10^4 per well i.e., 3 x 10^6 cells/96-well plate. Two hours before cell infection (to allow for adequate drug absorption and to test for possible prophylactic activity), the test samples (and respective dilutions) were added to the uninfected Vero E6 cells (ca. 80% confluent) and allowed to incubate at 37 ^{o}C in a humidified CO_2 atmosphere. Both a negative control (untreated cells)

and a positive control (remdesivir) were used to ensure valid results. All cells (both the test and control group) were infected with 100 plaque-forming units (pfu) per well, in a BSL3 facility, with the respective SARS-CoV-2 virus strains. After 1 h, following virus inoculation, the culture was layered with 100 µL low-melting agarose. The infected Vero E6 cells were subsequently incubated for 48 h at 37 °C, with daily inspections to note any observed virus-driven CPE plaque formation in the untreated control group.

After the 48 h incubation and testing period, the virus-containing plates were inactivated by the addition of 80 µL of formaldehyde (15% w/v) and allowed to incubate. Following 10 min of incubation, the mixture of formaldehyde, cell medium and agarose was removed and aliquots of the staining solution (crystal violet 0.1% w/v) (Sigma-Aldrich, Buchs, Switzerland) were added to each well and incubated for a further 5 min. Thereafter, the stain was removed from the wells by rinsing the plates with tap water before allowing them to air dry. The degree of viral CPE inhibition was determined based on the extent of plaque formation, i.e. distinct regions of cell death. To ensure accurate quantification of viral plaques, the wells were scanned and counted as described by Honko et al. (2020) [36], using an ImmunoSpot® S6 Analyser fitted with BioSpot software (Cleveland, USA). The images were processed using Fiji Image J 1.53q, where the images were converted to binary according to the Image J definition, the pixels of the selected areas were counted, and the 'Limit to threshold' option was enabled.

2.3.2.4 Cytotoxicity testing

The compounds' cytotoxicity was evaluated in a similar way to that described in Section 2.3.2.3, where Vero E6 cells were plated at a density of ca. 3 x 10^4 cells per well with 50 µL of complete culture medium (2% FBS) and cultured overnight to achieve a confluent monolayer. Stock solutions of the compounds were prepared and diluted to the testing concentration with the growth medium (DMEM with 2% FBS) before transferring a 50 µL aliquot of the solution to each well. Each well was diluted with agarose to a final 200 µL/well volume. Thereafter, the plates were incubated for 2 days (48 h) at 37 °C, as with the infection plates, before fixing with formaldehyde and staining with crystal violet.

2.3.2.5 Data analysis and statistics

The samples of interest were tested in duplicate; each experiment was repeated twice (two biological repeats) unless otherwise stated. The crystal violet-stained wells were captured/scanned using an ImmunoSpot® S6 Analyser fitted with BioSpot software, and the images were converted to binary images using Fiji (ImageJ) software [37], where the total area

of the damaged and/or healthy cells was calculated. The data were normalised to the negative and positive controls used, viz., the uninfected or remdesivir treated cells and untreated virus-infected cells. Statistical analysis and plotting were done using Prism v8.0.2 (GraphPad, San Diego, CA, USA), where the antiviral data were fitted to a sigmoidal curve. The IC_{50} values were calculated using a four-parameter logistic model and reported at a 95% confidence interval. The following equation was used to calculate the IC_{50} values: Y = Bottom + (Top − Bottom)/(1 + 10^((LogIC_{50}-X) × HillSlope)).

2.4 Results and discussion

2.4.1 Selection of plants

From the database search, ca. 120 plants were identified as possible candidates for potential screening against SARS-CoV-2. After applying the scoring criteria, 19 plants were selected (with access to plant material and availability taken into consideration). The 19 shortlisted plants had scores between 12 and 8 and are displayed in Table 2.1. The plants identified originated from 14 different families, with the majority originating from the Lamiaceae and Asteraceae families, which are already described as some of the more essential families of which many medicinal plants form part of and have biological applications [38,39].

Plant species with the highest scores (representing the highest priority) based on the criteria used were *Artemisia afra*, and *Sutherlandia frutescens,* with scores of 12. Five plants species *Clerodendrum glabrum, Lantana camara, Leonotis leonurus, Mentha longifolia* and *Selaginella dregei* scored 11; seven plants species *Helichrysum nudifolium, Helichrysum psilolepis, Pelargonium sidoides, Pittosporum viridiflorum, Podocarpus henkelii, Teclea gerrardii and Tetradenia riparia* scored 10; three plant species *Gunnera perpensa*, *Harpagophytum procumbens* and *Vangueria infausta* scored 9 and two plant species *Buddleja salviifolia* and *Siphonochilus aethiopicus* scored 8 (Table 2.1).

Table 2.1: Scores of selected plant species shortlisted for collection.

#	Plant species	Family	Traditional uses (1)	Published data (2)	Toxicity (3)	Plant part used (4)	Total Score
1	*Artemisia afra* Jacq. ex Willd.	Asteraceae	Traditionally used as a remedy for febrile conditions, headaches, coughs, colds and flu symptoms, malaria, constipation, intestinal worms, acne (and skin conditions), and gastrointestinal/respiratory conditions in South Africa [33,40]. **Score**: 3	A closely related species, *A. annua,* displayed antiviral activity against SARS-CoV-1, EC_{50} = 34.5 µg/mL [41]. *A. afra* was found to be active against the influenza virus [42]. [Recent/post selection]: Against SARS-CoV-2: EC_{50}: 0.09 ± 0.03 mg/mL [43]. **Score**: 3	Low. *In vivo* (rats): >1g/kg aqueous extra, oral administration [44]. Ethanol extracts: LD_{50}> 5 g/kg [40]. **Score**: 3	Leaves [33] **Score**: 3	12
2	*Buddleja salviifolia* (L.) Lam.	Scrophulariaceae (Buddlejaceae)	Traditionally used for stomach complaints, flatulence, mental and neurological illnesses, analgesic, anti-bacterial diarrhoea, coughs, colic and anti-inflammatory [33,45]. **Score**: 2	Genus is known to contain Saikosaponins which inhibit HCoV-229E [46,47]. **Score**: 2	Not tested. **Score**: 3	Leaves and Roots [33] **Score**: 1	8
3	*Clerodendrum glabrum E.Mey. (Volkameria glabra (E.Mey.) Mabb. & Y.W.Yuan)*	Lamiaceae	Traditionally used by the Zulu for coughs and fever. The Vhavenda use the plant for colds, sore throat, chest complaints and insect repellent [48]. Also taken for intestinal parasites and worms, snake bites, animal wounds and insomnia [33]. **Score**: 3	Extract active against Influenza A: EC_{50}=110.4 µg/mL (methanol leaf extract) [49]. **Score**: 3	Moderate. LC_{50} = 42.5 µg/mL (acetone leaf extracts)[50]. **Score**: 2	Leaves [33] **Score**: 3	11
4	*Gunnera perpensa* L.	Gunneraceae	Stomach ailments, menstrual pain, stomach bleeding, wounds. Roots are taken for abdominal pain, indigestion, colds, cancer, heart disease, hypertension, impotence, infertility, kidney problems, UTIs, GI problems, bladder problems, and wound dressing [33,51,52]. **Score**: 2	No *in vitro* bioassay results against viruses. **Score**: 3	Low, based on *in vivo* animal trials [53]. **Score**: 3	Leaves and rhizomes [33,51,52] . **Score**: 1	9
5	*Harpagophytum procumbens* (Burch.) DC ex Meisn. subsp. *procumbens*	Pedaliaceae	Used as an analgesic; for pregnancy complications, topical ointment for sores, GI disturbances, blood disorders, anti-inflammatory, rheumatic and general musculoskeletal pains, ulcers and boils [54]. Other sources describe its use for colds and flu, TB, asthma, constipation, fevers, painful joints, purifying blood, laxative, pain, diabetes and appetite stimulant [55]. **Score**: 3	Weak antiviral activity of harpagoside (known constituent) against vesicular stomatitis virus [55] **Score**: 2	Low, *in vivo* [54]. LD_{50} > 4.6g/kg (oral aqueous/methanol extract) [55]. **Score**: 3	Tuber/ Roots [54] **Score**: 1	9
6	*Helichrysum nudifolium* (L.) Less	Asteraceae	Used for colds and chest complaints, antipyretic, burns, colic, cough, flu, headache, infections, infertility, menstrual	Antiviral activity against HSV-LD (water/MeOH extract): 100$TCID_{50}$: 100 µg/mL [57].	Low. IC_{50} = 138.4 ± 0.03 µg/mL (water:MeOH	Leaves and roots [33,56].	10

			pain, otitis, lung infections, swelling, skin infections, and wounds [33,56]. **Score**: 3	**Score**: 3	extract) in Vero African green monkey kidney cells [57]. **Score**: 3	**Score**: 1	
7	*Helichrysum psilolepis* Harv.	Asteraceae	Dysmenorrhoea [58] **Score**: 1	Antiviral activity against HSV-LD (water/MeOH extract): 100TCID$_{50}$: 200 µg/mL [57]. **Score**: 3	Low. IC$_{50}$ = 277.80 ± 0.05 µg/mL (water:MeOH extract) in Vero African green monkey kidney cells [57]. **Score**: 3	Leaves [58] **Score**: 3	10
8	*Lantana camara* L.	Verbenaceae	Used as/for an antitumor, anti-bacterial, antihypertensive, tonic, expectorant, anti-rheumatic, malaria, skin rashes, anti-inflammatory, fever, coughs, influenza, stomach ache, cancers, chickenpox [59]. **Score**: 3	[Recent/post selection]: ca. 8 µg/mL in plaque-reduction SARS-CoV-2 assays [60]. **Score**: 2	Low. Brine shrimp leaf LC$_{50}$: 3251.8 µg/mL [61]. Low *in vivo* toxicity in mice and low cytotoxicity in Vero (leaf extract): IC$_{50}$ = 361.44 µg/mL (24h) [62] **Score**: 3	Leaves [59] **Score**: 3	11
9	*Leonotis leonurus* (L.) R.Br.	Lamiaceae	Used for hypertension, coughs, headaches, purgative, leprosy, coughs, common cold, influenza, bronchitis, wound healing, asthma, TB, jaundice, muscle cramps, diabetes, viral hepatitis, diarrhoea, dysentery, arthritis, piles, bladder and kidney, obesity, cancer and emetic for snake bites [33,63]. **Score**: 3	Antiviral activity of the extract against HIV. IC$_{50}$ = 120.6 µg/mL [64]. **Score**: 3	Low. Oral administration of aqueous extract: LD$_{50}$ >3.2g/kg in chronic toxicity studies. Methanol/Chloroform LD$_{50}$> 5 g/kg in rats (oral) alterations in haematological, liver and kidney functions were observed [64]. **Score**: 3	Leaves and stems [63] **Score**: 2	11
10	*Mentha longifolia* (L.) Huds. subsp. *polyadena* (Briq.) Briq.	Lamiaceae	Used for gastrointestinal issues like constipation, gall stones, stomachic, tonsilitis, and antiemetic. Use for respiratory illnesses like asthma, cough, dyspnea, common cold, anti-rheumatic, wound healing, anti-bacterial, deworming, antipyretic, headache, sedative, bladder stones, kidney stones, diuretic [65]. Used for painful menstruation, to induce labour, wounds and swelling [33]. **Score**: 3	Antiviral activity against HIV. 40% inhibition of HIC-2BaL at 10 µg/mL [66] [Recent/post selection]: Contains compounds with known antiviral activity against SARS-CoV-2 [67,68]. **Score**: 3	Low. *In vivo* LD$_{50}$ of aqueous/methanolic extract was 3750 mg/kg [69]. **Score**: 3	Leaves and stems [65] **Score**: 2	11
11	*Pelargonium sidoides* DC.	Geraniaceae	Traditionally used for pulmonary diseases, TB, sore throats, respiratory infections, gastrointestinal infections, hepatic disorders and dysmenorrhea [33,70].	Extract active against HSV-1 and HSV-2 [71]. Potent HIV-1 inhibitor (aq. Root extract): EC$_{50}$ = 8.13 µg/mL [72]. EPs® 7630 Activity against:	Low. EP7630 (Umckaloabo) CC$_{50}$: 557 µg/mL on A549 cells [75].	Roots [70] **Score**: 1	10

			Score: 3	H1N1 (IC_{50} = 9.45 ± 2.94 µg/mL); H3N2 (IC_{50} = 8.66 ± 1.06 µg/mL); RSV (IC_{50}= 19.65 ± 1.77 µg/mL); HCo-229E (IC_{50}= 44.50 ± 15.84 µg/mL) Parainfluenza 3 (IC_{50}= 74.35 ± 17.89 µg/mL); Coxsackie A9 (IC_{50}=14.80 ± 3.39 µg/mL) [73] [Recent/post selection]: *In silico* predictions of compounds of *P. sidoides* to be active against SARS-CoV-2 [74]. **Score**: 3	**Score**: 3		
12	*Pittosporum viridiflorum* Sims	Pittosporaceae	Traditionally used for febrile conditions, back pains, stomach ailments, abdominal, chest pains, cancer, gastrointestinal issues, inflammation, kidney complaints, malaria, pneumonia, cough, fever and as part of a mixture for influenza [76]. **Score**: 3	Active against Influenza A (methanol extract): EC_{50}=3.6 µg/mL [77]. **Score**: 3	Moderate IC_{50} = 54.6 µg/mL (Vero E6) leaf acetone extract [76]. **Score**: 2	Bark and leaves [76] **Score**: 2	10
13	*Podocarpus henkelii* Stapf ex Dallim. & Jacks.	Podocarpaceae	Genus at large is used for chest complaints, coughs, cholera, fever, asthma, arthritis, rheumatism, joint pains and venereal diseases, blood disorders, lung ailments, worms, cholera and distemper in dogs [78–80]. **Score**: 2	Antiviral activity against CDV. Acetone leaf extract EC_{50}=3.76 and LSDV (methanol extract) EC_{50}=3.36 µg/mL [81]. **Score**: 3	Not reported for fruit. **Score**: 3	Leaves and bark [82] **Score**: 2	10
14	*Selaginella dregei* (C.Presl) Hieron.	Selaginellaceae	*S. dregei* is not reported traditionally. Genus is, however, used in some parts of Africa for coughs. Other species used in the world for wounds, fitness, menstruation, heart disease, malaria, injury, headache, fever, snakebites, venereal diseases, gastric illnesses, cancer, kidney problems, asthma, gonorrhoea, bleeding, jaundice, hepatitis and fatigue [83]. **Score**: 2	Genus is known to contain uncinosides, with good antiviral activity against the respiratory syncytial virus (RSV). IC_{50} < 7 µg/mL [84]. **Score**:3	Not reported for species. **Score**: 3	Leaves **Score**: 3	11
15	*Siphonochilus aethiopicus* (Schweif.) B.L. Burt	Zingiberaceae	Traditionally used for coughs, colds, hysteria, asthma, dysmenorrhoea, hysteria influenza, malaria, pain, sinus issues, and animal use [33,85,86]. **Score**: 3	Essential oil and compounds isolated from the plant have shown good antiviral activity against Influenza A virus. The hydroxylated lactone of siphonochilone showed >123% inhibition at 50ug/mL and >30% at 50 µg/mL. The essential oil	Moderate to high. IC_{50} (aqueous rhizome extract) =125 µg/mL in VK cells. Similar cytotoxicity was observed in Caco-2 with Ethanol extract	Roots and Rhizomes [33,86]. **Score**: 1	8

				showed <35% inhibition at 50 µg/mL and siphonochilone >115% at 50 ug/mL [87,88]. **Score**: 2	of roots. 100 µg/mL induced 19.9% apoptosis [86,89]. **Score**: 2		
16	*Sutherlandia frutescens* (L.) R.Br.	Fabaceae	Used for Stomach ailments, diabetes, cancers, fever, wounds, stress, diarrhoea, blood purification, infections, pustules, chicken pox, influenza, intestinal complaints, uterine troubles, liver disease, inflammations, rheumatism, haemorrhoids, backache, cough, appetite improvement, colds, liver and bladder problems [90]. **Score**: 3	The plant contains compounds active against HIV target enzymes [91]. [Recent/post selection]: L-canavanine predicted *in silico* to act against SARS-CoV-2 [92]. **Score**: 3	Low. None were detected *in vivo* and phase I clinical trials [90] **Score**:3	Leaves [90] **Score**: 3	12
17	*Teclea gerrardii* I.Verd.	Rutaceae	Used for chest irritations associated with colds and coughs [33,93]. **Score**: 2	No *in vitro* bioassays conducted against viruses. **Score**: 3	Not tested **Score**: 3	Bark [33] **Score**: 2	10
18	*Tetradenia riparia* (Hochst.) Codd	Lamiaceae	Used for coughs, colds, sore throat, to induce vomiting, dengue fever, fevers, diarrhoea, boils and mumps, malaria (as part of a mixture), stomach ache, toothache, headache, influenza [33,94]. **Score**: 3	No antiviral activity against the herpes simplex, poliomyelitis, coxsackie, Semliki forest and Measles viruses [95]. **Score**: 2	Moderate. LC_{50} = 492 µg/mL (organic extract) in brine shrimp lethality assay [96]. **Score**: 2	Leaves [33,94]. **Score**: 3	10
19	*Vangueria infausta* Burch. subsp. *infausta*	Rubiaceae	Used for malaria and chest complaints, to enhance fertility, menstrual complaints, anthelmintics, coughs, chest complaints, pneumonia, abdominal complaints, diarrhoea, swollen legs, dental pain, and insomnia [33]. **Score**: 3	No *in vitro* data has been reported. **Score**: 3	Moderate. (Ethanol lead extract) LC_{50} = 144.7 µg/mL in brine shrimp assay. DCM:MeOH against L-6 cells IC_{50}=45.7 µg/mL [97]. **Score:** 2	Roots and leaves [33] **Score**: 1	9

2.4.2 Collection and extraction of plant material

The selected 19 plant species were obtained from various sources from July-October 2020. Six plant species, *Buddleja salviifolia* (L.) Lam., *Clerodendrum glabrum* E.Mey.(Volkameria glabra (E.Mey.) Mabb. & Y.W.Yuan), *Lantana camara* L., *Mentha longifolia* (L.) Huds. subsp. *polyadena* (Briq.) Briq., *Podocarpus henkelii* Stapf ex Dallim. & Jacks. and *Sutherlandia frutescens* (L.) R.Br were collected from Maine van der Schijff Botanical Garden, University of Pretoria, South Africa. Voucher specimens for these plants were deposited and identified at the H.G.W.J. Schweickerdt Plant Herbarium at University of Pretoria. Nine plant species were obtained from the University of Pretoria's plant repository, these being *Harpagophytum procumbens* (Burch.) DC ex Meisn. subsp. *procumbens*; *Helichrysum nudifolium* (L.) Less.

var. *pilosellum* (L.f.) Beentje.; *Helichrysum psilolepis* Harv.; *Pittosporum viridiflorum* Sims, *Selaginella dregei* (C.Presl) Hieron.; *Teclea gerrardii* I.Verd.; *Tetradenia riparia* (Hochst.) Codd; *Vangueria infausta* Burch. subsp. *infausta* and *Leonotis leonurus* (L.) R.Br. Four additional plant species were obtained from other sources: two species were obtained from the ARC, these being *Artemisia afra* Jacq. ex Willd. and *Siphonochilus aethiopicus* (Schweif.) B.L. Burt. Additionally, *Gunnera perpensa* L., was obtained from Pure Organics (FJ Isaacs) and *Pelargonium sidoides* DC., from Percival Pty Ltd.

A total of 31 plant extracts were prepared for the different respective plant species. The details of the respective extracts are described in Table 2.2 which included mostly the roots or leaves or stems of the plants. The DCM:MeOH extraction method was selected based on work conducted by Thornburg et al. (2004), who found that the DCM:MeOH extraction method used provided an unbiased extraction of both polar and non-polar compounds [34]. The work also found that a DCM:MeOH extract type worked well with a C8 SPE cartridge to provide adequate sample separation. From a biological point of view, this type of extraction is particularly valuable as both polar and non-polar compounds may prove bioactive. In view of potential extract commercialisation and clinical trials, a 96% ethanol and 60% ethanol extract was prepared of select plants, where toxic chemicals like DCM or MeOH cannot be utilised when preparing extracts for human consumption.

The extraction yields of the 31 plant extracts ranged from 1.7% to 27.1%. The percentage yields of the fractions generated from the 20 plant extracts were found to differ based on the extraction solvent, plant part used, and the type of compounds present within the plant. The yield distribution differed significantly between plants, with some plants having significantly more polar compounds (weight distribution skewed more toward the early fractions) and others more non-polar compounds (weight distribution skewed more toward the later fractions). The details of these plant extracts and fractions, including the voucher specimen numbers, harvest location, date and respective extract and fraction yields, are displayed in Table 2.2.

Table 2.2: Details of plant species collected, extraction yield and voucher specimen number.

#	Plant species[a]	Obtained from, collection site and date	Plant part used for extraction	Voucher specimen number /identification number	Extraction yield (calculated from dry plant material) (%w/w)	Fractions and yield (%w/w)
1	*Artemisia afra* Jacq. ex Willd.	ARC. Location: Roodeplaat, South Africa July 2020	Leaves and stems	Cultivated material provided by the ARC	• 96% Ethanol extract: 18.1% • 60% Ethanol extract: 25.6% • DCM:MeOH Extract: 27.1%	96% Ethanol extract Fraction 1: 9.6% Fraction 2: 11.4% Fraction 3: 11.1% Fraction 4: 17.6% Fraction 5: 18.3% Fraction 6: 10.0% Fraction 7: 11.5% DCM:MeOH Extract Fraction 1: 21.7% Fraction 2: 12.5% Fraction 3: 9.9% Fraction 4: 16.7% Fraction 5: 10.0% Fraction 6: 9.5% Fraction 7: 5.7%
2	*Buddleja salviifolia* (L.) Lam.	Maine van der Schijff Botanical Garden, University of Pretoria, South Africa August 2020	Leaves and stems	PRU 130595	DCM:MeOH Extract: 20.0%	Fraction 1: 1.4% Fraction 2: 20.5% Fraction 3: 2.9% Fraction 4: 13.1% Fraction 5: 9.9% Fraction 6: 18.2% Fraction 7: 7.3%
3	*Clerodendrum glabrum* E.Mey. (*Volkameria glabra* (E.Mey.) Mabb. & Y.W.Yuan)	Maine van der Schijff Botanical Garden, University of Pretoria, South Africa August 2020	Leaves	PRU 130598	DCM:MeOH Extract: 8.0%	Fraction 1: 7.2% Fraction 2: 11.0% Fraction 3: 12.3% Fraction 4: 19.5% Fraction 5: 14.7% Fraction 6: 11.3% Fraction 7: 5.1%
4	*Gunnera perpensa* L.	Pure Organics. Location: Uitenhage, South Africa February 2021	Leaves and stems	PRU 128787	• 96% Ethanol extract: 15.3% • 60% Ethanol extract: 18.5%	DCM:MeOH Extract Fraction 1: 4.2% Fraction 2: 12.1% Fraction 3: 9.1% Fraction 4: 8.3%

					• DCM:MeOH Extract: 8.0%	Fraction 5: 5.4% Fraction 6: 6.1% Fraction 7: 9.6%
5	*Harpagophytum procumbens (Burch) DC ex Meisn.* subsp. *procumbens*	CSIR. Location: Witdraai, Northern Cape, South Africa October 2013	Roots	ECD-CB06-043	DCM:MeOH Extract: 12.2%	Fraction 1: 10.2% Fraction 2: 13.9% Fraction 3: 4.8% Fraction 4: 36.3% Fraction 5: 12.3% Fraction 6: 9.7% Fraction 7: 4.3%
6	*Helichrysum nudifolium* (L.) Less.	University of Pretoria Plant Repository Location: Caslae Farm (31°3'25.8"S;30°11'33.1"E) March 2002	Roots	DS01816	DCM:MeOH Extract: 3.2%	Fraction 1: 8.3% Fraction 2: 17.6% Fraction 3: 14.2% Fraction 4: 21.8% Fraction 5: 8.6% Fraction 6: 13.9% Fraction 7: 7.1%
7	*Helichrysum psilolepis* Harv.	University of Pretoria Plant Repository Location: Eastern Orange Free State (27°49'30.3"S;28°56'16.5"E) December 2000	Whole plant	BP00394	DCM:MeOH Extract: 5.8%	Fraction 1: 12.0% Fraction 2: 14.2% Fraction 3: 8.2% Fraction 4: 8.4% Fraction 5: 13.8% Fraction 6: 19.4% Fraction 7: 8.5%
8	*Lantana camara* L.	Maine van der Schijff Botanical Garden, University of Pretoria, South Africa August 2020	Leaves and stems	PRU 130596	DCM:MeOH Extract: 13.2%	Fraction 1: 24.7% Fraction 2: 16.4% Fraction 3: 15.7% Fraction 4: 19.1% Fraction 5: 6.5% Fraction 6: 12.2% Fraction 7: 4.1%
9	*Leonotis leonurus* (L.) R.Br.	University of Pretoria Plant Repository Leaves: Location: Eastern Cape (31°36'18.2"S;29°26'26.8"E) August 2002 Stems: Location: Van Stadens Rivier (33°54'47.4"S;25°13'14.0"E)	Leaves; stems (separate)	Leaves: DS03410 Stems: FP00718	DCM:MeOH Extract (leaves): 17.7% DCM:MeOH Extract (stems): 7.5%	Leaves Fraction 1: 7.2% Fraction 2: 2.8% Fraction 3: 1.7% Fraction 4: 2.1% Fraction 5: 22.9% Fraction 6: 30.4% Fraction 7: 26.0% Stems Fraction 1: 22.7% Fraction 2: 37.1 Fraction 3: 6.9%

		April 2002				Fraction 4: 2.9% Fraction 5: 3.5% Fraction 6: 6.2% Fraction 7: 3.9%
10	*Mentha longifolia* (L.) Huds. subsp. *polyadena* (Briq.) Briq.	Maine van der Schijff Botanical Garden, University of Pretoria, South Africa August 2020	Leaves and stems	PRU 130593	DCM:MeOH Extract: 13.7%	Fraction 1: 8.5% Fraction 2: 15.2% Fraction 3: 9.7% Fraction 4: 10.1% Fraction 5: 6.7% Fraction 6: 10.5% Fraction 7: 8.7%
11	*Pelargonium sidoides* DC.	Percival, Pty Ltd Location: Eastern Cape	Roots and tuber	Code: 02P0056 Batch: D0470/15	• 96% Ethanol extract: 1.9% • 60% Ethanol extract: 12.3% • DCM:MeOH Extract: 1.7%	60% Ethanol extract Fraction 1: 13.2% Fraction 2: 16.9% Fraction 3: 19.3% Fraction 4: 12.8% Fraction 5: 7.8% Fraction 6: 9.6% Fraction 7: 7.3%
12	*Pittosporum viridiflorum* Sims	University of Pretoria Plant Repository Leaves: Location: Eastern Cape (31°37'32.7"S;29°27'51.1"E) August 2002 Bark: Location: Gqeberha (33°58'34.6"S;25°36'20.5"E) August 2002	Leaves and bark (separate)	Leaves: DS03359 Barks: FP01395	DCM:MeOH Extract: 9.3%	Fraction 1: 9.7% Fraction 2: 11.4% Fraction 3: 3.6% Fraction 4: 11.3% Fraction 5: 16.2% Fraction 6: 16.0% Fraction 7: 13.6%
13	*Podocarpus henkelii* Stapf ex Dallim. & Jacks.	Maine van der Schijff Botanical Garden, University of Pretoria, South Africa August 2020	Fruit	PRU 128788	• 96% Ethanol extract: • 60% Ethanol extract: • DCM:MeOH Extract: 18.1%	DCM:MeOH Extract Fraction 1: 18.0% Fraction 2: 24.8% Fraction 3: 11.7% Fraction 4: 6.6% Fraction 5: 1.4% Fraction 6: 11.2% Fraction 7: 2.8%
14	*Selaginella dregei* (C.Presl) Hieron.	University of Pretoria Plant Repository	Whole	EV00478	DCM:MeOH Extract: 2.6%	Fraction 1: 20.0% Fraction 2: 6.2%

		Location: Louwsburg (27°34'7"S;31°18'0"E) August 2002				Fraction 3: 7.3% Fraction 4: 7.5% Fraction 5: 5.7% Fraction 6: 14.2% Fraction 7: 11.2%
15	*Siphonochilus aethiopicus* (Schweif.) B.L. Burt	Fresh roots/rhizomes: ARC Location: Roodeplaat, South Africa July 2020 Old/aged roots/rhizomes: CSIR Location: Cultivated material CSIR December 2003	Roots and rhizomes	ARC (Fresh): Roodeplaat, Pretoria CSIR (Old): SNA/003	Fresh • 96% Ethanol extract: 16.1% • Hexane:MeOH Extract: 19.1% Old • 96% Ethanol extract: 18.1% • DCM:MeOH Extract: 21.1%	N/A
16	*Sutherlandia frutescens* (L.) R.Br.	Maine van der Schijff Botanical Garden, University of Pretoria, South Africa August 2020	Leaves, stems, flowers and pods	PRU 130594	DCM:MeOH Extract: 10.2%	Fraction 1: 21.0% Fraction 2: 16.3% Fraction 3: 8.5% Fraction 4: 11.3% Fraction 5: 17.7% Fraction 6: 7.3% Fraction 7: 5.6%
17	*Teclea gerrardii* I.Verd.	University of Pretoria Plant Repository Location: Eastern Cape (31°35'57.9"S;29°31'36.8"E) April 2002	Stems	DS02449	DCM:MeOH Extract: 2.5%	Fraction 1: 2.1% Fraction 2: 5.3% Fraction 3: 7.0% Fraction 4: 14.5% Fraction 5: 19.7% Fraction 6: 14.3% Fraction 7: 8.6%
18	*Tetradenia riparia* (Hochst.) Codd	University of Pretoria Plant Repository Location: Eastern Cape (31°35'57.9"S;29°31'36.8"E) September 2002	Leaves	DS04258	DCM:MeOH Extract: 7.7%	Fraction 1: 7.2% Fraction 2: 11.0% Fraction 3: 12.3% Fraction 4: 19.5% Fraction 5: 14.7% Fraction 6: 11.3% Fraction 7: 5.1%
19	*Vangueria infausta* Burch. subsp. *infausta*	University of Pretoria Plant Repository	Roots	QM00104	DCM:MeOH Extract: 2.4%	Fraction 1: 8.1% Fraction 2: 22.4% Fraction 3: 7.8% Fraction 4: 10.2%

		Location: Vaal river (26°54'46.2"S;27°23'36."7E) April 2002				Fraction 5: 11.6% Fraction 6: 6.2% Fraction 7: 8.0%
20	Method Blank	N/A October 2020	N/A	N/A	N/A	Fraction 1 (mg): 0.7 Fraction 2 (mg): 1.1 Fraction 3 (mg): 0.8 Fraction 4 (mg): 1.1 Fraction 5 (mg): 1.0 Fraction 6 (mg): 1.4 Fraction 7 (mg): 1.2

[a]As accepted and published on https://www.sanbi.org/ or provided by H.G.W.J. Schweickerdt Plant Herbarium.

2.4.3 Bioassay screening results

The plant extracts and fractions were screened in spike RBD/ACE2 interactions bioassays (AlphaScreens) and M^{pro} inhibition bioassays. The spike RBD/ACE2 interaction antagonism results are represented in Table 2.3, with the M^{pro} inhibition data in Table 2.4. Of the 30 different extracts screened, 14 had an IC_{50} < 30 µg/mL in spike RBD/ACE2 inhibition assays and only 3 (10% hit rate), which showed >80% inhibition at 10 µg/mL in M^{pro} inhibition bioassays. Some bioactivity was observed throughout multiple extracts originating from the same plant. Not taking this duplicate activity into account, 7 plant extracts (36.8%) out of the 19 different plants had an IC_{50} < 30 µg/mL in spike RBD/ACE2 bioassays, and only 2 plants extracts (10.5%) of the 19 were found to exhibit >80% inhibition at 10 µg/mL in M^{pro} inhibition assays. Of the 147 plant fractions screened, 37 (25.2% hit rate) were found to have an IC_{50} < 30 µg/mL in spike RBD/ACE2 inhibition assays and only 7 (4.8 % hit rate), which showed >80% inhibition at 10 µg/mL in M^{pro} inhibition bioassays (Table 2.3; Table 2.4).

Interestingly, some extracts showed little to no bioactivity while their semi-purified fractions showed considerable activity; the spike RBD/ACE2 inhibition activity of *Sutherlandia frutescens*, *Helichrysum psilolepis*, *Lantana camara* and *Leonotis leonurus* are good examples of this (Table 2.4). It was presumed that this observation was due to the concentration of the bioactive compound/s during the fractionation process or to the removal of lipids and other nuisance compounds (which bind irreversibly to the C8 stationary phase), which may mask the bioactivity and contribute to a false-negative result. Based on these results, the usefulness of extract pre-fractionation in preventing the emergence of false negatives is highlighted.

Among the bioactive samples, the extracts and fractions of *Gunnera perpensa* and *Podocarpus henkelii* displayed potent antagonistic activity against the spike RBD/ACE2 interaction, with their respective IC_{50} values found to be <1 µg/mL, significantly different to the method blank. These samples compared well with the positive control used, viz., REGN10987, a monoclonal antibody whose IC_{50} was found to be 0.025 µg/mL. The plants were prioritised for further studies based on their potent biological activity and high score in the selection criteria and well-reported traditional use. *G. perpensa* was of particular interest due to its recent use by a traditional health practitioner in regions of South Africa, where it is reportedly used for the treatment and management of COVID-19 [98]. Additionally, due to the observed bioactivity results of the *S. aetheopicus* extract, its selection score, broad traditional use and the recently reported bioactivity against the influenza RNA virus [88], its main compounds, siphonochilone and HLS were similarly prioritised for further studies.

Table 2.3: Bioassay results of the various plant extracts and fractions in the SARS-CoV-2 spike RBD/ACE2 inhibition screens. Data presented as the mean of duplicate analysis in a heatmap.

				Fractions (IC_{50} µg/mL)						
Plant	**Sample**	**Extract type**	**Extract (IC_{50} µg/mL)**	**F1**	**F2**	**F3**	**F4**	**F5**	**F6**	**F7**
Artemisia afra	Leaves and stems	96% Ethanol	>30	>30	>30	>30	>30	>30	>30	>30
		60% Ethanol	>30							
		DCM:MeOH	>30	>30	>30	>30	>30	5.01	>30	>30
Buddleja salviifolia	Leaves and stems	DCM:MeOH	>30	>30	>30	>30	>30	>30	>30	>30
Clerodendrum glabrum	Leaves	DCM:MeOH	>30	>30	>30	>30	>30	>30	>30	>30
Gunnera perpensa	Leaves and stems	96% Ethanol	0.06							
		60% Ethanol	0.0381							
		DCM:MeOH	0.0141	>30	0.0021	0.001	0.001	0.0034	0.001	0.001
Harpagophytum procumbens subsp. *procumbens*	Roots	DCM:MeOH	19.94	>30	>30	>30	>30	15.05	0.35	2.36
Helichrysum nudifolium	Roots	DCM:MeOH	6.70	>30	>30	>30	>30	7.60	0.19	0.63
Helichrysum psilolepis	Whole plant	DCM:MeOH	>30	>30	>30	>30	>30	2.66	>30	>30
Lantana camara	Leaves and stems	DCM:MeOH	>30	>30	>30	>30	>30	>30	>30	>30
Leonotis leonurus	Leaves	DCM:MeOH	>30	>30	>30	>30	>30	19.87	>30	>30
	Stems	DCM:MeOH	>30	>30	>30	>30	>30	7.18	>30	>30
Mentha longifolia subsp. polyadena	Leaves and stems	DCM:MeOH	>30	>30	>30	>30	>30	24.71	>30	>30
Pelargonium sidoides	Tubers/roots	96% Ethanol	2.01	>30	2.6	0.37	0.8	1.24	1.48	3.76
		60% Ethanol	1.78							
		DCM:MeOH	1.96							
Pittosporum viridiflorum	Bark	DCM:MeOH	>30	>30	>30	>30	>30	>30	>30	>30
Pittosporum viridiflorum	Leaves	DCM:MeOH	>30	>30	>30	>30	>30	>30	>30	>30
Podocarpus henkelii	Fruit	96% Ethanol	0.56							
		60% Ethanol	2.5							
		DCM:MeOH	0.48	13.69	1.3	0.194	0.31	1.77	1.211	18.18
Selaginella dregei	Whole plant	DCM:MeOH	>30	>30	>30	>30	>30	0.26	>30	>30
Siphonochilus aethiopicus	Roots and rhizomes	96% Ethanol	3.44							
		Hex:MeOH	11.47							
Sutherlandia frutescens	Leaves, stems, flower and pod	DCM:MeOH	>30	>30	>30	>30	>30	14.12	1.54	>30
Teclea gerrardii	Stems	DCM:MeOH	>30	>30	>30	>30	>30	>30	>30	>30
Tetradenia riparia	Leaves	DCM:MeOH	>30	>30	>30	13.46	>30	>30	>30	>30
Vangueria infausta subsp. *infausta*	Roots	DCM:MeOH	9.70	>30	>30	>30	20.80	28.76	18.62	>30
Method Blank		DCM:MeOH		>30	>30	>30	>30	>30	>30	>30

Table 2.4: Bioassay results of the various plant extracts and fractions in the SARS-CoV-2 M^{pro} inhibition screens. Data presented as the mean of duplicate analysis in a heat map.

			% Inhibition at 10 µg/mL							
Plant	**Sample**	**Extract type**	**Extract**	**Fractions**						
				F1	**F2**	**F3**	**F4**	**F5**	**F6**	**F7**
Artemisia afra	Leaves and stems	96% Ethanol	0.1	0.0	12.9	0.1	38.8	0.0	32.5	24.9
		60% Ethanol	100.0							
		DCM:MeOH	17.6	34.7	8.4	65.9	60.8	14.3	19.6	0.0
Buddleja salviifolia	Leaves and stems	DCM:MeOH	19.1	7.0	13.3	40.3	13.3	23.7	28.9	32.1
Clerodendrum glabrum	Leaves	DCM:MeOH	31.5	29.8	0.0	0.1	29.0	26.8	28.9	19.9
Gunnera perpensa	Leaves and stems	96% Ethanol	0.06							
		60% Ethanol	0.0381							
		DCM:MeOH	29.6	15.9	31.2	50.2	45.8	15.4	55.2	31.8
Harpagophytum procumbens subsp. *procumbens*	Roots	DCM:MeOH	10.9	33.2	0.1	20.7	17.6	11.4	31.8	15.8
Helichrysum nudifolium	Roots	DCM:MeOH	28.7	7.7	11.3	16.7	22.4	29.7	64.2	85.0
Helichrysum psilolepis	Whole plant	DCM:MeOH	9.9	3.6	21.9	50.0	36.2	13.1	86.6	24.7
Lantana camara	Leaves and stems	DCM:MeOH	28.7	6.0	17.6	20.6	33.5	4.3	87.5	14.6
Leonotis leonurus	Leaves	DCM:MeOH	20.1	7.6	4.0	5.5	4.8	8.8	12.7	6.6
	Stems	DCM:MeOH	7.1	0.1	0.0	0.1	0.0	16.4	58.8	36.0
Mentha longifolia subsp. polyadena	Leaves and stems	DCM:MeOH	25.6	5.8	1.8	26.2	13.5	16.3	33.7	19.8
Pelargonium sidoides	Tubers/roots	96% Ethanol	82.4	18.1	53.7	76.5	100.0	0.1	42.0	19.8
		60% Ethanol	100.0							
		DCM:MeOH	55.1							
Pittosporum viridiflorum	Bark	DCM:MeOH	35.1	6.2	14.8	25.4	26.5	18.5	24.3	75.2
Pittosporum viridiflorum	Leaves	DCM:MeOH	18.8	24.1	3.8	0.1	27.6	2.8	8.2	10.6
Podocarpus henkelii	Fruit	96% Ethanol	29.0							
		60% Ethanol	38.0							
		DCM:MeOH	14.1	13.7	8.9	0.0	0.0	27.3	85.8	30.0
Selaginella dregei	Whole plant	DCM:MeOH	20.9	8.6	11.4	5.0	34.9	40.5	81.4	36.6
Siphonochilus aethiopicus	Roots and rhizomes	96% Ethanol	44.1							
		Hex:MeOH	41.8							
Sutherlandia frutescens	Leaves, stems, flower and pod	DCM:MeOH	0.0	0.0	0.0	0.1	0.0	7.4	43.7	18.2
Teclea gerrardii	Stems	DCM:MeOH	30.1	6.9	0.1	26.1	33.1	38.0	17.1	44.2
Tetradenia riparia	Leaves	DCM:MeOH	19.0	15.0	5.9	14.6	9.9	11.8	39.7	18.6
Vangueria infausta subsp. *infausta*	Roots	DCM:MeOH	42.2	0.0	15.6	38.9	86.6	26.6	17.7	42.6
Method Blank		DCM:MeOH		17.9	34.0	15.0	6.8	18.5	59.4	20.1

Statistical analysis was conducted on the results of the bioassays using both unsupervised (principal components analysis (PCA)), and supervised (partial least squares (PLS)) multivariate analysis.

PCA was performed on the bioassay results (spike RBD/ACE2 inhibition and M^{pro} inhibition) of the fractions broadly to identify correlations within groupings of fractions. The cluster plot, using the fraction means (on a 95% CI), showed close correlation and significant overlap of the means of fractions 1 and 2, similarly with 3,4 and 7. Although not statistically significant ($p < 0.05$), fractions 5 and 6 were distinguishable from the other fractions and may be significant with a larger sample size. The first principal component represents roughly 64.5% of the observed variability in fractions due to the variance in activity in both spike and M^{pro} inhibition bioassays (Figure 2.9). The variations were likely due to the commonality of compound polarity present in the fractions.

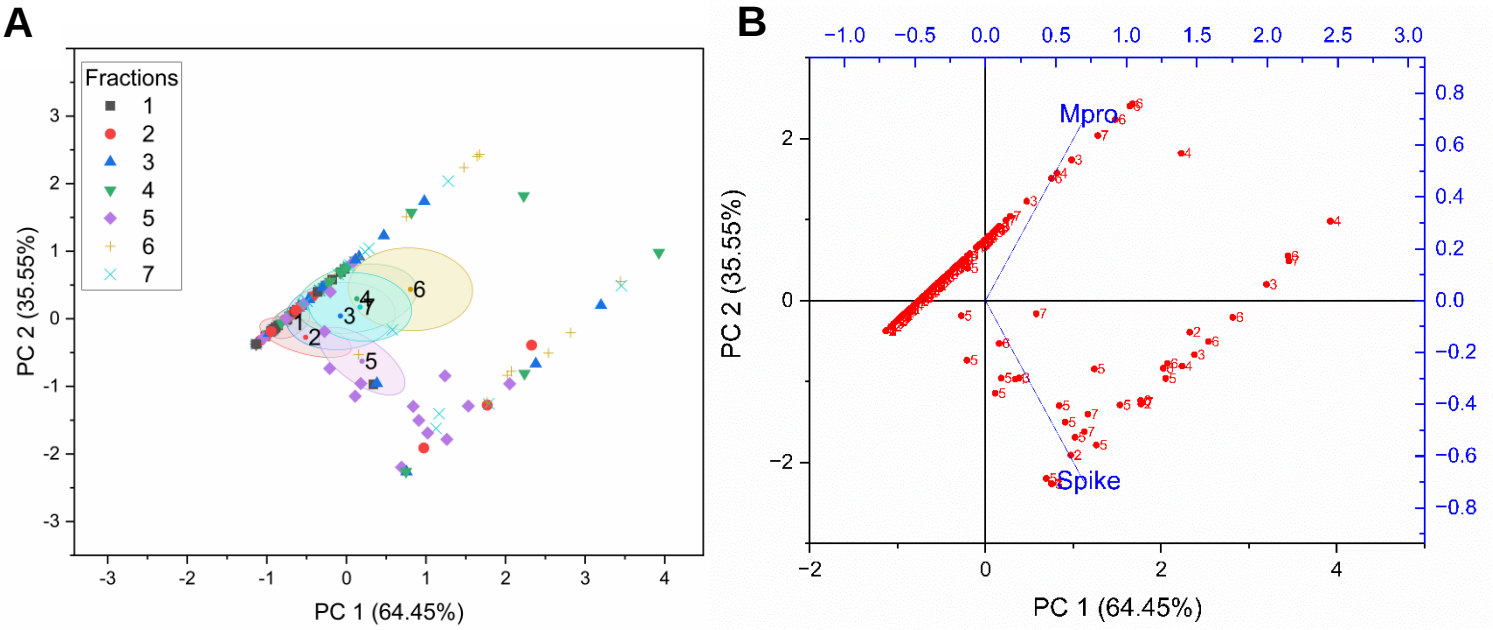

Figure 2.9: (**A**) Principal component analysis (PCA) based on the spike RBD/ACE2 interaction data and M^{pro} inhibition data for each fraction and a (**B**) PCA bi-plot. The 95% confidence ellipses are displayed for each fraction data set.

As an extension of the PCA conducted, which proposes to maximise the variance explained in a data set by combinations of independent variables (components), PLS proposes to explain the observed variance by reference to the response variables, i.e., the bioactivity [34]. To plot the PLS scores plot, the spike RBD/ACE2 interaction data were normalised to % inhibition where samples with IC_{50} >30 µg/mL were deemed inactive (0% inhibition). The PLS scores

plot obtained (Figure 2.10) concluded that fractions 4-7 contribute most of the biological activity. Fraction 5 is significantly separated from the other fractions, as already seen in the PCA, and contains compounds with selective activity against the spike RBD/ACE2 interaction. Interestingly, fraction 6 holds broad antiviral activity against the spike RBD/ACE2 interaction and the M^{pro} enzyme.

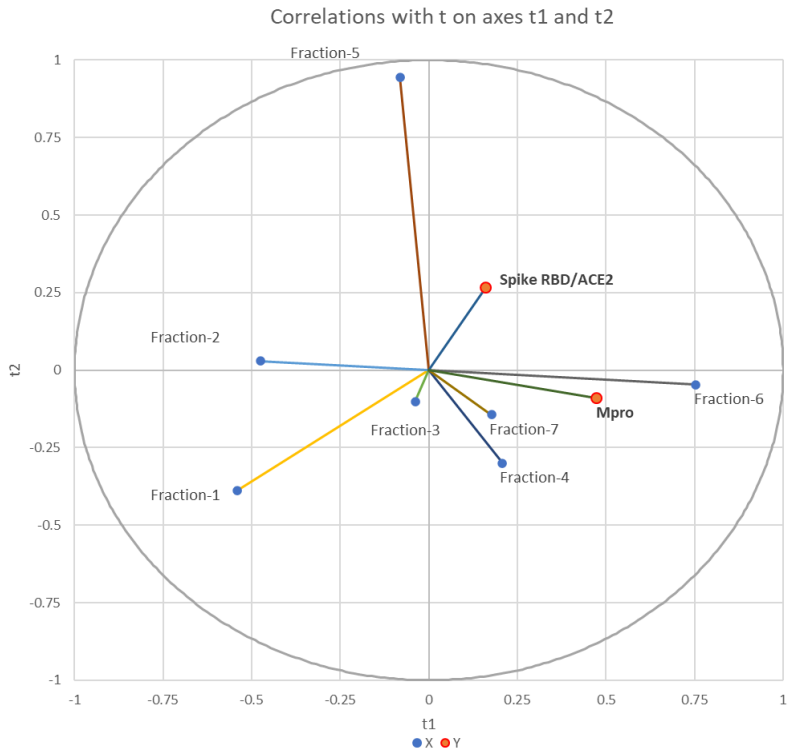

Figure 2.10: Partial least-squares (PLS) scores plot shows the correlation in bioactivity amongst the different fractions.

Based on these results, the highly polar fractions, presumed to contain very polar compounds, do not, on average, contain compounds with good antiviral activity. Although this data is unvalidated and limited in sample size and bioassay data, based on the data, the mid-polar natural product compounds are more likely to contain good antiviral candidates against the SARS-CoV-2 virus. This observation is in line with observations made by Thornburg et al. (2018) when employing the same fractionation technique [34].

2.5 Conclusion

This chapter highlights the potential of South African natural products and traditionally used plants to act as antiviral agents against SARS-CoV-2. The various biological assays used in this study are introduced. The chapter highlights how HTS methodology can assist in rapidly screening and identifying biological hits. The use of databases and a customised scoring criterion can play a prominent role in selecting and prioritising plants for biological screening, this being particularly valuable when the number of potential plants is immense. Additionally, the use of ultrasound-assisted micro-extraction and subsequent automated pre-fractionation of plant extracts facilitates a cost-effective and prompt means of screening a large subset of plants for an increased hit rate. Based on the enhanced bioactivity observed amongst the various fractions, the use of a C8 SPE cartridge reduces the occurrence of false negatives and potentially missing potent bioactive compounds present in low quantities in the plant. Through the use of multivariate statistics, similarities can be observed and conclusions drawn from large datasets, which allows for the prediction and prioritisation of select fractions for subsequent biological screening and investigation.

The HTS methodology allowed for the prioritisation of 3 plants, namely, *Gunnera perpensa*, *Podocarpus henkelii* and *Siphonochilus aethiopicus* for further biological and chemical investigations. Other biological hits are identified, which could serve as future subjects for investigation. The low hit rate observed, highlights one of the inherent challenges associated with natural product drug discovery. However, this challenge can be minimised by using newer screening techniques and technologies, such as pre-fractionation libraries and large-scale screening.

2.6 References

1 B. J. Goble, M. Lewis, T. R. Hill and M. R. Phillips, Coastal management in South Africa: Historical perspectives and setting the stage of a new era, *Ocean Coast. Manag.*, 2014, **91**, 32–40.

2 M. P. Mamathaba, K. Yessoufou and A. Moteetee, What does it take to further our knowledge of plant diversity in the megadiverse South Africa?, *Diversity*, 2022, **14**, 1–15.

3 S. S. Semenya and A. Maroyi, Data on medicinal plants used to treat respiratory infections and related symptoms in South Africa, *Data Br.*, 2018, **21**, 419–423.

4 M. F. Mahomoodally, Traditional medicines in Africa: An appraisal of ten potent african medicinal plants, *Evidence-Based Complement. Altern. Med.*, 2013, **2013**, 617459.

5 S. Bladt and H. Wagner, From the Zulu medicine to the European phytomedicine Umckaloabo., *Phytomedicine*, 2007, **14**, 2–4.

6 F. R. van Heerden, *Hoodia gordonii*: A natural appetite suppressant, *J. Ethnopharmacol.*, 2008, **119**, 434–437.

7 H. Kolodziej, Antimicrobial, antiviral and immunomodulatory activity studies of *Pelargonium sidoides* (EPs® 7630) in the context of health promotion, *Pharmaceuticals*, 2011, **4**, 1295–1314.

8 G. Porras, F. Chassagne, J. T. Lyles, L. Marquez, M. Dettweiler, A. M. Salam, T. Samarakoon, S. Shabih, D. R. Farrokhi and C. L. Quave, Ethnobotany and the role of plant natural products in antibiotic drug discovery, *Chem. Rev.*, 2021, **121**, 3495–3560.

9 C. Clarkson, V. J. Maharaj, N. R. Crouch, O. M. Grace, P. Pillay, M. G. Matsabisa, N. Bhagwandin, P. J. Smith and P. I. Folb, In vitro antiplasmodial activity of medicinal plants native to or naturalised in South Africa., *J. Ethnopharmacol.*, 2004, **92**, 177–191.

10 M. van de Venter, S. Roux, L. C. Bungu, J. Louw, N. R. Crouch, O. M. Grace, V. Maharaj, P. Pillay, P. Sewnarian, N. Bhagwandin and P. Folb, Antidiabetic screening and scoring of 11 plants traditionally used in South Africa., *J. Ethnopharmacol.*, 2008, **119**, 81–86.

11 A. Thakur, Y. S. Chun, N. October, H. O. Yang and V. Maharaj, Potential of South African medicinal plants targeting the reduction of Aβ42 protein as a treatment of Alzheimer's disease, *J. Ethnopharmacol.*, 2019, **231**, 363–373.

12 Z. L. Grange, T. Goldstein, C. K. Johnson, S. Anthony, K. Gilardi, P. Daszak, K. J. Olival, T. O'Rourke, S. Murray, S. H. Olson, E. Togami, G. Vidal, J. A. K. Mazet, K. Anderson, P. Auewarakul, L. Coffey, R. Corley, G. Dauphin, J. Epstein, K. Fukuda, S. Goodman, B. Han, J. Hughes, M. Jeggo, W. Karesh, R. Kazwala, T. Kelly, G. Keusch, M. Kurilla, J. Mackenzie, W. Markotter, C. Monagin, D. Morens, V. Munster, E. Muhlberger, P. Pandit, A. Peel, D. Pfeiffer, O. Restif, O. Tomori, J. Towner, S. Van Der Werf, S. VonDobschetz, S. Wacharapluesadee, M. Ward, L. Weirsma, M. Wilson, D. Wolking, K. Wongsathapornchai, L. Brierley, N. Null, C. Tambrana-Torellio, null null, A. Islam, S. Islam, Z. Raman, V. Hul, V. Duong, M. Mouiche, J. Nwobegahay, K. Coulibaly, C. Kumakamba, E. K. Syaluha, J.-P. Lukusa, D. Belay, N. Kebede, W. Ampofo, S. Bel-Nono, R. Suu-Ire, K. Douokoro, H. Dursman, I. Pamungkas, N. Rachmitasari, S. Saputro, W. Damanik, T. Kusumaningrum, M. Rambitan, B. Rey, D. Safari, A. Soebandrio, J. Triastuti, E. Abu-Basha, K. Allan, K. Joseph, M. Samson, B. Khamphaphonphane, W. Theppanga, J. Desmond, S. Samules, M. H. Lee, J. Lee, B. Damdinjav, E. Shiilegdamba, O. Aung, M. Bista, D. Karmacharya, R. Shrestha, J. Nziza, J.-C. Tumushime, M. M. Lo, A. Ndiaye, M. C. Seck, J. Bangura, E. Lavalie, G. Mwangoka, Z. Sijali, R. O. Okello, B. Ssebide, S. Wacharpluesadee, N. Nguyen, J. Epstein, E. Hagan, W. Karesh, A. Latinne, A. Laudisoit, H. Li, C. Machalaba, S. Martinez, N. Ross, A. Sullivan, C. Z. Torrelio, J. Mackenzie, R. Waldman, S. Morzaria, W. Kalpravidh, Y. Makonnen, S. Von Dubscheutz, F. Claes, K. Pelican, C. B. Behravesh, E. Mumford, J. P. Clark, T. D. Vu, K. Saylors, B. Edison, J. Euren, A. Gillis, C. Lange, M. LeBreton, D. McIver, D. O'Rourke, M. Valitutto, D. Zimmerman, J.

Belkhiria, B. Bird, H. Chale, E. Preston, N. Gardner, B. Genovese, K. Gonzalez, L. Keatts, T. Kelly, E. Leasure, C. Monagin, P. Pandit, N. Randhawa, B. Smith, W. Smith, A. Tremeau-Bravard, D. Wolking, C. Churchill, S. Olson, C. Walzer and A. Fine, Ranking the risk of animal-to-human spillover for newly discovered viruses, *Proc. Natl. Acad. Sci.*, 2021, **118**, e2002324118.

13 WHO, Coronavirus disease (COVID-19).

14 N. Thenon, M. Peyre, M. Huc, A. Touré, F. Roger and S. Mangiarotti, COVID-19 in Africa: Underreporting, demographic effect, chaotic dynamics, and mitigation strategy impact, *PLoS Negl. Trop. Dis.*, 2022, **16**, 1–24.

15 C. E. Hastie, D. J. Lowe, A. McAuley, A. J. Winter, N. L. Mills, C. Black, J. T. Scott, C. A. O'Donnell, D. N. Blane, S. Browne, T. R. Ibbotson and J. P. Pell, Outcomes among confirmed cases and a matched comparison group in the Long-COVID in Scotland study, *Nat. Commun.*, 2022, **13**, 5663.

16 S. Duffy, Why are RNA virus mutation rates so damn high?, *PLoS Biol.*, 2018, **16**, e3000003.

17 U. Hofer, Fooling the coronavirus proofreading machinery, *Nat. Rev. Microbiol.*, 2013, **11**, 662–663.

18 F. Robson, K. S. Khan, T. K. Le, C. Paris, S. Demirbag, P. Barfuss, P. Rocchi and W.-L. Ng, Coronavirus RNA proofreading: molecular basis and therapeutic targeting, *Mol. Cell*, 2020, **79**, 710–727.

19 W. T. Maphumulo and B. R. Bhengu, Challenges of quality improvement in the healthcare of South Africa post-apartheid: A critical review, *Curationi.*

20 A. A. Karim, A few pills a day could keep severe Covid away: What you need to know about two new treatments | Life, https://www.news24.com/life/wellness/body/condition-centres/infectious-diseases/coronavirus/a-few-pills-a-day-could-keep-severe-covid-away-what-you-need-to-know-about-two-new-treatments-20220127, (accessed 31 December 2022).

21 M. Cascella, M. Rajnik, A. Aleem, S. C. Dulebohn and R. Di Napoli, Features, evaluation, and treatment of Coronavirus (COVID-19), Treasure Island (FL), 2022.

22 L. J. Carter, L. V. Garner, J. W. Smoot, Y. Li, Q. Zhou, C. J. Saveson, J. M. Sasso, A. C. Gregg, D. J. Soares, T. R. Beskid, S. R. Jervey and C. Liu, Assay techniques and test development for COVID-19 diagnosis, *ACS Cent. Sci.*, 2020, **6**, 591–605.

23 I. Tietjen, J. Cassel, E. T. Register, X. Y. Zhou, T. E. Messick, F. Keeney, L. D. Lu, K. D. Beattie, T. Rali, P. Tebas, H. C. J. Ertl, J. M. Salvino, R. A. Davis and L. J. Montaner, The natural stilbenoid (–)-hopeaphenol inhibits cellular entry of SARS-CoV-2 USA-WA1/2020, B.1.1.7, and B.1.351 Variants, *Antimicrob. Agents Chemother.*, 2021, **65**, e0077221.

24 T. K. Christopoulos and E. P. Diamandis, Immunoassay configurations, *Immunoassay*, eds. E. P. Diamandis and T. K. Christopoulos, Academic Press, San Diego, 1996, pp. 227–236.

25 P. Held, *AlphaScreen™ Quantitation of cAMP using the Synergy™ 2 Multi-Mode Microplate Reader*, 2007.

26 D. C. Roger Bosse, Chantal Illy, Principles of AlphaScreen, amplified luminescent proximity homogenous assay, 2002.

27 W. Zhu, M. Xu, C. Z. Chen, H. Guo, M. Shen, X. Hu, P. Shinn, C. Klumpp-Thomas, S. G. Michael and W. Zheng, Identification of SARS-CoV-2 3CL protease inhibitors by a quantitative high-throughput screening, *ACS Pharmacol. Transl. Sci.*, 2020, **3**, 1008–1016.

28 A. Roy, G. H. Lushington, J. McGee and R. Chaguturu, in *Enzyme Technologies*, John Wiley & Sons, Ltd, 2013, pp. 1–53.

29 A. Baer and K. Kehn-Hall, Viral concentration determination through plaque assays: using traditional and novel overlay systems., *J. Vis. Exp.*, 2014, e52065.

30 T. Kodama, K. Ueno, T. Kondo, Y. Morozumi, A. Kato, S. Nagai, K. Shibuya and C.

Sasakawa, Spectrophotometric microplate assay for titration and neutralization of avian nephritis virus based on the virus cytopathicity., *J. Virol. Methods*, 2022, **299**, 114303.

31 L. Urda, M. H. Kreuter, J. Drewe, G. Boonen, V. Butterweck and T. Klimkait, The petasites hybridus CO2 extract (Ze 339) blocks SARS-CoV-2 replication in vitro, *Viruses*, 2022, **14**, 106.

32 S. Chaurasiya and M. M. Hitt, in *Adenoviral Vectors for Gene Therapy*, ed. D. T. B. T.-A. V. for G. T. (Second E. Curiel, Academic Press, San Diego, 2nd edn., 2016, pp. 85–112.

33 A. Hutchings and A. B. Scott, Alan Haxton. Lewis, Gillian. Bunningham, *Zulu medicinal plants : an inventory*, University of Natal Press, Pietermaritzburg, South Africa, 1996.

34 C. C. Thornburg, J. R. Britt, J. R. Evans, R. K. Akee, J. A. Whitt, S. K. Trinh, M. J. Harris, J. R. Thompson, T. L. Ewing, S. M. Shipley, P. G. Grothaus, D. J. Newman, J. P. Schneider, T. Grkovic and B. R. O'Keefe, NCI Program for natural product discovery: A publicly-accessible library of natural product fractions for high-throughput screening, *ACS Chem. Biol.*, 2018, **13**, 2484–2497.

35 F. W. Studier, Protein production by auto-induction in high density shaking cultures., *Protein Expr. Purif.*, 2005, **41**, 207–234.

36 A. N. Honko, Rapid quantification and neutralization assays for novel coronavirus SARS-CoV-2 using Avicel R RC-591 semi-solid overlay, 2020, 1–7.

37 J. Schindelin, I. Arganda-Carreras, E. Frise, V. Kaynig, M. Longair, T. Pietzsch, S. Preibisch, C. Rueden, S. Saalfeld, B. Schmid, J.-Y. Tinevez, D. J. White, V. Hartenstein, K. Eliceiri, P. Tomancak and A. Cardona, Fiji: an open-source platform for biological-image analysis, *Nat. Methods*, 2012, **9**, 676–682.

38 J. Michel, N. Z. Abd Rani and K. Husain, A review on the potential use of medicinal plants from Asteraceae and Lamiaceae plant family in cardiovascular diseases, *Front. Pharmacol.*, 2020, **11**, 852.

39 C. M. Uritu, C. T. Mihai, G.-D. Stanciu, G. Dodi, T. Alexa-Stratulat, A. Luca, M.-M. Leon-Constantin, R. Stefanescu, V. Bild, S. Melnic and B. I. Tamba, Medicinal plants of the family Lamiaceae in pain therapy: A review., *Pain Res. Manag.*, 2018, **2018**, 7801543.

40 A. du Toit and F. van der Kooy, *Artemisia afra*, a controversial herbal remedy or a treasure trove of new drugs?, *J. Ethnopharmacol.*, 2019, **244**, 112127.

41 S.-Y. Li, C. Chen, H.-Q. Zhang, H.-Y. Guo, H. Wang, L. Wang, X. Zhang, S.-N. Hua, J. Yu, P.-G. Xiao, R.-S. Li and X. Tan, Identification of natural compounds with antiviral activities against SARS-associated coronavirus., *Antiviral Res.*, 2005, **67**, 18–23.

42 D. D. Mphuthi, Anti-viral properties of wildeals (*Artemisia afra*) and wynruit (*Ruta graveolens*) as combination therapy and its effects on the renal system, North-West University, 2015.

43 C. Nie, J. Trimpert, S. Moon, R. Haag, K. Gilmore, B. B. Kaufer and P. H. Seeberger, In vitro efficacy of *Artemisia* extracts against SARS-CoV-2, *Virol. J.*, 2021, **18**, 182.

44 J. T. Mukinda and J. A. Syce, Acute and chronic toxicity of the aqueous extract of *Artemisia afra* in rodents, *J. Ethnopharmacol.*, 2007, **112**, 138–144.

45 M. B. Mabaleha, P. C. Zietsman, A. Wilhelm and S. L. Bonnet, Ethnobotanical survey of medicinal plants used to treat mental illnesses in the Berea, Leribe, and Maseru districts of Lesotho, *Nat. Prod. Commun.*, 2019, **14**, 1934578X19864215.

46 P.-W. Cheng, L.-T. Ng, L.-C. Chiang and C.-C. Lin, Antiviral effects of saikosaponins on human coronavirus 229E in vitro., *Clin. Exp. Pharmacol. Physiol.*, 2006, **33**, 612–616.

47 S. Khan, H. Ullah and L. Zhang, Bioactive constituents form *Buddleja* species, *Pak. J. Pharm. Sci.*, 2019, **32**, 721–741.

48 P. Mehrbod, M. A. Abdalla, E. M. Njoya, A. S. Ahmed, F. Fotouhi, B. Farahmand, D. A. Gado, M. Tabatabaian, O. G. Fasanmi, J. N. Eloff, L. J. McGaw and F. O. Fasina, South African medicinal plant extracts active against influenza A virus, *BMC Complement. Altern. Med.*, 2018, **18**, 1–10.

49 P. Mehrbod, M. Ali Abdalla, F. Fotouhi, J. Nicolaas Eloff, L. McGaw and O. Fasina Folorunso, Antiviral potential against influenza A virus of crude extracts from five South African medicinal plants, *65th Int. Congr. Annu. Meet. Soc. Med. Plant Nat. Prod. Res. (GA 2017)*.

50 M. Adamu, V. Naidoo and J. N. Eloff, Efficacy and toxicity of thirteen plant leaf acetone extracts used in ethnoveterinary medicine in South Africa on egg hatching and larval development of *Haemonchus contortus*., *BMC Vet. Res.*, 2013, **9**, 38.

51 F. K. Mammo, V. Mohanlall and F. O. Shode, *Gunnera perpensa* L.: A multi-use ethnomedicinal plant species in South Africa, *African J. Sci. Technol. Innov. Dev.*, 2017, **9**, 77–83.

52 A. Maroyi, From traditional usage to pharmacological evidence: systematic review of *Gunnera perpensa* L., *Evidence-based Complement. Altern. Med.*, 2016, 1720123.

53 M. Mwale and P. J. Masika, Toxicity evaluation of the aqueous leaf extract of *Gunnera perpensa* L. (Gunneraceae), *African J. Biotechnol.*, 2011, **10**, 2503–2513.

54 L. Grant, D. E. McBean, L. Fyfe and A. M. Warnock, A review of the biological and potential therapeutic actions of *Harpagophytum procumbens*, *Phyther. Res.*, 2007, **21**, 199–209.

55 N. Mncwangi, W. Chen, I. Vermaak, A. M. Viljoen and N. Gericke, Devil's Claw—A review of the ethnobotany, phytochemistry and biological activity of *Harpagophytum procumbens*, *J. Ethnopharmacol.*, 2012, **143**, 755–771.

56 A. Maroyi, *Helichrysum nudifolium* (L.) Less.: Review of its medicinal uses, phytochemistry and biological activities, *J. Pharm. Nutr. Sci.*, 2019, **9**, 189–194.

57 H. Heyman, Metabolomic comparison of selected *Helichrysum* species to predict their antiviral properties by Heino Heyman Submitted in partial fulfilment of the requirements of the degree of Magister Scientiae In the Faculty of Natural and Agricultural Sciences.

58 A. C. U. Lourens, A. M. Viljoen and F. R. Van Heerden, South African *Helichrysum* species: a review of the traditional uses, biological activity and phytochemistry, *J. Ethnopharmacol.*, 2008, **119**, 630–652.

59 M. A. Etuh, L. T. Ohemu and D. D. Pam, *Lantana camara* ethanolic leaves extracts exhibit anti-aging properties in *Drosophila melanogaster*: Survival-rate and life span studies, *Toxicol. Res. (Camb).*, 2021, **10**, 79–83.

60 R. S. Darwish, A. A. El-Banna, D. A. Ghareeb, M. F. El-Hosseny, M. G. Seadawy and H. M. Dawood, Chemical profiling and unraveling of anti-COVID-19 biomarkers of red sage (*Lantana camara* L.) cultivars using UPLC-MS/MS coupled to chemometric analysis, in vitro study and molecular docking, *J. Ethnopharmacol.*, 2022, **291**, 115038.

61 B. M. Pour and S. Sasidharan, In vivo toxicity study of *Lantana camara*, *Asian Pac. J. Trop. Biomed.*, 2011, **1**, 230–232.

62 B. M. Pour, L. Y. Latha and S. Sasidharan, Cytotoxicity and oral acute toxicity studies of *Lantana camara* leaf extract, *Molecules*, 2011, **16**, 3663–3674.

63 O. Mazimba, *Leonotis leonurus*: A herbal medicine review, *J. Pharacognosy Phytochem.*, 2015, **3**, 74–82.

64 B. N. Nsuala, G. Enslin and A. Viljoen, "Wild cannabis": a review of the traditional use and phytochemistry of *Leonotis leonurus*, *J. Ethnopharmacol.*, 2015, **174**, 520–539.

65 P. Mikaili, S. Mojaverrostami, M. Moloudizargari and S. Aghajanshakeri, Pharmacological and therapeutic effects of *Mentha longifolia* L. and its main constituent, menthol, *Anc. Sci. Life*, 2013, **33**, 131–138.

66 S. Amzazi, S. Ghoulami, Y. Bakri, A. Il Idrissi, S. Fkih-Tétouani and A. Benjouad, Human immunodeficiency virus type 1 inhibitory activity of *Mentha longifolia*, *Therapies*, 2003, **58**, 531–534.

67 R. Ben Mrid, N. Bouchmaa, I. Kabach, M. Sobeh, A. Zyad, M. Nhiri and A. Yasri, In silico screening of Moroccan medicinal plants with the ability to directly inhibit the novel coronavirus, SARS-CoV-2, 2020, 1–29.

68 A. M. Saab, M. Tacchini, G. Sacchetti, C. Contini, H. Schulz, I. Lampronti, R. Gambari,

H. Makhlouf, M. Tannoury, A. Venditti, A. Bianco and G. Racagni, Phytochemical analysis and potential natural compounds against SARS-CoV-2/COVID-19 in essential oils derived from medicinal plants originating from Lebanon. An information note, *Plant Biosyst.*, 2022, **156**, 855–864.

69 M. S. Alamgeer, M. S. Akhtar, Q. Jabeen, S. Bashir, M. N. H. Malik, H. U. Khan, M. S. U. Rahman, U. Salma, U. Mazhar and A. Q. Khan, Antihypertensive and toxicity studies of aqueous methanolic extract of *Mentha longifolia* L., *JAPS J. Anim. Plant Sci.*, 2013, 23:1622-1627.

70 K. Witte, E. Koch, H.-D. Volk, K. Wolk and R. Sabat, The *Pelargonium sidoides* extract EPs 7630 drives the innate immune defense by activating selected MAP kinase Pathways in Human Monocytes, *PLoS One*, 2015, **10**, 1–13.

71 P. Schnitzler, S. Schneider, F. C. Stintzing, R. Carle and J. Reichling, Efficacy of an aqueous *Pelargonium sidoides* extract against herpesvirus, *Phytomedicine*, 2008, **15**, 1108–1116.

72 M. Helfer, H. Koppensteiner, M. Schneider, S. Rebensburg, S. Forcisi, C. Müller, P. Schmitt-Kopplin, M. Schindler and R. Brack-Werner, The root extract of the medicinal plant *Pelargonium sidoides* is a potent HIV-1 attachment inhibitor, *PLoS One*, 2014, **9**, 1–12.

73 M. Michaelis, H. W. Doerr and J. Cinatl, Investigation of the influence of EPs® 7630, a herbal drug preparation from *Pelargonium sidoides*, on replication of a broad panel of respiratory viruses, *Phytomedicine*, 2011, **18**, 384–386.

74 F. Iacovelli, G. Costanza, A. Romeo, T. Cosio, C. Lanna, A. Bagnulo, U. Di Maio, A. Sbardella, R. Gaziano, S. Grelli, E. Squillaci, A. Miani, P. Piscitelli, L. Bianchi, M. Falconi and E. Campione, *Int. J. Environ. Res. Public Health*, 2022, 19.

75 L. L. Theisen and C. P. Muller, EPs® 7630 (Umckaloabo®), an extract from *Pelargonium sidoides* roots, exerts anti-influenza virus activity in vitro and in vivo, *Antiviral Res.*, 2012, **94**, 147–156.

76 B. Madikizela and L. J. McGaw, *Pittosporum viridiflorum* Sims (Pittosporaceae): A review on a useful medicinal plant native to South Africa and tropical Africa, *J. Ethnopharmacol.*, 2017, **205**, 217–230.

77 P. Mehrbod, M. A. Abdalla, E. M. Njoya, A. S. Ahmed, F. Fotouhi, B. Farahmand, D. A. Gado, M. Tabatabaian, O. G. Fasanmi and J. N. Eloff, South African medicinal plant extracts active against influenza A virus, *BMC Complement. Altern. Med.*, 2018, **18**, 1–10.

78 H. L. Li, H. C. Song, Y. Zhang and Y. G. Chen, Chemical constituents of the barks of *Podocarpus macrophyllus*, *Chem. Nat. Compd.*, 2016, **52**, 539–541.

79 H. S. Abdillahi, J. F. Finnie and J. Van Staden, Anti-inflammatory, antioxidant, anti-tyrosinase and phenolic contents of four *Podocarpus* species used in traditional medicine in South Africa, *J. Ethnopharmacol.*, 2011, **136**, 496–503.

80 V. P. Bagla, *Isolation and characterization of compounds from Podocarpus henkelii (Podocarpaceae) with activity against bacterial, fungal and viral pathogens*, University of Pretoria, Pretoria, 2013.

81 H. S. Abdillahi, G. I. Stafford, J. F. Finnie and J. Van Staden, Ethnobotany, phytochemistry and pharmacology of *Podocarpus sensu latissimo* (s.l.), *South African J. Bot.*, 2010, **76**, 1–24.

82 H. S. Abdillahi, G. I. Stafford, J. F. Finnie and J. Van Staden, Antimicrobial activity of South African *Podocarpus* species, *J. Ethnopharmacol.*, 2008, **119**, 191–194.

83 A. D. Setyawan, Traditionally utilization of *Selaginella*; field research and literature review, *Nusant. Biosci.*, 1970, **1**, 146–158.

84 L.-Y. Ma, S.-C. Ma, F. Wei, R.-C. Lin, P. P.-H. But, S. H.-S. Lee and S. F. Lee, Uncinoside A and B, two new antiviral chromone glycosides from *Selaginella uncinata*., *Chem. Pharm. Bull. (Tokyo).*, 2003, **51**, 1264–1267.

85 G. Fouche, S. Van Rooyen and T. Faleschini, Siphonochilus aethiopicus, a traditional

remedy for the treatment of allergic asthma, 2013, **3**, 2–7.

86 M. E. Light, L. J. McGaw, T. Rabe, S. G. Sparg, M. B. Taylor, D. G. Erasmus, A. K. Jäger, J. Van Staden and J. N. Eloff, Investigation of the biological activities of *Siphonochilus aethiopicus* and the effect of seasonal senescence, *South African J. Bot.*, 2002, **68**, 55–61.

87 L. Kruger, V. Maharaj, T. Klimkait and L. Urda, Die ontwikkeling van 'n inasemingsmiddel uit wildegemmer (*Siphonochilus aethiopicus*) vir die behandeling van 'n Influensa A-virus, *Suid-Afrikaanse Tydskr. vir Natuurwetenskap en Tegnol.*, 2020, **39**, 126.

88 L. Kruger, *Development of Siphonochilus aethiopicus as a treatment for colds and Influenza and gas chromatographic analysis of volatiles of an insect repellent*, 2020.

89 M. Erasmus, L. H. du Plessis and J. M. Viljoen, In-vitro cytotoxicity of various *Siphonochilus aethiopicus* (Schweinf.) B.L. Burtt extracts in combination with selected tableting excipients., *J. Pharm. Pharmacol.*, 2019, **71**, 1714–1724.

90 B. E. Van Wyk and C. Albrecht, A review of the taxonomy, ethnobotany, chemistry and pharmacology of *Sutherlandia frutescens* (Fabaceae), *J. Ethnopharmacol.*, 2008, **119**, 620–629.

91 S. M. Harnett, V. Oosthuizen and M. Van De Venter, Anti-HIV activities of organic and aqueous extracts of *Sutherlandia frutescens* and *Lobostemon trigonus*, *J. Ethnopharmacol.*, 2005, **96**, 113–119.

92 D. Dwarka, C. Agoni, J. J. Mellem, M. E. Soliman and H. Baijnath, Identification of potential SARS-CoV-2 inhibitors from South African medicinal plant extracts using molecular modelling approaches, *South African J. Bot.*, 2020, **133**, 273–284.

93 A. F. Kamdem Waffo, P. H. Coombes, N. R. Crouch, D. A. Mulholland, S. M. M. El Amin and P. J. Smith, Acridone and furoquinoline alkaloids from *Teclea gerrardii* (Rutaceae: Toddalioideae) of southern Africa, *Phytochemistry*, 2007, **68**, 663–667.

94 E.-F. Njau, J. Alcorn, J. Buza, M. Chirino-Trejo and P. Ndakidemi, Antimicrobial activity of *Tetradenia riparia* (Hochst.) Lamiaceae, a medicinal plant from tanzania, *European J. Med. Plants*, 2014, **4**, 1462–1478.

95 A. J. Vlietinck, L. Van Hoof, J. Totté, A. Lasure, D. V. Berghe, P. C. Rwangabo and J. Mvukiyumwami, Screening of hundred Rwandese medicinal plants for antimicrobial and antiviral properties, *J. Ethnopharmacol.*, 1995, **46**, 31–47.

96 H. Shirinda, C. Leonard, G. Candy and S. van Vuuren, Antimicrobial activity and toxicity profile of selected southern African medicinal plants against neglected gut pathogens, *S. Afr. J. Sci.*, 2019, **115**, 1–10.

97 A. Maroyi, Nutraceutical and Ethnopharmacological Properties of *Vangueria infausta* subsp. *infausta*, *Molecules*, 2018, **23**, 1089.

98 L. Invernizzi, P. Moyo, J. Cassel, F. J. Isaacs, J. M. Salvino, L. J. Montaner, I. Tietjen and V. Maharaj, Use of hyphenated analytical techniques to identify the bioactive constituents of *Gunnera perpensa* L., a South African medicinal plant, which potently inhibit SARS-CoV-2 spike glycoprotein–host ACE2 binding, *Anal. Bioanal. Chem.*, 2022, **414**, 3971–3985.

Chapter 3

Identification of bioactive compounds from *Gunnera perpensa* L. against SARS-CoV-2

3.1 Background

3.1.1 Geographical distribution, classification, and phytochemistry of *Gunnera perpensa* L.

Gunnera perpensa L. forms part of the genus '*Gunnera* L.', the sole genus in the family Gunneraceae and forms part of the Gunnerales order [1,2]. Known by many names across South Africa, the 'river pumpkin', 'uGhobo' (isiZulu), 'Qobo' (Sotho), 'Rivierpampoen' (Afrikaans) or Wild Rhubarb (English) is an erect, perennial plant which grows well along river banks and marshy areas in various parts of South Africa that experience moderate to heavy rainfall [1,3]. The plant has large leaves, resembling those of a pumpkin, with long thick stalks which provide support to the leaves. This species has branching horizontal rhizomes with small reddish flowers that form along a flowering stem which gets pollinated by the wind [1,4] (Figure 3.1).

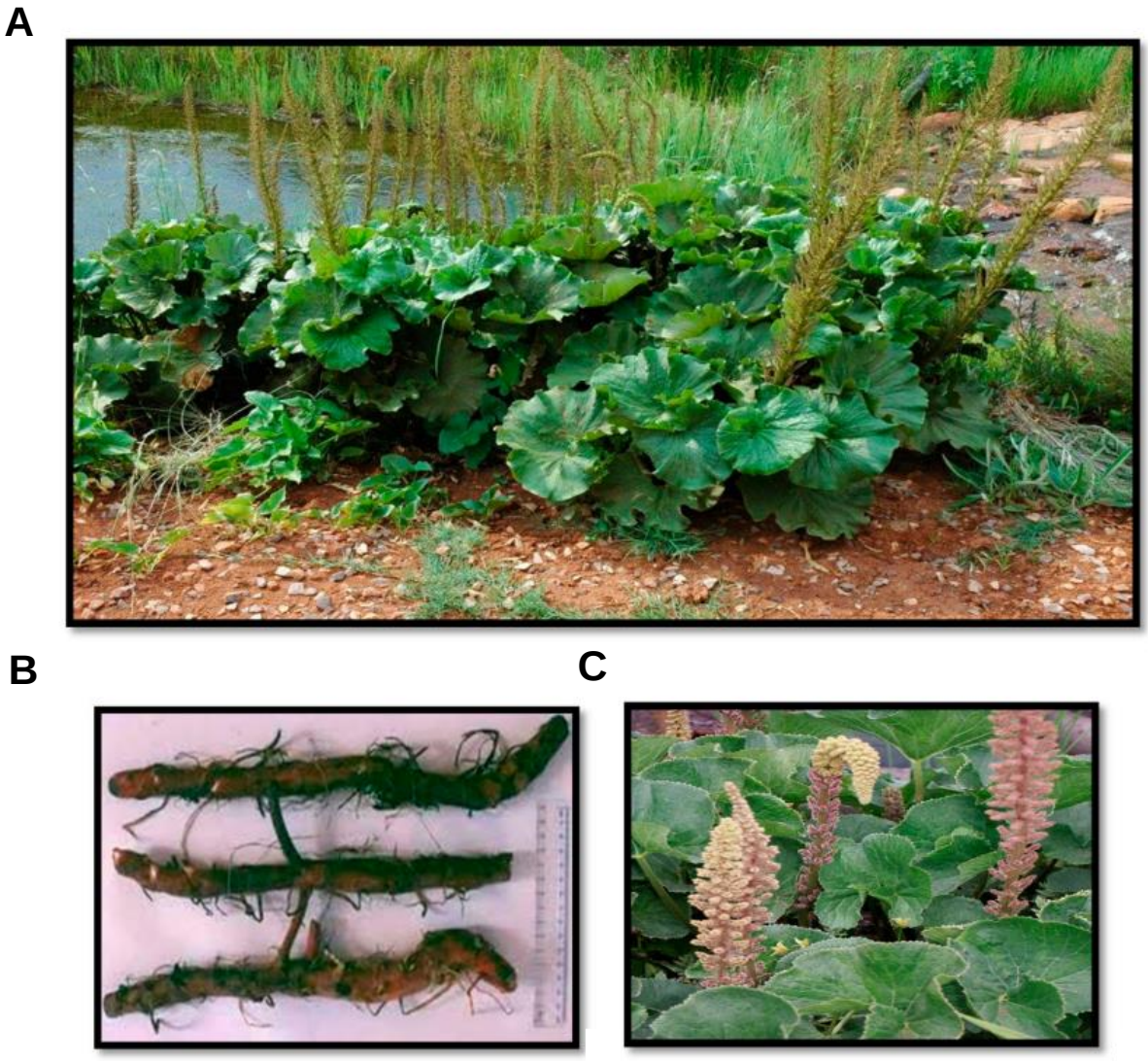

Figure 3.1: Picture adapted from Mammo et al. (2017) [1], which shows *Gunnera perpensa* L. (**A**) whole plant, (**B**) branching horizontal rhizomes with (**C**) a flower. Picture obtained with permission (Copyright © 2016 Taylor & Francis Group).

Although different *Gunnera* species are distributed in various parts of the world, *G. perpensa* L. is solely isolated to Africa and the only species distributed in Africa with its distribution stretching along mountains bordering the Great Rift Valley to Ethiopia and Sudan [4]. *G. perpensa* occurs naturally in 4 provinces in South Africa, viz. Western Cape, Eastern Cape, Free State and KwaZulu-Natal [1].

The plant has an extensive phytochemistry profile, with many secondary metabolites already isolated and characterised. A few well-reported compounds include: a phenylpropanoid

glucoside called Z-venusol **(15)**, Z-methyl lespedezate **(16)** and (Z)-lespedezic acid **(17)** [5]; ellagic acid-related compounds viz. ellagitannin α/β-punicalagin **(18)** [6], ellagic acid lactone **(19)**, 3,3′,4′-tri-O-methyl ellagic acid **(20)** [7], 3,3′,4′-tri-O-methylellagic acid-4-O-β-D-glucopyranoside **(21)** [5]; 1,4-benzoquinones: 2-methyl-6-prenyl-1,4-benzoquinone **(22a)** and3-hydroxy-2-methyl-5-(3-methyl-2-butenyl)benzo-1,4-quinone **(22b)** [8], sterols, tannins, glycosides and flavonoids [9] (Figure 3.2).

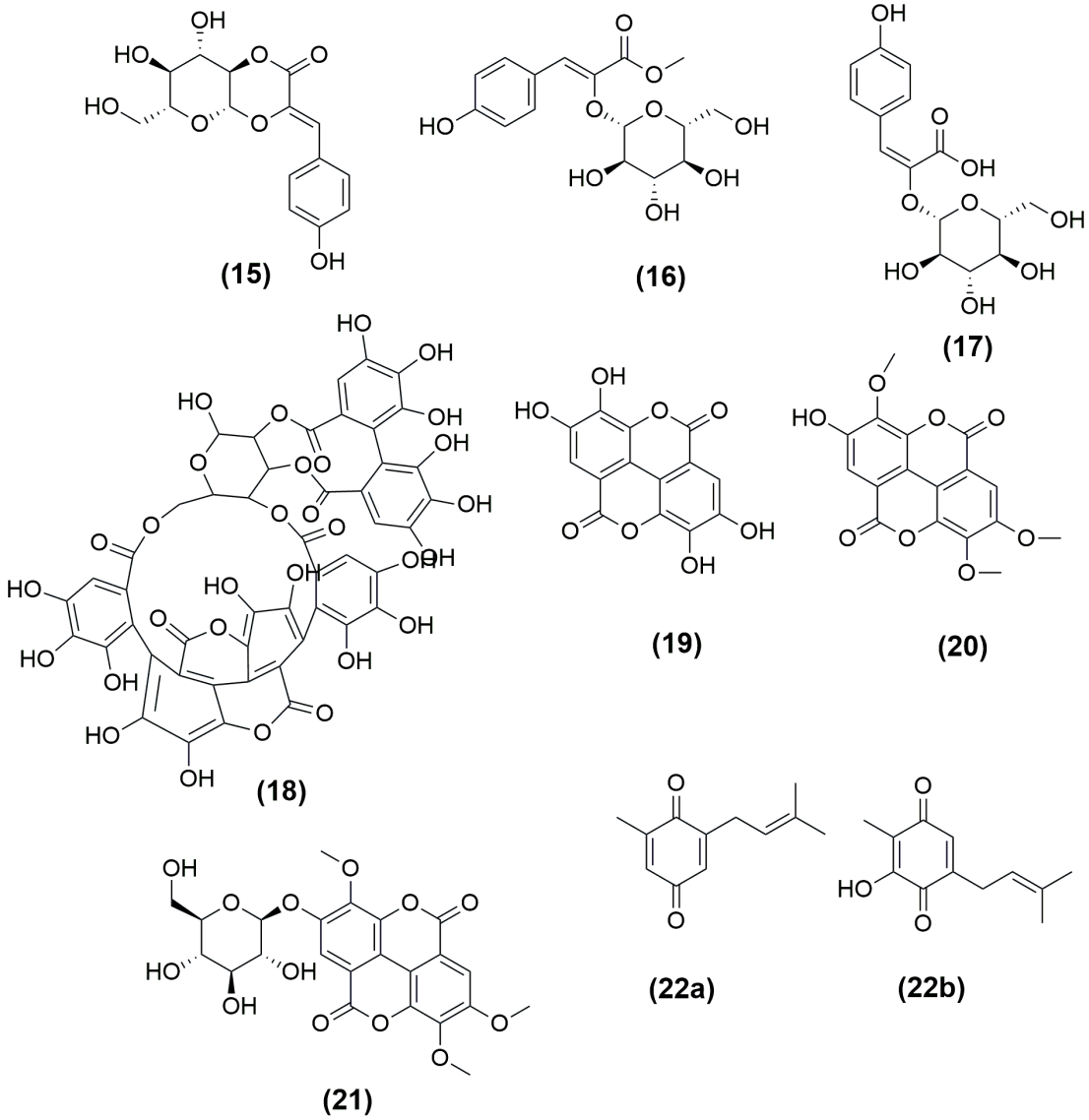

Figure 3.2: Key compounds identified in *Gunnera perpensa* L. Z-Venusol **(15)**; Z-methyl lespedezate **(16)**; (Z)-lespedezic acid **(17)**; punicalagin **(18)**; ellagic acid lactone **(19)**; 3,3',4'-tri-O-methylellagic acid lactone **(20)**; 3,3',4'-tri-O-methylellagic acid-4-O-ß-D-glucopyranoside **(21)**; 1,4-benzoquinones: 2-methyl-6-prenyl-1,4-benzoquinone **(22a)** and 3-hydroxy-2-methyl-5-(3-methyl-2-butenyl)benzo-1,4-quinone **(22b)**.

3.1.2 Traditional uses of *Gunnera perpensa* L.

Traditionally, *G. perpensa* L. is a well-known and widely used traditional plant, treasured by many traditional health practitioners in South Africa. Being native to South Africa, the plant forms part of many traditional medicines and concoctions used primarily in formulations by many different ethnic groups [2]. In South Africa, the entire plant is utilised in some form to treat a variety of illnesses ranging from mild ailments to severe illnesses. In most cases, the roots and rhizomes are reportedly used in the form of a decoction, tincture or infusion to treat cancer, colds, earache, endometritis, gonorrhoea, heart disease, hypertension, poor appetite, scabies, infertility, UTIs, bladder problems, gastrointestinal parasites and even syphilis [2,10]. Not only is it used in South Africa but also in other regions of Southern Africa, like Lesotho, where hot poultices made from the leaves are used for wounds and boils and even form part of a mixture used for colic in pregnant women, and expulsion of the placenta [11].

Recently, however, aerial parts of the plant are being used by a traditional health practitioner (Freddie J. Isaacs) in regions of South Africa (Uitenhage, Eastern Cape) as a prophylactic and treatment option for SARS-CoV-2 infections (personal communication). Briefly, water/ethanol decoctions are made from the dried aerial parts of the plants and administered orally twice daily. Freddie J Isaacs, the traditional health practitioner, provided this information to the University of Pretoria [12].

Based on this information, it was hypothesised that *G. perpensa* L. possess some antiviral compounds active against SARS-CoV-2.

3.1.3 Ion-mobility coupled mass spectrometry (IM-MS)

Pursuing bioactive secondary metabolites from plants and other organisms often requires complex separatory steps for adequate compound characterisation. Typical natural product characterisation workflows often utilise liquid chromatography-coupled mass spectrometry to gain structural information on the compounds. Due to the variation in sample complexity, the use of standardised methods often results in chromatographic peak overlap leading to a reduction in data quality and hence, a reduction in data accuracy [13].

From an analytical perspective, mass-spectrometry remains a fundamental technique for compound detection and characterisation. Various complementary techniques can be coupled/hyphenated with mass-spectrometry to assist in the separation of complex mixtures prior to MS analysis and hence overcome some of its shortcomings. Inline chromatography-

based separation, like liquid and gas chromatography, remains the most common, although they possess some limitations, especially when dealing with complex samples like crude extracts. The two most common difficulties involve achieving adequate resolution and separation of chemically similar compounds in complex mixtures, often due to low selectivity of the stationary phase to a particular compound. The second is ionisation efficiency and unpredictable in-source fragmentation, often due to Electrospray ionisation's (ESI) susceptibility to matrix effects [14], both crucial for identifying compounds and a significant drawback when building mass-spectral libraries.

In light of these limitations and the latest advances in analytical technology, multiple separatory steps can be coupled to allow for a multi-dimensional separatory approach to increase the separation of compounds prior to mass spectrometric analysis. Ion mobility spectrometry (IMS) is a valuable technique which acts as a form of gas-phase electrophoresis where a buffer gas (He or N_2) and electric field separate ionised compounds based on their inherent physical properties, like charge, shape and size [14]. Although various IMS designs exist, the principle remains the same; larger molecules (with larger cross-sectional areas) collide more frequently with the drift gas and thus have longer drift times. Conversely, molecules with smaller cross-sectional areas collide less frequently with the drift gas and have shorter drift times [15]. Significantly, the molecule's secondary structure, i.e. folding, can also affect its mobility through the buffer gas [16]. Naturally, this makes it appealing in the analysis of lipids, proteins and peptides and, from a small molecule point of view, practically possible to separate anomers and other very similar isomers [17].

Not only does IMS provide an additional dimension of separation, but it can also provide an additional level of confidence by providing details on the molecule's drift time and collisional cross-section area. Data, which is becoming popular as a means to tentatively identify compounds using online IMS databases or collisional cross section (CCS) prediction software, often utilising AI technology and machine learning [18].

Based on the information obtained by IMS and integrability with LC, the technique can be used as a complementary metric to LC-MS analysis and aid in characterising complex samples.

3.2 Materials and Methodology

3.2.1 Reagents and standards

The DCM, MeOH and FA analytical grade (AR) extraction solvents were purchased from Merck, South Africa (Merck, Darmstadt, Germany). The solvents used in the fractionation and HPLC purification, viz., the super purity HPLC grade MeOH and ACN, were purchased from Romil-SpS™, Microsep, South Africa (Waterbeach, Cambridge, UK) and the EtOAc from Sigma-Aldrich (Merck, Darmstadt, Germany). The α/β-punicalagin **(18)** and punicalin **(23)** high-purity reference standards were similarly purchased from Merck, South Africa.

3.2.2 Plant material and processing

Processed *G. perpensa* L. plant material was provided by the traditional knowledge holder (F.J. Isaacs). The plant material was prepared by collecting the aerial parts of the plant from a cultivation site in Uitenhage, Eastern Cape, South Africa. The aerial parts of the plant were air-dried and ground into a powder with the use of a hammer mill. The plant's identity was confirmed, and a voucher specimen was deposited at the H.G.W.J. Schweickerdt Herbarium (University of Pretoria) and was assigned the following voucher specimen number: PRU 128787.

3.2.3 Extraction

Extraction was performed in a batch fashion where 70.5 g of the dried, ground plant material was placed in a 1 L Erlenmeyer flask with 200 mL of DCM:MeOH (1:1) (in a 10:1 ratio of solvent (mL) to plant material (g)) and stirred on a shaker bed overnight. Thereafter, the solution was filtered using a Büchner funnel and Whatman No. 1 filter paper and stored at 4 °C. A subsequent extract cycle was done (on the same plant material) with 200 mL of 100% MeOH overnight, replicating the type of extract made by the ultrasound-assisted micro-extraction used for screening. The solution was similarly filtered and combined with the DCM:MeOH (1:1) extract and concentrated on a rotary evaporator before drying down to completion in an SP Genevac HT6 (Genevac Ltd., Ipswich, UK), yielding a dry crude extract. The dry crude extract's yield was noted before being stored at 4 °C prior to further analysis.

3.2.4 Primary fractionation

Primary fractionation on a small quantity of extract was conducted as described in Chapter 2, Section 2.2.4, a method adapted from Thornburg et al. (2018) [19]. Subsequently, for further chemical analysis and isolation, 4.3 g of extract was fractionated using a C8 SPE cartridge and a Gilson GX-241 ASPEC® liquid handler fitted with a Verity® 4060 pump controlled with TRILUTION® software. In this case, seven different eluent systems were used in series to elute fractions rich in compounds with similar polarity. The eluent systems ranged from highly polar to non-polar in nature, viz.: 95:5 (H_2O:MeOH); 80:20 (H_2O:MeOH); 60:40 (H_2O:MeOH); 40:60 (H_2O:MeOH); 20:80 (H_2O:MeOH); 100% MeOH and 1:1 (ACN:MeOH). Seven fractions were generated, one for each eluent system and collected in separate collection vessels on a volume-based collection method. Due to the variation in eluent systems, the fractions ranged from highly polar (fraction 1) to moderately non-polar (fraction 7). These fractions were dried in individually pre-weighed polytops using a Genevac HT6, their yields recorded, and samples stored at 4 °C until analysis.

3.2.5 Ultra-Performance Liquid Chromatography-Ion Mobility Separation-Quadrupole Time-of-Flight MS (UPLC-IMS-HRMS)

3.2.5.1 Chromatographic conditions

As described in Invernizzi et al. (2022) [12], the crude, primary, tertiary and pure compounds, viz., (Z)-lespedezic acid **(17)**, punicalin **(23)** and α/β-punicalagin **(18)** were analysed concurrently on a Waters Acquity UPLC system (Waters Corp., MA, USA), fitted with a binary solvent delivery system and an auto-sampler. The dried DCM:MeOH *G. perpensa* L. extract and fractions were prepared at 1000 ppm and 500 ppm concentrations, respectively with the pure compounds prepared at a 200 ppm concentration. The samples were prepared by dissolving them in a H_2O:ACN (4:1) solution before filtering through a 0.22 µm syringe filter to ensure no particulate matter was present.

Compound separation and analysis was conducted on an ACQUITY UPLC® HSS T3 (2.1 × 150 mm, 1.8 µm) column (Waters Inc., Milford, MA, USA). A 0.01% ammonium formate buffer was incorporated into the mobile phase to ensure uniform ionisation states of the compounds. Separation was achieved using a linear gradient elution method employing H_2O (0.1% FA, 0.01% ammonium formate) as solvent A and ACN (0.1% FA) as solvent B. The solvent method ran as follows: 97% solvent A held for 0.1 min, a linear increase to 100 % solvent B at 14 min, and a 2 min column wash hold (14-16 min) before returning to starting conditions to equilibrate

the column (16.5-20 min). A constant column temperature of 40 °C was used at a uniform flow rate of 0.4 mL/min with an injection volume of 5 µL.

3.2.5.2 UPLC-IMS-HRMS instrumentation and MS conditions

All UPLC-IMS-HRMS analyses, i.e., separation and detection, were conducted on a Waters® Synap G2 high-definition mass spectrometer (HDMS) (Waters Inc., Milford, MA, USA). The system comprised of a Waters ACQUITY UPLC® coupled to a quadrupole mass filter. The system comprises a Triwave™ ion mobility (IM) cell and a high-resolution time-of-flight (TOF) mass analyser. System operation and data collection were done using MassLynx™ v. 4.1 (Waters Inc., Milford, MA, USA) software. MS calibration was done using the Intellistart software function with sodium formate clusters and calibrated over a mass range of 50-1200 Da. Optimisation of MS source parameters was done for ESI negative mode and conditions set as follows: sampling cone voltage of 25.0 V, cone gas flow of 10 L/h, source temperature of 120 °C, desolvation gas flow of 600.0 L/h, extraction cone voltage set at 4.0 V, desolvation temperature of 350 °C and a capillary voltage of 2.4 kV. To correct for any experimental drift, an internal lock mass standard was used, which consisted of a 2 ng/µL solution of leucine enkephalin (*m/z* 555.2693), infused directly into the source at a rate of 3 µL/min. Infusion of the lock mass standard was done intermittently every 10 s.

3.2.5.3 Ion mobility conditions

The ion mobility spectrometry (IMS) conditions were optimised as follows: a nitrogen gas flow of 90 mL/min with a helium gas flow of 180 mL/min for the helium cell. A 650 m/s IMS wave velocity and a wave height of 40.0 V. A wave velocity ramp of 300 to 600 m/s was used with a transfer wave velocity of 191 m/s with a transfer wave height of 0.1 V. The helium cell DC voltage was optimised at 35.0 V with a trap DC bias of 45.0 V. A mobility separation delay was set at 450 µs. To ensure valid results, IMS calibration was performed with the ‘Waters Major Mix Calibration Sample’ with Driftscope (v. 2.8), prior to sample analysis. From this, the experimental CCS error was determined to be <3.7% (0.66 ± 0.8%).

3.2.5.4 Data acquisition in the UPLC-IMS-HRMS analysis

Data collection was done on a continuous basis, with mass spectral scans collected every 0.3 s with mass-to-charge ratios (*m/z*) of 50 to 1200 Da being recorded. Data collection was done

in a data-independent acquisition (DIA) fashion. Two energy functions were used, viz., a low and a high collision energy (MS^E). Collision energies were set at 10 V and 30 V for the low and high MS transfer collision energies respectively.

3.2.5.5 Processing of the UPLC-IMS-HRMS data

UNIFI® Scientific Information System (Waters Inc., Milford, MA, USA) was used for all data processing. UNIFI® processing settings were optimised as follows: chromatographic peak width settings and intensity threshold set to 'automatic'. To avoid the presence of false positives, the high and low energy function's intensity thresholds were set to 5.0 and 5.0 detector counts, respectively. The retention time's tolerance window was optimised to ±0.1 min to prevented the selection of artefact peaks. MS processing settings were optimised as follows: a 15.0 ppm target mass tolerance and a ±10.0 mDa for the fragmentation match tolerance. The maximum relative intensity threshold was set at 0.01 for mass targets with the same *m/z* ratio. The IMS processing settings were set to a 5.0% CCS tolerance. All MS data were lock mass corrected by UNIFI® software automatically prior to data processing. Tentative compound identification was made using the Waters Chinese Traditional Medicine Library integrated into UNIFI and 'The Dictionary of Natural Products' (DNP). For compound confirmation, the monoisotopic mass, molecular formula, MS/MS fragmentation pattern, retention time, CCS data and drift time were used to conclusively confirm the presence of the compounds in all active fractions. To remain unbiased, a threshold was set in which the compounds were only reported as "found", if the mass spectral peaks corresponded closely to those of the standards. More specifically, the compounds were only reported as "found", if the retention time (RT) between samples (with reference to the standards) was observed within 0.1 min and the observed CCS values were observed to be within 5% of the purchased standards.

3.2.5.6 UPLC-IMS-HRMS method validation

To ensure that the UPLC-IMS-HRMS method used in the study was valid, the method was partially validated in accordance with International Conference on Harmonization (ICH) guidelines [20]. The method was validated for specificity, linearity, precision and quantification parameters, viz., limit of detection (LOD) and limit of quantification (LOQ).

3.2.5.7 Method specificity

Method specificity was evaluated by analysing the punicalin **(23)**, α/β-punicalagin **(18)**, blank, and DCM:MeOH extract on the same UPLC instrument, using the same injection volumes, MS and chromatographic conditions on the same day. Evaluation and comparison of component (peak) retention times and mass spectral peaks were used to determine the selectivity of the analytical method used. The mass spectra of each respective peak were extracted and compared with the relevant spectra at peak start, apex and peak end to assess peak purity.

3.2.5.8 Method linearity

Method linearity validation was carried out by preparing standard solutions of the punicalin **(23)** and α/β-punicalagin **(18)** standards in a 1-50 µg/mL and 5-80 µg/mL concentration range, respectively. A 5-point calibration curve was constructed for each compound, and each individual sample was analysed in triplicate. A standard curve was constructed by plotting the mass spectral mean peak areas versus the respective analyte concentration employing linear regression analysis.

3.2.5.9 Method precision

Intra-day variations (repeatability) were used to evaluate the method precision, i.e. precision under the same conditions in a short space of time. This was done by analysing the independently prepared samples on the same day. Method repeatability was examined by preparing three different working solutions of the *G. perpensa* DCM:MeOH extract. Repeatability and precision data were expressed as percentage relative standard deviation (%RSD). A 5% RSD cut-off was set with values found to be with ±5% RSD deemed acceptable. Intra-day precision, i.e., %RSD were determined by measurement of peak area of the reference standard.

3.2.5.10 Limit of detection (LOD) and limit of quantification (LOQ)

The LOD and LOQ were determined with the use of the following equations **(i)** and **(ii)**:

$$\text{LOD} = \frac{3.3\sigma}{S} \qquad \textbf{(i)}$$

and

$$LOQ = \frac{10\sigma}{S} \quad \textbf{(ii)}$$

with S denoting the gradient of the calibration curve and σ the standard deviation of the calibration curve.

3.2.5.11 Quantification of punicalin (23) and α/β-punicalagin (18)

The quantity of the active constituents in the DCM:MeOH extract was evaluated by preparing a 5-point calibration curve of each compound, set up by performing a serial dilution of the 2 working ellagitannin solutions. The quantity of the two compounds was reported based on a DCM:MeOH extract and based on a dry weight basis of the DCM:MeOH extract, reported as (%w/w). Since the ellagitannins exist as reversible anomers [21], the total sum of each compound was reported as the total punicalin **(23)** and α/β-punicalagin **(18)**, respectively.

3.2.6 Secondary fractionation using flash chromatography

A secondary fractionation step was conducted on a Buchi Pure C-815 Flash system (Buchi, Flawil, Switzerland) fitted with a UV detector and an evaporative light scattering detector (ELSD). Primary fraction 3 (labelled as LI-1-54D) from the SPE (520 mg) was dissolved in 1.5 mL of a 3:2 (H_2O:MeOH) solution and filtered using a 0.22 µm syringe filter. Separation was done using a gradient method employing a Buchi EcoFlex C18 (50 µm, 20 g) cartridge. The solvent system consisted of H_2O (0.1% FA) as solvent A and MeOH (0.1 % FA) as solvent B and ran at a flow rate of 40 mL/min. The elution method ran as follows: 95% solvent A, held for 6 min, a linear gradient change to 92% solvent A over 1.3 min, a second linear change to 79% solvent A over 8.2 min before a final linear gradient change to 0% solvent A over 4.4 min. A column wash at 100% solvent B followed for 25 min. The UV detector was set to monitor the following wavelengths (λ): 254 nm, 265 nm, 230 nm and 320 nm and collection was set to trigger automatically should an absorbance signal of more than 0.05 AU be detected. From this, 3 secondary fractions (labelled as LI-1-61A to LI-1-61C) were collected, dried and stored at 4 °C.

3.2.7 Tertiary fractionation

The 3 secondary fractions (labelled as LI-1-61A to LI-1-61C) produced from the flash chromatography system were further analysed on a Waters chromatographic system,

equipped with a Waters photodiode array (PDA) detector (Model 2998) and ACQUITY QDa detector (Waters, Milford, MA, USA). The samples were prepared at a 1000 ppm concentration in a H_2O:MeOH (9:1) solution. Initial analysis and method development was conducted on an analytical column (Xbridge® BEH analytical C18 OBD™ (4.6 x 150 mm, 5 µm)) before upscaling to preparative scale. A satisfactory chromatographic method was developed, which consisted of H_2O (0.1% FA) and MeOH (0.1% FA) used as solvent A and solvent B, respectively. The chromatographic method ran as follows: an initial isocratic solvent hold at 95% solvent A (0-1 min) before an exponential change (gradient 8) to 0% solvent A (1-18 min) followed by a subsequent column washing (18-21 min) before returning to the initial starting conditions to re-equilibrate the column (21.5-25.5 min). A 1.1 mL/min flow rate and an injection volume of 5 µL were used.

The secondary fractions 1 and 2 (labelled as LI-1-61A and LI-1-61B) were combined (380 mg) and fractionated using a preparative HPLC-PDA-MS. The combined fractions were dissolved in 1.0 mL H_2O:MeOH (9:1) before filtering using a 0.22 µm nylon filter. Fractionation was done by means of a single injection (1.0 mL), on an Xbridge® Prep C18 OBD™ (19 × 250 mm, 5 µm) column. A modified gradient method was used and developed based on the analytical work conducted. The solvent system consisted of H_2O (0.1% FA) and MeOH (0.1% FA) as solvents A and B, respectively. The chromatographic method was optimised with a flow rate of 19.0 mL/min and ran as follows: 5% solvent B for 5 min, an exponential change (gradient 8) to 100% solvent B over 25 min (5-30 min), a 4 min column wash (30-34 min) followed by a linear return to starting conditions and an 8 min equilibration stage (34.5-43 min).

For both analytical and preparatory work, the QDa (MS) was set to acquire in ESI negative mode, with data collection set at a range from 150 Da to 1100 Da. The source temperature was kept at 120 °C, with a probe temperature of 500 °C. The capillary voltage was set to 0.80 kV, and the cone voltage to 13.75 V. The PDA detector settings were optimised as follows: a sampling rate of 10 points/sec, a UV scan range of 210-400 nm and a resolution of 2.4 nm.

A time-based collection was used in which collection was done on an ongoing basis with fractions collected at 1.5 min intervals. Where peaks overlapped between collected fractions (based on the observed MS and UV spectra), the fractions were combined, these being fractions 4-6 (labelled as LI-1-62D to LI-1-62F), 9-10 (labelled as LI-1-62I to LI-1-62J), 12-13 (labelled as LI-1-62L to LI-1-62M) and 17-22 (labelled as LI-1-62Q to LI-1-62V). The resulting 13 fractions were dried using an SP Genevac HT6 before noting yields and storing at 4 °C prior to further analysis.

3.2.8 Mass-directed HPLC isolation of α/β-punicalagin (18)

Mass-directed HPLC isolation of α/β-punicalagin **(18)** from the tertiary fraction 8 (labelled as LI-1-62H) was accomplished using an Agilent 1260 Infinity Series PLC (Agilent Technologies, Santa Clara, CA, USA). The system was equipped with an online SPE solution and fitted with a Bruker amazon SL IonTrap mass spectrometer (Bruker Daltonics, Bremen, Germany). The fraction (labelled as LI-1-62H) (13 mg) was dissolved in a 4:2 (H_2O:MeOH) solution and prepared at a 13 000 ppm concentration. Compound separation was accomplished using Luna® C18(2) (250 × 4.6 mm, 5 µm) column, with Oasis® online SPE trapping cartridges used for collection. A gradient method was employed for the separation and collection. The solvents consisted of H_2O (0.1% FA) and MeOH (0.1% FA) as solvents A and B, respectively. The gradient method was optimised by using a flow rate of 0.5 mL/min: 80% solvent A for 15 min, a linear decrease to 0% solvent A at 15.5 min, and an isocratic column hold at 0% solvent A until 20 min before returning to starting conditions at 23 min. Prior to the subsequent injection, a 5 min column equilibration step was used.

Mass-directed collection (trapping) was used with the MS set to ESI negative mode. Peaks corresponding to *m/z* 541 and a λ_{max} = 217 nm, 258 nm, and 378 nm were trapped. The resulting compound was dried using an SP Genevac HT6 before recording its yield and stored at 4 °C prior to further analysis (Figure 3.3).

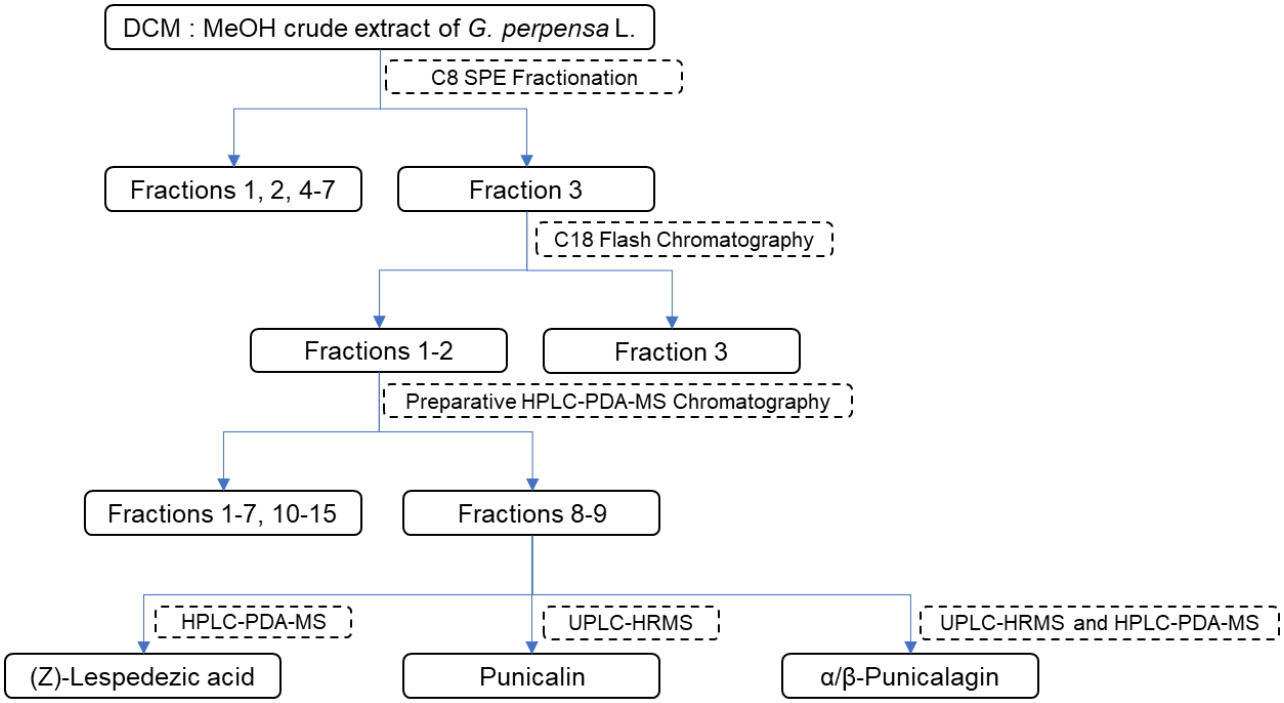

Figure 3.3: Graphical representation of the bioassay-guided fractionation which led to the eventual identification of punicalin **(23)**, α/β-punicalagin **(18)** and (Z)-lespedezic acid **(17)** from the *G. perpensa* L. DCM:MeOH crude extract.

3.2.9 Isolation of (Z)-lespedezic acid (17)

The isolation of (Z)-lespedezic acid **(17)** was carried out using the same Waters HPLC-PDA-MS system described in Section 3.2.7 Tertiary fractionation. The elution method was however modified to allow for base-peak resolution of the (Z)-lespedezic acid **(17)** peak. The tertiary fraction 9 (labelled as LI-1-62I) (25.69 mg) was dissolved in MeOH:H_2O (2:8) and initially analysed on an analytical column (Xbridge® BEH analytical C18 OBD™ (4.6 x 150 mm, 5 µm)) before upscaling to semi-preparative scale.

After satisfactory method development and compound separation, the method was upscaled for separation on an Xbridge® Prep C18 OBD™ (10 × 250 mm, 5 µm) column with H_2O (0.1% FA) and MeOH (0.1% FA) used as solvent A and solvent B, respectively. The elution method utilised a 5 mL/min flowrate and ran as follows: an initial hold at 95% solvent A for 0.1 min before an exponential change (gradient 8) to 0% solvent A over 17 min before an isocratic column wash with 100% solvent B for 3 min before a return to starting conditions at 20.50 min and a 3.5 min re-equilibration step (20.4-24 min) prior to the next injection.

A time-based collection method was utilised where (Z)-lespedezic acid **(17)** was targeted based on its mass and UV absorbance. These being *m/z* 365 $[M+Na]^+$ and λ_{max} = 302 nm.

The collected compound was transferred into a pre-weighed polytop, and dried down using an SP Genevac HT6 before recording its yield and storing at 4 °C before NMR analysis (Figure 3.3).

3.2.10 NMR Analysis

The identity of the collected compounds viz. α/β-punicalagin **(18)** and (Z)-lespedezic acid **(17)** was confirmed using NMR spectroscopy. α/β-Punicalagin **(18)** was dissolved in 500 µL acetone-d6 (Sigma-Aldrich, Milwaukee, WI, USA), and analysed on a 400 MHz Bruker Advance III NMR spectrometer fitted with a Prodigy BBI probe, at 25 °C. The operating frequency for the ^1H was set at 400.21 MHz.

(Z)-Lespedezic acid **(17)** was dissolved in 500 µL D_2O and analysed in a 5 mm NMR tube. Subsequent NMR analysis was conducted at 25 °C on a Bruker 500 MHz NMR, fitted with a BBO 500 S1 prodigy probe (cryoprobe). The operating frequency for the ^1H and ^{13}C was 500.0031 MHz and 125.738 MHz, respectively.

Data processing was done using ACDLabs Spectrus Processor v 2021.1.1. All chemical shifts are reported in ppm (δ-scale), with coupling constants "*J* ", reported in Hertz (Hz). Trace protons from the deuterated solvent were used to calibrate the resulting spectra i.e., 2.05 ppm for acetone-d6 and 4.79 ppm for D_2O.

3.2.11 Plaque-based SARS-CoV-2 bioassays

Gunnera perpensa L. extract, fractions and pure compounds were tested in viral plaque-based bioassays conducted personally, at the University of Basel, Department of biomedicine, under the supervision of Professor Thomas Klimkait. The bioassays were carried out as described in Chapter 2, Section 2.3.2. The initial samples, viz., the extract and primary fractions, were tested against the Wuhan strain of the SARS-CoV-2 virus (the only variant available at the time) at 25 µg/mL. The bioassays of the pure compounds, viz., (Z)-lespedezic acid **(17)** (isolated from *G. perpensa*), α/β-punicalagin **(18)** (purchased reference standard) and punicalin **(23)** (purchased reference standard) were performed in a dose-dependent manner and tested against clinical isolates of the Wuhan, Beta and Delta variants of the SARS-CoV-

2 virus. Supplementary bioassays were performed on the ellagitannins, where bioactivity was assessed against the Omicron variant of the SARS-CoV-2 virus. Additionally, cytotoxicity testing was conducted on the pure compounds using healthy Vero E6 cell lines to estimate the cytotoxic concentration (CC_{50}) and calculate the selectivity index (CC_{50}/IC_{50}) of the compounds. The compounds were evaluated for response in a dose-dependent manner which ranged from 46.10-0.02 µM for α/β-punicalagin **(18)**, 63.90-0.03 µM for punicalin **(23)** and 265.59-1.46 µM for (Z)-lespedezic acid **(17)**. To ensure valid results, remdesivir was used as a positive control, being widely reported as an antiviral against SARS-CoV-2 *in vitro* [22–24], similarly being an FDA-approved drug for use in severe SARS-CoV-2 cases [25].

3.2.12 AlphaScreen binding assays and M^{pro} inhibition assay

The *G. perpensa* L. derived samples, which included the extract, fractions and pure compounds, viz., (Z)-lespedezic acid **(17)**, punicalin **(23)** and α/β-punicalagin **(18)**, were tested for any antiviral activity against SARS-CoV-2 enzymes. The analyses were conducted by collaborators at the Wistar institute (USA) under the supervision of Professor Ian Tietjen where the samples were screened in AlphaScreen spike RBD/ACE2 inhibition assays and M^{pro} inhibition assays with methodology previously described in Tietjen et al. (2021) and Invernizzi et al. (2022) [12,23] and similarly described in Chapter 2, Section 2.3.1**.** To ensure valid results, the extract and fractions were screened in triplicate in a dose-dependent manner. The control-neutralising antibodies REGN10987 (imdevimab) and REGN10933 were used as positive controls and for comparison purposes.

3.2.13 Viral CPE quantitative assay

Compound synergism/additive effects were assessed using viral CPE quantitative assay, i.e., cell viability restoration assays by collaborators at the Wistar Institute (USA) with the methodology previously described in Chapter 2, Section 2.3.1 and Tietjen et al. (2021) [23]. Briefly, 5 combinations of the ellagitannins were prepared and tested in viral CPE quantitative assays against the wild-type (WT) strain of the SARS-CoV-2 virus to test for potential synergistic or additive effects. These combinations being: 10:1 punicalin:α/β-punicalagin; 3:1 punicalin:α/β-punicalagin; 1:1 punicalin:α/β-punicalagin; 1:3 punicalin:α/β-punicalagin; 1:10 punicalin:α/β-punicalagin together with punicalin **(23)** and α/β-punicalagin **(18)** tested

separately. To ensure valid results, the samples were screened in triplicate in a dose-dependent manner.

3.2.14 Molecular docking

To better understand the mechanism of action (MOA) of the compounds, molecular docking was performed using the Schrödinger software suite, release 2022-1, with the OPLS4 force field. The ligand structures, viz., punicalin **(23)**, α/β-punicalagin **(18)** and (Z)-lespedezic acid **(17)**, were downloaded from the PubChem database and prepared (minimised) using *ligprep*. Protonation states were predicted using Epik and predicted based on a pH of 7.0 ± 2.0 [26,27]. The protein structure 6LZG was obtained from the Protein Data Bank (PDB) and prepared using the *protein preparation wizard* [28], with missing side chains and loops filled with PRIME [29,30]. Protonation states were assigned by the software, and energy minimisation was performed to ensure favourable constraints of the protein. Receptor grids were generated using the software's *receptor grid generation* feature with default settings. The grids were centred at interacting residues *viz.* Q493, Q498, N501, F486, K417, and F456 [31]. Subsequent molecular docking was performed using *Glide* extra precision (XP) [32]. Default settings were used where all ligand structures were treated as 'flexible' with a minimum of 5 poses generated for each ligand. Docking poses were minimised with strain correction terms applied post-docking.

3.3 Results and discussion

3.3.1 Extraction, fractionation, bioassays and UPLC-IMS-HRMS analysis

A sequential ultrasonicator-mediated extraction method was used to produce a small quantity of extract for the initial antiviral screening. Based on the good bioactivity and high yield obtained from the DCM:MeOH extraction method, in comparison to the ethanol-based extracts (cf. Table 2.2 and Table 2.3), the DCM:MeOH extraction method was used for subsequent analyses. The DCM:MeOH extraction of 12 g of plant material yielded 960 mg (8% yield) of extract. Subsequent SPE fractionation of a 250 mg portion of the dried extract yielded 7 semi-pure fractions with the percentage yield (% w/w) ranging from 4.2% to 12.12% (Table 3.1).

The generic DCM:MeOH extraction was performed to ensure the extraction of both polar and non-polar compounds, this was done to avoid a skewed and biased analysis approach. In order to speed up the process of identifying the bioactive compound/s and to remove nuisance

compounds which could interfere with bioassay data (either by producing a false positive or false negative) [30]. The spread of the percentage yields observed confirms the successful broad-spectrum extraction.

Table 3.1: Mass and yield (w/w%) of the extract and primary fractions produced from the fractionation of the *G. perpensa* DCM:MeOH extract.

Sample	Mass (mg)	Yield* (%w/w)
Dry plant material	12 000	N/A
Extract	960	8.0
Fraction 1	10.5	4.2
Fraction 2	30.3	12.1
Fraction 3	22.7	9.1
Fraction 4	20.7	8.3
Fraction 5	13.5	5.4
Fraction 6	15.2	6.1
Fraction 7	24.0	9.6

*Based on 250 mg of extract used

The extract and fractions were screened in the spike RBD/ACE2 bioassays and M^{pro} inhibition bioassays (described in Chapter 2, section 2.3.1) and in SARS-CoV-2 plaque-based bioassays (described in Chapter 2, section 2.3.2) at 25 µg/mL.

In the AlphaScreen bioassays, the *G. perpensa* L. extract and fractions (2-7) showed potent activity (not observed in the method blank), with their IC_{50} values found to be in the low ng/mL range (Figure 3.4; Table 3.2). Most fractions presented with a low IC_{50} value, with the activity of Fraction 3 observed to be IC_{50} < 0.001 µg/mL. The positive control, REGN10987, was similarly found to disrupt the spike RBD/ACE2 interaction with an IC_{50} value of 0.025 µg/mL (Figure 3.4; Table 3.2).

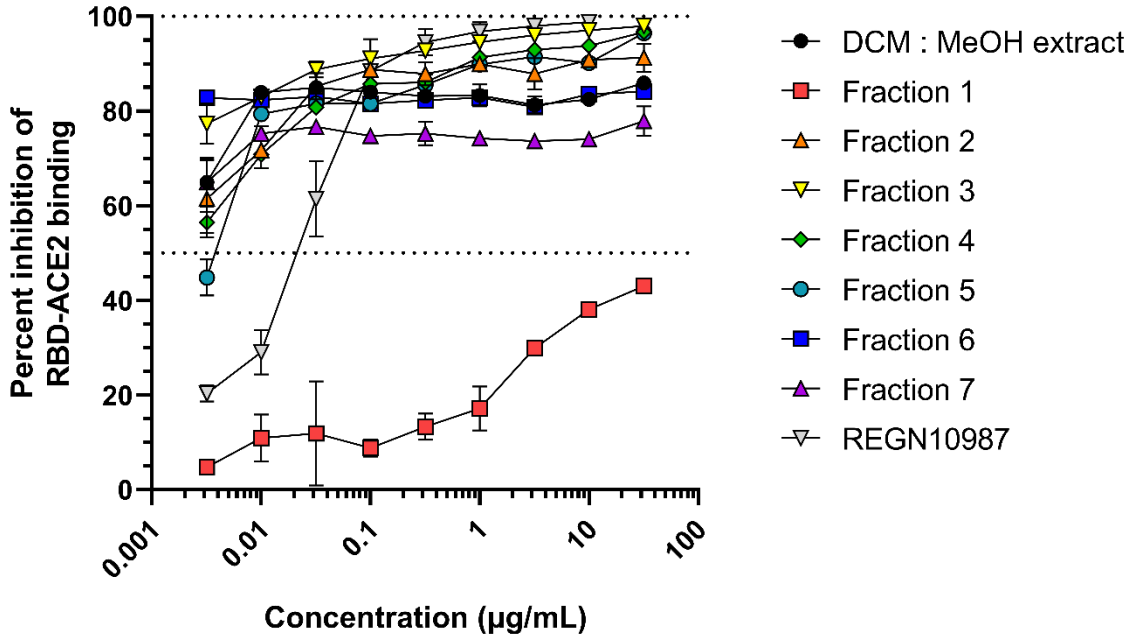

Figure 3.4: Dose-response curved of the *G. perpensa* extract, primary fractions and the control antibody (REGN10987) to inhibit spike RBD/ACE2 interaction by disrupting luminescence in AlphaScreen bioassays against the WT (USA-WA1/2020).

Table 3.2: Summary of IC_{50} values for the extract and primary fractions in the spike RBD/ACE2 AlphaScreen-based bioassay against the WT (USA-WA1/2020).

Sample	IC_{50} (µg/mL)
DCM:MeOH extract (*G. perpensa*)	<0.001
Fraction 1	>32
Fraction 2	0.0021
Fraction 3	<0.001
Fraction 4	<0.001
Fraction 5	0.0034
Fraction 6	<0.001
Fraction 7	<0.001

In contrast to the AlphaScreen bioassays, the extract and fractions showed poor M^{pro} inhibition, with their IC_{50} values found to range between 56.27 µg/mL and >100 µg/mL (n=1) with no significant activity observed for any of the samples (Figure 3.5; Table 3.3).

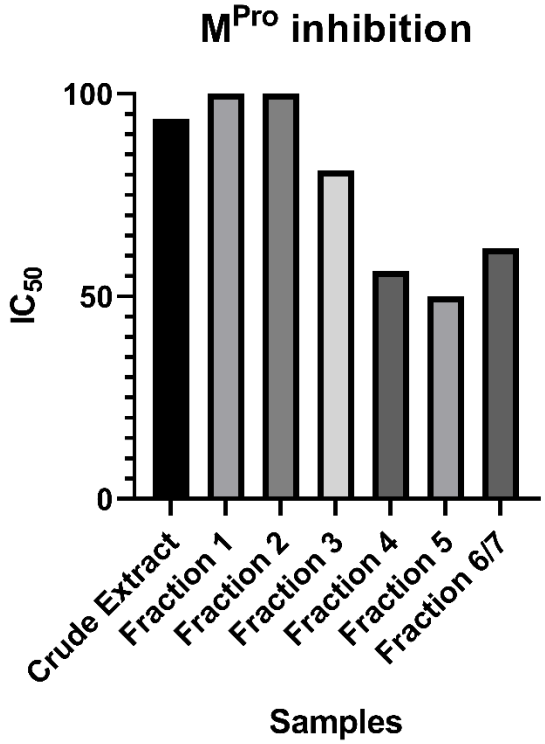

Figure 3.5: M^{pro} inhibition data (IC_{50}) of the *G. perpensa* extract and primary fractions.

Table 3.3: M^{pro} inhibition data (IC_{50}) of the *G. perpensa* extract and primary fractions.

Sample	IC_{50} (µg/mL)
Extract	93.81
Fraction 1	>100
Fraction 2	>100
Fraction 3	81.05
Fraction 4	56.28
Fraction 5	49.97
Fraction 6	61.99
Fraction 7	93.81

In the single-point whole-cell antiviral SARS-Cov-2 bioassay Fraction 3 and Fractions 6/7 were the only fractions which showed any whole-cell antiviral activity in the plaque-based bioassays with Fraction 3 presenting approximately 25% inhibition of the viral cytopathic effect on the virus (Figure 3.6).

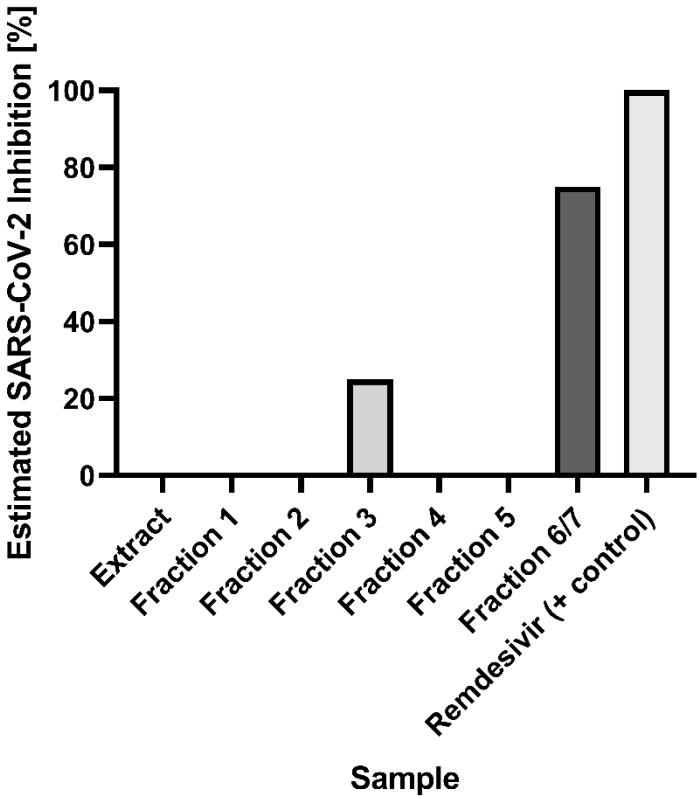

Figure 3.6: Single-point bioassay results of the *G. perpensa* extract, primary fractions and the positive control (remdesivir) to inhibit plaque formation in plaque-based bioassays against the SARS-CoV-2 Wuhan strain at 25 µg/mL.

With COVID-19 being a relatively new virus, only a few antiviral bioassays were available at the time of research. Amongst the available bioassays, the viral spike RBD and viral M^{pro} inhibition bioassays remain widespread due to them being favourable targets for pharmaceuticals [33]. Subsequent evaluation of the extract and fractions for antiviral activity against SARS-CoV-2, showed the samples to have high selectivity towards inhibiting the RBD/ACE2 interaction against the WT(USA-WA1/2020). Although both Fraction 3 and Fraction 6/7 showed activity in the plaque-based bioassays (Figure 3.6), Fraction 3 was particularly interesting because its antiviral activity correlated with its antiviral activity observed in the enzyme-based bioassays (Figure 3.5).

UPLC-IMS-HRMS analysis of the DCM:MeOH extract showed the presence of a broad range of compounds, ranging from highly polar to highly non-polar (Figure 3.7). A comparison of the extract and the bioactive primary Fraction 3 showed similarities in a few of the more polar intense peaks (Figure 3.7). Comparison of their respective accurate mass, molecular formulae and mass fragmentation patterns with that found in the Dictionary of Natural Products lead to the tentative identification of punicalin **(23)**, α/β-punicalagin **(18)** and (Z)-lespedezic acid **(17)** (Figure 3.8).

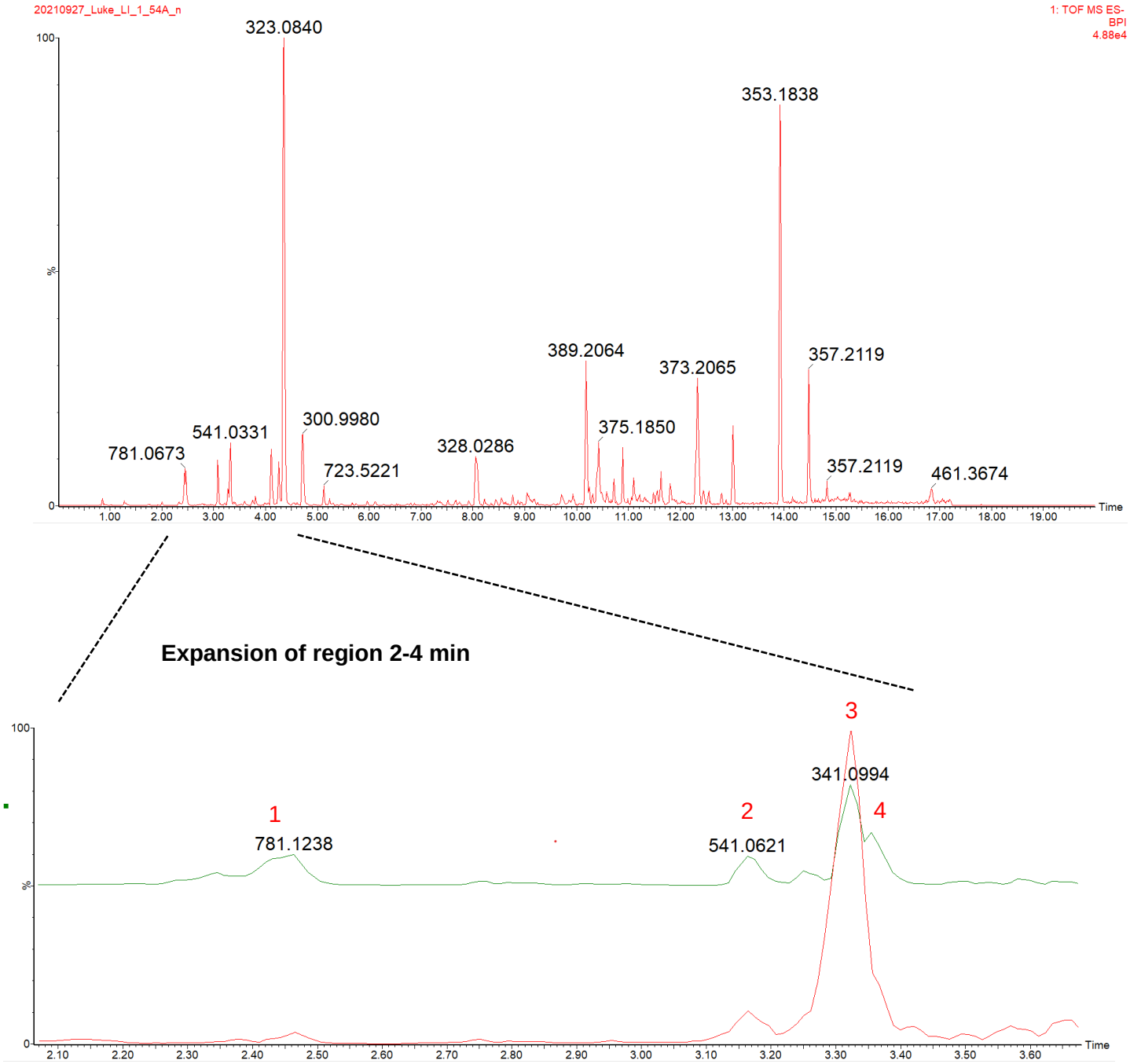

Figure 3.7: UPLC-IMS-HRMS BPI chromatogram of the crude extract (top) and an overlay with the bioactive primary Fraction 3 (bottom) analysed in ESI negative mode. Expansion of the 2-4 min region highlights compounds common to both samples and hypothesised to be the bioactive compounds, highlighted as peaks 1-4. The compounds punicalin **(23)** (peak 1), (RT: 2.45 min); α/β-punicalagin **(18)** (peak 2/4) (RT: 3.20; 3.50 min) and (Z)-lespedezic acid **(17)** (peak 3) (RT: 3.43 min) are highlighted.

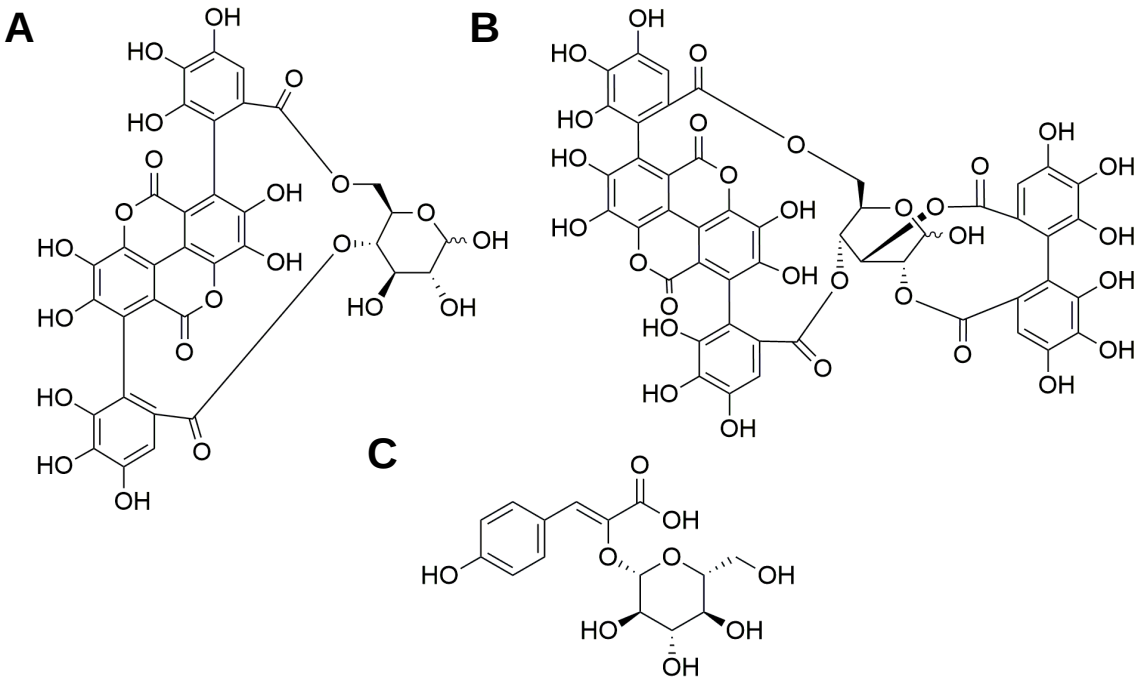

Figure 3.8: Molecular structures of the compounds tentatively identified in the bioactive primary fraction. (**A**) Ellagitannins punicalin **(23)** (**B**) α/β-punicalagin **(18)** and (**C**) (Z)-lespedezic acid **(17)**.

More specifically, punicalin **(23)** was observed at *m/z* 781.0560 $[M-H]^-$ (RT: 2.45 min) where the peak was found to have a monoisotopic mass of 782.0633 Da with an accompanying mass error of 3.0 mDa, and a molecular formula of $C_{34}H_{22}O_{22}$ (calculated 782.0603 Da). The compound was found to have an observed drift time of 3.79 ms and a CCS of 250.32 $Å^2$. The MS^E fragmentation pattern showed the presence of 3 intense peaks, *viz.*, *m/z* 781 being the quasi-molecular ion $[M-H]^-$, *m/z* 601 and *m/z* 301 being the formation of gallagic acid and ellagic acid (Figure 3.9). These peaks, including *m/z* 721, are in agreement with previously reported results (Table 3.4) [34,35].

The α/β-punicalagin **(18)** peaks were observed at *m/z* 541.0234 $[M-2H]^{2-}$ (RT: 3.20 min) and *m/z* 541.0251 $[M-2H]^{2-}$ (RT: 3.50 min) where the peaks were found to have a monoisotopic mass of 1084.0673 Da (mass error -4.8 mDa) and 1084.0665 (mass error -2.8 mDa), respectively. The peaks had a molecular formula of $C_{48}H_{28}O_{30}$ (calculated 1084.0665 Da). The anomeric peaks were found to have an observed drift time of 1.91 and 1.87 ms and a CCS of 345.60 and 341.33 $Å^2$, respectively for the peaks at RT 3.20 min and RT 3.50 min. Further

analysis of the high energy MS fragmentation pattern for α/β-punicalagin **(18)** showed the presence of 5 intense peaks (Supplementary Data, Figure S3.2), these being the *m/z* 1083 belonging to the $[M-H]^-$ quasi-molecular ion, *m/z* 541 belonging to the doubly charged quasi-molecular ion $[M-2H]^{2-}$, *m/z* 781 originating from the loss of gallagic acid from α/β-punicalagin **(18)** and the formation of punicalin **(23)** (Figure 3.9). Interestingly, gallagic acid is widely reported as displaying an *m/z* 601, despite its molecular weight being 638 g/mol [36–38]. The only explanation is that the compound undergoes a double internal esterification forming a stable intermediate within the MS as displayed in Figure 3.9. Further to this, the presence of *m/z* 301 indicated the formation of ellagic acid from the fragmentation of α/β-punicalagin **(18)** and gallagic acid [36]. These 5 intense peaks are widely reported in the literature as key fragments formed from α/β-punicalagin **(18)** (Table 3.4) [36,39].

(Z)-Lespedezic acid **(17)** was observed at *m/z* 341.0848 (RT: 3.43 min), where the peaks were found to have a monoisotopic mass of 342.0926 Da with an accompanying mass error of 2.5 mDa, and a molecular formula of $C_{15}H_{18}O_9$ (calculated 342.0951 Da). To date, no MS^E fragmentation pattern for (Z)-lespedezic acid **(17)** has been reported in the literature. The proposed fragmentation pattern explains the presence of the 2 intense MS peaks observed, viz., *m/z* 179 and *m/z* 135 (Supplementary Data, Figure S3.3); these represent the formation of 4-hydroxyphenylpyruvic acid due to the loss of the β-D-glucose sugar moiety before the subsequent loss of the carboxylic acid group (Figure 3.10).

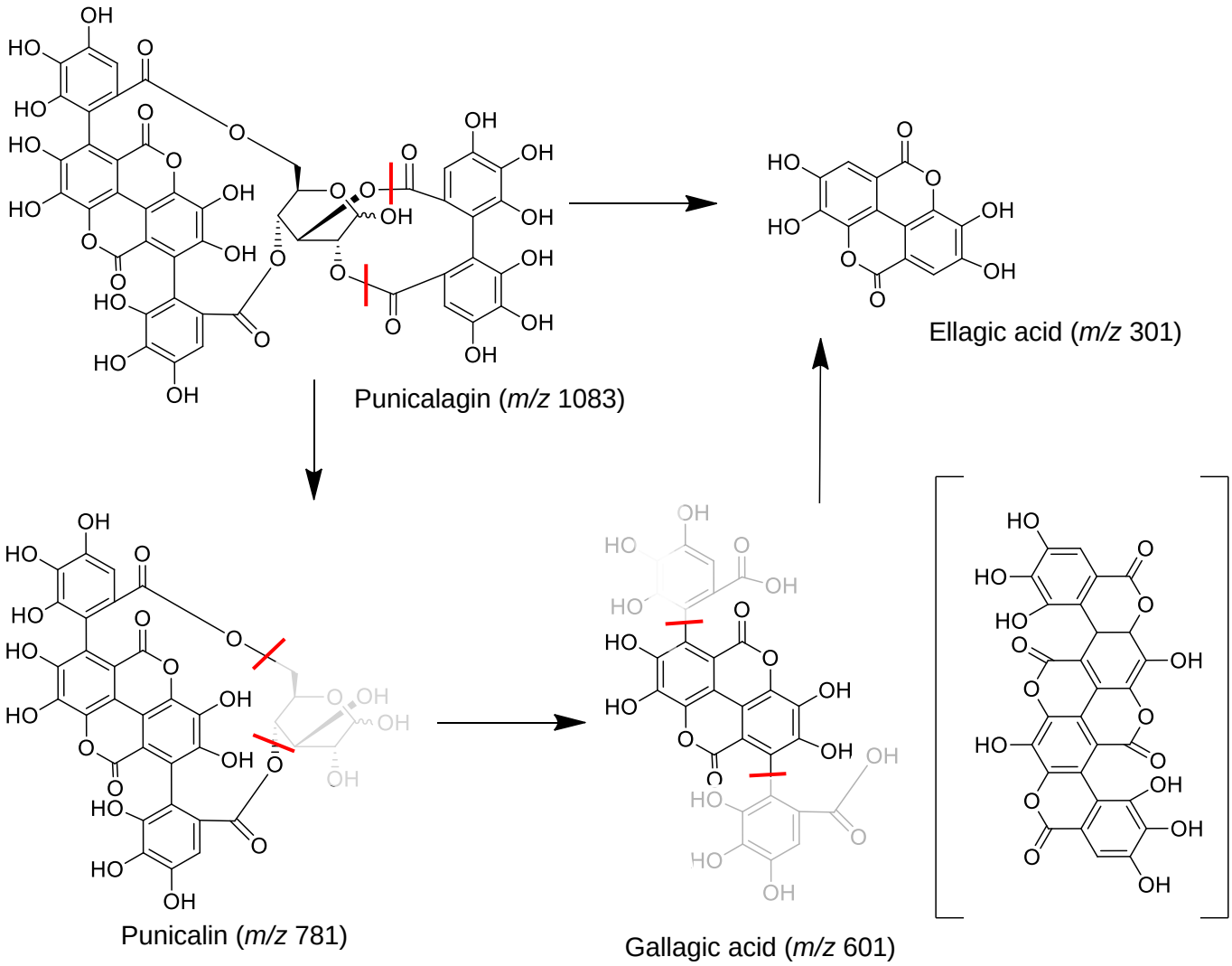

Figure 3.9: Representative fragmentation pathway of α/β-punicalagin **(18)** and punicalin **(23)**, and its proposed fragmentation in ESI negative mode, adapted from Mininel et al. (2014) [36]. The proposed stable ester of gallic acid, fromed by double internal esterification, is also shown (*m/z* 601).

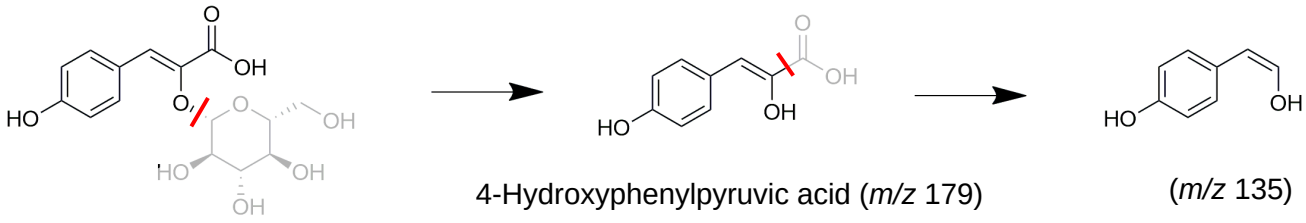

(Z)-Lespedezic acid (*m/z* 341)

Figure 3.10: Representative fragmentation pathway of (Z)-lespedezic acid **(17)**, and its proposed method of fragmentation in ESI negative mode.

Table 3.4: UPLC-IMS-HRMS data of the key compounds of interest, viz., punicalin **(23)**, α/β-punicalagin **(18)** and (Z)-lespedezic acid **(17)**.

Compound	Observed *m/z*[a] (Da)(Mass error (mDa))	Observed quasi-molecular ion	Molecular formula	Calculated monoisotopic mass (Da)[b]	RT[c] (min)	Observed drift (ms)	Observed CCS[d] (Å^2)	Observed fragment (*m/z*)(mass error (mDa))	Literature (MS Fragments)
Punicalin (23)	781.0560 (3.0)	$[M-H]^-$	$C_{34}H_{22}O_{22}$	782.0603	2.45	3.79	250.32	721.0336 (1.7) 600.9910 (1.4) 448.9786 (-0.1)	[34,35]
α/β-Punicalagin (18)	541.0234 (-4.8)	$[M-2H]^{2-}$	$C_{48}H_{28}O_{30}$	1084.0665	3.20	1.91	345.60	600.9900 (0.4) 541.0256 (−0.4) 300.9963 (−2.7) 275.0171 (−2.7)	[36,39]
α/β-Punicalagin (18)	541.0251 (-2.8)	$[M-2H]^{2-}$	$C_{48}H_{28}O_{30}$	1084.0665	3.50	1.87	341.33	600.9895 (−0.2) 541.0239 (−2.1) 300.9969 (−2.0) 275.0180 (−1.7)	[36,39]
(Z)-Lespedezic acid (17)	341.0848 (2.5)	$[M-H]^-$	$C_{15}H_{18}O_9$	342.0951	3.43	2.02	182.96	135.0420 (-3.2) 179.0344 (0.0)	N/A

[a]*m/z*, mass to charge ratio; [b]determined directly from molecular formula; [c]*RT,* retention time; [d]*CCS*, collisional cross section

Overall, the observed MS spectra, MS fragmentation pattern and accurate mass align well with that reported for the punicalin **(23)** and (Z)-lespedezic acid **(17)** and are similarly reported to occur within the plant [1,5]. Likewise, the 2 chromatographic peaks for α/β-punicalagin **(18)** align well with that reported in literature where α/β-punicalagin **(18)** exists as a reversible mixture of α/β anomers, giving rise to 2 peaks with different retention times [21].

Interestingly, punicalin **(23)** and α/β-punicalagin **(18)** are the only compounds with published biological activity against microorganisms. Punicalin **(23)** is reported to possess antiviral activity and was found to inhibit HIV-1 reverse transcriptase with an IC_{50} of 0.11 µg/mL, the hepatitis B virus covalently closed circular DNA and also reported to inhibit the hepatitis C virus (HCV) NS3/4A protease with an IC_{50} of <0.1 µM [40–42]. In addition to the antiviral activity, punicalin **(23)** is also reported to have antihepatotoxic, antibacterial and anticancer activity [43].

α/β-Punicalagin **(18)** is reported to possess antiviral activity and was found to inhibit the herpes simplex type 1 (HSV-1) *in vitro* in plaque assays with an EC_{50} value of 21.69 µg/mL [44]. The

compound is also reported to possess antiviral activity against HSV-2, HIV and Influenza virus [45–47]. In addition, the compound is also reported to have strong antibacterial, antioxidant, antiproliferative, antigenic and hepatoprotective activity [48].

Based on previous literature reporting the antiviral activity of α/β-punicalagin **(18)** against SARS-CoV-2 [49], it was hypothesised to be the bioactive compound.

3.3.2 Secondary/tertiary fractionation, antiviral bioassays and UPLC-IMS-HRMS analysis

Additional quantities of the bioactive primary fractions were obtained by performing a batch extraction on 70.5 g of plant material, followed by the SPE method. An extraction yield of 11.0% was obtained for the batch extraction process, with the subsequent yields of the primary fractions comparing well with those reported initially in Table 3.1.

Due to the complexity of the primary fractions, secondary fractionation was performed on primary fraction 3 (labelled as LI-1-54D) (520 mg) using flash chromatography on a Buchi Pure C-815 Flash system employing a reverse phase cartridge. The fractionation gave rise to 3 secondary fractions with the following masses: secondary fraction 1 (labelled as LI-1-61A) (230 mg); secondary fraction 2 (labelled as LI-1-61B) (150 mg) and secondary fraction 3 (labelled as LI-1-61A) (120 mg).

HPLC-PDA-MS analysis of the secondary fractions revealed similarities in the chemical composition of fractions 1 and 2 (LI-1-61A and LI-1-61B), including the presence of the compound of interest, viz., α/β-punicalagin **(18)** at *m/z* 541 $[M-2H]^{2-}$ with an accompanying UV maximum absorbances (λ_{max}) at 217 nm, 258 nm, and 378 nm (Figure 3.11). Based on the UV and MS data, fractions 1 and 2 were combined.

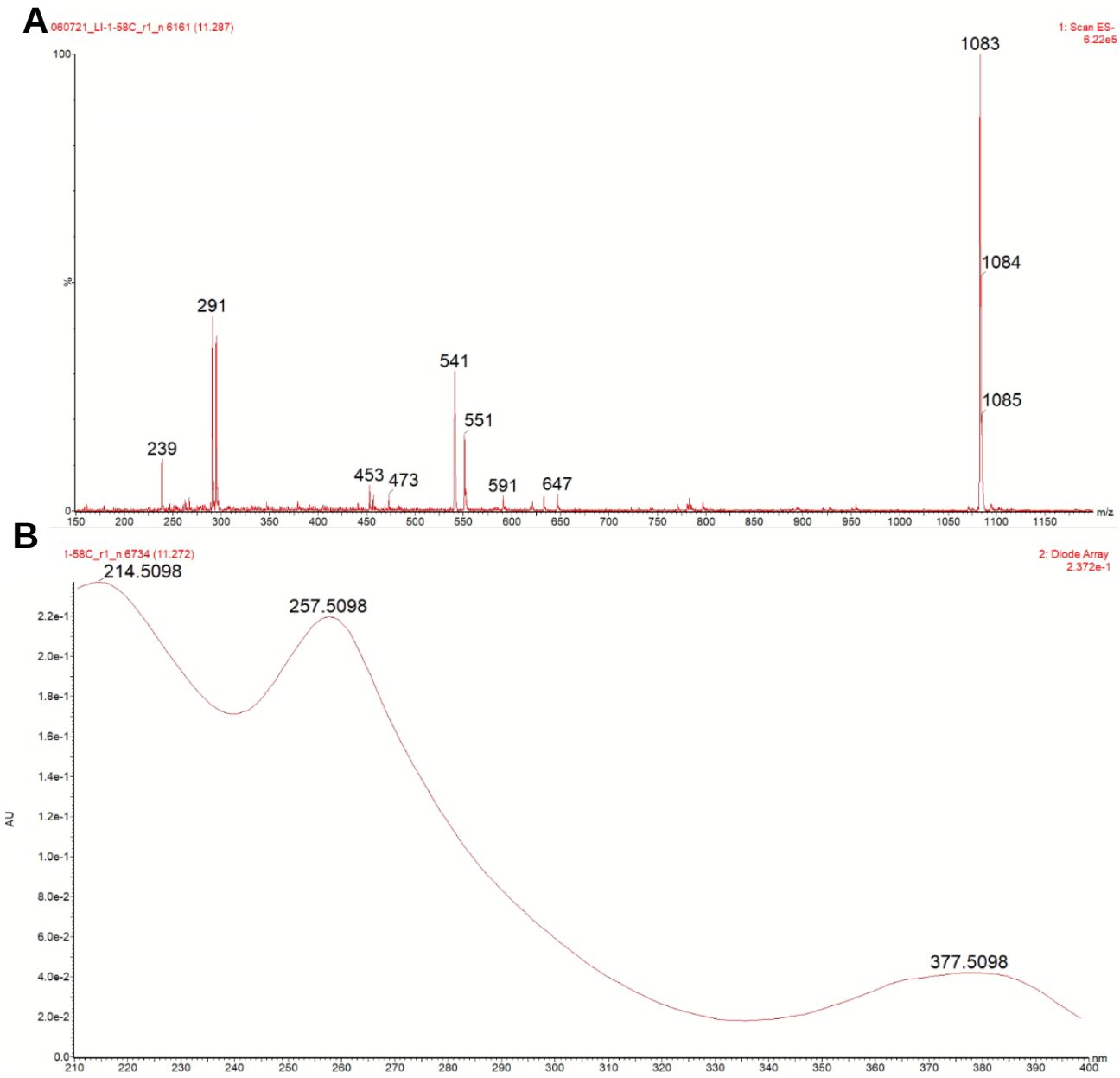

Figure 3.11: Representative example of the MS (**A**) and UV (**B**) spectra of α/β-punicalagin **(18)** obtained from the Waters HPLC-PDA-MS instrument.

Tertiary fractionation of the combined secondary fractions (LI-1-61A and LI-1-61B) (380 mg) was conducted using the prep-HPLC-PDA-MS instrument. The fractionation process gave rise to 22 tertiary fractions, some of which were combined based on MS and UV peak overlap (Figure 3.12), yielding 13 tertiary fractions with varying yields (Table 3.5: Mass and yield (%) of the tertiary fractions produced from the HPLC-PDA-MS). A broad-spectrum polarity of the compounds was observed, with compounds eluting both towards the start and end of the

solvent gradient (Figure 3.12). This tertiary fractionation step was done to prevent bias in the drug discovery approach, ensuring no additional bioactive compounds were present and that the detected bioactivity was not originating from an artefact introduced during the purification process.

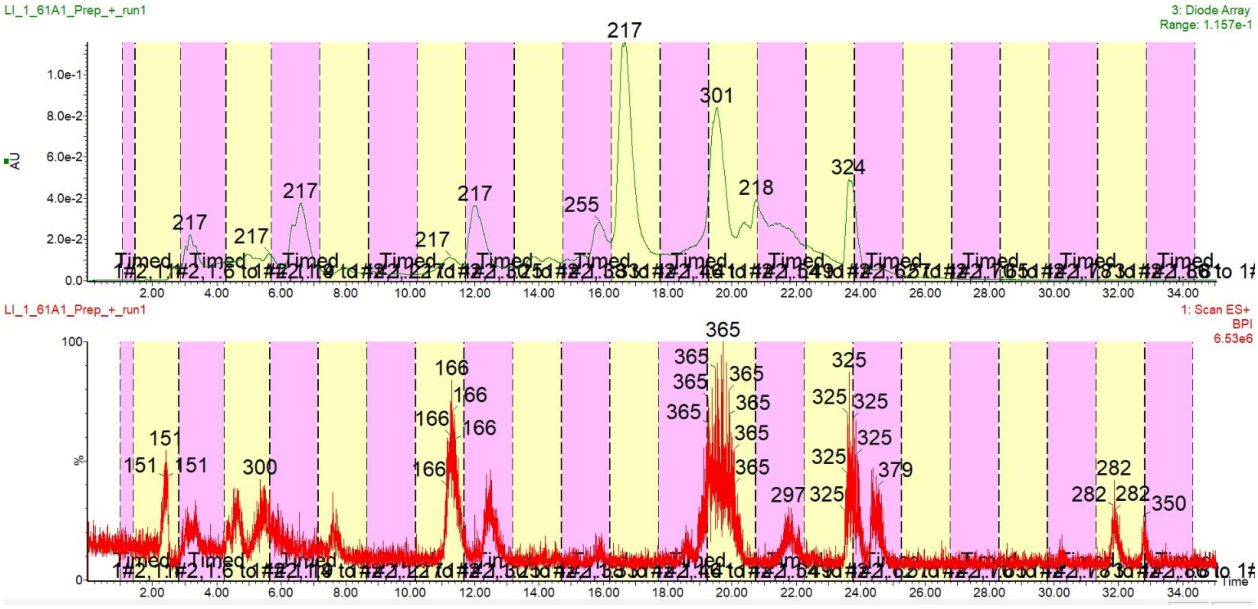

Figure 3.12: HPLC-PDA-MS chromatogram of the secondary fraction 1/2 from *G. perpensa*.

Table 3.5: Mass and yield (%) of the tertiary fractions of Secondary Fraction 1 and 2, produced from the HPLC-PDA-MS

Sample	Mass (mg)	Yield (%w/w)
Fraction 1	55.33	14.56
Fraction 2	19.11	5.03
Fraction 3	13.89	3.66
Fraction 4	15.35	4.04
Fraction 5	8.56	2.25
Fraction 6	8.86	2.33
Fraction 7	31.05	8.17
Fraction 8	13.00	5.91
Fraction 9	25.69	6.76
Fraction 10	19.17	5.04
Fraction 11	19.18	5.05
Fraction 12	5.75	1.51
Fraction 13	4.1	1.08

The tertiary fractions were screened in spike RBD/ACE2 antiviral bioassays. In these screens, Tertiary Fraction 2-8 demonstrated repeatable and potent RBD/ACE2 disrupting ability (Figure 3.13), with IC_{50} values ranging from 0.0028 to 0.012 µg/mL, which compared well with the positive control used REGN10987 (Table 3.6). The fractions similarly showed good antiviral activity against the Wuhan strain in the plaque-based bioassays. Of note, Fractions 6-8 presented a 75% inhibition of viral-induced cytopathic effect at 25 µg/mL (Figure 3.14: Single point bioassay (n=1) results of the *G. perpensa* extract, tertiary fractions and the positive control (remdesivir) to inhibit plaque formation in plaque-based bioassays against the Wuhan strain. Samples were tested at 25 µg/mL.). Surprisingly, the extract presented no inhibition against viral cytopathic effect in the plaque bioassays highlighting the advantage of the SPE clean-up where possible minor bioactive compounds were concentrated, and their activities detected and/or possible nuisance compounds were removed, which hide the bioactivity of the sample.

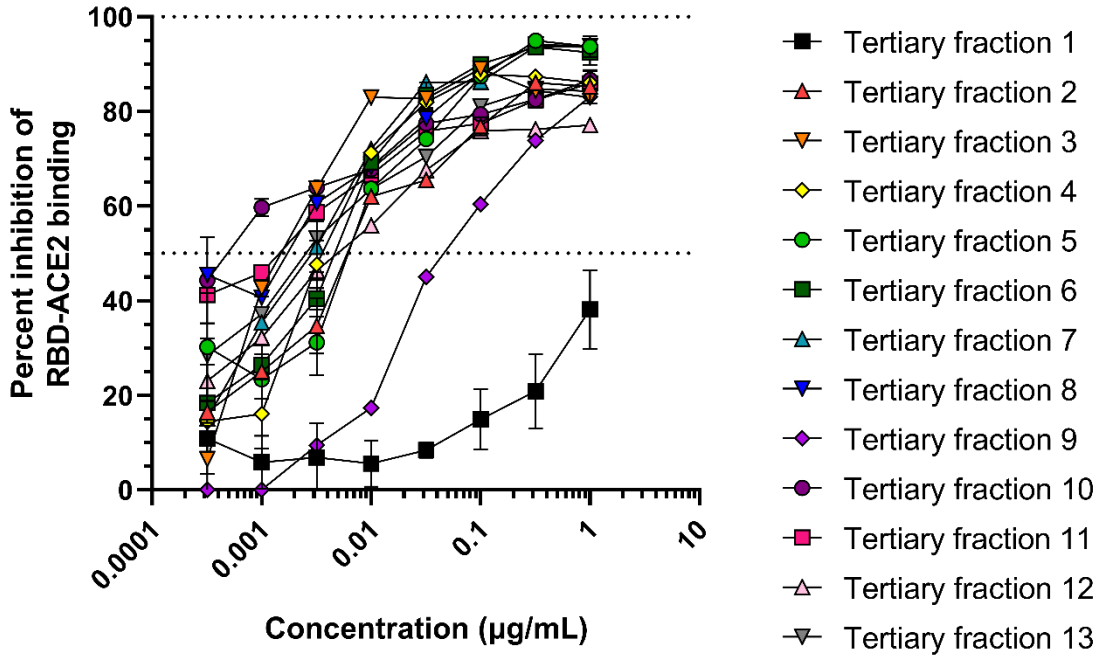

Figure 3.13: Dose-response curve of the *G. perpensa* tertiary fractions to inhibit spike RBD/ACE2 interaction by disrupting luminescence in AlphaScreen assays against the WT(USA-WA1/2020).

Table 3.6: Summary of the IC_{50} value of the tertiary fractions in the spike RBD/ACE2 AlphaScreen-based bioassay against the WT (USA-WA1/2020).

Sample	IC_{50} (µg/mL)
Tertiary fraction 1	29.8
Tertiary fraction 2	0.012
Tertiary fraction 3	0.0018
Tertiary fraction 4	0.0045
Tertiary fraction 5	0.0078
Tertiary fraction 6	0.0053
Tertiary fraction 7	0.0034
Tertiary fraction 8	0.0028
Tertiary fraction 9	0.069
Tertiary fraction 10	0.0017
Tertiary fraction 11	0.00050
Tertiary fraction 12	0.013
Tertiary fraction 13	0.0073
REGN10987	0.025 (0.18*)

*IC_{50} (nM)

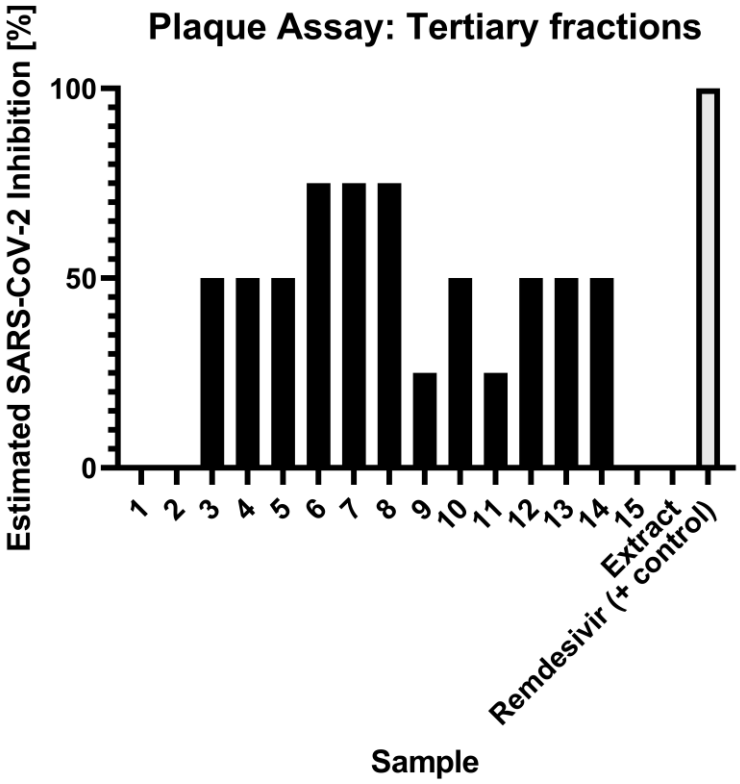

Figure 3.14: Single point bioassay (n=1) results of the *G. perpensa* extract, tertiary fractions and the positive control (remdesivir) to inhibit plaque formation in plaque-based bioassays against the Wuhan strain. Samples were tested at 25 µg/mL.

UPLC-IMS-HRMS analysis of the bioactive Tertiary Fractions 3-9 and extract, in ESI negative mode, showed the presence of very polar compounds (eluting between 1 to 6 min) (Figure 3.15). Subsequent analysis of the peak's respective MS spectra, accurate mass, and fragmentation pattern led to the tentative identification of the ellagitannins punicalin **(23)** (RT: 2.45 min) and α/β-punicalagin **(18)** (RT: 3.20; 3.50 min) in Fractions 3-8 (Figure 3.15), visible as major peaks. The HPLC-PDA-MS results obtained during the analysis of the secondary fractions further support the presumed identity of α/β-punicalagin **(18)**, with UV (λ_{max}) absorbances and *m/z* closely matching that of published data [50].

Lespedezic acid **(17)** was tentatively identified in bioactive Fraction 9. The peaks were found to have the same accurate mass, ion mobility drift time, CCS and retention time as those described in Table 3.4.

Due to the large and complex structure of the ellagitannins, the compounds did not elute as clear, sharp peaks but instead dragged along the C18 HPLC column, explaining their presence

in multiple tertiary fractions. Although a buffered eluent solution was used in an attempt to maintain uniform ionisation states of the compounds, this did not prevent peak broadening when working with larger quantities, as when preparatory work was conducted and hence explained the broad spread of the ellagitannins amongst multiple fractions and the observed broad-spectrum activity of many of the tertiary fractions.

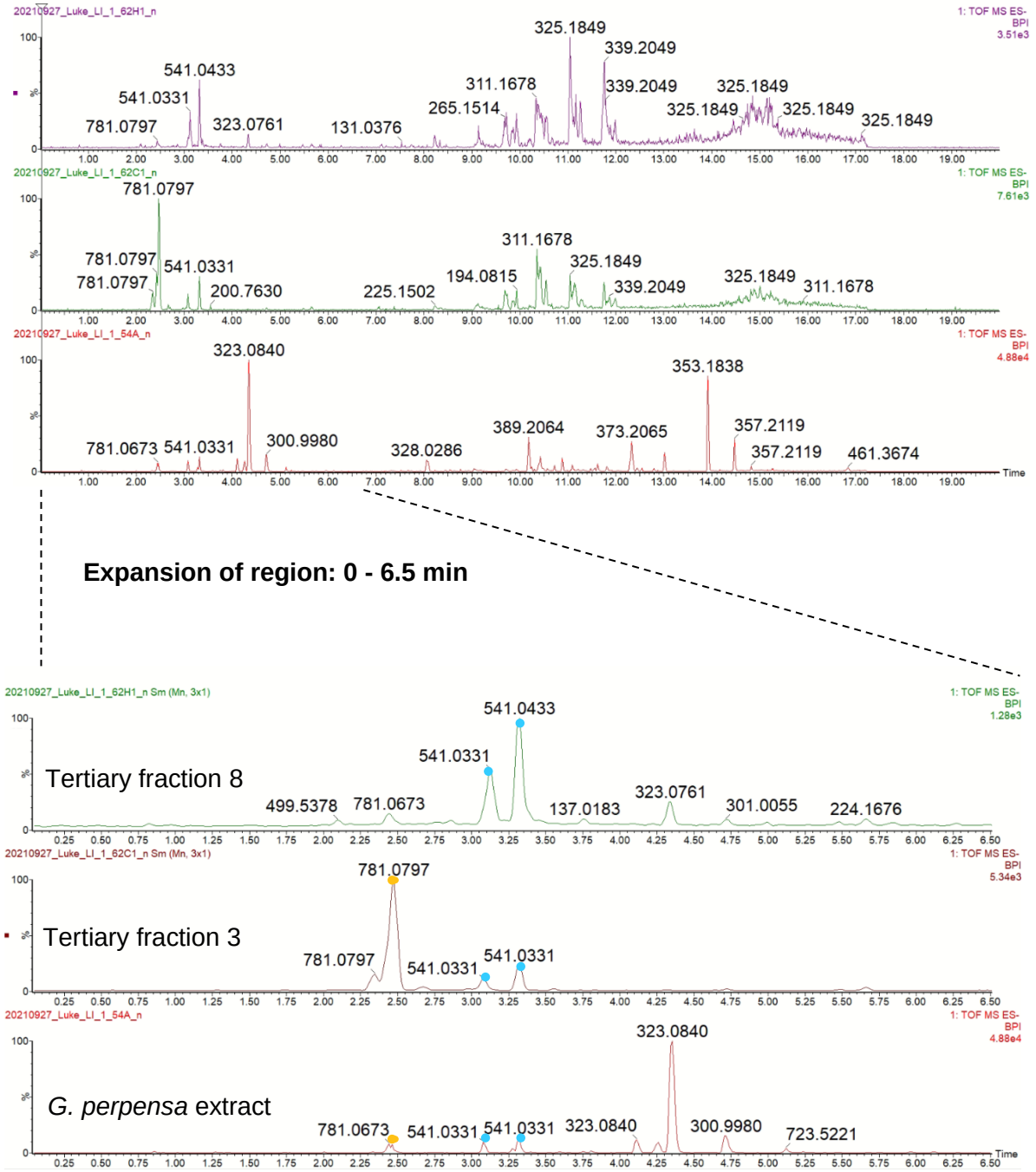

Figure 3.15: UPLC-IMS-HRMS BPI chromatogram of the bioactive tertiary fraction and *G. perpensa* extract analysed in ESI negative mode. Similarities and presumed bioactive compounds are marked. The compounds • punicalin **(23)** (RT: 2.45 min) and • α/β-punicalagin **(18)** (RT: 3.20; 3.50 min) are the compounds most likely contributing to the spike RBD/ACE2 inhibition activity and whole cell viral cytopathic inhibition.

The UPLC-IMS-HRMS results of the bioactive tertiary fractions further substantiate the hypothesis that α/β-punicalagin **(18)** likely contributes to the observed bioactivity; this is based on previous literature describing the phenolic class's antiviral activity against SARS-CoV-2 [49]. However, this cannot be claimed *a priori* without the other compounds (punicalin **(23)** and (Z)-lespedezic acid **(17)**) being tested against the virus.

3.3.3 Isolation and structure elucidation of α/β-punicalagin (18)

Further purification of tertiary fraction 8 (13.0 mg) with the use of an Agilent LC-SPE instrument led to the isolation of 1.0 mg (7.7% yield) of α/β-punicalagin **(18)**. The compound was isolated in the form of a yellow amorphous powder.

^{1}H NMR analysis of the sample revealed the presence of 2 anomeric proton signals (in a 1:1 ratio) suggesting a compound mixture. Specifically, one anomeric hydrogen signal, visible as a doublet, at 5.09 ppm (1H, d, J = 3.67 Hz) and another, visible as a doublet, at 4.76 ppm (1H, d, J = 8.56 Hz) (Supplementary Data, Figure S3.4). These two signals were believed to be the α-punicalagin **(18)** anomeric hydrogen and the β-punicalagin **(18)** anomeric hydrogen, respectively. These significant proton chemical shifts compared well with those described in the literature [51]. Interestingly, punicalagin **(18)** is well described to exist as a reversible mixture of anomers in solution, supporting our findings where 2 well-resolved UPLC chromatographic peaks were found upon analysis (Figure 3.15) [21]. Naturally, this makes the isolation, analysis and distinguishing of a particular anomer very difficult as any attempt to analyse the compound requires solvation, resulting in the spontaneous formation of the reversible anomeric mixture equilibrium.

3.3.4 Isolation and structure determination of (Z)-lespedezic acid (17)

(Z)-Lespedezic acid **(17)** (4.2 mg), *m/z 365* $[M+Na]^{+}$ (λ_{max} = 302 nm) was isolated from Tertiary Fraction 9 (25.69 mg) using a semi-prep HPLC-PDA-MS instrument. The resulting chromatogram is displayed in Figure 3.16. The resulting compound was isolated in the form of a green amorphous powder.

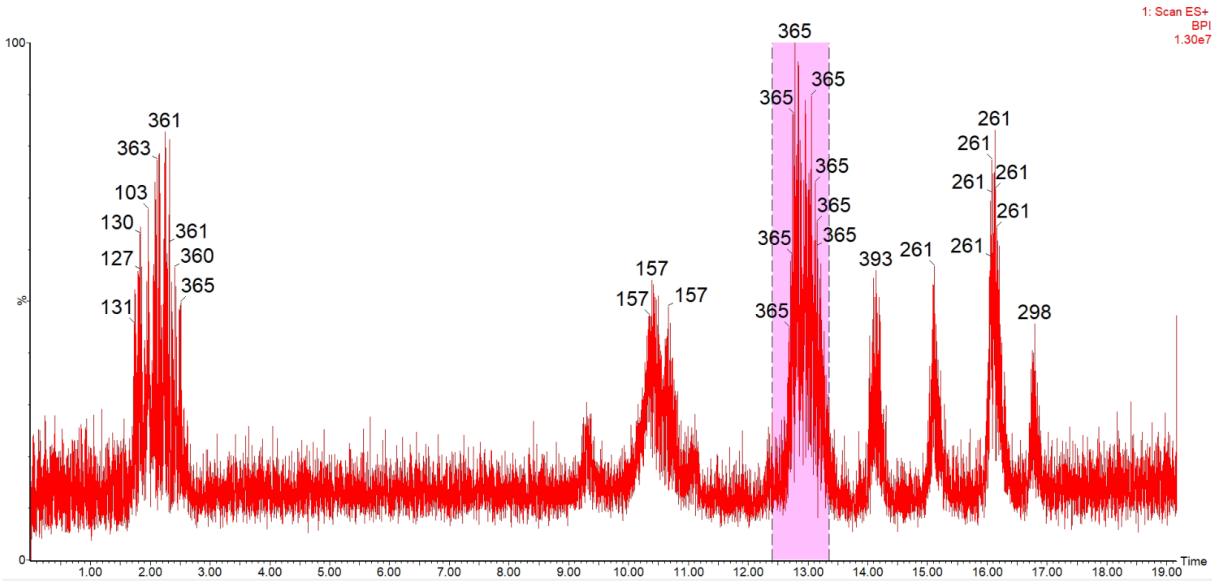

Figure 3.16: HPLC-MS BPI chromatogram of the secondary fractions analysed in ESI positive mode on a Waters HPLC-PDA-MS instrument illustrating the collection of (Z)-lespedezic acid **(17)**, *m/z* 365 $[M+Na]^+$.

NMR analyses, viz., ^1H and ^{13}C NMR spectroscopic analysis, were used to confirm the compound's identity.

The NMR data of compound **(17)** (Figure 3.17) is summarised in Table 3.7. Specifically, the recorded ^{13}C NMR spectra showed the presence of 13 signals (Supplementary Data, Figure S3.5). A presumed *O*-glucose moiety was observed at δ_C 60.0-100.8, a carbonyl carbon at δ_C 167.8 (C-1), four protonated aromatic carbons at δ_C 115.1 (C-6/8) and 132.1, three quaternary carbons at δ_C 139.4 (C-2), δ_C 124.5 (C-4) and δ_C 156.5 (C-7), and a protonated olefinic carbon at δ_C 125.4 (C-3). The ^1H NMR spectrum of compound **(17)** shows the presence of a para-substituted aromatic ring (2H, δ_H 6.76, d, J = 8.24 Hz, H-6/8; 2H, δ_H 7.60, d, J = 8.24 Hz, H-5/9), an anomeric carbohydrate signal (1H, δ_H 4.9, H-1', d, J = 7.78 Hz) and the presence of an olefinic proton (1H, δ_H 6.92) (Supplementary Data, Figure S3.5 and Figure S3.6). The conformation (cis or trans) of the alkene is hypothesised to be of a cis nature (Z conformation) by comparing the chemical shift of the olefinic proton with published data of (Z)-methyl lespedezate **(16)** (Figure 3.17), a closely related compound [6]. The comparison of the NMR data of the compounds is detailed in Table 3.7. The NMR data correlated well between the two compounds (Table 3.7) with one notable difference, that being the absence of the methoxy signal (δ_H 3.81) in the ^1H NMR of (Z)-lespedezic acid **(17)** and a small difference in the ^{13}C chemical shift for C-1 between the two compounds (Table 3.7). Interestingly, research

conducted by Shigemori et al. (1990) [52], on the difference between the Z and E- isomer of methyl lespedezate **(16)**, demonstrated that a marked difference in the ^{1}H chemical shifts can be observed for the olefinic proton (H-3) in the E and Z-isomer. They found that the ^{1}H chemical shift of the Z-isomer (δ_H 6.73 ppm) to be considerably more deshielded and hence observed at a more downfield position when compared to the E conformer (δ_H 6.12 ppm) [52].

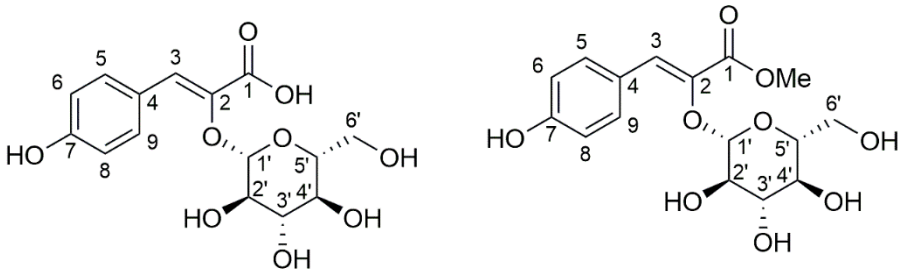

Figure 3.17: (Z)-Lespedezic acid **(17)** (left) and (Z)-methyl lespedezate **(16)** (right).

Table 3.7: Comparison of ^{1}H and ^{13}C data of (Z)-lespedezic acid **(17)** and Z-methyl lespedezate **(16)** analysed in D_2O and CD_3OD, respectively.

	^{1}H and ^{13}C data of Z-lespedezic acid (17) (D_2O, 500 MHz)		**^{1}H and ^{13}C data of Z-methyl lespedezate (16) (CD_3OD, 500 MHz) in literature** [6]	
Position	**δ ^{1}H (ppm, *J* in Hz)**	**δ ^{13}C (ppm)**	**δ ^{1}H (ppm, *J* in Hz)**	**δ ^{13}C (ppm)**
1		167.8		166.6
2		139.4		139.9
3	6.92 (1H, s)	125.4	6.98 (1H, s)	125.9
4		124.5		126.7
5	7.60 (2H, d , *J* = 8.2)	132.1	7.74 (2H, d, *J* = 8.1)	133.7
6	6.76 (2H, d, *J* = 8.2)	115.1	6.77 (2H, d, *J* = 8.6)	116.2
7		156.5		159.9
8	6.76 (2H, d, *J* = 8.2)	115.1	6.77 (2H, d, *J* = 8.6)	116.2
9	7.60 (2H, d, *J* = 8.2)	132.1	7.74 (2H, d, *J* = 8.2)	133.7
OMe		N/A	3.81 (3H, s)	52.6
β-glucose				
1'	4.90 (1H, d, *J* = 7.8)	100.8	5.10 (1H, d, *J* =12.5)	102.8
2'	3.46 (1H, t, *J* = 9.2)	73.2	3.48 (1H, t, *J* = 7.9)	75.7
3'	3.39 (1H, t, *J* = 9.1)	75.3	3.41 (1H, t, *J* = 9.0)	78.0
4'	3.31 (1H, t, *J* = 9.4)	68.9	3.34 (1H, t, *J* = 9.0)	71.4
5'	3.22 (1H, m)	75.9	3.21 (1H, ddd, *J* = 1.9, 2.4, 3.3)	78.4
6'	a. 3.52 (1H, dd, *J* = 12.4, 5.3) b. 3.6 (1H, dd, *J* = 12.3, 1.8)	60.0	a. 3.59 (1H, dd, *J* = 5.4, 5.5) b. 3.73 (1H, dd, *J* =1.7, 1.8)	62.5

In addition to the NMR data, the UV absorbance of a compound can also provide an indication of the compound's conformation. A trans alkene conformation is known to have superior conjugation and hence has a UV maximum absorbance at a much longer wavelength compared to it's cis counterpart [53,54]. The observed UV maxima was found to be at λmax = 302 nm, which corresponds very closely to the literature UV absorbance for the cis conformation of methyl lespedezate **(16)** (λmax = 300 nm)[55].

The NMR, UV and UPLC-IMS-HRMS data, viz., the monoisotopic mass, mass error and fragmentation pattern (Table 3.4), provide compounding evidence of the compound's identity. In the absence of an analytic standard of the respective Z or E-isomer, these literature findings provide strong evidence for the presence of the (Z) conformer and corroborate work conducted

by Khan et al. (2004), which describes the isolation of the (Z) isomer of methyl lespedezate **(17)** from *G. perpensa* [5].

3.3.5 UPLC-IMS-HRMS analysis and bioactive compound confirmation of punicalin and α/β-punicalagin

UPLC-IMS-HRMS analysis was conducted on the bioactive samples (*G. perpensa* extract and the bioactive Tertiary Fractions (3-8)) and the purchased ellagitannin reference standards to provide additional confirmation on the identity of the compounds. The expanded UPLC-HRMS chromatograms are displayed in Figure 3.18 where the α/β-punicalagin **(18)** chromatographic peaks were found to occur at a retention time of 3.20 min and 3.50 min for the 2 anomers, respectively. Additionally, punicalin's **(23)** chromatographic peak was observed at a retention time of 2.45 min. The observed monoisotopic mass and retention time of the ellagitannin peaks in the plant samples correlate well with those of the purchased standards (Figure 3.18).

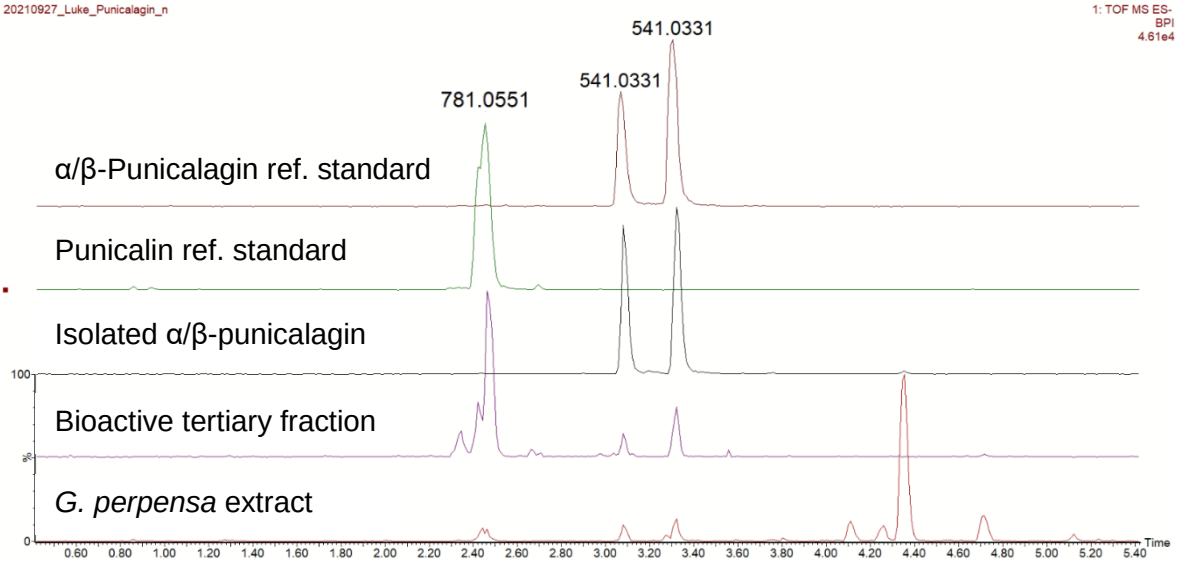

Figure 3.18: UPLC-IMS-HRMS chromatograms of the *G. perpensa* extract, bioactive tertiary fraction, isolated α/β-punicalagin **(18)** and the respective reference standards, viz., punicalin **(23)** (RT: 2.45 min) and α/β-punicalagin **(18)** (RT: 3.20; 3.50 min).

A representative ion mobility contour plot of the α/β-punicalagin **(18)** standard is displayed in Figure 3.19. The comparison of the UPLC-IMS-HRMS data of the ellagitannins in the samples (Tertiary Fractions 3 to 8)) and the data of the purchased reference standards are also displayed in Table 3.8.

Minimal variation in the monoisotopic mass, observed ion mobility drift and CCS values of the ellagitannins were observed between the peaks in the *G. perpensa* samples and the peaks in the reference standards. In addition, it can be noted that the retention times and mass fragmentation data of the standards match closely to those of the compounds present in the samples (Figure 3.18; Table 3.8), providing conclusive evidence of the correct identification of the compounds present in the bioactive fraction and hence, making this the first confirmed report of punicalin **(23)** occurring in *G. perpensa*.

Interestingly, a comparison of the same qualifier quasi-molecular ions of α-punicalagin **(18)** and β-punicalagin's **(18)** CCS and drift time showed no significant difference. However, as expected, distinct differences in drift time and CCS area were observed for $[M-H]^-$ and $[M-2H]^{2-}$ quasi-molecular ions of peaks with the same retention time, these being 5.53 ms and 1.92 ms for the $[M-H]^-$ and $[M-2H]^{2-}$ quasi-molecular ion respectively (Figure 3.19; Table 3.9). A plot of retention time vs drift time (Figure 3.19A) illustrates how compounds, like the quasi-molecular ions of α/β-punicalagin **(18)**, which coelute on UPLC, can be separated further using ion mobility chromatography based on their respective drift time.

With the addition of ion-mobility data, a 3rd dimension of separation (Figure 3.19) and data was acquired, which provided additional confidence in the reported results, a particularly useful technique when dealing with complex mixtures [56]. With ion mobility coupled mass spectrometry gaining popularity, CCS libraries are becoming more and more important as these provide theoretical and/or experimental ion mobility data [57,58]. Data addition to these libraries relies on such studies to provide data, especially those where reference standards were used. Advances in IM-MS, like cyclic ion mobility (cIM) [59] might provide significant results between anomers, providing an added assurance in complex mixtures, especially where a 3rd dimension of separation would prove helpful, natural products being a particularly fitting field.

Due to the complex nature of the ellagitannin compounds, this additional confirmation step was prudent to confirm their identity and quantify their concentrations unequivocally.

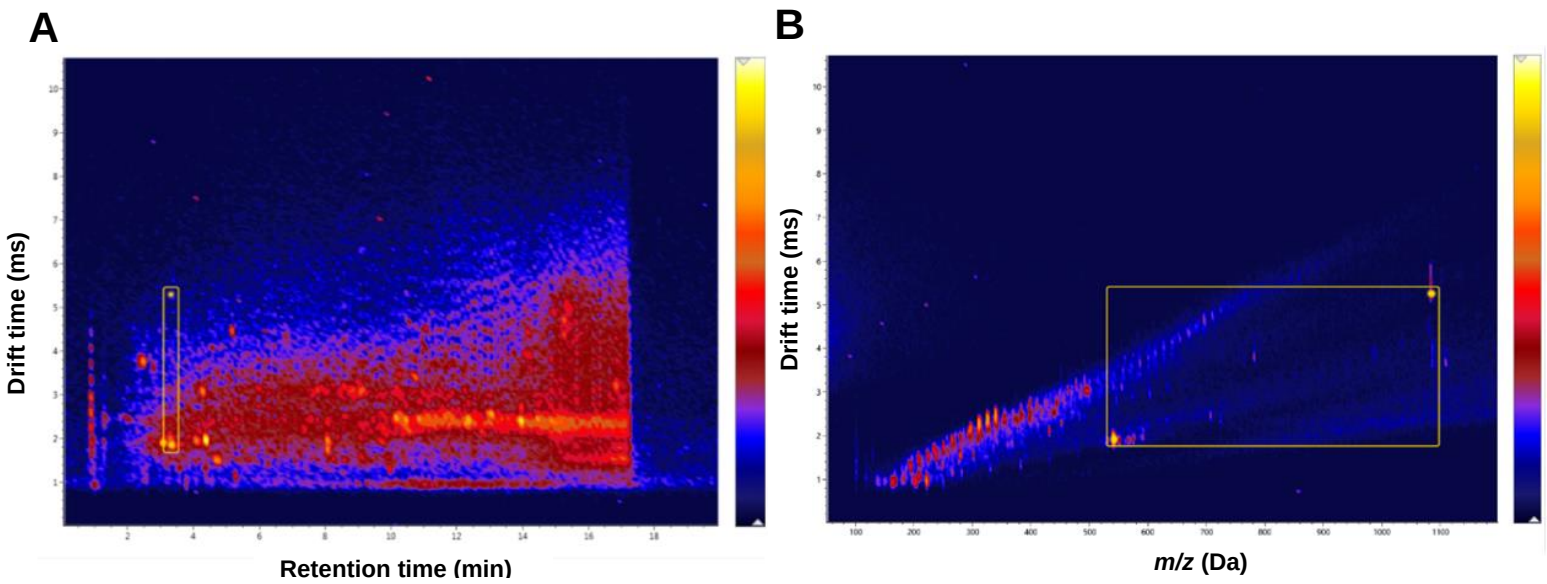

Figure 3.19: (**A**) Representative ion mobility contour plot of the α/β-punicalagin **(18)** standard, generated by UNIFI® with retention time (min) versus drift time (ms), providing a 3rd dimension of separation, clearly separating the different quasi-molecular ions in the same peak. (**B**) An ion mobility contour plot of the α/β-punicalagin **(18)** standard, with drift time (ms) versus *m/z* (Da) showing different drift times for the 2 separate quasi-molecular ions of the respective α/β anomeric peaks (**B**).

Table 3.8: Confirmed identity of the 2 small molecules from the bioactive fraction and DCM:MeOH extract of *G. perpensa* from UPLC-IMS-HRMS analysis.

Compound	Observed *m/z*[a] (Da)(Mass error (ppm))	Observed quasi-molecular ion	RT[b] (min)	Observed drift (ms)(%error)	Observed CCS[c] (Å^2)(% error)	Observed fragment (*m/z*)(mass error (mDa))
Punicalin (23)	781.0546 (2.0)	$[M-H]^-$	2.45	3.79 (1.81)	250.32 (1.00)	721.0336 (1.7) 600.9910 (1.4) 448.9786 (-0.1)
α/β-Punicalagin (18)	541.0234 (− 4.8)	$[M-2H]^{2-}$	3.20	1.91 (0.00)	345.60 (0.03)	600.9900 (0.4) 541.0256 (− 0.4) 300.9963 (− 2.7) 275.0171 (− 2.7)
α/β-Punicalagin (18)	541.0251 (− 1.7)	$[M-2H]^{2-}$	3.50	1.87 (2.60)	341.33 (1.48)	600.9895 (− 0.2) 541.0239 (− 2.1) 300.9969 (− 2.0) 275.0180 (− 1.7)

[a]*m/z*, mass to charge ratio; [b]*RT,* retention time; [c]*CCS*, collisional cross-section; [*]Error relative to standard; [**]Common in purchased standards; [#]RT found to be within 0.1 min margin with purchased standards

Table 3.9: Quasi-molecular ions of the α/β-punicalagin **(18)** peaks observed for the $[M-H]^-$ and $[M-2H]^{2-}$ quasi-molecular ions. Data generated from UPLC-IMS-HRMS and processed using UNIFI®.

Compound	Observed *m/z*[a] (Da) (mass error (ppm))	Observed quasi-molecular ion	RT[b] (min) Observed	Observed drift (ms)*	Observed CCS[c] (Å^2)*
α/β-Punicalagin **(18)**	1083.0714 (9.9)	$[M-H]^-$	3.50	5.53	303.92
	541.0289 (5.4)	$[M-2H]^{2-}$		1.92	346.46

[a]*m/z*, mass-to-charge ratio; [b]*RT*, retention time; [c]*CCS*, collisional cross-section; [*]Within confidence interval of instrument.

3.3.6 Quantification of α/β-punicalagin (18) and punicalin (23) using UPLC-IMS-HRMS and method validation

The UPLC-IMS-HRMS method was partially validated according to ICH guidelines [20]. This was done using multiple analytical parameters, viz., method specificity, linearity, precision and LOD, LOQ quantification parameters. Quantification of the ellagitannins in the DCM:MeOH extract was also performed with the use of standard calibration curves.

3.3.6.1 Specificity

The specificity of the UPLC-IMS-HRMS method was assessed by analysing the analytical standards of punicalin **(23)** and α/β-punicalagin **(18)** in the DCM:MeOH extract of *G. perpensa* and the respective blanks. A strong positive correlation in terms of component retention times and mass spectral peaks was obtained between the DCM:MeOH extract and the respective standards (cf. Figure 3.18; cf. Table 3.8; Supplementary Data Figure S3.8 and Figure S3.7). The chromatographic peaks (start, middle and end) were analysed and found to be of high purity, with the extracted MS spectra correlating well between peak start, middle and peak end.

3.3.6.2 Linearity, LOD and LOQ

Method linearity was validated by analysing the 5 concentrations of each analyte, viz., punicalin **(23)** and α/β-punicalagin **(18)**. Their respective concentration ranges were 1-50 µg/mL and 5-80 µg/mL for punicalin **(23)** and α/β-punicalagin **(18)**, respectively. Linear calibration curves were obtained for both compounds for the tested ranges with a strong positive correlation coefficient obtained for both punicalin **(23)** and α/β-punicalagin **(18)**, namely 0.9998 and 0.9997, respectively (Table 3.10; Figure 3.20; Figure 3.21).

LOD and LOQ calculations were performed for each analyte of interest. The LOD and LOQ for punicalin **(23)** were found to be 0.27 µg/mL and 0.81 µg/mL, respectively. Similarly, the LOD and LOQ for α/β-punicalagin **(18)** (as the sum of both anomer peaks) were calculated to be 1.4 µg/mL and 4.1 µg/mL, respectively (Table 3.10). The results indicate that the method exhibited good sensitivity.

Table 3.10: Parameters used for the quantification of punicalin **(23)** and α/β-punicalagin **(18)** in the *G. perpensa* DCM:MeOH extract.

Compound	Linear range (µg/mL)	Regression equation	r^2	LOD[a] (µg/mL)	LOQ[b] (µg/mL)
α/β-Punicalagin (18)[#]	1-50	y = 179.9x + 98.792	0.9998	0.27	0.81
Punicalin (23)	5-80	y = 236.57x + 2059.1	0.9997	1.4	4.1

[#]Reported as the sum of the 2 isomers (anomers); [a]Limit of detection; [b]Limit of quantification

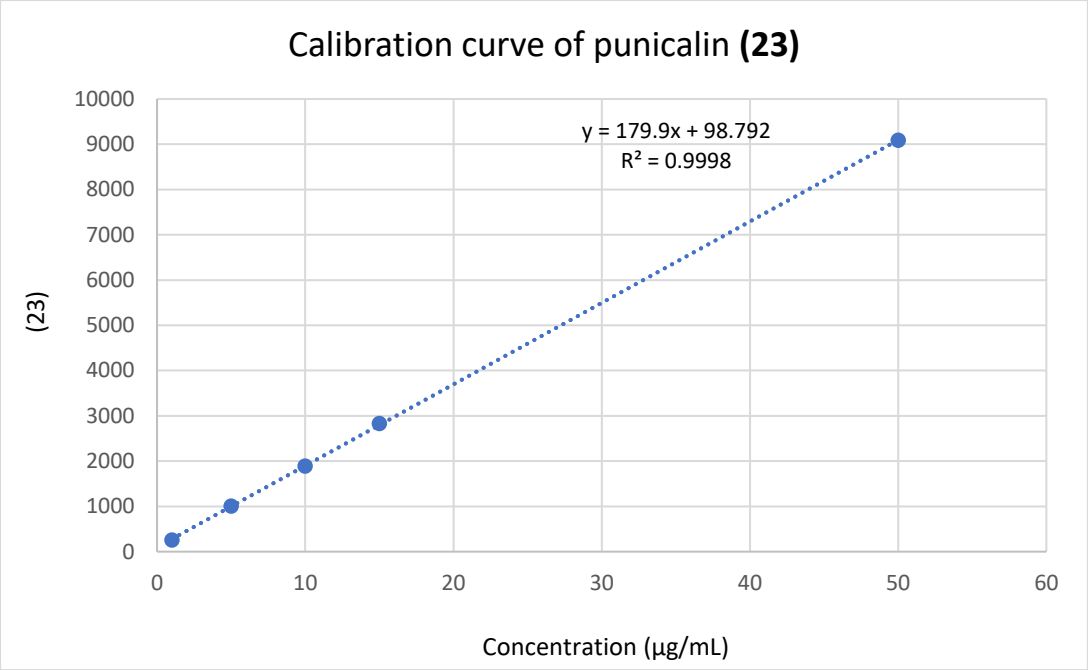

Figure 3.20: Calibration curve of the punicalin **(23)** standard generated from UPLC-IMS-HRMS analysis. Analyses were performed in triplicate, and the mean area was plotted. Repeats showed %RSD<5%.

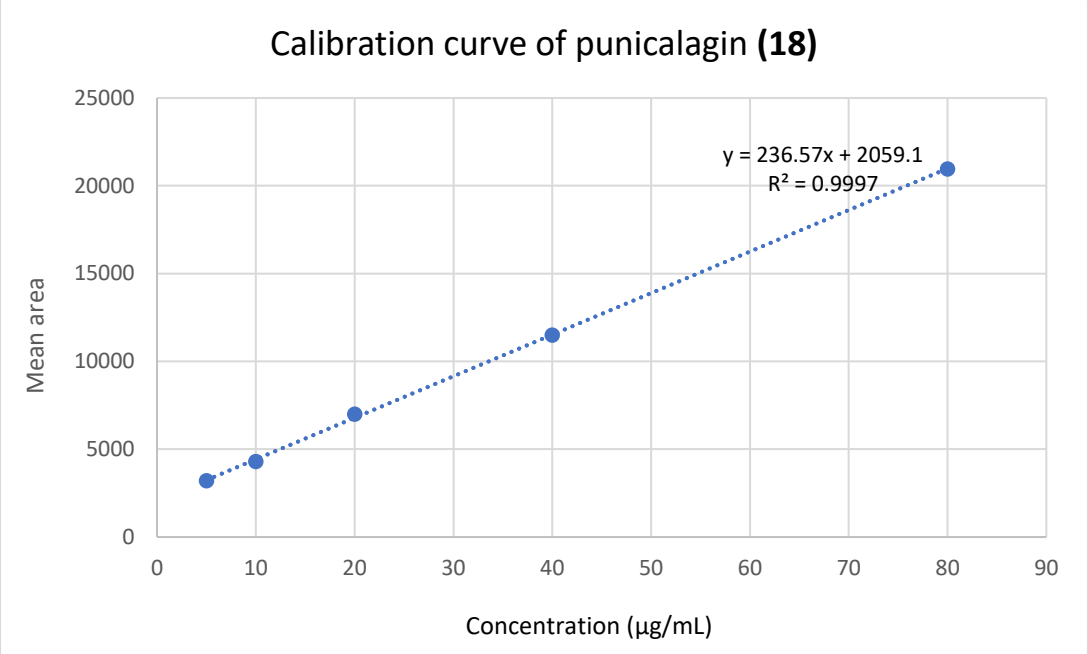

Figure 3.21: Calibration curve of the sum of α/β-punicalagin **(18)** standard generated from UPLC-IMS-HRMS analysis. Analyses were performed in triplicate, and the mean area was plotted. Repeats showed %RSD<5%.

3.3.6.3 Precision

Method precision was assessed by performing intra-day UPLC analyses. The standard solutions (5 different solutions prepared by serial dilution) were analysed in 3 replicates during the course of the day, with the results displayed in Table 3.11. The %RSD of the respective ellagitannin standards was found to be <5%, indicating an acceptable level of precision for the analysis.

Table 3.11: Intra-day precision of the UPLC-IMS-HRMS method of the marker compounds punicalin **(23)** and α/β-punicalagin **(18)**.

Concentration (µg/mL)	Inter-day precision (*n*=3)	
	Mean area	**%RSD**
Punicalin (23)		
1	257.67	4.50
5	1004.33	1.46
10	1886.67	3.66
15	2829.33	4.57
50	9084.33	4.02
α/β-Punicalagin (18)		
5	3200.33	4.67
10	4301.67	4.12
20	7001.67	2.55
40	11501.67	3.59
80	20960.33	4.76

3.3.6.4 Percentage of punicalin (23) and α/β-punicalagin (18) in the extract

The concentration of punicalin **(23)** and α/β-punicalagin **(18)** in the DCM:MeOH extract was determined using the prepared 5-point calibration curves and respective curve equations. The concentration of punicalin **(23)** and α/β-punicalagin **(18)** was calculated to be 2.12 ± 0.15% and 1.51 ± 0.15% (%w/w), respectively. Furthermore, the concentration of the ellagitannins in the dried plant material (based on a DCM:MeOH extraction and a 9.2% extraction yield), was found to be 0.19 ± 0.01% and 0.14 ± 0.01% (%w/w) for punicalin **(23)** and α/β-punicalagin **(18)**, respectively.

3.3.7 Antiviral screens of punicalin (23) and α/β-punicalagin (18)

The purchased ellagitannin standards were rescreened in AlphaScreen-based technology against the WT, Beta, Deta and Omicron variants of concern and in plaque-based bioassays (Wuhan, beta, delta and omicron variants) in a full-dose response manner. The IC_{50} of punicalin **(23)** and α/β-punicalagin **(18)** in the spike RBD/ACE2 inhibition assay (AlphaScreen) was found to be 9 nM and 29 nM against the WT(USA-WA1/2020) (Figure 3.22), respectively. Compared to the positive control, REGN10987, a monoclonal antibody found to have an IC_{50} value of 0.18 nM (Figure 3.22), the compounds compared reasonably well.

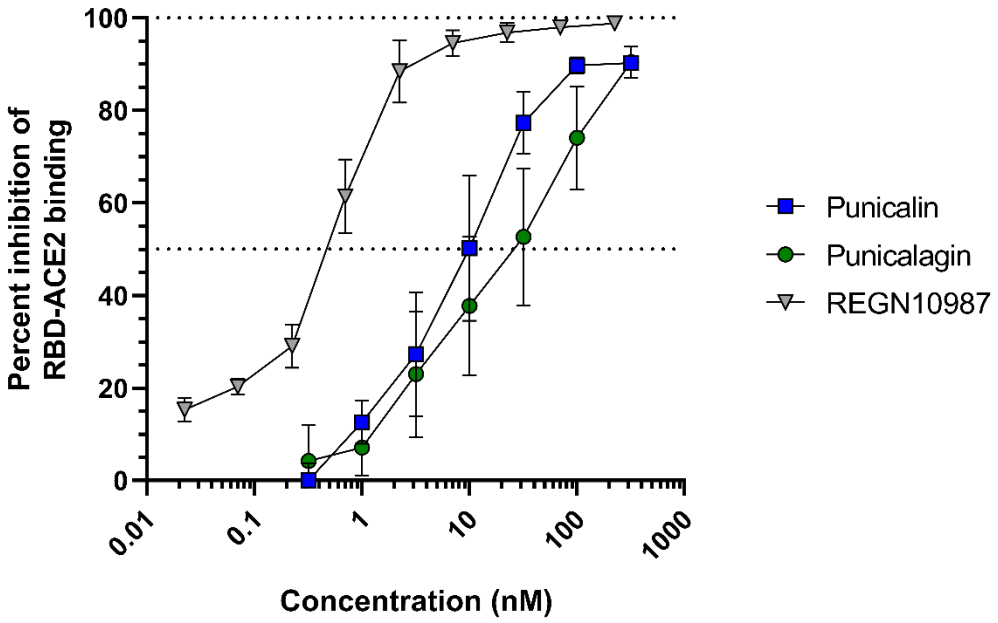

Figure 3.22: Dose-response curves denoting the ability of the pure compounds punicalin **(23)** and α/β-punicalagin **(18)** to antagonise the SARS-CoV-2 spike RBD-host ACE2 protein binding in AlphaScreen assays against the WT(USA-WA1/2020). REGN10987 was used as the positive control. Data are represented as the mean of the multiple replicates (n=3) with SEM.

Further spike RBD/ACE2 inhibition of the compounds against the Beta, Delta, Lambda and Omicron variants of concern was conducted and showed both α/β-punicalagin **(18)** and punicalin **(23)** to possess repeatably good antagonist activity against the spike RBD/ACE2 interaction, irrespective of the particular variant.

The IC_{50} values of punicalin **(23)** ranged between 9.5 nM (Delta) and 35.4 nM (Lambda), with the IC_{50} values of α/β-punicalagin **(18)** ranging from 6.6 nM (Beta) and 13.3 nM (Omicron) (Figure 3.23; Table 3.12). The compounds showed comparable results to the positive controls, REGN10933 and REGN10987, against the WT, Beta, Delta and Lambda variants of concern. Interestingly, the two ellagitannins showed significantly better activity against the Omicron variant of concern when compared to the positive controls (Table 3.12).

This data highlights the non-selective inhibition (in terms of variant) against the various SARS-CoV-2 variant spike proteins. It is not surprising that the monoclonal antibodies show varying results against the different variants as these are highly selective to a particular spike phenotype and often show decreased activity when any mutation occurs, leading to decreased interaction at the fragment antigen-binding region (Fab region) of the antibody. In this case, the Lambda variant is well published to exhibit multiple mutations, 7 out of the 8 associated with the viral spike protein [60] and hence evade a lot of the previous antibodies produced by previous infections or elicited by the vaccines. This highlights the inherent need for the body to continuously produce different antibodies against highly mutable viruses, like influenza and COVID-19.

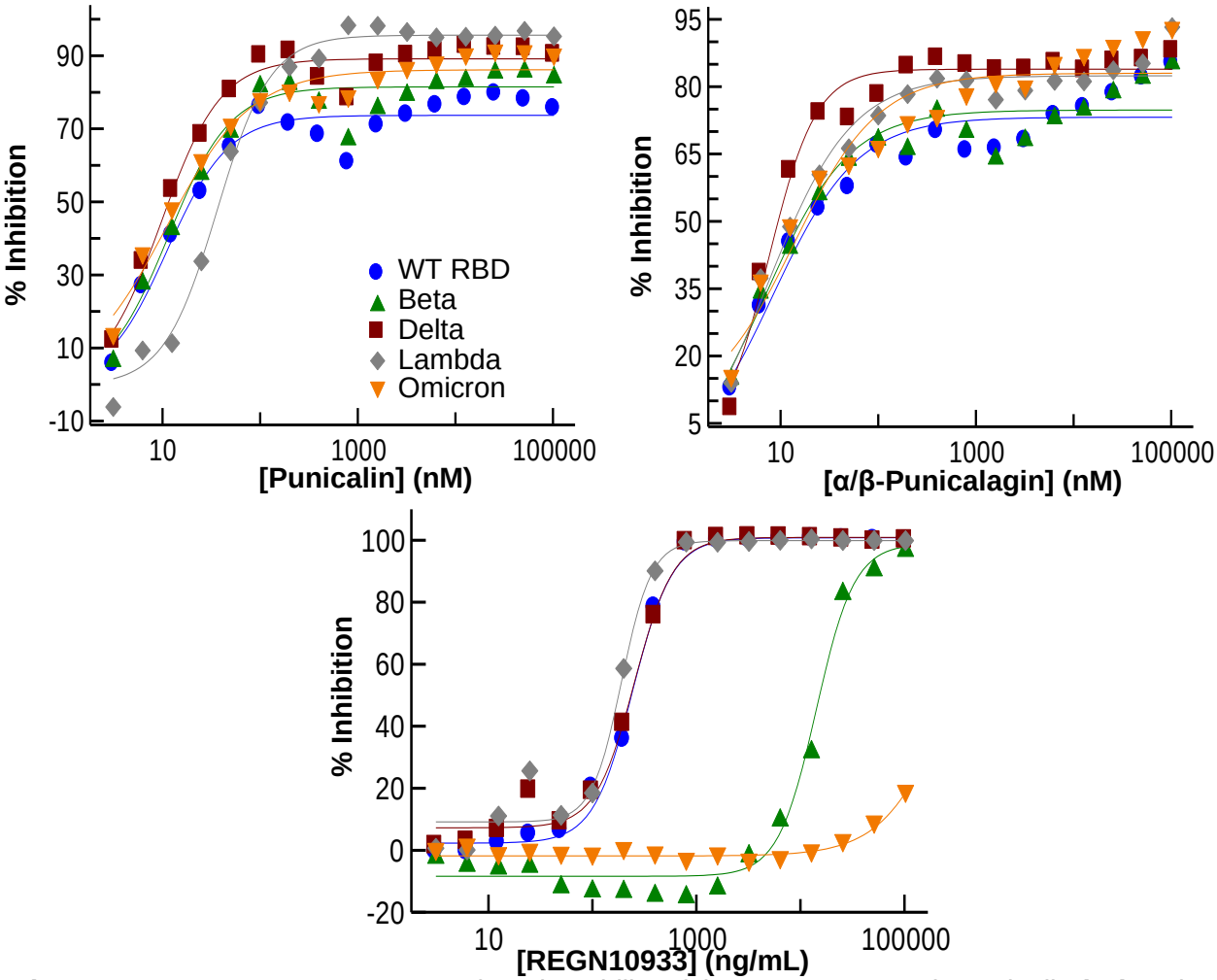

Figure 3.23: Dose-response curves denoting ability of the pure compounds punicalin **(23)** and α/β-punicalagin **(18)** to antagonise the SARS-CoV-2 spike RBD-host ACE2 protein binding in AlphaScreen-based assays against the WT(USA-WA1/2020), Beta, Delta, Lambda and Omicron variants of concern. REGN10933 was used as the positive control and illustrated for comparison. Data is represented as the mean of the multiple replicates (n=3) with SEM.

Table 3.12: IC_{50} values of the ellagitannins, and the positive control monoclonal antibodies REGN10933 and REGN10987 against the WT, Beta, Delta, Lambda and Omicron variants of concern in spike RBD/ACE2 AlphaScreen-based bioassays.

IC_{50} (nM)	REGN10933	REGN10987	Punicalin (23)	α/β-Punicalagin (18)
WT	1.7	10.6	10.9	8.1
Beta	99.8	5.0	11.2	6.6
Delta	1.8	2.1	9.5	7.4
Lambda	1.3	6.4	35.4	7.1
Omicron	>700	>700	10.6	13.3

In the whole cell plaque-based bioassays, punicalin **(23)** was found to inhibit the formation of virus-driven cytopathic changes, specifically in a dose-dependent fashion, against the Wuhan strain (Wild type), Beta, Delta and Omicron variants of SARS-CoV-2 (Figure 3.24). The IC_{50} values for punicalin **(23)** were found to be 7.44 µM against the Wuhan variant with a CC_{50} = 199.6 µM with minor noticeable cytotoxicity observed in healthy Vero E6 cells at concentrations exceeding 6.4 µM. The SI was found to be 26.83 and a goodness of fit (r^2) = 0.9578. Additionally, against the Beta variant, the IC_{50} value of punicalin **(23)** IC_{50} was found to be IC_{50} = 7.63 µM, SI= 26.17 and goodness of fit (r^2) = 0.9021; Delta variant: IC_{50} = 13.52 µM, SI=14.76 and goodness of fit (r^2) = 0.9994 and 1.210 µM against the recent Omicron variant with a SI=164.96 and a goodness of fit (r^2) = 0.9869 (Figure 3.24).

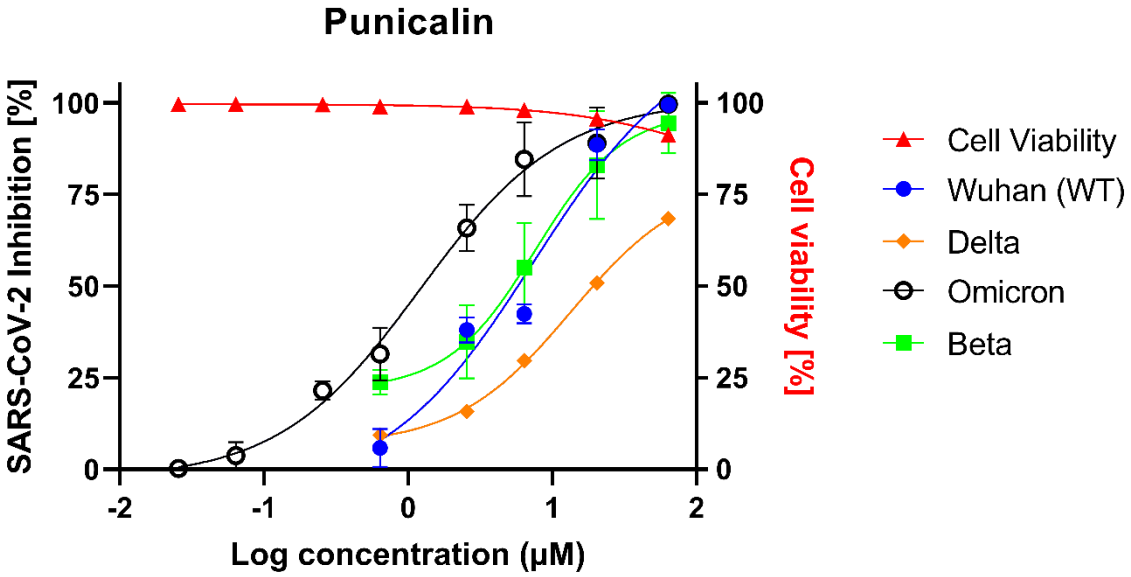

Figure 3.24: Antiviral and cytotoxic activity (▲) of punicalin **(23)** against SARS-CoV-2 (Wuhan (●), Delta (♦), Omicron (○) and Beta var. (■)) in Vero E6 cells. Inhibition of SARS-CoV-2 infection (%) is represented in the legend, with the red triangles representing cell viability (%). Cytotoxicity data expressed as the mean of two replicates (n=2) and results analysed on a 95% confidence interval. Antiviral activity expressed as a single analysis (n=1) for the Delta and Beta variant as the mean of a single repeat (n=2) for activity against the Wuhan strain.

Similarly, in the whole cell plaque-based bioassays, α/β-punicalagin **(18)** was found to inhibit the formation of virus-driven cytopathic changes, specifically in a dose-dependent fashion, against the Wuhan strain (Wild type), Beta, Delta and Omicron variants of SARS-CoV-2 (Figure 4.26). The IC_{50} value of α/β-Punicalagin **(18)** was found to be 3.95 µM against the Wuhan variant with a CC_{50} = 241.70 µM with minor noticeable cytotoxicity observed in healthy Vero E6 cells at concentrations exceeding 14.75 µM. The SI was found to be 61.16 and a goodness of fit (r^2) = 0.9578. Additionally, against the Beta variant, the IC_{50} value of α/β-punicalagin **(18)** was found to be IC_{50} = 11.27 µM, SI= 21.45 and goodness of fit (r^2) = 0.8877; Delta variant: IC_{50} = 13.52 µM, SI=17.87 and goodness of fit (r^2) = 0.9994 and 1.21 µM against the recent Omicron variant with a SI=199.75 and a goodness of fit (r^2) = 0.9869 (Figure 3.25).

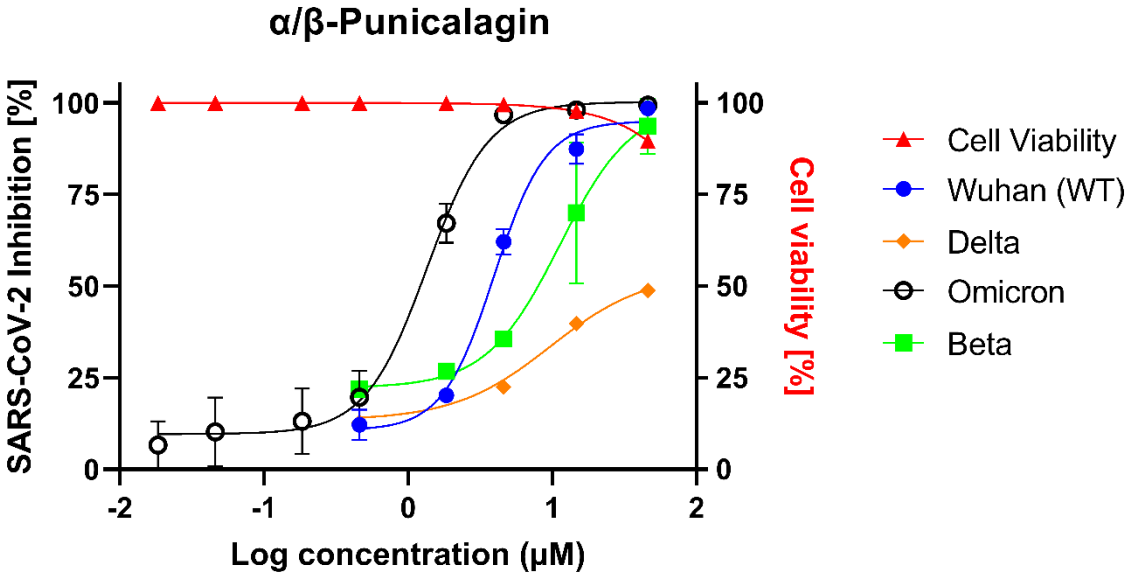

Figure 3.25: Antiviral and cytotoxic activity (▲) of α/β-punicalagin **(18)** against SARS-CoV-2 (Wuhan (●), Delta (♦), Omicron (○) and Beta var. (■)) in Vero E6 cells. Inhibition of SARS-CoV-2 infection (%) is represented in the legend, with the red triangles representing cell viability (%). Cytotoxicity data expressed as the mean of two replicates (n=2) and results analysed on a 95% confidence interval. Antiviral activity expressed as a single analysis (n=1) for the Delta and Beta variant as the mean of a single repeat (n=2) for activity against the Wuhan strain.

Various combinations of the ellagitannins were prepared and tested in viral CPE quantitative assays in order to determine if the ellagitannin combinations yield any additive or synergistic potential.

The EC_{50} values for the various solutions were found to range between 5.0 μM and 24.9 μM. Interestingly, the punicalin:α/β-punicalagin (10:1) and punicalin:α/β-punicalagin (3:1) combinations had the lowest EC_{50} value, namely 5.01 and 8.42 μM, respectively, indicating enhanced activity relative to the punicalin **(23)** and α/β-punicalagin **(18)** solutions (Figure 3.26; Table 3.13). Similarly, both of these solution ratios were found to show significant synergism ($p < 0.05$; paired Student's t-test) as determined by the Bliss Independence model [61].

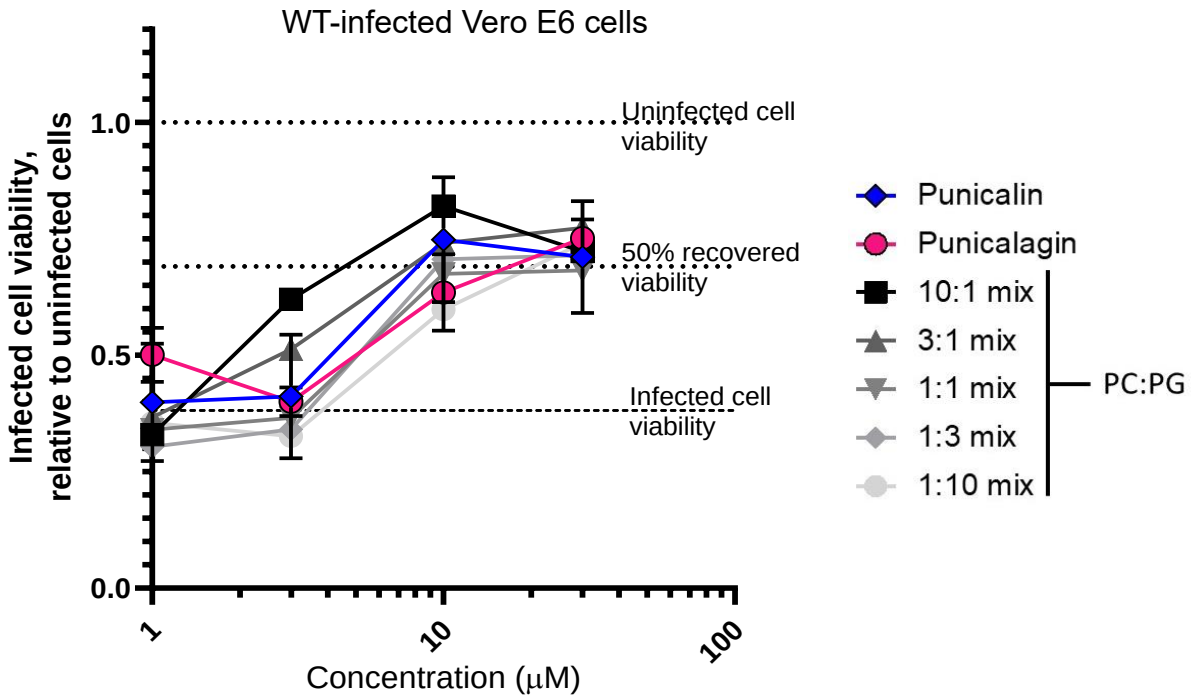

Figure 3.26: Antiviral activity of punicalin **(23)** and α/β-punicalagin **(18)** combinations against WT-infected Vero E6 cells

Table 3.13: EC_{50} values of punicalin **(23)** and α/β-punicalagin **(18)** combinations. (*) denotes significant synergism ($p < 0.05$; paired Student's t-test) as determined by the Bliss Independence model [61].

Combination	EC_{50} (μM)
Punicalin (PC)	14.2
Punicalin:α/β-punicalagin (10:1)	5.0
Punicalin:α/β-punicalagin (3:1)	8.4
Punicalin:α/β-punicalagin (1:1)	19.9
Punicalin:α/β-punicalagin (1:3)	12.1
Punicalin:α/β-punicalagin (1:10)	16.3
α/β-Punicalagin (PG)	24.9

Previous research by Du et al. (2021) did find α/β-punicalagin **(18)** to possess antiviral activity against the SARS-CoV-2 virus, with the mechanism of action concluded to be against the viral 3CL protease (M^{pro}) [49]. Our data contradict these results and show that both ellagitannins potently possess RBD/ACE2 antagonistic activity, which presumably prevents the virus from entering the host cell. Further mechanistic studies are required to reconcile these inconsistent

reports using replication-competent viruses. Some natural product compounds, however, often target more than one structure/process, which may enhance their activity and possibly set higher genetic barriers to viral resistance.

3.3.8 Antiviral screens of (Z)-lespedezic acid (17)

The isolated (Z)-lespedezic acid **(17)** was screened in M^{pro} inhibition assays, spike RBD/ACE2 AlphaScreen-based bioassays against the WT SARS-CoV-2 enzymes and in whole cell plaque-based bioassays to assess the compound's potential antiviral activity.

The IC_{50} value of (Z)-lespedezic acid **(17)** against the SARS-CoV-2 M^{pro} was found to be 90.91 µg/mL (265.59 µM) (n=1) and the IC_{50} in the spike RBD/ACE2 inhibition assay found to be IC_{50} = 0.0404 ± 0.0056 µg/mL (0.1180 ± 0.0164 µM) (n=2).

Additionally, (Z)-lespedezic acid **(17)** was found to inhibit the formation of virus-driven cytopathic effects, specifically in a dose-dependent fashion, against the Wuhan strain (Wild type), Beta and Delta variants of SARS-CoV-2 in the plaque-based bioassays (Figure 3.27). The IC_{50} was found to be 10.41 µM against the Wuhan variant, with no noticeable cytotoxicity observed in healthy Vero E6 cells at any tested concentration. The CC_{50} was thus found to be above 146.1 µM. Additionally, the IC_{50} value of (Z)-lespedezic acid **(17)** was found to be IC_{50} = 40.49 µM; CC_{50} > 146.1 µM and IC_{50} = 24.07 µM; CC_{50} > 146.1 µM; against the Beta and Delta variants, respectively (Figure 3.27). It should be noted that the positive control, remdesivir, displayed complete inhibition of viral-induced cytopathic effect at all concentrations tested (n=3), and as such, no IC_{50} could be calculated.

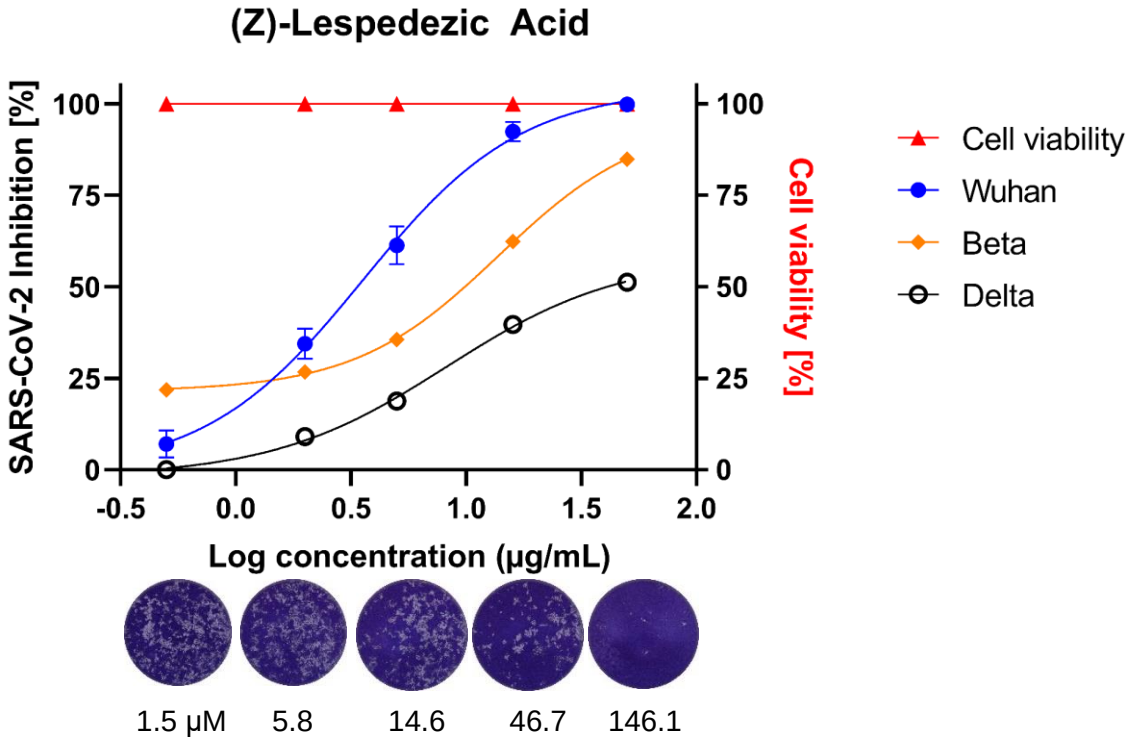

Figure 3.27: Antiviral and cytotoxic activity (▲) of (Z)-lespedezic acid **(17)** against SARS-CoV-2 (Wuhan (●), Delta var. (○) and Beta var. (♦)) in Vero E6 cells. Inhibition of SARS-CoV-2 infection (%) is represented in the legend, with the red triangles representing cell viability (%). Cytotoxicity data expressed as the mean of two replicates (n=2) and results analysed on a 95% confidence interval. Antiviral activity expressed as a single analysis (n=1) for the Delta and Beta variant as the mean of a single repeat (n=2) for activity against the Wuhan strain.

Based on the observed bioactivity in the enzymatic bioassays, it is presumed that (Z)-lespedezic acid **(17)** acts by inhibiting spike RBD/ACE2 interaction, thus preventing entry into the host cell. Although, the compound did not show as significant biological activity as the positive controls, i.e., REGN10933 and REGN10987 with IC_{50} = 1.7 nM and 10.6 nM, respectively, in RBD/ACE2 inhibition bioassays, nor in the plaque-based bioassays, the compound does show promise as a drug lead and may well be a key contributor of the activity observed *in vitro*, in combination with the other antiviral compounds.

3.3.9 Molecular docking

Molecular modelling was used to investigate further the mechanism of action of the bioactive compounds against the SARS-CoV-2 spike protein. The prepared ligands, viz., punicalin **(23)**, α/β-punicalagin **(18)** and (Z)-lespedezic acid **(17)** and their various energy-minimised conformers, were docked using Glide XP [32] onto the selected SARS-CoV-2 spike protein crystal structure (6LZG), centred around the spike-ACE2 interacting residues, viz., Q493, Q498, N501, F486, K417, and F456 [31].

Suitable interactions and poses were observed for the ellagitannins and (Z)-lespedezic acid **(17)** within the RBD of the spike protein. A comparison of the compound's docking scores found β-punicalagin to have the best docking score, namely -9.217 kcal/mol. Additionally, α-punicalagin, punicalin **(23)** and (Z)-lespedezic acid **(17)** similarly also had good docking scores of -8.686 kcal/mol, -7.891 kcal/mol and -7.917 kcal/mol, respectively. Specifically, hydrogen bonds were found to be the key form of interaction with the ligand, of which the majority occurred with the ellagic acid moiety. Hydrogen bonds were observed to occur between the alcohol moieties of β-punicalagin and the Y449, Q493 and G496, Y453 residues. The proposed interaction between S494, N501 and β-punicalagin are unique in that they occur via bridging water molecules (Figure 3.28). These key interactions are predicted to inhibit interaction with the ACE2 receptor of the host cell and thus interfere with cell entry. The interaction made with N501 is particularly important as it is heavily involved in ACE2 attachment.

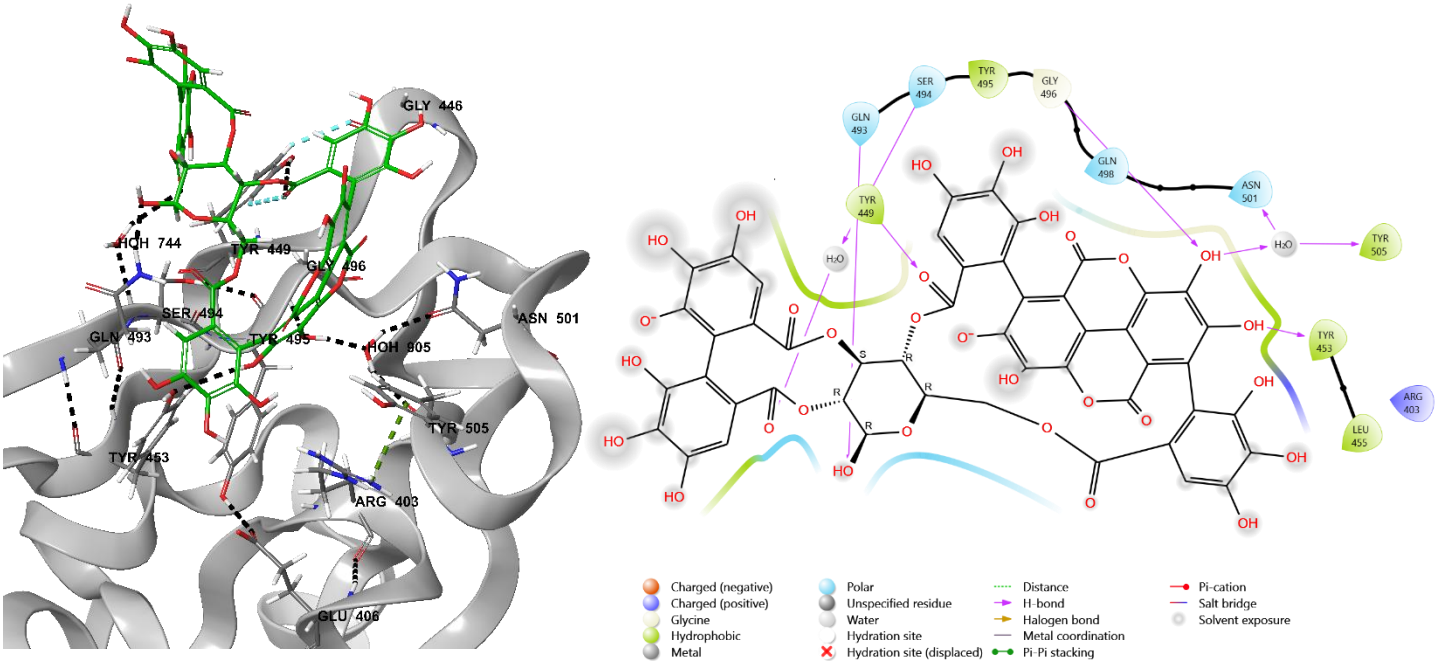

Figure 3.28: Binding pose and schematic representation of the interactions β-punicalagin **(18)** makes with surrounding residues of the SARS-CoV-2 spike enzyme (6LZG).

Unlike β-punicalagin, various bonds were hypothesised to enable the interaction of punicalin **(23)** and the RBD of the spike protein. In addition to the common hydrogen bonds, π-π stacking interactions and π-cation interactions were also noted. Hydrogen bonds were observed to occur between an alcohol moiety of punicalin **(23)** and the Y449 residue. Two additional interactions were noted to occur between the ellagic acid moiety and the Y505 residue by means of a water bridge. A π-π stacking interaction was noted between Y453 moiety and the ellagic acid moiety. The R403 residues were also found to partake in bonding with the ligand in a dual fashion, partaking in both a hydrogen bonding interaction and π-cation interaction due to its (+1) formal charge at pH 7 (Figure 3.29). These key interactions are predicted to inhibit interaction with the ACE2 receptor of the host cell, thus interfering with cell entry. It should be noted that although no direct interactions were observed with the key RBD residues, any stabilised ligand close to the spike RBD/ACE2 key interaction residues, would naturally cause a change in the secondary structure of the enzyme and likely interfere with attachment to the host ACE2 receptor.

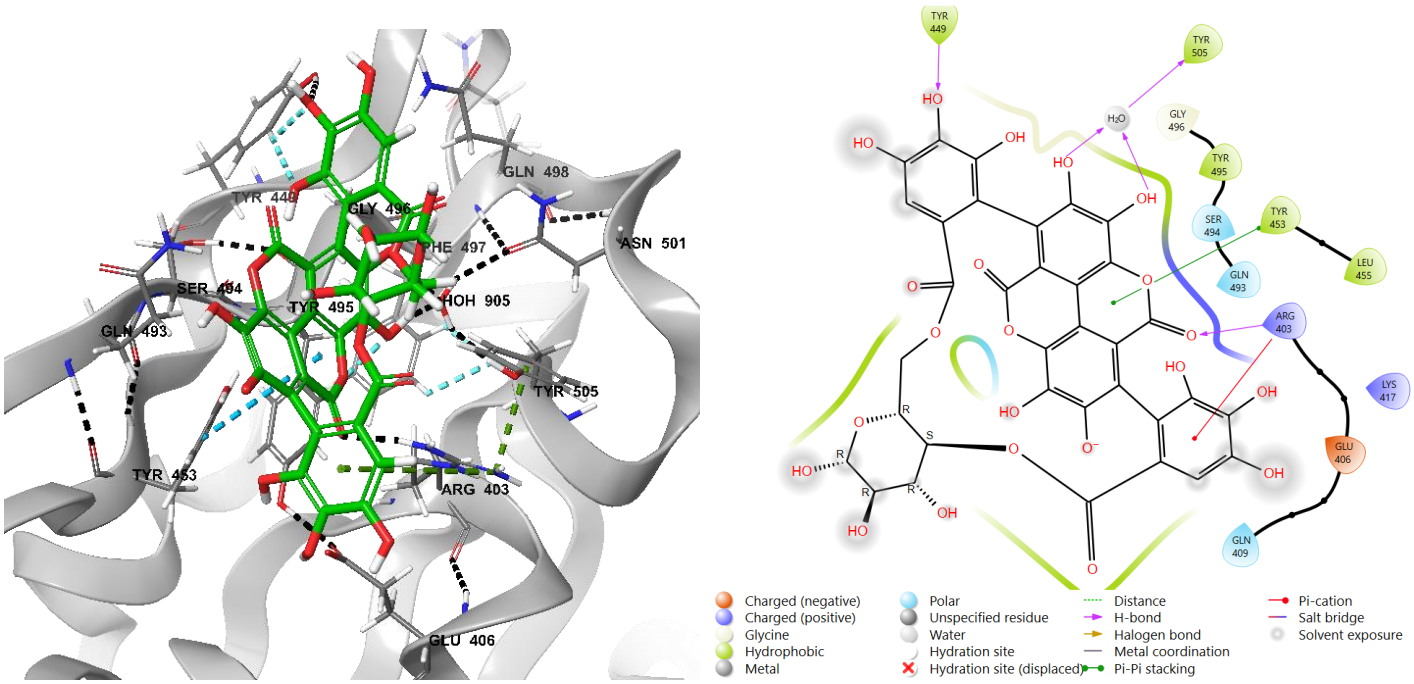

Figure 3.29: Binding pose and schematic representation of the interactions punicalin **(23)** makes with surrounding residues of the SARS-CoV-2 spike enzyme (6LZG).

Various bonds are hypothesised to enable the interaction of (Z)-lespedezic acid **(17)** and the RBD of the spike protein. In addition to the regular hydrogen bonding interactions, a π-cation interaction was also noted. Hydrogen bonds were observed to occur between the phenol moiety of (Z)-lespedezic acid **(17)** and the E406 residue. Additional interactions were noted to

occur between the glucose moiety and the Y453, Q493, S494, G496, and Y505 residue by means of a water bridge. The R403 residue was also found to partake in bonding via a π-cation interaction when the phenol moiety, due to R403's (+1) formal charge at pH 7 (Figure 3.30). These key interactions are predicted to inhibit interaction with the ACE2 receptor of the host cell, thus interfering with cell entry. It should be noted that although only 1 direct interaction was observed with one of the key RBD residues (Q493), any stabilised ligand close to the spike RBD/ACE2 key interaction residues would naturally cause a change in the secondary structure of enzyme and likely interfere with attachment to the host ACE2 receptor.

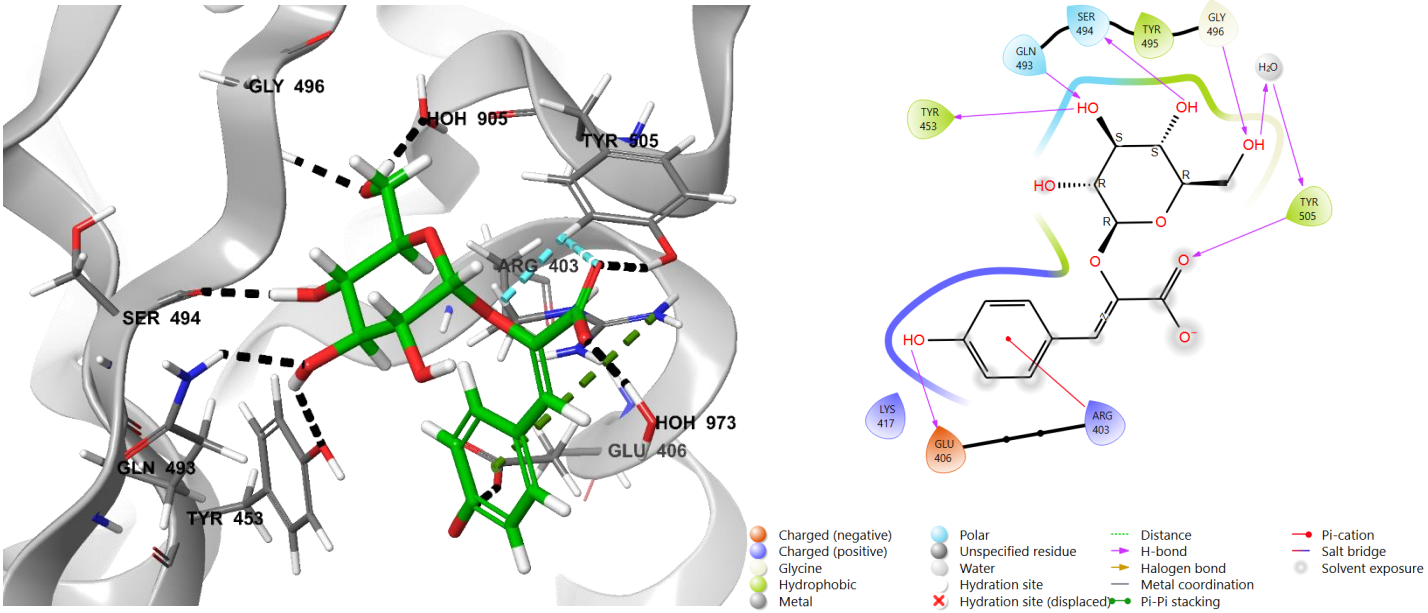

Figure 3.30: Binding pose and schematic representation of the interactions (Z)-lespedezic acid **(17)** makes with surrounding residues of the SARS-CoV-2 spike enzyme (6LZG).

Based on the observed molecular docking results, punicalin **(23),** α/β-punicalagin **(18)** and (Z)-lespedezic acid **(17)** makes extensive interactions with residues in and around the spike protein's active site and could competitively inhibit binding to the ACE2 receptor. The main interacting residues and key residues making up the RBD of the spike protein are Q493, Q498, N501, F486, K417, and F456 [31]. These key amino acids form the spike RBD and are responsible for the strong interactions with the host ACE2 receptor. The importance of these residues and the binding pocket as a whole make this structure (and the interacting residues) a promising target in the hope of preventing viral entry. This location has previously been the target for *in silico* investigations described in the literature [62,63], with some research providing *in vitro* data of molecules presumed to act in this binding pocket [64]. The docking

results align well with the biological data observed against the virus, specifically, spike RBD/ACE2 interaction inhibition.

3.4 Conclusion

Despite new vaccines and treatments against SARS-CoV-2, the development of new variants could present additional catastrophic problems economically and in the world of health. This chapter highlights the advantages of using hyphenated analytical techniques in natural product chemistry to enable rapid identification of the bioactive compounds from natural products, an underdeveloped source of drug discovery. Despite natural products being a reliable resource in drug discovery, much research is done using purely *in silico* and computational screening methods, with little *in vitro* work done to substantiate the claims. The work presented follows a systematic screening of extracts through to the pure bioactive compounds by incorporating various hyphenated analytical techniques like ion mobility coupled mass spectrometry which provide an essential third dimension of separation, beneficial when dealing with complex samples like plant extracts.

Amongst other possible bioactive compounds present in the traditionally used plant, *G. perpensa* L., punicalin **(23)**, α/β-punicalagin **(18)** and (Z)-lespedezic acid **(17)** were found to be key compounds contributing to the observed biological activity of the plant extract and fractions. This report being the first to describe punicalin's **(23)** occurrence in the plant.

Although the ellagitannins were found to be in very low concentrations in the extract, clear activity was observed despite the sample's complexity due to the bioactive compound's biological potency. The mechanism of action of the ellagitannins and (Z)-lespedezic acid **(17)** was shown to likely be via inhibition of the spike RBD/ACE2 interaction, preventing the cellular entry of the virus.

The observed biological activity and polarity of the compounds provide credence to the plant's current traditional use and method of preparation. The results provide new hope for the investigation of natural product compounds and natural product chemistry in the probe for novel antiviral compounds against SARS-CoV-2. The compounds identified may serve as new antiviral drug leads against SARS-CoV-2, especially important in resource-limited regions.

3.5 References

1 F. K. Mammo, V. Mohanlall and F. O. Shode, *Gunnera perpensa* L.: A multi-use ethnomedicinal plant species in South Africa, *African J. Sci. Technol. Innov. Dev.*, 2017, **9**, 77–83.

2 A. Maroyi, From traditional usage to pharmacological evidence: systematic review of *Gunnera perpensa* L., *Evidence-Based Complement. Altern. Med.*, 2016, 2016:1720123

3 L. J. Mathibe, The strength of *Gunnera perpensa* 's "evidence of traditional use", *South African Fam. Pract.*, 2016, **58**, S39–S40.

4 L. Wanntorp and H. E. Wanntorp, The biogeography of *Gunnera* L.: Vicariance and dispersal, *J. Biogeogr.*, 2003, **30**, 979–987.

5 F. Khan, X. K. Peter, R. M. Mackenzie, L. Katsoulis, R. Gehring, O. Q. Munro, F. R. Van Heerden and S. E. Drewes, Venusol from *Gunnera perpensa*: Structural and activity studies, *Phytochemistry*, 2004, **65**, 1117–1121.

6 X. K. Peter, *Structure and synthesis of Gunnera perpensa secondary metabolites*, University of KwaZulu-Natal, 2007.

7 K. B. Brookes and M. F. Dutton, Bioactive components of the uteroactive medicinal plant, *Gunnera perpensa* (or ugobo), *S. Afr. J. Sci.*, 2007, **103**, 187–189.

8 S. E. Drewes, F. Khan, S. F. van Vuuren and A. M. Viljoen, Simple 1,4-benzoquinones with antibacterial activity from stems and leaves of *Gunnera perpensa*, *Phytochemistry*, 2005, **66**, 1812–1816.

9 M. B. C. Simelane, O. A. Lawal, T. G. Djarova and A. R. Opoku, In vitro antioxidant and cytotoxic activity of *Gunnera perpensa* L. (Gunneraceae) from South Africa, *J. Med. Plants Res.*, 2010, **4**, 2181–2188.

10 A. Hutchings and A. B. Scott, Alan Haxton. Lewis, Gillian. Bunningham, *Zulu medicinal plants : an inventory*, University of Natal Press, Pietermaritzburg, South Africa, 1996.

11 A. Moteetee and B.-E. van Wyk, Moteetee and van Wyk, 2011, *Bothalia*, 2011, **228**, 209–228.

12 L. Invernizzi, P. Moyo, J. Cassel, F. J. Isaacs, J. M. Salvino, L. J. Montaner, I. Tietjen and V. Maharaj, Use of hyphenated analytical techniques to identify the bioactive constituents of *Gunnera perpensa* L., a South African medicinal plant, which potently inhibit SARS-CoV-2 spike glycoprotein–host ACE2 binding, *Anal. Bioanal. Chem.*, 2022, **414**, 3971–3985.

13 F. Carnevale Neto, T. N. Clark, N. P. Lopes and R. G. Linington, Evaluation of ion mobility spectrometry for improving constitutional assignment in natural product Mixtures, *J. Nat. Prod.*, 2022, **85**, 519–529.

14 K. Masike, M. A. Stander and A. de Villiers, Recent applications of ion mobility spectrometry in natural product research, *J. Pharm. Biomed. Anal.*, 2021, **195**, 113846.

15 G. M. Bou-Assaf and A. G. Marshall, eds. D. J. Houde and S. A. B. T.-B. C. of P. in D. B. (Second E. Berkowitz, Elsevier, 2020, pp. 333–374.

16 W. W. Christie and X. Han, in *Oily Press Lipid Library Series*, eds. W. W. Christie and X. B. T.-L. A. (Fourth E. Han, Woodhead Publishing, 2012, pp. 277–303.

17 J. Ujma, D. Ropartz, K. Giles, K. Richardson, D. Langridge, J. Wildgoose, M. Green and S. Pringle, Cyclic ion mobility mass spectrometry distinguishes anomers and open-ring forms of pentasaccharides, *J. Am. Soc. Mass Spectrom.*, 2019, **30**, 1028–1037.

18 Z. Zhou, X. Shen, J. Tu and Z.-J. Zhu, Large-scale prediction of collision cross-section values for metabolites in ion mobility-mass spectrometry, *Anal. Chem.*, 2016, **88**, 11084–11091.

19 C. C. Thornburg, J. R. Britt, J. R. Evans, R. K. Akee, J. A. Whitt, S. K. Trinh, M. J. Harris, J. R. Thompson, T. L. Ewing, S. M. Shipley, P. G. Grothaus, D. J. Newman, J. P. Schneider, T. Grkovic and B. R. O'Keefe, NCI Program for natural product discovery: A publicly-accessible library of natural product fractions for high-throughput screening,

ACS Chem. Biol., 2018, **13**, 2484–2497.

20 D. W. G. Harron, Technical requirements for registration of pharmaceuticals for human use: The ICH process, in *The Textbook of Pharmaceutical Medicine*, 2013, pp. 447–460.

21 J. Lu, K. Ding and Q. Yuan, Determination of punicalagin isomers in pomegranate husk, *Chromatographia*, 2008, **68**, 303–306.

22 K. B. Ku, H. J. Shin, H. S. Kim, B.-T. Kim, S.-J. Kim and C. Kim, Repurposing screens of FDA-approved drugs identify 29 inhibitors of SARS-CoV-2, *J. Microbiol. Biotechnol.*, 2020, **30**, 1843–1853.

23 I. Tietjen, J. Cassel, E. T. Register, X. Y. Zhou, T. E. Messick, F. Keeney, L. D. Lu, K. D. Beattie, T. Rali, P. Tebas, H. C. J. Ertl, J. M. Salvino, R. A. Davis and L. J. Montaner, The natural stilbenoid (–)-hopeaphenol inhibits cellular entry of SARS-CoV-2 USA-WA1/2020, B.1.1.7, and B.1.351 Variants, *Antimicrob. Agents Chemother.*, 2021, **65**, e0077221

24 L. Urda, M. H. Kreuter, J. Drewe, G. Boonen, V. Butterweck and T. Klimkait, The Petasites hybridus CO2 Extract (Ze 339) Blocks SARS-CoV-2 replication in vitro, *Viruses*, 2022, **14**, 106

25 R. T. Eastman, J. S. Roth, K. R. Brimacombe, A. Simeonov, M. Shen, S. Patnaik and M. D. Hall, Remdesivir: A review of its discovery and development leading to emergency use authorization for treatment of COVID-19., *ACS Cent. Sci.*, 2020, **6**, 672–683.

26 J. C. Shelley, A. Cholleti, L. L. Frye, J. R. Greenwood, M. R. Timlin and M. Uchimaya, Epik: A software program for pKa prediction and protonation state generation for drug-like molecules, *J. Comput. Aided. Mol. Des.*, 2007, **21**, 681–691.

27 J. R. Greenwood, D. Calkins, A. P. Sullivan and J. C. Shelley, Towards the comprehensive, rapid, and accurate prediction of the favorable tautomeric states of drug-like molecules in aqueous solution, *J. Comput. Aided. Mol. Des.*, 2010, 24, 591–604.

28 G. Madhavi Sastry, M. Adzhigirey, T. Day, R. Annabhimoju and W. Sherman, Protein and ligand preparation: Parameters, protocols, and influence on virtual screening enrichments, *J. Comput. Aided. Mol. Des.*, 2013, **27**, 221–234.

29 M. P. Jacobson, D. L. Pincus, C. S. Rapp, T. J. F. Day, B. Honig, D. E. Shaw and R. A. Friesner, A hierarchical approach to all-atom protein loop prediction, *Proteins Struct. Funct. Genet.*, 2004, **55**, 351–367.

30 M. P. Jacobson, R. A. Friesner, Z. Xiang and B. Honig, On the role of the crystal environment in determining protein side-chain conformations, *J. Mol. Biol.*, 2002, **320**, 597–608.

31 B. Jawad, P. Adhikari, R. Podgornik and W.-Y. Ching, Key interacting residues between RBD of SARS-CoV-2 and ACE2 receptor: Combination of molecular dynamics simulation and density functional calculation, *J. Chem. Inf. Model.*, 2021, **61**, 4425–4441.

32 R. A. Friesner, R. B. Murphy, M. P. Repasky, L. L. Frye, J. R. Greenwood, T. A. Halgren, P. C. Sanschagrin and D. T. Mainz, Extra precision glide: Docking and scoring incorporating a model of hydrophobic enclosure for protein-ligand complexes, *J. Med. Chem.*, 2006, **49**, 6177–6196.

33 C. Gil, T. Ginex, I. Maestro, V. Nozal, L. Barrado-Gil, M. Á. Cuesta-Geijo, J. Urquiza, D. Ramírez, C. Alonso, N. E. Campillo and A. Martinez, COVID-19: Drug targets and potential treatments, *J. Med. Chem.*, 2020, **63**, 12359–12386.

34 N. Teixeira, P. Nabais, V. de Freitas, J. A. Lopes and M. J. Melo, In-depth phenolic characterization of iron gall inks by deconstructing representative Iberian recipes, *Sci. Rep.*, 2021, **11**, 1–11.

35 E. Sentandreu, M. Cerdán-Calero and J. M. Sendra, Phenolic profile characterization of pomegranate (*Punica granatum*) juice by high-performance liquid chromatography with diode array detection coupled to an electrospray ion trap mass analyzer, *J. Food*

Compos. Anal., 2013, **30**, 32–40.

36 F. J. Mininel, C. S. Leonardo Junior, L. G. Espanha, F. A. Resende, E. A. Varanda, C. Q. F. Leite, W. Vilegas and L. C. Dos Santos, Characterization and quantification of compounds in the hydroalcoholic extract of the leaves from *Terminalia catappa* Linn. (Combretaceae) and their mutagenic activity, *Evidence-based Complement. Altern. Med.*,2014, 2014:676902.

37 M. Abid, H. Yaich, S. Cheikhrouhou, I. Khemakhem, M. Bouaziz, H. Attia and M. A. Ayadi, Antioxidant properties and phenolic profile characterization by LC–MS/MS of selected Tunisian pomegranate peels, *J. Food Sci. Technol.*, 2017, **54**, 2890–2901.

38 J. P. Stanoeva, N. Peneva, M. Stefova and V. Gjamovski, Identification and quantification of phenolic compounds in pomegranate juices from eight macedonian cultivars, *Maced. J. Chem. Chem. Eng.*, 2019, **38**, 149–160.

39 P. Aguilar-Zárate, J. E. Wong-Paz, M. Michel, J. Buenrostro-Figueroa, H. R. Díaz, J. A. Ascacio, J. C. Contreras-Esquivel, G. Gutiérrez-Sánchez and C. N. Aguilar, Characterisation of pomegranate-husk polyphenols and semi-preparative fractionation of punicalagin, *Phytochem. Anal.*, 2017, **28**, 433–438.

40 V. Martino, J. Morales, J. J. Martínez-Irujo, M. Font, A. Monge and J. Coussio, Two ellagitannins from the leaves of *Terminalia triflora* with inhibitory activity on HIV-1 reverse transcriptase., *Phytother. Res.*, 2004, **18**, 667–669.

41 C. Liu, D. Cai, L. Zhang, W. Tang, R. Yan, H. Guo and X. Chen, Identification of hydrolyzable tannins (punicalagin, punicalin and geraniin) as novel inhibitors of hepatitis B virus covalently closed circular DNA., *Antiviral Res.*, 2016, **134**, 97–107.

42 B. U. Reddy, R. Mullick, A. Kumar, G. Sudha, N. Srinivasan and S. Das, Small molecule inhibitors of HCV replication from pomegranate., *Sci. Rep.*, 2014, **4**, 5411.

43 Y. Wang, H. Zhang, H. Liang and Q. Yuan, Purification, antioxidant activity and protein-precipitating capacity of punicalin from pomegranate husk, *Food Chem.*, 2013, **138**, 437–443.

44 A. El-Aguel, R. Pennisi, A. Smeriglio, I. Kallel, M. P. Tamburello, M. D'Arrigo, D. Barreca, A. Gargouri, D. Trombetta, G. Mandalari and M. T. Sciortino, *Punica granatum* peel and leaf extracts as promising strategies for HSV-1 treatment., *Viruses*, 2022, **14**, 2639.

45 G. Nonaka, I. Nishioka, M. Nishizawa, T. Yamagishi, Y. Kashiwada, G. E. Dutschman, A. J. Bodner, R. E. Kilkuskie, Y. C. Cheng and K. H. Lee, Anti-AIDS agents, 2: Inhibitory effects of tannins on HIV reverse transcriptase and HIV replication in H9 lymphocyte cells., *J. Nat. Prod.*, 1990, **53**, 587–595.

46 M. Haidari, M. Ali, S. 3rd Ward Casscells and M. Madjid, Pomegranate (*Punica granatum*) purified polyphenol extract inhibits influenza virus and has a synergistic effect with oseltamivir., *Phytomedicine*, 2009, **16**, 1127–1136.

47 J. Arunkumar and S. Rajarajan, Study on antiviral activities, drug-likeness and molecular docking of bioactive compounds of *Punica granatum* L. to Herpes simplex virus - 2 (HSV-2)., *Microb. Pathog.*, 2018, **118**, 301–309.

48 C. Gosset-Erard, M. Zhao, S. Lordel-Madeleine and S. Ennahar, Identification of punicalagin as the bioactive compound behind the antimicrobial activity of pomegranate (*Punica granatum* L.) peels., *Food Chem.*, 2021, **352**, 129396.

49 R. Du, L. Cooper, Z. Chen, H. Lee, L. Rong and Q. Cui, Discovery of chebulagic acid and punicalagin as novel allosteric inhibitors of SARS-CoV-2 3CLpro, *Antiviral Res.*, 2021, **190**, 105075.

50 U. A. Fischer, R. Carle and D. R. Kammerer, Identification and quantification of phenolic compounds from pomegranate (*Punica granatum* L.) peel, mesocarp, aril and differently produced juices by HPLC-DAD-ESI/MSn, *Food Chem.*, 2011, **127**, 807–821.

51 E. Puljula, G. Walton, M. J. Woodward and M. Karonen, Antimicrobial activities of ellagitannins against *Clostridiales perfringens*, *Escherichia coli*, *Lactobacillus plantarum* and *Staphylococcus aureus*, *Molecules*, 2020, **25**, 3714.

52 H. Shigemori, N. Sakai, E. Miyoshi, Y. Shizuri and S. Yamamura, Bioactive substances from *Lespedeza cuneata* L.G. Don and their biological activities, *Tetrahedron*, 1990, **46**, 383–394.
53 K. B. Brookes, *Chemical investigation of isihlambezo or traditional pregnancy-related medicines*, 2004.
54 E. Havinga and R. J. F. Nivard, Ultraviolet absorption spectra and stereochemical structure of plant growth substances of the cis cinnamic acid type and of stilboestrol, *Recl. des Trav. Chim. des Pays-Bas*, 1948, **67**, 846–854.
55 L. Viornery, C. Saliba, J. B. Daskiewicz, C. Bayet, G. Comte, B. Fenet, G. Gutierrez and D. Barron, Phenylpropanoids from *Umbilicus pendulinus*, *Chem. Pharm. Bull. (Tokyo).*, 2000, **48**, 1768–1770.
56 F. Lanucara, S. W. Holman, C. J. Gray and C. E. Eyers, The power of ion mobility-mass spectrometry for structural characterization and the study of conformational dynamics, *Nat. Chem.*, 2014, **6**, 281–294.
57 Z. Zhou, M. Luo, X. Chen, Y. Yin, X. Xiong, R. Wang and Z. J. Zhu, Ion mobility collision cross-section atlas for known and unknown metabolite annotation in untargeted metabolomics, *Nat. Commun.*, 2020, **11**, 1–13.
58 J. Goshawk, G. Barknowitz and M. Mccullagh, The development of a natural products library using ion - mobility enabled mass spectrometry, 2019.
59 K. Giles, J. Ujma, J. Wildgoose, S. Pringle, K. Richardson, D. Langridge and M. Green, A cyclic ion mobility-mass spectrometry system, *Anal. Chem.*, 2019, **91**, 8564–8573.
60 M. Darvishi, F. Rahimi and A. Talebi Bezmin Abadi, SARS-CoV-2 Lambda (C.37): An emerging variant of concern?, *Gene reports*, 2021, **25**, 101378.
61 K. Richard, C. Schonhofer, L. B. Giron, J. Rivera-Ortiz, S. Read, T. Kannan, N. N. Kinloch, A. Shahid, R. Feilcke, S. Wappler, P. Imming, M. Harris, Z. L. Brumme, M. A. Brockman, K. Mounzer, A. V Kossenkov, M. Abdel-Mohsen, K. Andrae-Marobela, L. J. Montaner and I. Tietjen, The African natural product knipholone anthrone and its analogue anthralin (dithranol) enhance HIV-1 latency reversal., *J. Biol. Chem.*, 2020, **295**, 14084–14099.
62 R. V. Chikhale, S. S. Gurav, R. B. Patil, S. K. Sinha, S. K. Prasad, A. Shakya, S. K. Shrivastava, N. S. Gurav and R. S. Prasad, Sars-cov-2 host entry and replication inhibitors from Indian ginseng: an in-silico approach, *J. Biomol. Struct. Dyn.*, 2021, **39**, 4510–4521.
63 O. Zarei, H. Kleine-Weber, M. Hoffmann and M. Hamzeh-Mivehroud, Development and evaluation of peptidomimetic compounds against SARS-CoV-2 spike protein: an in silico and in vitro study, *Mol. Inform.*, 2022, **41**, 2100231.
64 C. J. Day, B. Bailly, P. Guillon, L. Dirr, M. Von Itzstein, T. Haselhorst and P. Jennings, Multidisciplinary approaches identify compounds that bind to human ACE2 or SARS-CoV-2 spike protein as candidates to block SARS-CoV-2-ACE2 receptor interactions, *MBio*, 2021, **12**, 1–14.
65 T. Limpanuparb, C. Areekul, P. Montriwat and U. Rajchakit, Blue bottle experiment: learning chemistry without knowing the chemicals, *J. Chem. Educ.*, 2017, **94**, 730–737.

Chapter 4

Investigation of the hydroxylated lactone of siphonochilone as an antiviral agent against SARS-CoV-2

4.1 Background on *Siphonochilus aethiopicus* (African Ginger)

4.1.1 Geographical distribution, classification, phytochemistry and traditional use

Siphonochilus aethiopicus (Schweinf.) B.L. Burtt. lies amongst the most popular South African indigenous plants, revered greatly for its broad medicinal properties [1,2]. Known by many names across South Africa, African Ginger forms part of the ginger family, Zingiberaceae, and its presence is solely restricted to Africa, with its distribution stretching from Senegal in northwest Africa, to southern Africa where South Africa, Zimbabwe and Zambia are examples of a few countries home to the plant [3]. Due to its high popularity amongst traditional health practitioners, the plant is widely exploited, leading to a significant decline in naturally occurring plants [3]. Since 2006, the plant has been placed on the SANBI Red list (Critically Endangered) due to its dwindling numbers in South Africa. In South Africa, *S. aethiopicus* is currently only found in the region between the Limpopo Lowveld and Swaziland, and this is after current trends demonstrate its complete extinction in the KwaZulu-Natal province (SANBI) [4].

S. aethiopicus is a deciduous aromatic rhizomatous plant that flowers annually in the spring/summer months, producing purple and white flowers. Its leaves resemble the common ginger plant (*Zingiber officinale*), possessing similarly large, hairless, green leaves that grow directly from its cone-shaped rhizome [5]. The plant does not grow very tall during the summer before collapsing and going dormant in the winter, typically around May (Figure 4.1) [6].

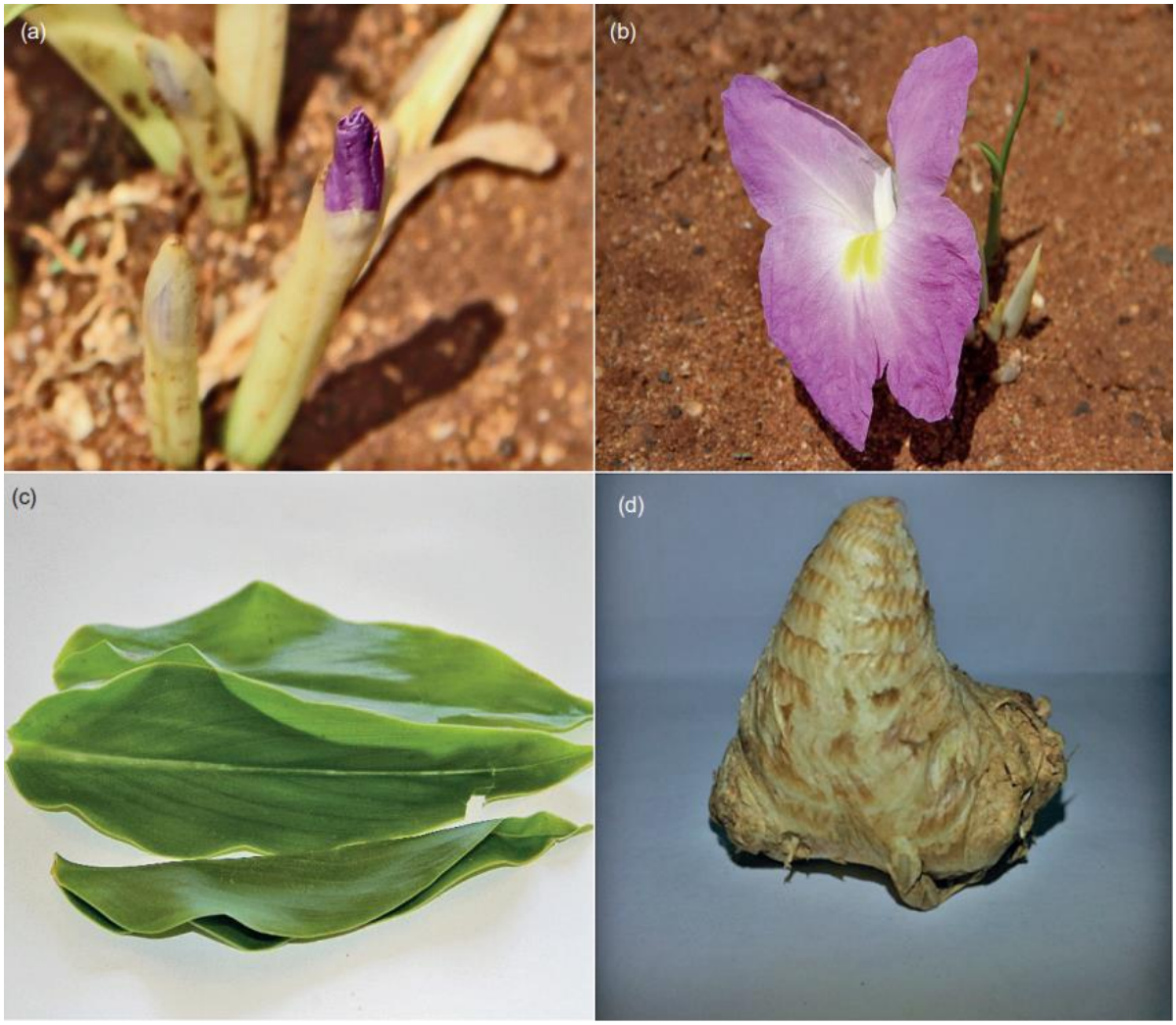

Figure 4.1: *S. aethiopicus* (Schweinf.) B.L. Burtt. (**A**) Flower bud, (**B**) flower, (**C**) leaves and (**D**) rhizome obtained (with permission: Copyright © Taylor & Francis Group) from Mokgehle et al. (2019) [7].

Like other members of the ginger family, *S. aethiopicus*, is widely sought after for its dense, aromatic rhizome, making its harvest a destructive practice which significantly influences its already low population numbers [1,3].

The plant, particularly the rhizome and root, are used throughout Africa as a traditional medicine, with a reportedly broad range of uses [3]. Some notable uses by the traditional health practitioners in Southern Africa include uses for respiratory-related infections like coughs, colds, influenza, asthma and sinus issues [1]. The most popular means of administration of the roots and rhizomes being by hot or cold infusions, steaming and inhaling the vapours and chewing of the fresh roots and rhizomes [1,8]. According to Adebayo et al.

(2021), *S. aethiopicus* is similarly used in other parts of Africa where the plant is used for the treatment of stomach infections, diarrhoea, hysteria, female infertility, menstrual pain and even for parasitic infections like malaria and schistosomiasis [3].

A reasonable amount of research, including phytochemistry, has been conducted on the rhizomes and roots of the plant, mainly due to their popularity and extensive use amongst traditional health practitioners. The fresh rhizomes and roots are particularly aromatic when cut/crushed and have been reported to contain a vast range of phytochemicals, both volatile and non-volatile. These are primarily dominated by various terpenes, particularly sesquiterpenes, diterpenes and monoterpenes, many of which have been tested in different biological assays [2,3,9].

Some notable compounds referred to in literary works by Adebayo et al. (2021) include the furanoterpenoids (Figure 4.2): 4aαH-3,5α,8aβ-trimethyl-4,4a,9-tetrahydro-naphtho[2,3-b]-furan-8-one (siphonochilone) **(24)**; 9aβ-hydroxy-4aαH-3,5α,8aβ-trimethyl-4,4a,8a,9-tetrahydronaphtho-([2,3b]-dihydrofuran-2-one)-8-one (hydroxylated lactone of shiphonochilone (HLS), reported with relative stereochemistry) **(25)**; 4aαH-3,5α,8aβ-trimethyl-4,4a,8a,9-tetrahydronaphtho-([2,3b]-dihydrofuran-2-one)-8-one **(26)**; 4aαH-3,5α,8aβ-trimethyl-4,4a,8a-trihydronaphtho-([2,3b]-dihydrofuran-2-one)-8-one **(27)**; epi-curzerenone; furanodienone; 8(17),12E-labdadiene-15,16-dial; 15-hydroxy-8(17),12E-labdadiene-16-al; 16-oxo-8(17),12E-labdadiene-15-oic acid and the diarylheptanoids like 2,3-diacetoxy-7-(3",4"-dihydroxy-5"-methoxyphenyl)-1-(4'-hydroxy-3'-methoxyphenyl)-5-heptene [3].

The volatilome of the plant is highly complex, with a few major small volatile compounds tentatively identified by GC-MS analysis in a study by Noudogbessi et al. (2012). These included: curzerenone, intermedeol, palmitic acid, α-cadinol, β-pinene, α-humulene, caryophyllene oxide, tetradecanoate ethyl, methyl salicylate and geranyl octanoate [10]. Additionally, during a second study conducted by Naudé et al. (2016) researching the volatile organic compounds (VOC) present in the fresh roots and rhizomes of the plant, α-ocimene, ß-ocimene and eucalyptol (1,8-cineole) **(28)**, amongst others, were found to be additional major compounds in the plant (Figure 4.2). In the study, eucalyptol's presence was confirmed with the use of a standard and, interestingly, only found to occur in fresh rhizomes and roots [11].

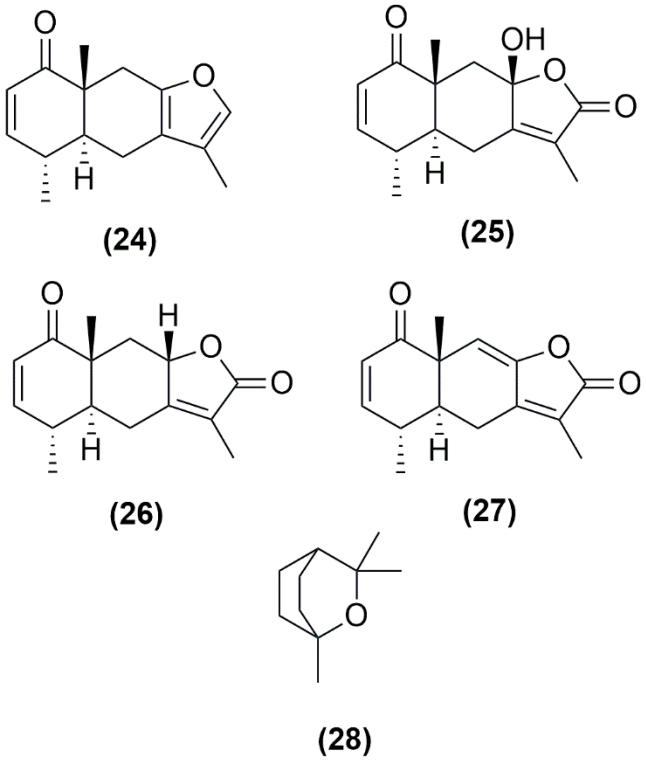

Figure 4.2: Structures of some of the main constituents of *S. aethiopicus* being (as published) 4aαH-3,5α,8aβ-trimethyl-4,4a,9-tetrahydro-naphtho[2,3-b]-furan-8-one (siphonochilone) **(24)**; 9aβ-hydroxy-4aαH-3,5α,8aβ-trimethyl-4,4a,8a,9-tetrahydronaphtho-([2,3b]-dihydrofuran-2-one)-8-one (hydroxylated lactone of shiphonochilone (HLS), reported with relative stereochemistry) **(25)**; 4aαH-3,5α,8aβ-trimethyl-4,4a,8a,9-tetrahydronaphtho-([2,3b]-dihydrofuran-2-one)-8-one **(26)**; 4aαH-3,5α,8aβ-trimethyl-4,4a,8a-trihydronaphtho-([2,3b]-dihydrofuran-2-one)-8-one **(27)** and eucalyptol (1,8-cineole) **(28)**.

Extensive work has already been conducted on the plant and some of its compounds, where they were evaluated for biological activity against bacteria, fungi and against trypanosomiasis, including being screened for anti-inflammatory, anti-asthmatic, antioxidant and antimalarial properties [3,12].

Recent research conducted by Kruger (2019) found both siphonochilone **(24)** and HLS **(25)** to have significant antiviral activity against Influenza A, with minimal/no activity observed for the extract/essential oil [13]. However, little antiviral work had been conducted on the plant at the time of writing, with none reported for SARS-CoV-2.

4.1.2 Hydroxylated lactone of siphonochilone (HLS) and its reported bioactivity

One of the earlier reported compounds, the “hydroxylated lactone of siphonochilone” or HLS **(25)** was first reported by Lategan et al. (2009) [9]. Interestingly, HLS was initially thought to occur naturally in the plant and hence merely reported as an additional phytochemical. Only recently, new studies have shown that HLS may form post-harvest due to post-harvesting practices and storage conditions. This formation was described in a recent article by Zongwe et al. (2018) and observed again by Chunga et al. (2022). The authors predicted, utilising computational studies, that HLS **(25)** forms directly from the primary compound in the fresh plant material, siphonochilone **(24)**, by means of an auto-oxidation reaction [14,15].

Interest in the plant and compounds grew when both HLS **(25)** and siphonochilone **(24)** were found to be highly active against the Influenza A-type virus *in vitro*. In the study, siphonochilone was found to have an IC_{50} value of 20.97 µg/mL and HLS an IC_{50} value of 9.20 µg/mL, both of which compared well with the positive control, ribavirin, which was found to have an IC_{50} value of 2.16 µg/mL in viral cytopathic effect (CPE) bioassays [13]. Since both Influenza-A and the SARS-CoV-2 virus are enveloped ssRNA viruses, it was hypothesised that HLS **(25)** would similarly exhibit antiviral activity against SARS-CoV-2.

Interestingly, HLS **(25)** also possess other biological data, where it has been shown to act as an anti-plasmodial agent, active against both the D10 strain of the parasite with an IC_{50} value of 18.13 ± 1.56 µg/mL and against the K1 strain, with an IC_{50} value of 16.71 ± 1.75 µg/mL with no overt cytotoxicity observed [9].

4.2 Importance of correct storage and post-harvest practices

Post-harvesting practices, although often overlooked, play a fundamental role in preventing losses and ensuring a consistent, viable product with a long shelf life [16]. Amongst others, post-harvesting techniques like handling, drying, storage conditions, duration of storage and even the specific processing methods used, contribute to the overall quality and consistency within a product batch. Stringent, adequate, and most importantly, consistent post-harvest practices remain fundamental, not only to preserve outward appearances but also to preserve the chemical integrity of the product, i.e., its so-called chemical fingerprints, chemical constituents, and as a result, active ingredients [17]. Although the general post-harvest practices may appear consistent, small nuances in drying, storage time, and storage temperature may have a profound effect on the chemical integrity of the product, greatly influencing the concentration of various secondary metabolites. These effects are demonstrated experimentally in a few new research works [17–21].

Post-harvest practices can play a positive role, where an increase in the active compounds of interest is observed, as with the curing of cannabis [22] or a negative role, where active compound degradation is observed, leading to a low concentration of active compounds. A good example is the incorrect storage of common fruits, like bananas [23].

When evaluating these different post-harvest practices and their effects, stability studies and quality control can be performed experimentally and systematically, but it might also prove helpful to refer to the traditional preparation in order to gain further valuable information. An excellent example of how traditional knowledge may aid in determining optimal post-harvest practices is how *Sceletium tortuosum* is prepared traditionally compared to commercially. *S. tortuosum* is an indigenous South African plant used traditionally for its medicinal and psychoactive properties [24]. Traditional preparations of the plant by the KhoiSan people involve a lengthy preparation method, which involves crushing the plant material and storing it in canvas or skin bags over a period of a few days to allow it to ferment [25]. Compared chemically to a regular non-fermented sample, the fermented, traditionally prepared product yields more significant quantities of the bioactive compound, viz., mesenbrine, supporting the traditional means of preparation or post-harvest practices [26].

S. aethiopicus may be another example of how post-harvest practices influence the plant's chemical profile. Traditionally, fresh roots and rhizomes of *S. aethiopicus* are used for cold and flu symptoms, and typically administered by inhalation of the steam [3]. Interestingly, in work conducted by Naudé et al. (2016), the main volatile compound, eucalyptol **(28)** was primarily found only in the headspace of the fresh plant material, with conclusions made that the drying processes resulted in the loss of VOC like essential oils. The work furthermore illustrates the relevance of eucalyptol **(28)** as it directly links with the reported traditional use and reported efficacy of *S. aethiopicus* as a decongestant and eucalyptol itself having been shown to reduce mucus hypersecretion and asthma [11]. This does bring about an important question regarding the true active compound in the generic extractions performed by many scientists which primarily use dried and ground plant material.

Similar comparative work between fresh and dried *S. aethiopicus* rhizomes and roots was conducted by Kruger (2019), who similarly noted a stark difference in chemical composition between fresh and dried (aged) plant material. In the work, siphonochilone **(24)** and HLS **(25)** were of specific relevance, where HLS was noted to occur in high concentrations in aged plant material but very low in fresh plant material [13].

It is interesting to note that although it is claimed that fresh plant material is used traditionally, one cannot rule out the risk that fresh plant material could not indeed undergo changes in

chemical composition during the long journeys taken by traditional health practitioners from the point of harvest to the point of consumption, often in very harsh conditions.

In general, no grand conclusion can be drawn that any post-harvest practice would result in a loss of bioactivity since this is absolutely correlated and only true for a group of compounds, typically unstable to the post-harvest condition in question.

4.3 The role of synthetic chemistry in natural product drug discovery

Natural product chemistry remains one of the most valuable drug discovery approaches, however, it does not come without its challenges, many of which hamper its popularity amongst pharmaceutical and drug discovery researchers [27]. Despite newer technologies, challenges relating to sample complexity and the laborious process of identifying the bioactive compound/s amongst a surfeit of chemical entities, still exist. Additionally, the difficulty in obtaining sufficient quantities of the bioactive compound in order to conduct critical biological experiments and the additional challenge in obtaining sufficient quantities for the ultimate commercialisation of the compounds remains a significant limitation [28].

Synthetic or semi-synthetic production of natural product compounds is often used to overcome many of these limitations. Occasionally the entire natural product molecule (either as it occurs in the plant or a more active derivative) can be synthesised ab initio in a way which proves viable in the long term, the production of acetylsalicylic acid (aspirin) being a good example [29]. In this way, the synthetically produced drug overcomes many of the limitations experienced had the drug been isolated from natural products. Alternatively, pharmaceuticals can also be produced in a semi-synthetic manner, where a parent molecule is isolated from the plant before undergoing synthetic derivatisation, or modification, to produce the final commercial product. This process is often done to increase the drug's bioactivity or selectivity, allowing nature to build the complex stereoselective parent compound before final, and often simple, modifications are done.

While some commercially available drugs are still obtained on a large scale directly from plants, the majority of natural product-inspired drugs have moved beyond this and rely solely on synthetic/semi-synthetic production to overcome the limitations observed in natural product chemistry. Although this is not always possible or a viable option, especially when the natural product of interest is stereochemically complex and the synthetic reaction is time consuming, costly, dangerous or merely does not result in a high enough yield. Such is the case with morphine and its few opiate derivates, where the natural product-based pharmaceuticals are not synthesised but obtained commercially from the plant and, in this case, from the opium

poppy (*Papaver somniferum*). This is partly due to the relatively high concentration obtained from the plant, the compound's complexity and the difficulty in finding a viable, cost-effective synthetic pathway to successfully produce the compounds [30].

In comparison, a few well-known commercial drugs are produced by means of semi-synthesis, where a natural product precursor is used to produce the final product. This is typically done when the product possesses complex stereochemistry, and by using the naturally produced precursor would mitigate this issue. Well-known examples of natural product-derived commercial drugs that are semi-synthesised commercially include paclitaxel, the anticancer drug isolated from *Taxus brevifolia* as well as the very common antibiotic, penicillin [27].

Nonetheless, the connection between natural product chemistry and synthetic chemistry remains an all-important complementary coalition and an essential partnership in the upscale of products during commercialisation.

4.4 Materials and Methodology

4.4.1 Reagents and standards

The DCM, MeOH and FA analytical grade (AR) extraction solvents were purchased from Merck, South Africa (Merck, Darmstadt, Germany). The solvents used in the fractionation and HPLC purification, viz., the super purity HPLC grade MeOH and ACN were purchased from Romil-SpS™, Microsep, South Africa (Waterbeach, Cambridge, UK) and the EtOAc, methylene blue and GC-grade acetone from Sigma-Aldrich (Merck, Darmstadt, Germany).

4.4.2 Plant material

The plant material, consisting of the roots and rhizomes of *S. aethiopicus*, was obtained from the South Africa's Council for Scientific and Industrial Research (CSIR) in the form of a course ground powder (Batch nr: SNA/003). The plant material had been stored for >5 years at ambient room temperature in sealed packets.

4.4.3 Batch extraction

In order to obtain sufficient quantities of HLS **(25)** for screening against SARS-CoV-2, a batch extraction was conducted on old plant material (>5 years old) likely to contain HLS **(25)**. Dried, ground roots and rhizomes (70 g) were placed in 1 L Erlenmeyer flasks with DCM in a 10:1 ratio of solvent (mL) to plant material (g). The plant material was extracted overnight on a shaker bed. The solvent was subsequently decanted, and the plant material underwent a second round of extraction with 100% DCM overnight, at the same solvent-to-plant material

ratio. Thereafter, the 2 extract solutions were combined, filtered (using a Büchner funnel and Whatman No. 1 filter paper) and concentrated using a rotary evaporator. The concentrated extract was dried down to completion using an SP Genevac HT6 (Genevac Ltd., Ipswich, UK), whereafter the yield was noted, and the dried extract was stored at 4 °C prior to further processing and analysis.

4.4.4 Fractionation of *S. aethiopicus* extract

To produce a sample with a high concentration of HLS **(25)**, 2.0 g of the extract was fractionated using a C8 SPE cartridge and a Gilson GX-241 ASPEC® liquid handler fitted with a Verity® 4060 pump controlled with TRILUTION® software as described in Chapter 2, Section 2.2.4 with a modification to the solvent systems. In this case, 10 different eluent systems were used in series to elute fractions rich in compounds with similar polarity. The eluent systems ranged from highly polar to moderately non-polar in nature, namely: 95:5 (H_2O:MeOH); 90:10 (H_2O:MeOH); 80:20 (H_2O:MeOH); 70:30 (H_2O:MeOH); 60:40 (H_2O:MeOH); 50:50 (H_2O:MeOH); 40:60 (H_2O:MeOH); 30:70 (H_2O:MeOH); 20:80 (H_2O:MeOH) and 1:1 (ACN:MeOH). Ten fractions were generated, one for each eluent system and collected in separate collection vessels on a volume-based collection method. Due to the variation in eluent systems, the fractions ranged from highly polar (fraction 1) to moderately non-polar (fraction 10)(labelled as LI-1-56B to LI-1-56J). These fractions were dried in individually pre-weighed polytops using a Genevac HT6, their yields recorded, and samples stored at 4 °C until analysis was conducted.

4.4.5 HPLC-PDA-MS purification and isolation of HLS (25)

The 10 fractions generated by SPE fractionation and the semi-synthetic reaction mixture containing HLS (cf. Section 4.4.7) were prepared individually for HPLC-PDA-MS analysis by dissolving each sample in ACN before filtering with a 0.22 µm nylon filter to remove particles. The samples were prepared at a concentration of 5000 ppm and analysed in both ESI positive and ESI negative mode on a Waters chromatographic system equipped with a Waters photodiode array (PDA) detector (Model 2998) and ACQUITY QDa detector (Waters, Milford, MA, USA) with separation of compounds and method development performed on an analytical column (Xbridge® BEH analytical C18 OBD™ (4.6 x 150 mm, 5 µm)) before upscaling to preparative scale. A satisfactory chromatographic method was developed, which consisted of H_2O (0.1% FA), and ACN (0.1% FA) used as solvent A and solvent B, respectively. The stepwise chromatographic method ran as follows: an initial isocratic solvent hold at 80% solvent A (0-18 min) before a linear change (step) to 0% solvent A (18-19 min) followed by a

subsequent column washing (19-21 min) before returning to the initial starting conditions to re-equilibrate the column (21-25.5 min). A 1.1 mL/min flow rate and an injection volume of 5 µL was used.

After satisfactory method development and compound separation, the method was upscaled for separation on an Xbridge® Prep C18 OBD™ (19 × 250 mm, 5 µm) column with H_2O (0.1% FA) and ACN (0.1% FA) used as solvent A and solvent B, respectively. The 3 SPE samples (labelled as LI-1-56G to LI-1-56I) found to contain HLS **(25)** (544.16 mg), and the semi-synthetic HLS mixture (cf Section 4.4.7) identified through analytical scale analysis, were prepared for purification by preparing a concentrated solution of the fraction at ca. 300 000 ppm in ACN. The elution method was optimised as a stepwise method and was run as follows: an initial isocratic solvent hold at 80% solvent A (0-25 min) before a linear change (step) to 0% solvent A (25-26.7 min) followed by a subsequent column washing (26.7-30 min) before returning to the initial starting conditions to re-equilibrate the column (30-37 min). The solvent flow rate was 19 mL/min with an injection volume of 600 µL.

Based on the optimum MS ionisation mode, the QDa mass spectrometer was set to acquire in ESI positive mode, with data collection set from 150 Da to 850 Da. The source temperature was kept constant at 120 °C, with a probe temperature of 600 °C. The capillary voltage was set to 0.80 kV and the cone voltage to 30.00 V. The PDA detector settings were optimised as follows: a sampling rate of 10 points/sec, a UV scan range of 210-400 nm and a UV resolution of 2.4 nm.

A mass-to-charge-based collection method was used to trigger collection and was done by performing Selected Ion Recording (SIR) of *m/z* 263 $[M+H]^+$ of HLS **(25),** and collection triggered when a detector response of >1200000 was detected, i.e., minimum intensity threshold (MIT). Similarly, 'peak collection end' was set to trigger when the peak gradient fell below 95. Multiple injections were done, and the same chromatographic peak was collected in multiple collection tubes, which were later combined. The collated tubes containing the selected compound were dried in an SP Genevac HT6 and weighed prior to storing at 4 °C.

4.4.6 NMR analysis of HLS (25)

The naturally occurring HLS **(25)** (12.6 mg) was dissolved in 500 µL CD_2Cl_2 and analysed on a 400 MHz Bruker Advance III NMR spectrometer fitted with a Prodigy BBI probe. 1D and 2D were conducted at room temperature, i.e., 25 °C. The operating frequency for the ^1H and ^{13}C was 400.21 MHz and 100.63 MHz, respectively. All chemical shifts are reported in ppm (δ-

scale), with coupling constants "*J* ", reported in Hertz (Hz). Trace protons from the deuterated solvent were used to calibrate the resulting spectra, i.e., 5.32 ppm for CD_2Cl_2.

4.4.7 Semi-synthetic conversion of siphonochilone (24) into HLS (25)

The oxidation reaction was carried out using siphonochilone **(24)** crystals available in the laboratory. These were previously obtained by steam distillation and identified by Kruger (2019) [13]. Quality control, by UPLC-HRMS analysis, was done to ensure that the crystals were still viable. The UPLC-HRMS analysis was done by preparing a 200 ppm solution of siphonochilone crystals **(24)** in ACN and analysing them on a UPLC-HRMS, similar to the analyses described in Chapter 3, Section 3.2.5.

A modified semi-synthetic method adapted from Xu et al. (2008) [31] was used where 180 mg of the siphonochilone **(24)** crystals were dissolved in 15 mL of distilled acetone. The solution was placed in a 50 mL round bottom flask before adding 5 mg of Methylene Blue powder (2 mol %). The solution was stirred until no solid particles were observed. The round bottom flask was capped, and the solution was placed in direct sunlight for 3 days. The solution was stirred semi-continuously with the intermittent release of the glass stopper to ensure no excessive pressure build-up. Thereafter, the solution was allowed to dry by evaporation before recording the yield and storing it at -40 °C to prevent further potential reactions. A single purification step was conducted using semipreparative HPLC, using the same method and instrumentation described in Section 4.4.5. The resulting sample was dried using an SP Genevac HT6 before recording the yields and storing at -40 °C.

4.4.8 UPLC-HRMS analysis of siphonochilone (24) and HLS (25)

The samples of siphonochilone **(24)** and HLS **(25)**, both natural and semi-synthetic, were prepared at a 50 ppm concentration in MeOH and analysed using the same instrumentation and MS source conditions described in Chapter 3, Section 3.2.5. The samples were analysed in both ESI positive and ESI negative ionisation modes. A minor modification was made regarding the solvent system used, where solvent A consisted of H_2O (0.1% FA) and MeOH (0.1% FA) as solvent B.

4.4.9 Single Crystal X-ray Diffraction (SCXRD) analysis

SCXRD analysis was conducted on both synthetic and naturally formed HLS **(25)**. These were prepared by dissolving the HLS **(25)** powder in 500 µL of MeOH before placing them in a polytop with a perforated lid and leaving them undisturbed at room temperature. After 2 days,

fine needle-like crystals appeared, and the polytop was sealed to avoid further solvent evaporation and ultimate dehydration of the crystals.

Multiple single crystals of HLS **(25)**, with different morphologies, were analysed in duplicate on a Rigaku XtaLAB Synergy-R diffractometer with diffraction measurements performed at 150 K with the use of an Oxford Cryogenics Cryostat. The instrument is fitted with a rotating-anode X-ray source (monochromated Cu Kα radiation (k = 1.54184 Å)) and a HyPix CCD detector. Absorption and data reduction were made using CrysAlis^{Pro} v. 1.171.40.39a. The analysed structures were solved using intrinsic phasing with SHELXT. Subsequent refinement was done using SHELXL-2014/7 and using the SHELXLE interface. To ensure chemical accuracy, all H atoms were placed in geometrically idealised positions, additionally constrained to ride on their parent atoms. Structural elucidation of the target structures was done using Olex software [32]. Refinement and collection parameters are described in Table 4.4 and Table 4.6. The X-ray crystallographic coordinates of HLS have been deposited at the Cambridge Crystallographic Data Centre (CCDC), with deposition numbers CCDC: 2250651.

4.4.10 Plaque-based bioassays of the sesquiterpenes

The compounds, HLS **(25)** and its precursor, siphonochilone **(24)**, were personally tested in viral plaque-based bioassays at the University of Basel, under the supervision of Prof. Thomas Klimkait. The bioassays were carried out as described in Chapter 2, Section 2.3.2. The bioassays were performed in a dose-dependent manner against clinical isolates of the Wuhan, Beta and Delta variants of the SARS-CoV-2 virus. Various concentrations of the compounds were prepared by serial dilution and ranged from 217-2.1 µM for siphonochilone and 190.6-1.9 µM for HLS. To ensure valid results, remdesivir was used as a positive control, being widely reported as an antiviral against SARS-CoV-2 *in vitro* [33–35], similarly being an FDA approved drug for use in severe SARS-CoV-2 cases [36]. Additionally, cytotoxicity testing was conducted in healthy Vero E6 cell lines to estimate the cytotoxic concentration (CC_{50}) and to calculate the selectivity index (CC_{50}/IC_{50}) of HLS **(25)**.

4.4.11 AlphaScreen binding assays and M^{pro} inhibition assays

HLS **(25)** was tested for antiviral activity against the SARS-CoV-2 spike and M^{pro} enzymes. These analyses were conducted by collaborators at the Wistar institute (USA) where HLS **(25)** was screened in AlphaScreen spike RBD/ACE2 inhibition assays and M^{pro} inhibition assays with methodology previously described in Tietjen et al (2021) and Invernizzi et al. (2022) and similarly described in Chapter 2, Section 2.3.1 [34,37]**.**

4.4.12 Molecular docking and molecular dynamic simulations of HLS (25)

Molecular modelling was performed using the Schrödinger software suite, release 2022-1 with the OPLS4 force field. The 3D ligand structure of HLS was obtained from the SCXRD analysis and further minimised using *ligprep*. Protonation states were predicted using Epic and predicted based on a pH of 7.0 ± 2.0 [38,39]. The protein structures of the SARS-CoV-2 helicase and papain-like protease (PLPro) 7NNG and 7TZJ, respectively, were obtained from the PDB and prepared using the *protein preparation wizard* [40], with missing side chains and loops filled with PRIME [41,42]. Protonation states were assigned, and energy minimisation was performed to ensure favourable constraints of the protein – performed by the software. Receptor grids were generated using the *receptor grid generation* feature of the software using the default settings. The grids were centred at the coordinates of the co-crystallised ligand molecule or inhibitor, and molecular docking was performed using *Glide* extra precision docking (XP) [43]. Default settings were used where all ligand structures were treated as 'flexible' with a minimum of 5 poses generated for each ligand. Docking poses were minimised with strain correction terms applied post-docking.

In order to assess the viability and stability of the generated complex poses, molecular dynamic simulations were performed at the CSIR's Centre for High-Performance Computing (CHPC) using Desmond [44]. Relevant systems were built for the complexes in orthorhombic box shapes. The edges were placed 10 Å from the protein, and the orthorhombic box was solvated using the TIP3P water model [45]. Sodium and chloride ions (0.15 M NaCl) were used to neutralise the system. The systems contained ca. 53 000 atoms and were minimised using the default relaxation protocol. Initially, short production/simulation runs were performed for 100 ns in order to observe the stability of the ligand within the binding site. The simulations were further inspected for equilibration and stability of the ligand by plotting RMSD plots. Systems where stabilisation occurred, and no further movement of the ligand was observed, were subjected to a further 100 ns run. NPT conditions were used using the Nose-Hoover thermostat of 310 K and particle-mesh Ewald electrostatics with a cut-off of 9 Å. Frames were recorded at intervals of 250 ps, and time-step calculations were performed every 2 fs. All simulations were analysed using the 'Simulation Interaction Diagram' module within the Schrödinger Suite.

4.4.13 ADMET properties

The ADMET properties of HLS and the positive control, remdesivir, were evaluated using *in silico* methods. SwissADME (http://www.swissadme.ch/index.php) [46] was used to predict physicochemical properties, lipophilicity, water-solubility, pharmacokinetics, drug-likeness,

medicinal chemistry properties, and bioavailability scores of the two molecules, viz., HLS **(25)** and remdesivir. This ADMET evaluation determined whether the compound holds potential as an oral medication.

4.5 Results and discussion

4.5.1 Extraction, fractionation and isolation of HLS

Sufficient quantities of HLS were obtained by the batch extraction of 65 g of aged plant material using DCM as the extraction solvent. An extract yield of 11.8% was obtained for the extraction process. Subsequent fractionation of the dried extract yielded 10 semi-pure fractions with a percentage yield ranging from 0.34% (Fraction 1) to 35.60% (Fraction 10), detailed in Table 4.1.

Based on previous research having suggested that HLS **(25)** forms post-harvest from a precursor molecule, siphonochilone [15], and the fact that HLS was shown to occur in high quantities in old plant material [13], isolation was conducted from old plant material rather than fresh plant material. HLS **(25)**, being a relatively non-polar compound and based on previous work conducted by Kruger 2019 [13], DCM was chosen as the extraction solvent. The percentage yield distribution observed in Table 4.1, confirms a more selective extraction of non-polar compounds, with greater masses observed in the later, more non-polar fractions.

Table 4.1: Mass and yield (%) of the extract, primary fractions and pure compound produced by fractionation of the *S. aethiopicus* DCM extract.

Sample	Mass (mg)	Yield (%w/w)
Dry plant material	65 000	N/A
Extract	7 700	11.8
Fraction 1	6.5	0.34*
Fraction 2	7.29	0.37*
Fraction 3	8.15	0.41*
Fraction 4	21.46	1.08*
Fraction 5	48.80	2.45*
Fraction 6	150.08	7.54*
Fraction 7	131.07	6.59*
Fraction 8	304.17	15.28*
Fraction 9	507.85	25.52*
Fraction 10	708.41	35.60*

*Based on 1.99 g of extract

Analytical scale HPLC-PDA-MS analysis of the 10 fractions showed the presence of a well-resolved peak (RT: 16.8 min) with a nominal mass matching that expected for HLS **(25)** in Fractions 6-8 (544.16 mg) (Figure 4.3). Two major peaks were observed on the mass spectrum, namely, *m/z* 245 $[M+H-H_2O]^+$ and *m/z* 263 $[M+H]^+$ and a single max UV absorbance at (λ_{max}) = 224 nm, which closely match the wavelength described in the literature for HLS (Figure 4.4) [13].

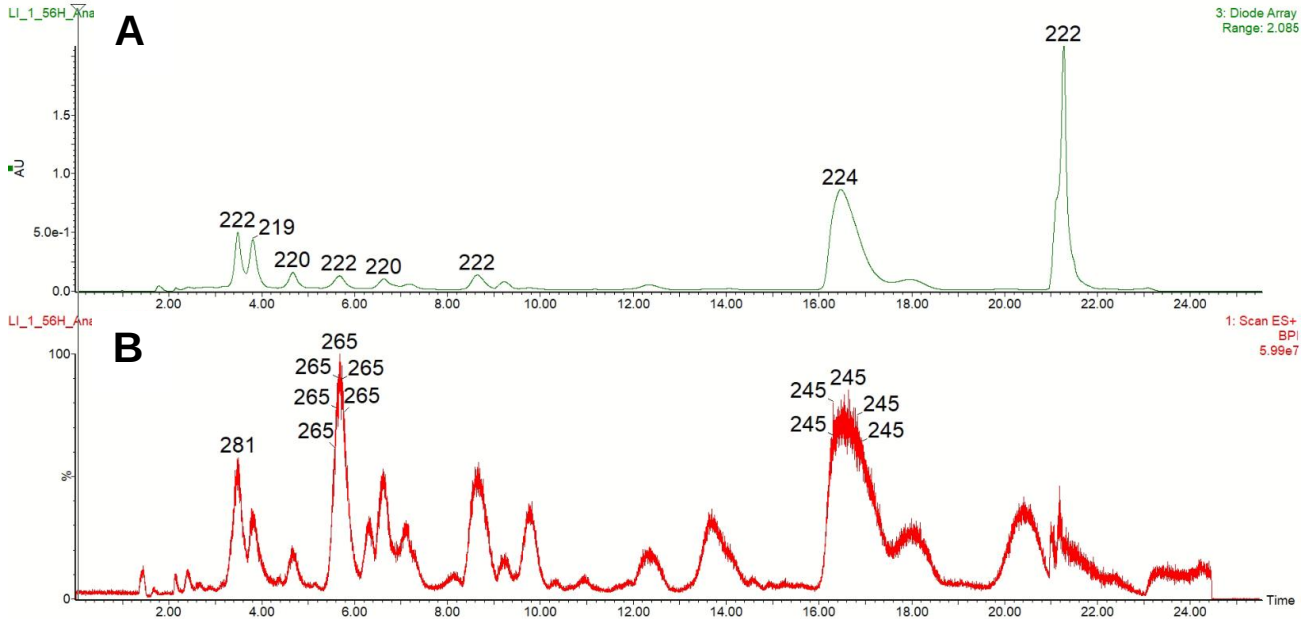

Figure 4.3: (**A**) Representative UV chromatogram and (**B**) BPI MS chromatogram of primary Fraction 9 of *S. aethiopicus* analysed on a C18 analytical column in ESI positive mode on a Waters HPLC-PDA-MS instrument.

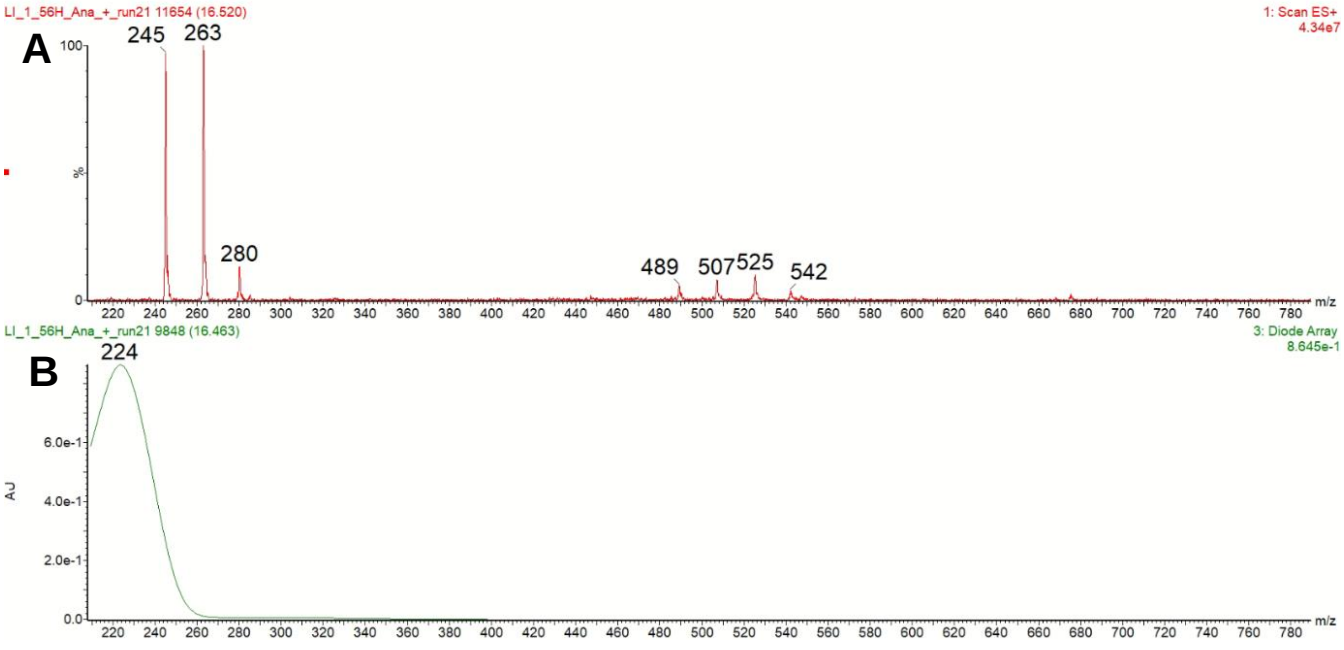

Figure 4.4: (**A**) Mass spectrum and (**B**) UV spectra of peak *m/z* 245 corresponding to HLS **(25)**, obtained from the Waters HPLC-PDA-MS instrument.

The analytical chromatographic method was upscaled for separation and isolation on a prep-HPLC-PDA-MS, where a large volume injection was performed on a preparatory column. The resulting MS chromatogram showed the presence of 7 major peaks (Figure 4.5). Of them, HLS, *m/z* 245 $[M+H-H_2O]^+$ was tentatively identified based on a similar *m/z* and λ_{max} as observed on the analytical scale analysis. Peak (RT: 21 min), *m/z* 245, was collected, dried and weighed. The resulting compound was found to be in the form of a pale-yellow powder and weighed 24.2 mg (1.22% yield based on a 1.99 g of extract).

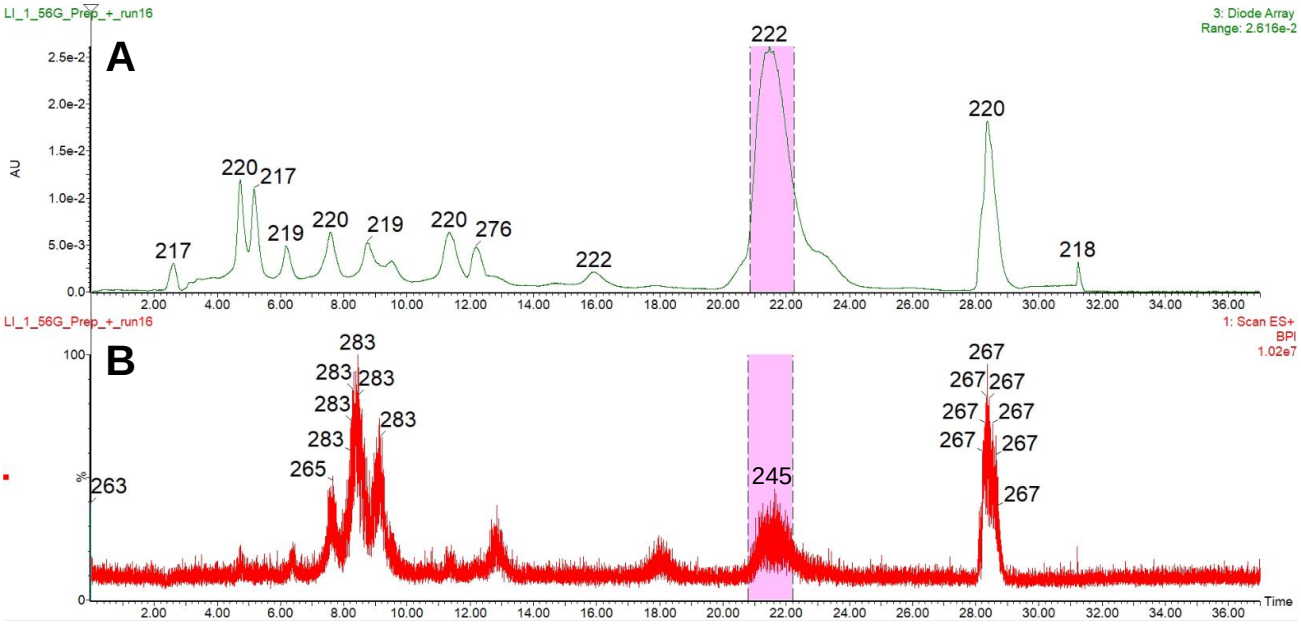

Figure 4.5: UV chromatogram (**A**) and BPI MS chromatogram (**B**) of the combined primary fractions of *S. aethiopicus* analysed in ESI positive mode on a Waters HPLC-PDA-MS instrument illustrating the collection of HLS *m/z* 245 $[M+H-H_2O]^+$.

4.5.2 Structure confirmation of HLS (25)

UPLC-HRMS analysis was conducted to acquire and confirm the accurate mass and fragmentation pattern of the isolated HLS **(25)**. A single major peak was observed in ESI positive ionisation mode for the isolated compound (Figure 4.6). The peak, corresponding to HLS **(25)**, appeared at *m/z* 245.1168 $[M+H-H_2O]^+$ (RT: 6.8 min) and was found to have a monoisotopic mass of 262.1198 Da with an accompanying mass error of -0.7 mDa, and a molecular formula of $C_{15}H_{18}O_4$ (calculated 262.1205 Da). The accurate mass, molecular formula and mass fragmentation pattern (Supplementary Data, Figure S4.1) correlated well with that expected for HLS (Table 4.2).

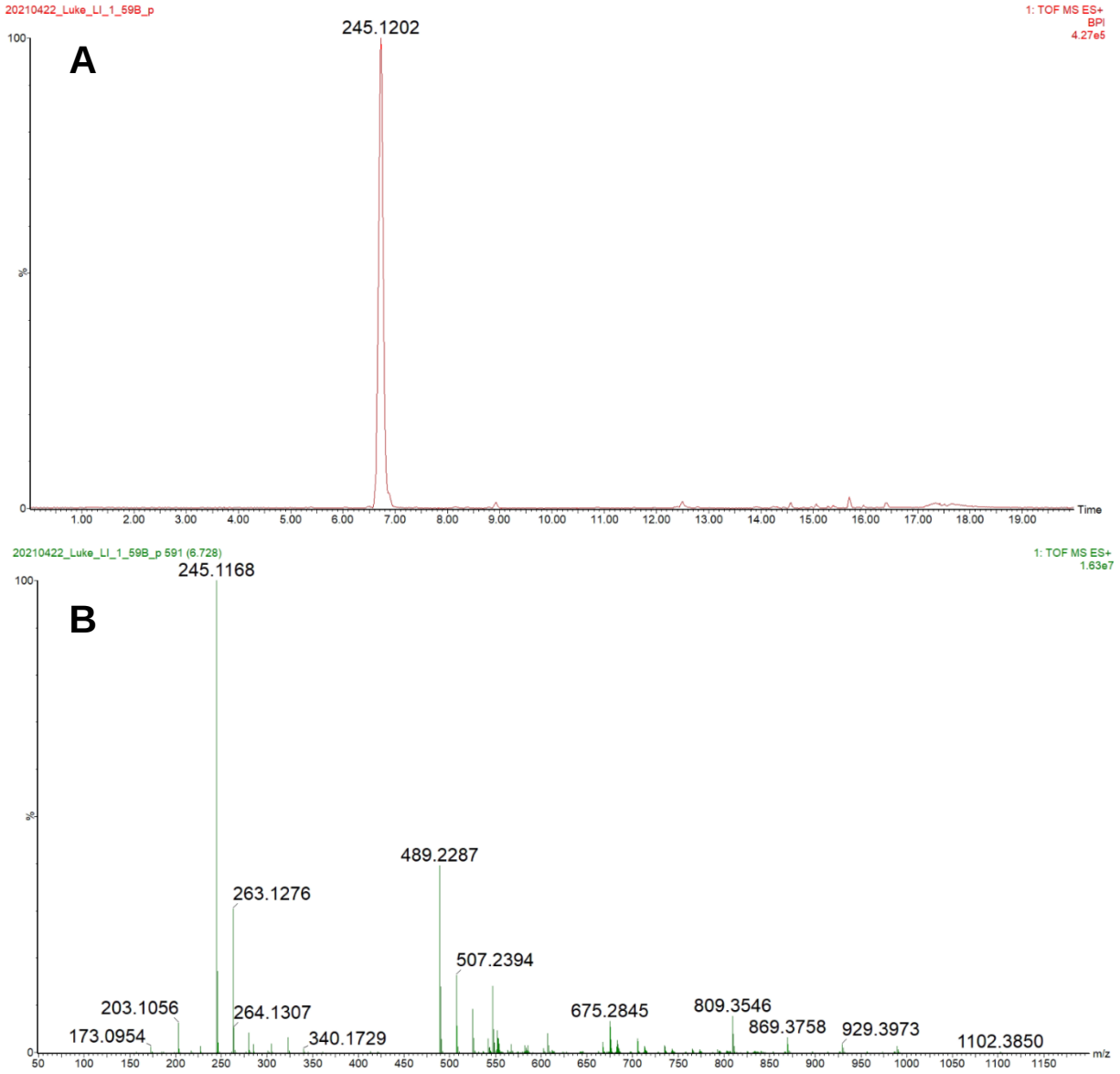

Figure 4.6: (**A**) UPLC-HRMS (BPI) generated chromatogram of the isolated HLS **(25)** in ESI positive mode and (**B**) the lockmass corrected low energy MS spectra of *m/z* 245.1202 (RT: 6.8 min).

Table 4.2: UPLC-HRMS data of HLS **(25)** isolated from aged *S. aethiopicus* plant material.

Compound	Observed *m/z*[a] (Da)(Mass error (mDa))	Observed quasi-molecular ion	Molecular formula	Calculated monoisotopic mass (Da)	RT[c] (min)	Observed fragment (*m/z*)(Mass error (mDa))
HLS (25)	245.1168 (-0.7)	$[M+H-H_2O]^+$	$C_{15}H_{18}O_4$	262.1205	6.8	117.0693 (-1.1) 141.0693 (-1.1) 203.1054 (-1.8)

[a]*m/z,* mass-to-charge ratio, reported as the quasi-molecular ion; [b]determined directly from the molecular formula; [c]*RT*, retention time.

1D and 2D NMR analyses were performed to confirm the identity of the compound (Supplementary Data, Figure S4.2-S4.7). ^{13}C NMR (Supplementary Data, Figure S4.3) analysis confirmed the presence of two carbonyl moieties at δ_C 203.5 (C-8) and δ_C 172.3, an oxygen-bearing carbon at δ_C 103.9 (C-9a), methylene groups at δ_C 24.6 (C-4) and δ_C 44.2 (C-9); methine group at δ_C 154.4 (C-6) and δ_C 126.3 (C-7); methyl group at δ_C 123.0 (C-3), δ_C 34.4 (C-5) and δ_C 45.4 (C-8a) and quaternary carbons at δ_C 45.4 (C-8a), δ_C 159.0 (C-3a) and δ_C 123.0 (C-3). The multiplicity of carbons was confirmed by HSQC-DEPT experiments (Supplementary Data, Figure S4.4). From the ^1H NMR spectra (Supplementary Data, Figure S4.2), the hydrogens belonging to the α,β-unsaturated carbonyl (olefinic hydrogens) were assigned to H-6 (1H, δ_H 6.67, dd, J = 10.07, 1.94 Hz) and H-7 (1H, δ_H 5.83, dd, J = 10.09, 2.77 Hz). The splitting pattern of H-5 (1H, δ_H 2.48, m) guided the determination of its position by coupling to 5-Me (3H, δ_H 1.22, d, J = 7.16) and H-4a (1H, δ_H1.56, m). The two additional methyl groups were observed at δ_H1.79 (3H, d, J = 1.31 Hz, 3-Me) and δ_H 1.33 (3H, s, 8a-Me).

The $2J_{CH}$, $3J_{CH}$ and $4J_{CH}$ bond correlations observed in the HMBC data confirmed the correct placement of the moieties (Supplementary Data, Figure S4.5). One olefinic proton (δ_H 5.83) was assigned at C-7 with HMBC correlations observed between C-5 and C-8a. A second olefinic proton (δ_H 6.67) was assigned at C-6 with HMBC correlations observed between C-4a and atoms at C-5, 5-Me, C-8, 8a-Me. The structure of the furanone ring was established based on the HMBC correlations between 3-Me (δ_H 1.79) and C-2 (δ_C 172.3); C-3 (δ_C 123.0) and C-3a (δ_C 159.0) respectively. Finally, the observed splitting pattern at δ_H 2.59 (1H, d, H-9_{ax}) and δ_H 1.63 (1H, d, H-9_{eq}) together with their COSY correlations, were assigned to the methylene group at C-9.

Additionally, a few key COSY correlations (Supplementary Data, Figure S4.6) also provided assurance and guided in the determination of the correct structure. The correlation being

between H-4_{ax} and 3-Me; H-5 and 5-Me, H-7 and H-5, H-6 and finally, the correlation between H-9_{eq} and 8a-Me.

Proton-bearing carbons were determined by HSQC analyses, with moiety arrangement determined by HMBC and COSY analyses (Table 4.3). NOESY was used to determine the relative configuration at C-4_{eq}, C-4a, 5-Me, 9-OH, C-9_{eq}, and C-9a (Figure 4.7). Important NOESY correlations were observed between C-9a and 9-OH, C-9_{eq}. Additional strong NOESY correlations were observed between C-4a and 5-Me, C-4_{eq} (Supplementary Data, Figure S4.7).

Table 4.3: ^{1}H, ^{13}C, HMBC and COSY data of HLS **(25)** analysed on a 400 MHz in CD_2Cl_2.

Position	$\delta^{1}H$ (ppm, *J* in Hz)	$\delta^{13}C$ (ppm)	HMBC (H→C)	COSY
2		172.3		
3		123.0		
3a		159.0		
4_{ax}	2.38 (1H, m)	24.6	C-3, C-3a, C-4a, C-5, C-8a	H-4a,3-Me, H-4_{eq}
4_{eq}	2.84 (1H, dd, *J* = 13.63, 3.73)		C-3, C-3a, C-4a, C-8a, C-9a	H-4a, H-4_{ax}
4a	1.56 (1H, m)	50.5	C-5, C-8, C-8a, 8a-Me	H-4_{ax}, H-4_{eq}
5	2.48 (1H, m)	34.4	C-4, 5-Me	5-Me, H-7, H-6
6	6.67 (1H, dd, *J* = 10.07, 1.94)	154.4	C-4a, C-5, 5-Me, C-8	H-7, H-5
7	5.83 (1H, dd, *J* = 10.09, 2.77)	126.3	C-5, C-8a	H-6, H-5
8		203.5		
8a		45.4		
9_{eq}	1.63 (1H, d, *J* = 14.21)	44.2	C-8, C-8a, 8a-Me, C-9a	H-9_{ax}, 8a-Me
9_{ax}	2.59 (1H, d, *J* = 14.41)		C-3a, C-4a, C-5, C-8a, 8a-Me, C-9a	H-9_{eq}
9a		103.9		
3-Me	1.79 (3H, d, *J* = 1.31)	8.6	C-2, C-3, C-3a, C-4, C-9a	H-4_{ax}
5-Me	1.22 (3H, d, *J* = 7.16)	18.5	C-4a, C-5, C-6	H-5
8a-Me	1.33 (3H, s)	17.1	C-4a, C-8, C-8a, C-9	H-9_{eq}
9a-OH	3.84 (1H, br s)			

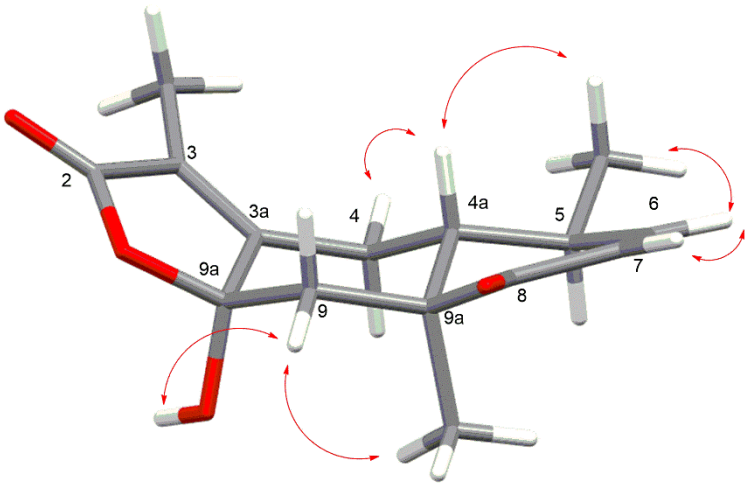

Figure 4.7: Selected NOE correlations for HLS **(25).**

The NMR data, together with the UPLC-HRMS data, viz., the monoisotopic mass, mass error and fragmentation pattern, provides conclusive evidence of the identity of the compound with the ^{1}H and ^{13}C NMR data of HLS **(25)** comparing well with that reported by Lategan et al. (2009) (Table 4.3) [9].

4.5.3 Single Crystal X-ray Diffraction

Single crystals, suitable for X-ray diffraction, were successfully grown of HLS **(25)** by evaporative crystallisation. Small, fine, translucent, needle-like crystals were obtained and successfully analysed by X-ray diffraction spectroscopy (Supplementary Data, Figure S4.8). The resulting crystal data and parameters are displayed in Figure 4.8 and Table 4.4, respectively. Molecules of HLS **(25)** were found to crystallise in an orthorhombic space group $P2_12_12_1$ with Z=4 (Z'=1). The absolute configuration of HLS **(25)** was obtained with the Flack parameter found to be 0.01(5) (Figure 4.8). Of particular note, the observed absolute configurations of the 4 chiral centres at positions C-5, C-4a, C-8a and C-9a were found to be of the (*S*) and (*R*) configuration for positions C-5 and C-4a, respectively and similarly, (*S*) and (*R*) for stereocenters C-8a and C-9a, respectively. The compound's decalin rings took on a puckered low energy configuration, as expected for non-aromatic cyclic rings, and can be seen in Figure 4.8B. No abnormal bond angles or bond lengths were noted (Table S4.1).

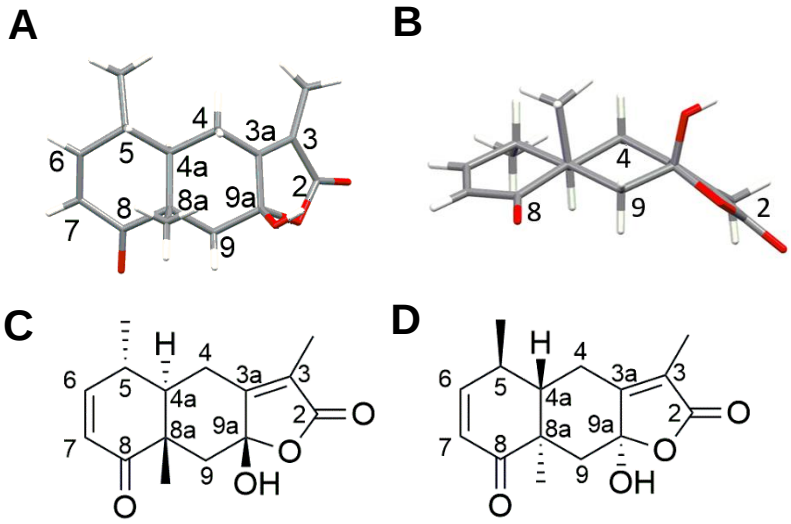

Figure 4.8: (**A**) SCXRD structure of HLS **(25)**, processed with Mercury v 2021.3.0. (**B**) Puckered configuration of the 2 fused ring structures of HLS. (**C**) Stick diagram illustrating the absolute configuration of HLS. (**D**) HLS structure and relative configuration as published originally [9].

Table 4.4: SCXRD refinement and collection parameters of HLS **(25).**

Compound	**HLS (25)**
Emp. Formula	$C_{15}H_{18}O_4$
CCDC Identifier	2250651
Molecular weight (g.mol^{-1})	262.28
Crystal description	Translucent needles
Crystal system	Orthorhombic
Space group	$P2_12_12_1$
a (Å)	7.68550
b (Å)	12.74480
c (Å)	13.50880
α (º)	90.00
β (º)	90.00
γ (º)	90.00
Volume (Å^3)	1323.19 (2)
Z	Z: 4 Z':1
F(000)	560.0
Independent refl.	2778 [R_{int} = 0.0268, R_{sigma} = 0.0150]
Completeness (%)	100
Data/Restr/Para	2778/0/176
Goodness of fit on F2	1.117
Final R1 indexes	0.0282
wR2 indices (all data)	0.0698
Largest diffraction peak and hole (e.Å^{-3})	0.16/-0.20
Flack parameter	0.01 (5)

Crystal packing was found to be facilitated by strong intermolecular hydrogen bonds (D-H...A (°) of 177.0°; 2.858 Å) between 9a-OH (H as donor) and the carbonyl (O) attached to C-8 as the hydrogen bond acceptor (Figure 4.9; Figure S4.9; Figure S4.10).

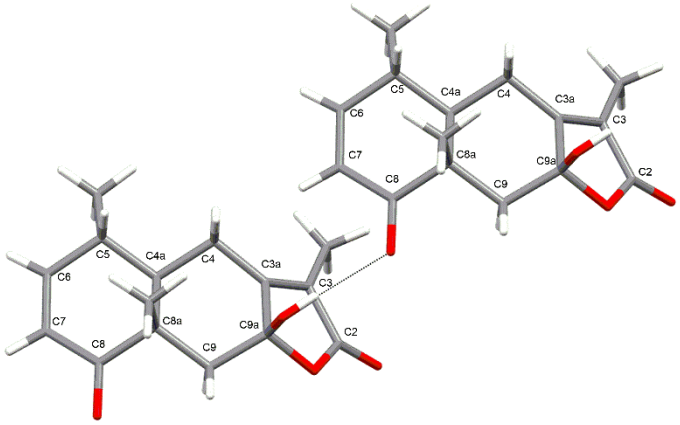

Figure 4.9: SCXRD structure of HLS **(25)**, illustrating the intermolecular hydrogen bond between 9a-OH and the carbonyl oxygen of C-8.

The observed structure of HLS **(25)** was found to be in accordance with the UPLC-HRMS data, viz., the monoisotopic mass, mass error and fragmentation pattern, including the described NMR data. Interestingly, although the relative configuration correlated with that observed in the NOE experiments and similarly matched that originally published by Lategan et al. (2009) (Figure 4.8D), the absolute configuration was found to be different. Particularly, the configuration at the four stereocenters, viz., C-5, C-4a, C-8a and C-9a were found to contradict of that previously published.

As demonstrated, SCXRD has the unique ability to determine the absolute configuration of a molecule [47] and thus overcome a significant shortcoming of traditional NMR spectroscopy. The absolute configuration determination is an integral step in pharmaceutical chemistry where slight variations in the molecule's absolute configuration, at even a single chiral centre, could mean the difference between efficacy and toxicity. Thalidomide, a widely used drug in the late 1950s, and its highly toxic (*S*)-enantiomeric isomer being a prime example, where the (*R*)-enantiomer had sedative effects, the (*S*)-enantiomer was teratogenic and caused over 200 cases of congenital disabilities [48].

4.5.4 Plaque-based bioassays of the sesquiterpenes

The sesquiterpenes, siphonochilone **(24)** and HLS **(25)** were evaluated in a dose-dependent manner for cytotoxicity and potential antiviral activity against the Wuhan, Beta and Delta variant of SARS-CoV-2 in whole-cell plaque-based bioassays at the University of Basel.

The siphonochilone **(24)** used was previously isolated by Kruger (2019) by means of steam distillation [13]. The compound was analysed by UPLC-HRMS, which showed the presence of a single major peak with an accurate mass matching that of siphonochilone (Figure S4.11; Figure S4.12) as described in Kruger (2019) [13].

In the biological assays, siphonochilone **(24)** was found to be severely cytotoxic at high concentrations (>21.7 µM), with close to 0% cell viability observed at concentrations above 21.7 µM (Figure 4.10). The CC_{50} was found to be CC_{50} = 19.5 µM with the IC_{50} value being incalculable via the four-parameter statistical model due to the severe cytotoxicity and lack of measurable activity. Although no accurate IC_{50} could be determined, it was observed that siphonochilone **(24)** showed an inhibition of 36.63% of the virus-induced CPE at its highest non-toxic concentration (0.94 µM) against the Wuhan variant, a 52.7% inhibition against the Beta variant and a 75.2% inhibition against the Delta SARS-CoV-2 variant. Since no accurate IC_{50} value could be calculated for siphonochilone **(24)** due to insufficient data points, no selectivity index could be calculated. However, based on the observed cytotoxicity and viral inhibition data, siphonochilone **(24)** displayed a narrow selectivity index. Interestingly, a similar type of cell necrosis is well documented in the literature and observed to occur with the administration of fresh *S. aethiopicus* extract, of which siphonochilone **(24)** is a major compound [2,49].

The positive control, remdesivir, displayed no cytotoxicity and demonstrated a 100% inhibition of viral-induced CPE at all tested concentrations.

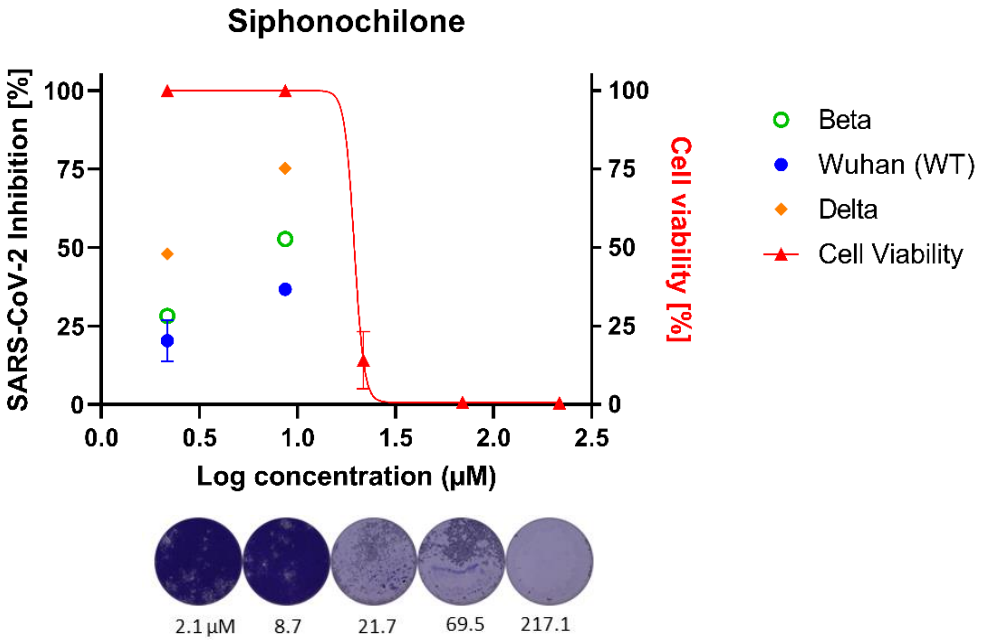

Figure 4.10: Antiviral and cytotoxic activity (▲) of siphonochilone against SARS-CoV-2 (Wuhan (●), Delta var. (♦) and Beta var. (○)) in Vero E6 cells. Inhibition of SARS-CoV-2 infection (%) is represented in the legend. Cytotoxicity data expressed as the mean of two replicates (n=2) and results analysed on a 95% confidence interval. Antiviral activity expressed as a single analysis (n=1) for the Delta and Beta variant as the mean of a single repeat (n=2) for activity against the Wuhan strain.

In contrast to siphonochilone **(24)**, HLS **(25)** was found to inhibit the formation of virus-driven cytopathic changes, specifically in a dose-dependent fashion, against the Wuhan strain (Wild type) of SARS-CoV-2 (Figure 4.11). The IC_{50} was found to be IC_{50} = 8.352 µM (goodness of fit (r^2) = 0.9924) with no noticeable cytotoxicity in healthy Vero E6 cells at any tested concentration. The CC_{50} was hence found to be > 191 µM and the selectivity index (SI) found to be > 23 against the Wuhan strain of the SARS-CoV-2 virus.

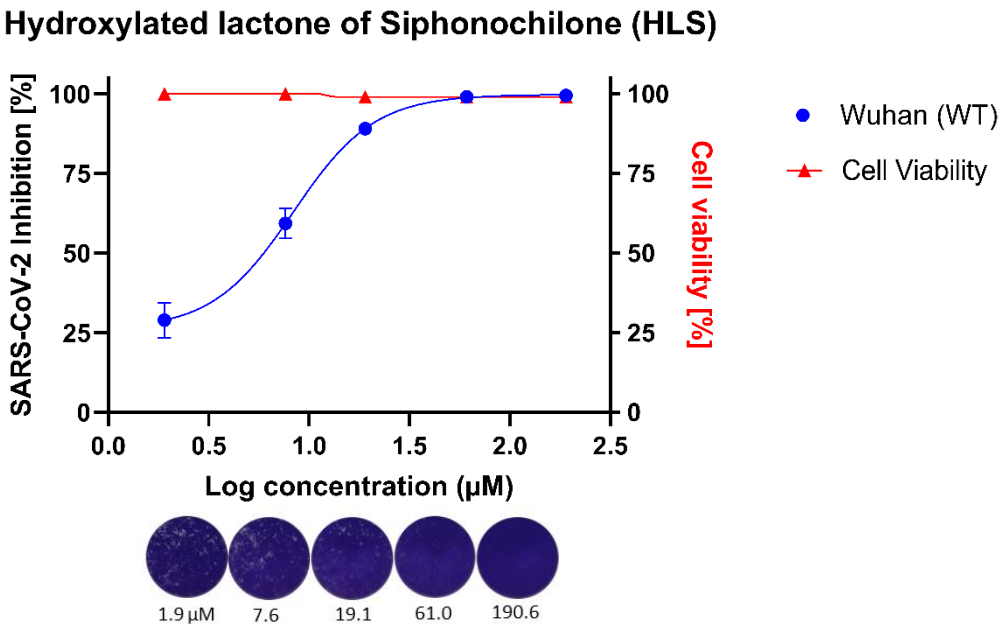

Figure 4.11: Antiviral and cytotoxic activity (▲) of HLS **(25)** against SARS-CoV-2 (Wuhan (●)) in Vero E6 cells. Inhibition of SARS-CoV-2 infection (%) is represented in the legend. Data expressed as the mean of two replicates and results analysed on a 95% confidence interval. HLS **(25)** goodness of fit (r^2) = 0.9924. IC_{50} = 8.352 µM; CC_{50} > 191 µM; SI > 23.

HLS **(25)** was similarly tested against the Delta and Beta variants of the SARS-CoV-2 virus. In comparison to the Wuhan strain of the virus, HLS **(25)** was found to have an IC_{50} value of IC_{50} = 11.45 µM; CC_{50} > 191 µM; SI > 17 against the Delta variant with a goodness of fit (r^2) = 0.9967 (Figure 4.12A) and IC_{50} = 15.26 µM; CC_{50} > 191 µM; SI > 12.5 against the Beta variant with a goodness of fit (r^2) = 0.9994 (Figure 4.12B). The positive control, remdesivir, displayed no cytotoxicity and demonstrated 100% inhibition of viral-induced CPE at all tested concentrations.

Overall, in stark contrast to siphonochilone **(24)**, HLS **(25)** showed no noticeable cytotoxicity at any tested concentration and presented high antiviral activity against the multiple variants of concern with similar bioactivity. HLS **(25)** presents consistent antiviral activity against the multiple variants of concern. This antiviral data is in agreement with the antiviral data observed against Influenza-A where an IC_{50} = 9.20 µg/mL was reported for HLS **(25)** [13].

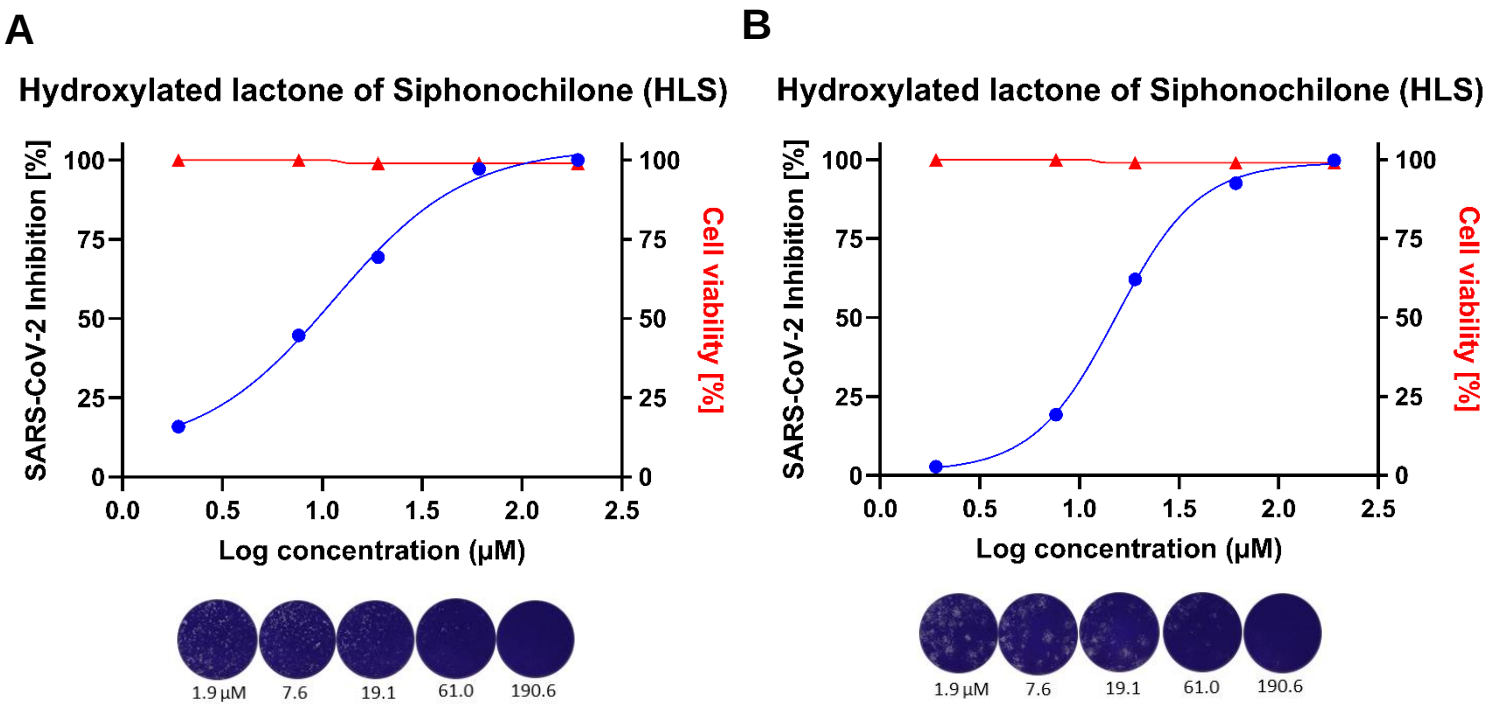

Figure 4.12: Antiviral activity of HLS **(25)** against SARS-CoV-2 ((**A**) Delta var. and (**B**) Beta var.) in Vero E6 cells. Inhibition of SARS-CoV-2 infection (%) is represented by the blue circles (●) and the cell viability (%) by the red triangles (▲). Data expressed as the mean of two replicates and results analysed on a 95% confidence interval. (**A**) Against the Delta variant: HLS goodness of fit (r^2) = 0.9967. IC_{50} = 11.45 µM; CC_{50} > 191 µM; SI > 17. (**B**) Against the Beta variant: HLS goodness of fit (r^2) = 0.9994. IC_{50} = 15.26 µM; CC_{50} > 191 µM; SI > 12.5.

Although the positive control, remdesivir, demonstrated 100% inhibition at all concentrations in our studies and the IC_{50} hence not calculated, the literature IC_{50} for remdesivir is reported to be between 1-11 µM [35]. Remdesivir is widely reported as an antiviral against SARS-CoV-2 *in vitro* and, similarly an FDA-approved drug for severe SARS-CoV-2 cases [33–36]. In comparison to remdesivir's reported IC_{50} value, the IC_{50} value of HLS **(25)** is comparable, with subsequent repeats warranted to provide a better estimate. Since the cells were preincubated with HLS **(25)** prior to infection, HLS **(25)** may provide some prophylactic activity, protecting the cells against infection. Interestingly, based on the consistent bioactivity observed been variants, it is hypothesised that HLS acts on a non-mutating and stable target of the SARS-CoV-2 virus. Most variant mutations that led to the development of the Beta and Delta variant were confined to the spike protein, so it is expected that HLS does not act as an entry inhibitor [50,51].

Based on the selectivity index and low cytotoxicity, HLS **(25)** is presumed to have a high therapeutic index or window of safety, an essential characteristic of good pharmaceuticals, allowing regular dosing without risk of adverse side effects [52]. Based on these favourable characteristics of HLS **(25)** and a significant increase in activity and substantial decrease in cytotoxicity observed between the reduced compound, siphonochilone **(24)**, and its oxidised derivative, HLS **(25)**, investigations into possible semi-synthetic means of and mechanism of action determination were warranted.

4.5.5 Semi-synthetic conversion of siphonochilone to HLS

The conversion of siphonochilone **(24)** to HLS **(25)** was carried out using methylene blue as a photosensitiser in the presence of sunlight and an oxygen-containing atmosphere via the proposed reaction illustrated in Figure 4.13.

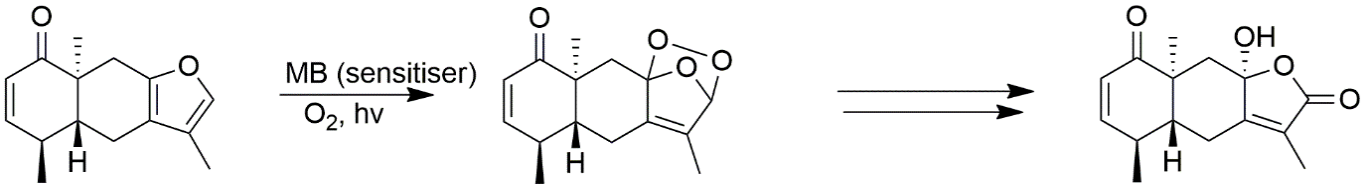

Figure 4.13: Scheme showing the formation of HLS **(25)** via a photo-diels-alder reaction of siphonochilone **(24)** with singlet oxygen generated from the photosensitiser methylene blue (MB).

The solution underwent a visually noticeable colour change over the course of the day, changing from an initial bright blue colour to a translucent solution. However, to confirm the success of the reaction, samples were taken from both the starting compound as well as the product mixture after reaction completion and analysed by UPLC-HRMS. The resulting chromatograms are presented in Figure 4.14. The chromatogram of the reactant, siphonochilone **(24),** showed the presence of a significant peak at RT: 11.5 min (Figure 4.14A). The compound's monoisotopic mass was found to be 230.1305 Da with an accompanying mass error of -0.2 mDa, and a molecular formula of $C_{15}H_{18}O_2$ (calculated 230.1307 Da) which corresponds to the observed *m/z* 231.1373 $[M+H]^+$ quasi-molecular ion of siphonochilone **(24)**. In addition to this, the fragmentation pattern and molecular formula correspond with that expected for siphonochilone **(24)** (Table 4.5) (Supplementary Data, Figure S4.12) [13].

In contrast to siphonochilone's chromatogram, the chromatograms generated by the product mixture (post-reaction) showed the disappearance of the siphonochilone **(24)** molecular ion peak (RT 11.5 min) and the appearance of multiple peaks matching the *m/z* observed for HLS **(25)**, viz., *m/z* 245.1183 (Figure 4.14 (B and C)). A distinct peak (*m/z* 245.1168) was noted at RT 6.8 min, which corresponded well with the peak noted for the HLS **(25)**, which was previously isolated and characterised using NMR and SCXRD analysis (Figure 4.14C). Comparison of the monoisotopic mass and fragmentation pattern of peak *m/z* 245.1168 (RT: 6.8 min) (Figure 4.14B) with the previously characterised HLS **(25)** showed minimal differences, highlighting the successful formation of HLS **(25)** (Table 4.5).

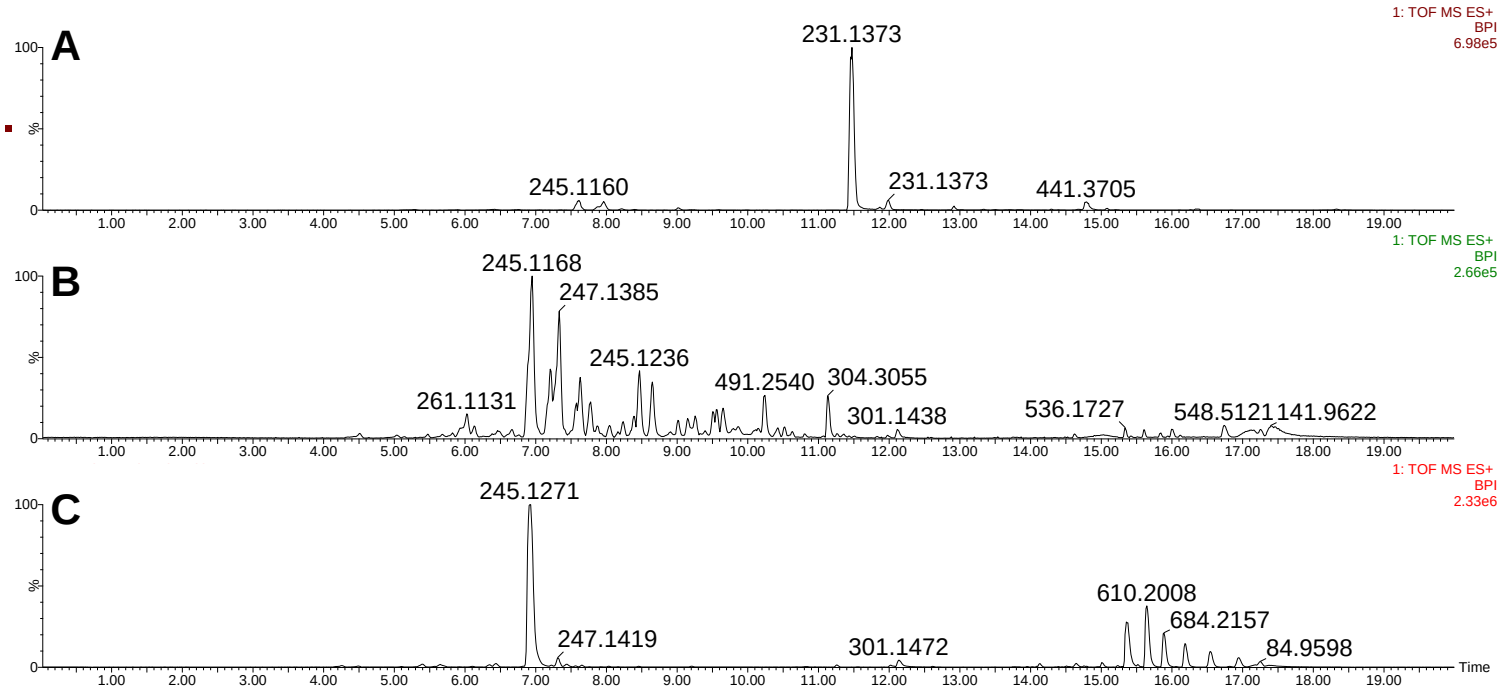

Figure 4.14: UPLC-HRMS results of (**A**) the siphonochilone-containing reactant solution, (**B**) the product mixture and (**C**) HLS **(25)** isolated (from plant material) and analysed on NMR. Similar retention times (RT: 6.8 min) and mass-to-charge are noted for HLS **(25)** (*m/z* 245.1271) for both the semi-synthetic version and that isolated from aged plant material.

Table 4.5: UPLC-HRMS data of the key compounds of interest, viz., siphonochilone **(24)** and HLS **(25)**, both the isolated and semi-synthetic.

Compound	Observed *m/z*[a] (Da)(Mass error (ppm))	Observed quasi-molecular ion	Molecular formula	Calculated monoisotopic mass (Da)[b]	RT[c] (min)	Observed fragment (*m/z*)(mass error (mDa))
Siphonochilone	231.1385 (-0.2)	$[M+H]^+$	$C_{15}H_{18}O_2$	230.1307	11.0	91.0548 (0.1) 109.0653 (0.2) 123.0815 (0.5) 135.0819 (0.9)
HLS (Identified with NMR/XRD)	245.1183 (0.7) 263.1283 (0.5)	$[M+H-H_2O]^+$ $[M+H]^+$	$C_{15}H_{18}O_4$	262.1205	6.8	91.0541 (1.4) 105.0722 (1.8) 117.0694 (-1.0) 135.0831 (2.1)
HLS (Semi-synthetic)	245.1178 (-1.3) 263.1283 (-0.8)	$[M+H-H_2O]^+$ $[M+H]^+$	$C_{15}H_{18}O_4$	262.1205	6.8	91.0541 (-1.5) 105.0722 (-1.5) 117.0694 (-1.5) 135.0831 (-1.4)

[a]*m/z,* mass-to-charge ratio, reported as the quasi-molecular ion; [b]Determined directly from molecular formula; [c]*RT*, Retention time

In order to assess the yield and correct stereoselective conversion of siphonochilone **(24)** (180 mg) of the reaction, prep-HPLC was used to isolate HLS **(25)** (*m/z* 245) prior to crystallisation and subsequent SCXRD analysis.

HPLC-PDA-MS chromatographic analysis of the mixture showed a few significant peaks similar to those observed in Figure 4.14B. Of note, compound *m/z* 245 had the same retention time (RT: 21.8 min) as that of the HLS **(25)** previously isolated. The resulting product was light yellow in colour and weighed 4.24 mg, equating in a 3.1% yield for the reaction.

The resulting product crystallised successfully by evaporative crystallisation and appeared as fine, translucent, needle-like crystals. The resulting crystal data and parameters are displayed in Table 4.6. Overall, the molecules were found to crystallise in an orthorhombic space group $P2_12_12_1$ with Z=4 (Z'=1). The absolute configuration of the compound was obtained with the Flack parameter found to be 0.07 (8). The compound's decalin rings took on a puckered low energy configuration, as expected and previously seen (cf. Figure 4.8). No abnormal bond angles or bond lengths were noted. The resulting structure confirms the correct identity and

absolute configuration of HLS **(25)** (Figure 4.15). Based on the observed chromatogram and Flack parameter, the resulting compound was of high purity with no racemic mixture formation.

Table 4.6: Crystal data and structure refinement parameters of the semi-synthetic version of HLS **(25)**.

Compound	**HLS (25)**
Emp. Formula	$C_{15}H_{18}O_4$
CCDC Identifier	2250651 (as for the natually occuring HLS **(25)**)
Molecular weight (g.mol^{-1})	262.29
Crystal description	Translucent needles
Crystal system	Orthorhombic
Space group	$P2_12_12_1$
a (Å)	6.67030
b (Å)	7.38960
c (Å)	27.8522
α (°)	90.00
β (°)	90.00
γ (°)	90.00
Volume (Å^3)	1372.86 (3)
Z	Z: 4 Z':1
F(000)	560.0
Independent refl.	2892 [R_{int} = 0.0324, R_{sigma} = 0.0179]
Completeness (%)	100
Data/Restr/Para	2892/0/177
Goodness of fit on F2	1.083
Final R1 indexes	0.0332
wR2 indices (all data)	0.0859
Largest diffraction peak and hole (e.Å^{-3})	0.15/-0.27
Flack parameter	0.07(8)

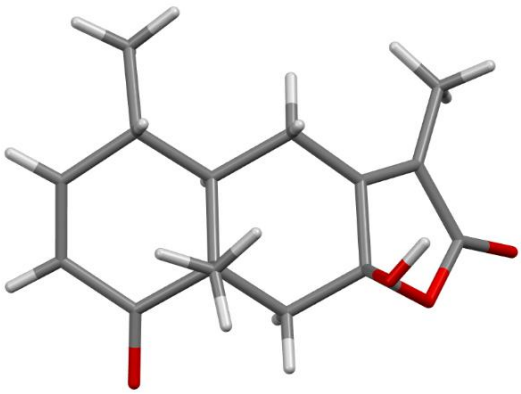

Figure 4.15: SCXRD structure of semi-synthetic HLS **(25)**, processed with Mercury v 2021.3.0.

The importance of developing a synthetic method to rapidly produce biologically active natural products cannot be underestimated. The success of a synthetic route greatly determines the drug's commercialising potential and viability. Naturally, this step is paramount when the only current source of the compound is aged plant material, as is the case with *S. aethiopicus* and HLS **(25)**.

As demonstrated, pure siphonochilone crystals were successfully oxidised with the use of oxidising agents. Weak oxidising agents were especially due to the presence of multiple alkene moieties in siphonochilone **(24)** and the need to prevent extreme modifications of the carbon backbone. This was also done to mimic the natural auto-oxidation and absence of strong oxidising agents, simulating the conditions described in the literature and investigating the hypothesis that siphonochilone is converted to HLS post-harvest, hypothesised by Zongwe et al. (2018) [15].

The reaction utilised a well-reported method of oxidation, namely, the use of photosensitisers in the presence of visible light and an oxygen-containing atmosphere. These types of molecules are extraordinary in their ability to convert inert molecular oxygen ($^3O_2$) into its singlet, highly reactive energy state ($^1O_2$) (Figure 4.16). Oxygen, in such a state, is significantly more electrophilic and possesses the ability to rapidly oxidise substrates like unsaturated carbon-carbon bonds, neutral nucleophiles and anions usually not affected by oxygen in its ground state. As further highlighted in research conducted by DeRosa et al. (2002), singlet state molecular oxygen is highly reactive and versatile as a synthetic reagent and is able to react with a wide range of compounds. Of note is its ability to partake in [4+2] cycloaddition

reactions where the singlet oxygen acts as a strong dienophile, closely mimicking a classical Diels-Alder reaction [53]. These reactions are well published in the literature [54,55].

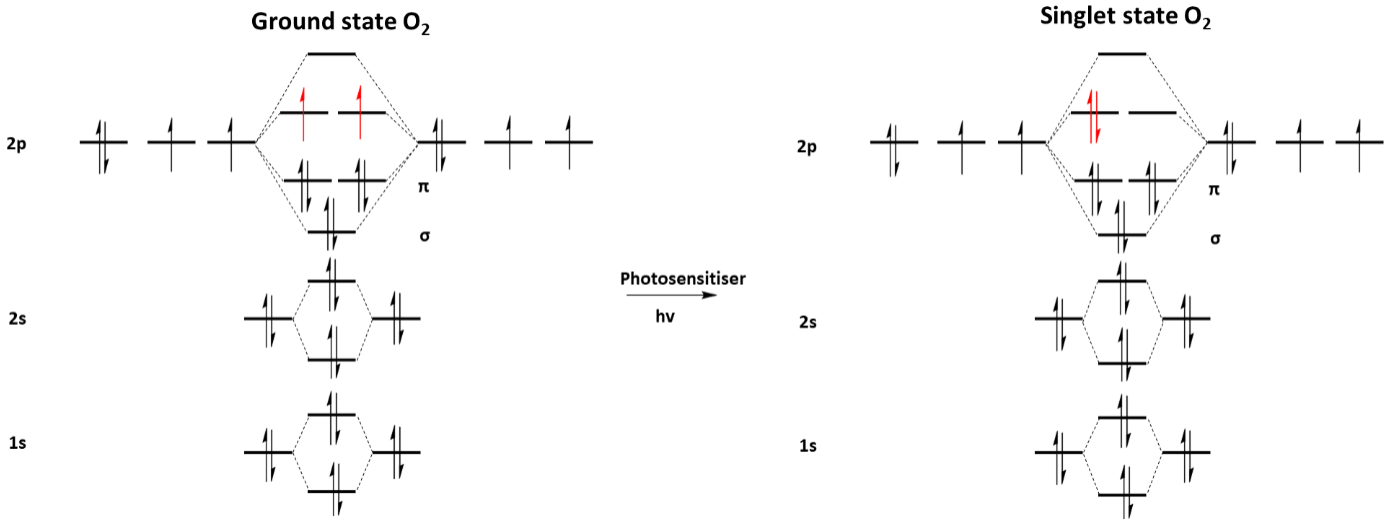

Figure 4.16: Diatomic orbitals of ground state molecular O_2 and its conversion to the high energy singlet state.

Multiple photosensitisers exist, ranging from organic dyes to even transition metal complexes. DeRosa et al. (2002) highlight that these photosensitisers are ranked by their singlet oxygen-generating ability and measured by their quantum yield [53].

The same study highlights the properties of an effective photosensitiser. These being: "(1) high absorption coefficient in the spectral region of the excitation light; (2) a triplet state of appropriate energy ($E_T \geq 95$ kJ mol^{-1}) to allow for efficient energy transfer to ground state oxygen; (3) high quantum yield of the triplet state ($\phi_T > 0.4$) and long triplet state lifetimes ($\tau_T > 1$ µs), since the efficiency of the photosensitiser is dependent on the photophysical properties of its lowest excited triplet state; and (4) high photostability [53]".

Of the more common photosensitisers, methylene blue (Figure 4.17), a phenothiazinium dye, possesses one of the more significant quantum yields of singlet oxygen, making it a favourable photosensitiser to use in synthetic chemistry [53,56].

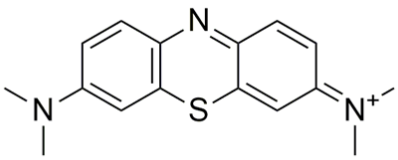

Figure 4.17: Structure of the photosensitiser methylene blue.

The unique chemical structure of siphonochilone **(24)**, with its unsaturated carbon-carbon bonds, make it a prime target for oxidation by singlet state oxygen ($^1O_2$). The oxidation reaction of siphonochilone and the singlet oxygen occurs via a photo-Diels Alder, i.e., a [4+2] cycloaddition reaction where the singlet oxygen acts as the dienophile. This sort of reaction is particularly valuable in that stereoselective conversion is accomplished, as noted by the observed Flack parameter of the semi-synthetic HLS **(25)** (cf. Table 4.6) and the closely corresponding chromatographic, mass spectrometry and crystallographic data observed for the synthetic and naturally occurring compound. Stereospecific reactions are a key trait of a Diels-Alder reaction. These findings support the hypothesis made by Zongwe et al. (2018), where HLS **(25)** forms post-harvest from siphonochilone [15].

Although methylene blue successfully produces singlet oxygen, one of its shortcomings, as with other photosensitisers, is that while the dye produces the reactive singlet oxygen species, the photosensitiser itself is not immune to reactions with the singlet oxygen, which is non-selective. This reaction destroys the conjugation of the photosensitiser compound and hence destroys its ability to form more singlet oxygen [53]. This explanation lends credence to the observed colour change observed where the solution changed from blue to colourless.

This study is not the first report where complex molecules like natural products are successfully oxidised using UV radiation and methylene blue, achieving a reasonable yield and reduced reaction time [57–60].

Notably, the singlet oxygen-producing property of methylene blue and mode of oxidation of siphonochilone **(24)** must not be confused with the typical oxidation reaction where methylene itself partakes in the reaction and acts as a hydrogen acceptor [31,61–63]. Although not observed in the conversion of siphonochilone **(24)** to HLS **(25)**, an excellent example of where methylene blue acts as an oxidising agent and partakes in the main reaction is the so-called “blue bottle” experiment in which a reducing agent, like glucose, undergoes oxidation non-selectively (Figure 4.18) [62].

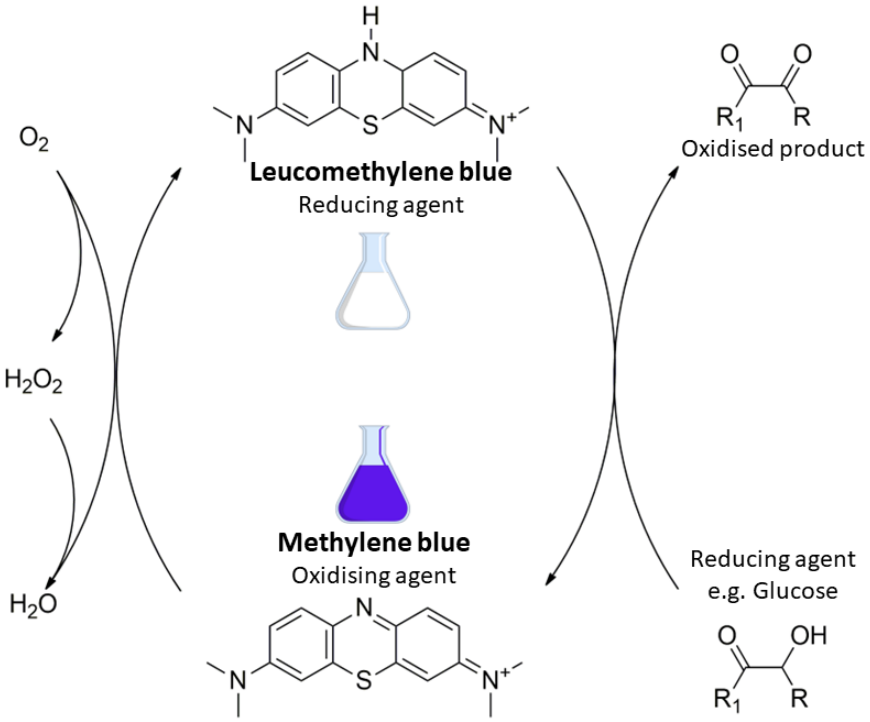

Figure 4.18: Blue bottle experiment representation adapted from Limpanuparb et. al. (2017) [62].

These findings highlight the versatility of methylene blue and singlet oxygen in synthetic chemistry and their ability to accelerate reactions that would only occur naturally over an extended period, which is especially valuable in drug discovery research.

4.5.6 Antiviral activity of semi-synthetic HLS

The semi-synthetically produced HLS **(25)** was screened in SARS-CoV-2 plaque-based bioassays and was found to inhibit the formation of virus-driven cytopathic changes, specifically in a dose-dependent fashion, against the Wuhan strain (Wild type), Beta and Delta variants of SARS-CoV-2 (Figure 4.19). The IC_{50} value was found to be IC_{50} = 8.734 µM against the Wuhan variant, with no noticeable cytotoxicity observed in healthy Vero E6 cells at any tested concentration. The CC_{50} was found to be above CC_{50} = 191 µM. Additionally, the IC_{50} value of HLS was found to be IC_{50} = 15.37 µM; CC_{50} > 191 µM and IC_{50} = 15.17 µM; CC_{50} > 191 µM; against the Beta and Delta variants, respectively (Figure 4.19).

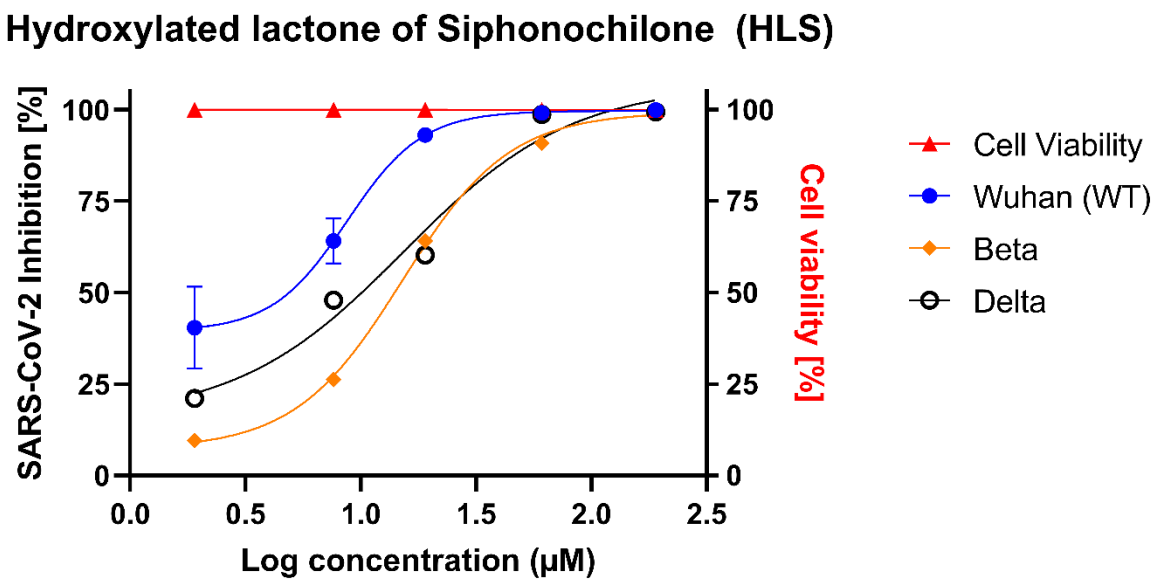

Figure 4.19: Antiviral and cytotoxic activity (▲) of the semi-synthetic HLS **(25)** against SARS-CoV-2 (Wuhan (●), Delta var. (○)and Beta var. (♦)) in Vero E6 cells. Inhibition of SARS-CoV-2 infection (%) is represented in the legend. Cytotoxicity data is expressed as the mean of two replicates (n=2), and results analysed on a 95% confidence interval. Antiviral activity expressed as a single analysis (n=1) for the Delta and Beta variant as the mean of a single repeat (n=2) for activity against the Wuhan strain.

The observed bioactivity data corresponds closely with that found for the naturally occurring HLS **(25)** isolated from the aged plant material (cf. Section 4.5.4, Figure 4.11 and Figure 4.12) with minimal deviations observed in the respective IC_{50} and CC_{50} values. These results demonstrate clear equivalence in antiviral activity between the two samples. This additional screening step is crucial in synthetic chemistry because biological activity could be altered due to the inadvertent formation of racemic mixtures or other isomers that are often produced as part of a synthetic reaction.

4.5.7 AlphaScreens and M^{pro} inhibition assays

The potential mechanism of action of HLS **(25)** was evaluated in spike RBD/ACE2 interaction inhibition (AlphaScreens) and M^{pro} inhibition bioassays.

HLS **(25)** was found to show very poor spike RBD/ACE2 inhibition, with its IC_{50} value found to be IC_{50} > 30 µg/mL (n=3). HLS **(25)** similarly showed very weak M^{pro} inhibition activity, with a mere 9.4% and 4.7% inhibition measured at 100 µg/mL and 10 µg/mL, respectively (Figure 4.20).

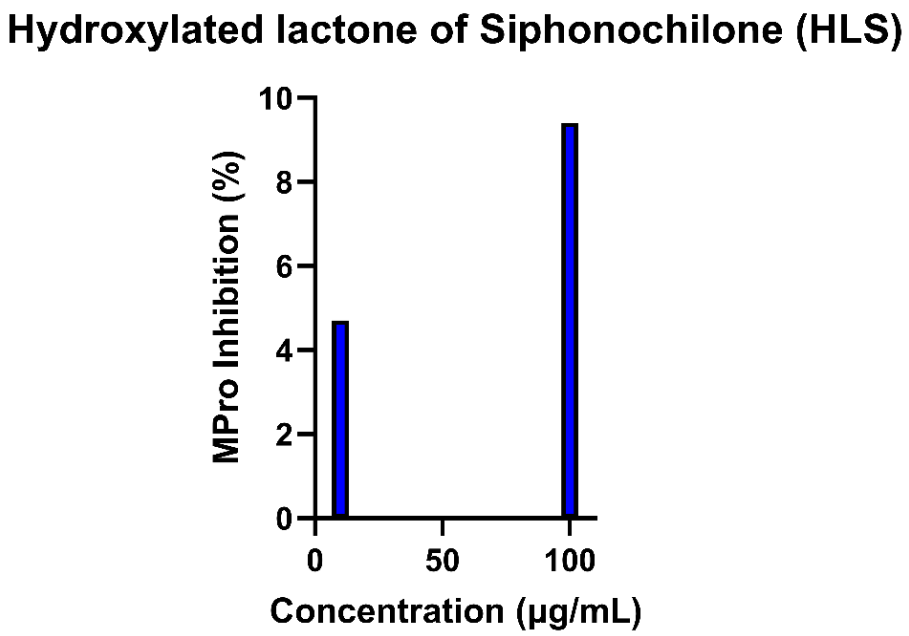

Figure 4.20: Antiviral activity of HLS **(25)** (n=3) against SARS-CoV-2 M^{pro} at 100 µg/mL and 10 µg/mL illustrating the small degree of M^{pro} inhibition.

Although HLS **(25)** was shown to have potent antiviral activity in whole-cell bioassays based on the observed enzymatic results, HLS **(25)** did not appear to act by inhibiting viral entry. Although these results do not provide information on the correct mechanism of action of the virus, it is relevant to note that the results corresponded well with the hypothesis made that HLS **(25)** acts on a non-mutating enzyme/structure of the SARS-CoV-2 virus where similar antiviral activity was noted against the various SARS-CoV-2 strains. These strains possess key fundamental mutations restricted to the spike protein [64].

It should be noted that although HLS **(25)** was also inactive against one of the fundamental and stable enzymes, the 3CL protease (M^{pro}), various other fundamental enzymes are also used by the virus and play a key role in its functioning. Of the various other viral enzymes, papain-like protease (PLpro) and helicase enzymes are good examples [65–67]. HLS's target

may indeed be the same in both the Influenza-A and SARS-CoV-2 RNA viruses, lending credence to its corresponding antiviral activity observed against the Influenza-A virus which was found to be 9.20 µg/mL in recent works by Kruger (2019) [13].

4.5.8 Molecular docking studies

4.5.8.1 SARS-CoV-2 NSP13 Helicase

Molecular modelling was used to investigate the possible mechanism of action of HLS **(25)** with SARS-CoV-2 PLpro and helicase earmarked as potential targets.

The prepared ligand, HLS **(25)** and its various energy-minimised conformers, were docked using Glide XP [43] into the selected SARS-CoV-2 helicase enzyme's crystal structure, centred around the active site residues Q404, R443 and R567.

Suitable interactions and poses were observed for HLS **(25)** within the NTP binding pocket, specifically, hydrogen bonds were observed to occur between the alcohol moieties of HLS and the R443, S289 and a H290 residues. The proposed interaction between H290 and HLS **(25)** is unique in that it occurs via a bridging water molecule (Figure 4.21). The docking pose was found to have a good docking score of -5.265 kcal/mol.

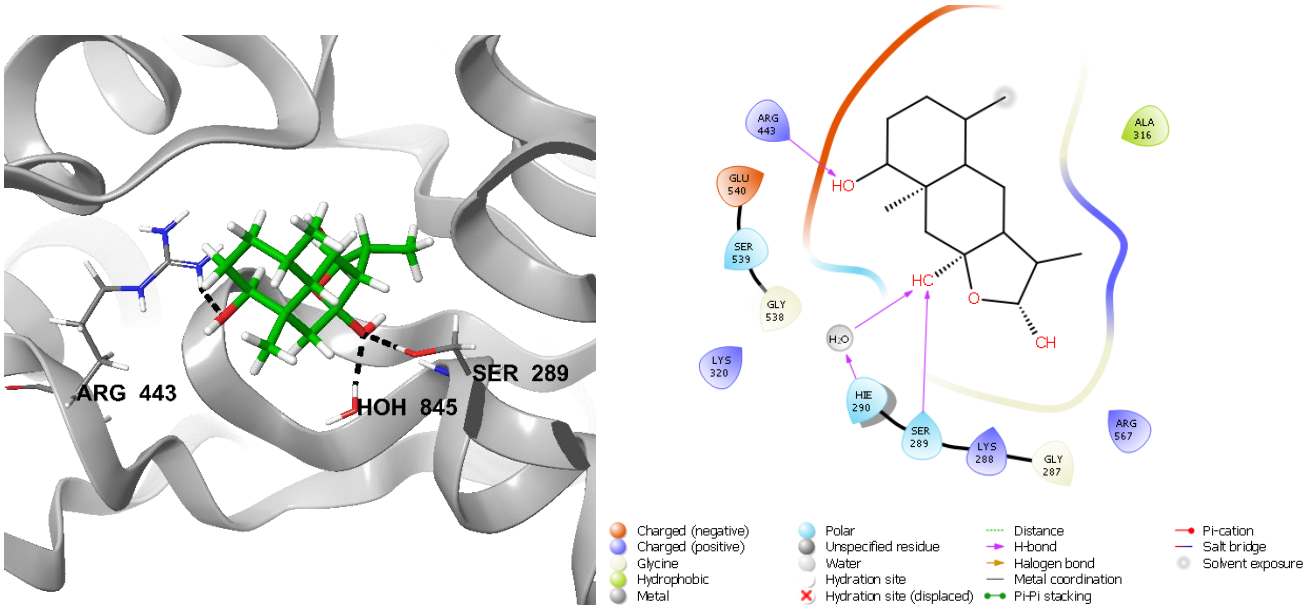

Figure 4.21: Binding pose and schematic representation of the interactions HLS **(25)** makes with surrounding residues of the SARS-CoV-2 helicase enzyme

As explained in Chapter 1, Section 1.3.1, the SARS-CoV-2 NSP13 helicase enzyme possesses a NTP-dependent 5' to 3' double-stranded DNA/RNA unwinding capability *in vitro*, but surprisingly, it primarily functions as a RNA helicase *in vivo* [65]. The enzyme utilises the energy of nucleotide triphosphate hydrolysis to catalyse the unwinding of double-stranded DNA or RNA [68].

The individual phosphate moieties of the NTP interact with a few important residues of the helicase enzyme, making its binding pocket and interacting residues a promising region to target in the hope of preventing the attachment of NTP, and preventing its hydrolysis for energy. The γ-phosphate makes extensive interactions with side chains Q404, R443 and R567 which form part of motifs III, IV, and VI, respectively. This location has previously been targeted in literature [69] with some research providing *in vitro* data of molecules presumed to act in this ATP binding pocket [65]. Upon further investigation, reports of low molecular weight compounds have been predicted to inhibit the SARS-CoV-2 helicase enzyme [68]. Based on this, visual inspection of publicly available crystal structures of the SARS-CoV-2 helicase enzyme led to the selection of 7NNG, deposited as enzyme-ligand (inhibitor) co-crystallised complexes. This complex was chosen because the active site and interacting residues are well-defined.

Based on the observed molecular docking results, HLS **(25)** makes extensive interactions with the active site residues and could competitively inhibit the NTP from binding to the NSP13 helicase enzyme, thus inhibiting its function. Overall, this might explain the experimentally observed activity, although further *in vitro* data would be required to confirm this experimentally.

4.5.8.2 SARS-CoV-2 PLpro

The prepared ligand, HLS, and its various minimised conformers were docked using Glide XP [43] into the selected crystal structure of PLpro, centred in place of the original co-crystallised inhibitor (3k) present in the BL2 region.

Suitable interactions and poses were observed for HLS **(25)** within the PLpro substrate binding pocket (Figure 4.22A), specifically interacting well with the active site of the enzyme viz. BL2 region, interacting with similar residues as the original co-crystallised ligand, 3k, present in the PDB deposition (Figure 4.22B). HLS **(25)** was observed to form hydrogen bonds with amino acids in the enzyme exclusively and these interactions were found to occur between GLN269 (via a water bridge), CYS270 and ASP164 (Figure 4.22C). ASP164 is a key interacting residue of the known co-crystallised inhibitor, 3k. Interestingly, the docking score of HLS compared

well with the co-crystallised inhibitor, 3k, where a docking score of -6.06 kcal/mol and -5.601 kcal/mol was observed for each compound, respectively.

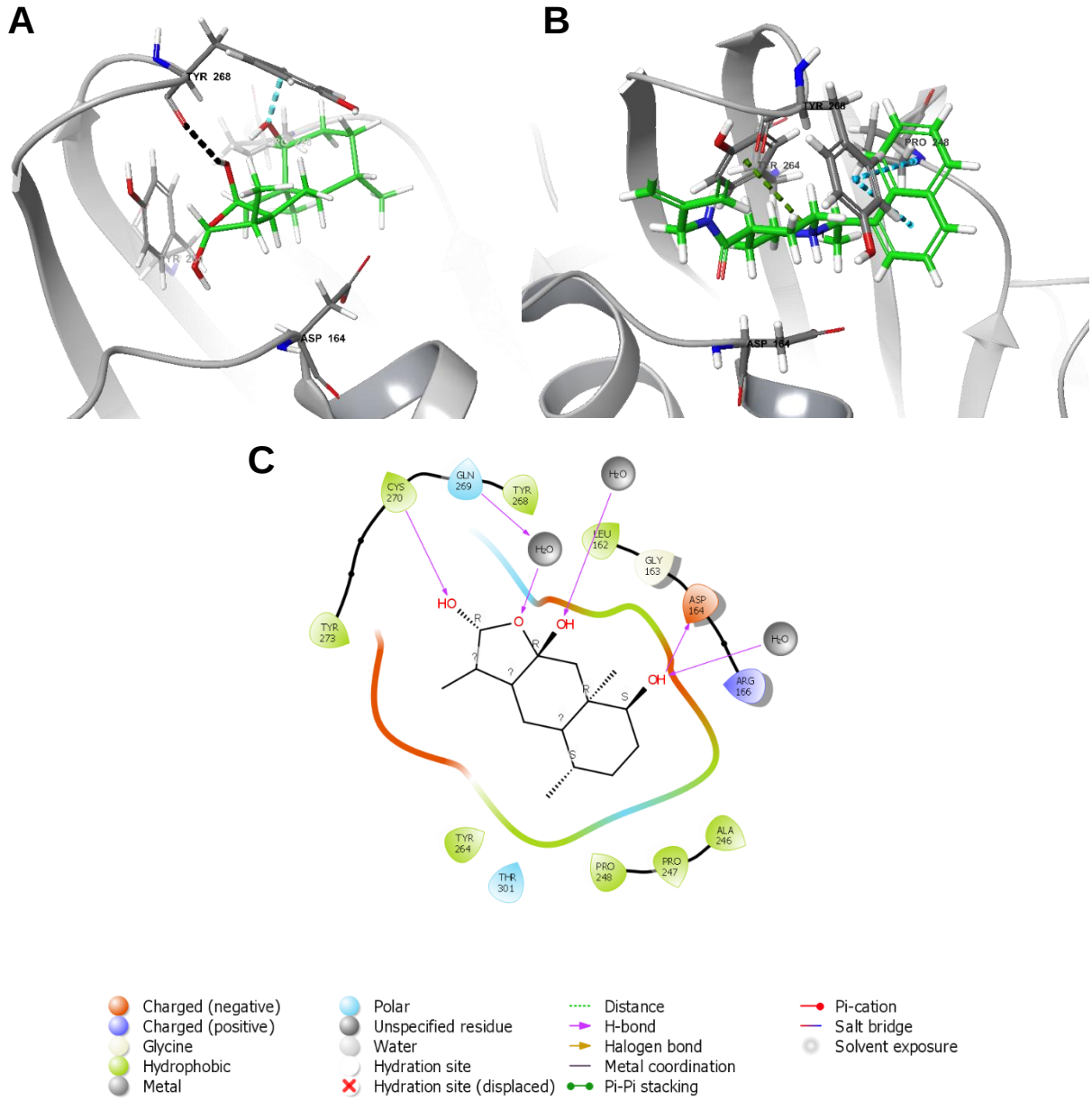

Figure 4.22: (**A**) Binding pose of the interactions HLS and (**B**) inhibitor 3k makes with surrounding residues of the SARS-CoV-2 PLpro enzyme. (**C**) Interaction diagram of HLS and the PLpro enzyme, once stabilised after a 100 ns simulation.

As explained in Chapter 1, Section 1.3.1, the SARS-CoV-2 papain-like protease enzyme forms part of the multi-domain protein nsp3 which is responsible for releasing the first 4 nsps from the SARS-CoV-2 polyprotein. This is done by hydrolysing amino acid sequences with a particular motif, specifically Leu-Xaa-Gly-Gly sequences (Xaa being Asn, Lys or Lys). A few human proteins also contain this motif, making it a target for hydrolysis by PLpro, thus disrupting host signalling processes [70]. The active region of the enzyme, termed BL2, is a channel required by the PLpro to hold the C-terminal tail of its usual substrates, viz. ubiquitin and ISG15. The substrates are held in place by a flexible loop (amino acid 267-272), which consists of an extended β-hairpin which folds over the compound binding site, keeping it in place [70].

Reports of low molecular weight compounds have also been shown to act on PLpro *in vitro* [70]. Based on this, visual inspection of publicly available crystal structures of PLpro, led to the selection of PDB: 7TZJ, deposited as an enzyme-ligand (inhibitor) co-crystallised complex. The inhibitor lies within the enzyme's binding site and imposes the observed biological activity.

Like inhibitor 3k, HLS **(25)** targets the same active site, which could lead to the observed biological activity.

4.5.8.3 MD Simulations

To further assess the stability of the pose within the PLpro enzyme, MD simulations were performed. A stable binding pose was obtained for HLS **(25)** within the BL2 region, as was observed with the known PLpro inhibitor 3k (PDB 7TZJ) [70]. During the initial 60 ns of the simulation, slight shifts occurred in the BL2 loop, but for the remainder of the simulation, the ligand (HLS **(25)**) was noted to be stable with a root-mean-square deviation (RMSD) of less than 4 Å (Figure 4.23). The MD simulation illustrated how the small molecular and alcohol moieties form strong hydrogen bonds with a few key amino acids in the BL2 region. Considering the interactions between HLS **(25)** and the surrounding enzyme residues and the stability of the ligand during the MD simulation, it is likely that HLS **(25)** binds to the SARS-CoV-2 PLpro, which might explain the antiviral activity noted experimentally.

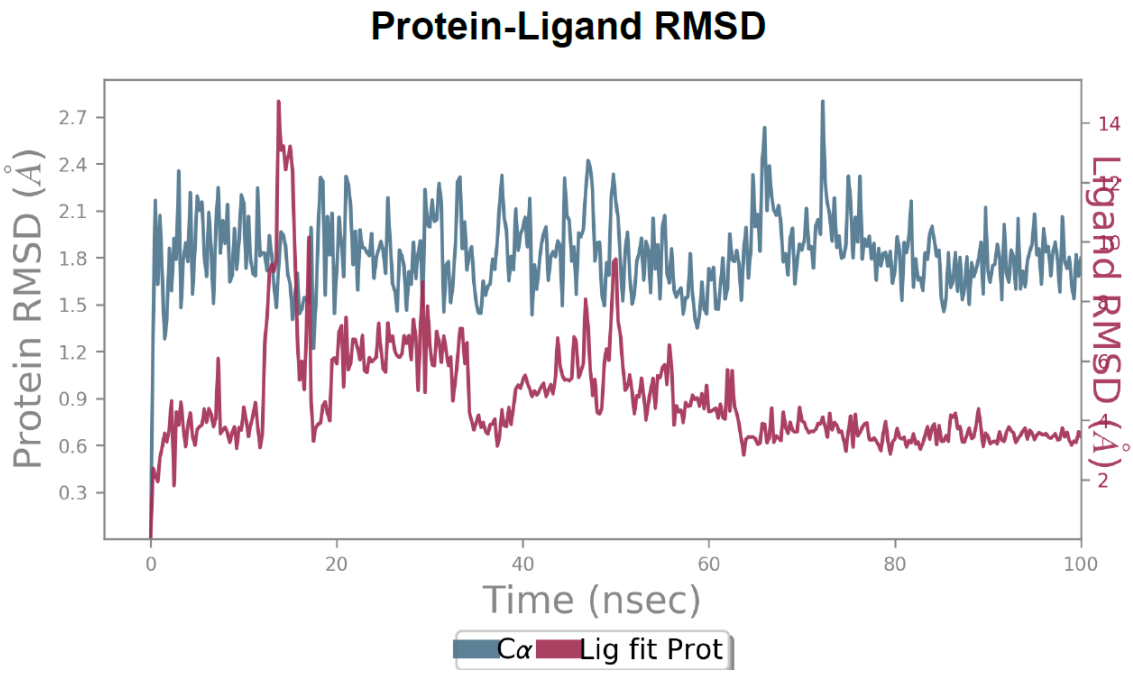

Figure 4.23: A plot of HLS **(25)** RMSD concerning the protein's backbone during the 100 ns MD simulation, graph generated with Schrödinger v. 2022-1.

A recent article by Wu et al. (2020) suggests that the SARS-CoV-2 enzymes PLpro and helicase, being genetically well-conserved and crucial for viral reproduction, present possible targets for SARS-CoV-2 therapeutic drugs [67]. Based on this knowledge and the data obtained from the MD simulations, HLS **(25)** may be a unique and important novel antiviral agent which targets stable enzymatic targets like helicase or more likely, the PLpro of RNA viruses.

4.5.9 ADMET Analysis

SwissADME (http://www.swissadme.ch) was used to evaluate HLS's potential as an oral drug based on its physicochemical properties, drug-likeness and pharmacokinetics [46]. Remdesivir, the FDA-approved antiviral and bioassay positive control, was also evaluated for comparative purposes.

The bioavailability radar of HLS **(25)** and remdesivir is drawn based on the compounds physicochemical properties and displayed in Figure 4.24. The shaded pink region highlights the ideal properties of a drug with the darker lines illustrating the predicted properties of the drug.

Based on the generated radars, HLS **(25)** falls within the optimal range for each parameter, predicting HLS **(25)** to be orally bioavailable (Figure 4.24) and an ideal candidate for an orally administered pharmaceutical. Self-administration via the oral route is a particularly common route of administration for several pharmaceuticals. Pharmaceuticals that can be administered in this way prevent patients from having to visit clinics and hospitals for administration as these can be administered at home, a valuable quality of a drug during pandemics by reserving and freeing up hospitals for severe cases. In contrast to HLS **(25)**, remdesivir only falls within the optimal range for 3 out of the 6 parameters for an orally administered drug. Interestingly, *in vivo* data supports this low bioavailability prediction and provides credence for IV administration in a hospital setting [71].

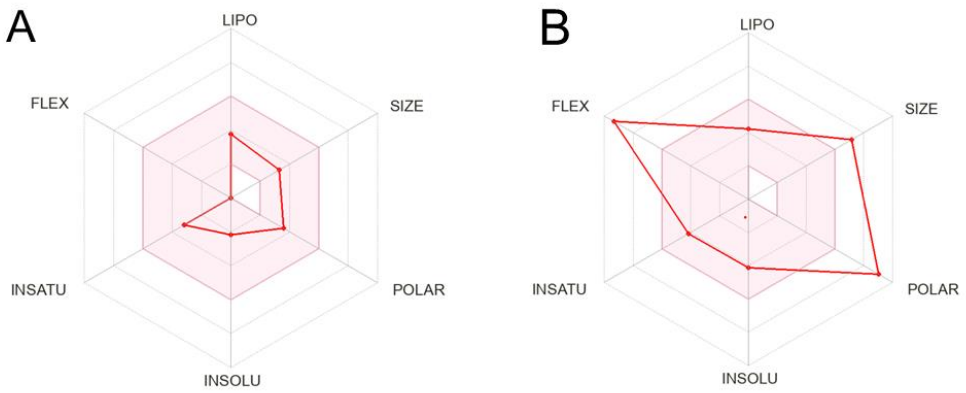

Figure 4.24: (**A**) Bioavailability radars generated on SwissADME for HLS and (**B**) remdesivir.

Futhermore, to assess the 2 compounds' drug-likeness based on their inherent physicochemical properties, five different rule-based filters were used to establish and evaluate oral drug candidates. These are defined as follows [72]:

i. Lipiniski's rule of 5 [73]: MW ≤ 500 g.mol^{-1}, logP ≤ 4.15, hydrogen bond acceptors ≤ 10 and hydrogen bond donors ≤ 5.

ii. Ghose's filter [74]: MW between 160 and 480 g.mol^{-1}, WLOGP between -0.4 and 5.6, molar refractivity between 40 and 130 and number of atoms between 20 and 70.

iii. Veber's filter [75]: number of rotatable bonds ≤ 10 and a TPSA ≤ 140.

iv. Egan's filter [76]: WLOGP ≤ 5.88 and TPSA ≤ 131.6

v. Muegge's filter [77]: $200 \leq MW \leq 600$, $-2 \leq$ XLOGP3 (lipophilicity) ≤ 5, TPSA ≤ 150, number of rings ≤ 7, number of rotatable bonds ≤ 15, number of carbon atoms > 4, number of heteroatoms > 1, hydrogen bond acceptors ≤ 10 and hydrogen bond donors ≤ 5.

The outcome of the drug-likeness evaluation based on the above rules (i-v) for HLS **(25)** and remdesivir is displayed in Table 4.7 and shows that HLS **(25)** agrees with Lipinski, Ghose, Veber, Egan and Muegge's rules and similarly predicted not to inhibit any hepatic CYP enzymes, providing positive reassurance that HLS **(25)** may be a good lead as an oral pharmaceutical.

Table 4.7: Physiochemical, lipophilicity, pharmacokinetic and drug-likeness parameters of HLS **(25)** and the RDA-approved drug remdesivir, assessed by SwissADME [46].

Parameters	**HLS (25)**	**Remdesivir**
Formula	$C_{15}H_{18}O_4$	$C_{27}H_{35}N_6O_8P$
Molecular weight ($g.mol^{-1}$)	262.30	602.58
No. of rotatable bonds	0	14
No. of H bond acceptors	4	12
No. of H bond donors	1	4
Topological Polar Surface area, TPSA ($[Å]^2$)	63.60	213.36
Lipophilicity, log P	1.76	1.54
Water Solubility, log S	-2.16	-4.12
GI absorption	High	Low
BBB permeant	Yes	No
P-gp substrate	No	Yes
CYP1A2 inhibitor	No	No
CYP2C19 inhibitor	No	No
CYP2C9 inhibitor	No	No
CYP2D6 inhibitor	No	No
CYP3A4 inhibitor	No	Yes
Skin permeation, log K_P (Cm/S)	-7.12	-8.62
Drug-likeness (based on rules)	Yes	No

There is an ever-present hope that compounds with a high *in vitro* bioactivity eventually make it to clinical trials amongst drug-discovery chemists. However, a vast difference exists between *in vitro* and *in vivo* bioassays, particularly due to the intricate processes and modifications that the administered compounds (potential drugs) undergo *in vivo*, which are often absent within *in vitro* bioassays. It is thus no surprise that many drug candidates fail during this *in vivo* testing phase, despite displaying potent biological activity *in vitro*, much of this being due to unforeseen adverse side effects [78]. This is similarly true for pharmaceuticals designed for oral ingestion by humans, where good pharmaceuticals are required to have a good balance of efficacy and safety, both of equal importance. The disruption of this balance would mean the difference between the final success or failure of the potential drug, despite potent activity against the individual target.

Orally administered pharmaceuticals undergo, broadly speaking, 4 major processes *in vivo*: absorption into the bloodstream for eventual distribution to the targets, metabolism and modification of the drug by the body and eventual excretion of the compound [79]. The success of the drug relies heavily on these critical processes.

In order to unequivocally determine exactly how a compound would respond to each of these processes, actual *in vitro* and *in vivo* biological assays need to be conducted. These however take time and are often very costly and require large quantities of the compound, quantities which are often difficult to acquire without synthetic means. This is especially a big challenge in natural product chemistry, partially due to the complexity of the compounds and the often-limited quantities present in the plant.

Recent advances in *in silico* ADME analyses, however, prove especially useful in such instances for primary-level screening of potential drugs, helping to reduce pharmacokinetic-related failure during late-stage trials, *in vivo* and clinical trials [80], thereby reducing costs and time which might have been wasted in *in vivo* biological assays. These *in silico* ADME predictors provide vital information related to oral bioavailability, these being drug lipophilicity (*LogP*), membrane permeability and hepatic metabolism. This is done by assessing the drug's chemical characteristics according to well-published rules in order to determine their drug-likeness namely, Lipinski [73], Ghose [74], Veber [75], Egan [76] and Muegge [77] and to support drug discovery efforts.

4.6 Conclusion

Despite natural products being a reliable resource in drug discovery, much research is currently focused on *in silico* experiments and computational screening methods, with little *in vitro* work done to substantiate the claims. This chapter goes beyond typical *in silico* work and follows a systematic drug discovery approach with thorough proof-of-concept studies completed for HLS **(25)**, providing a candidate ready for upscale.

By coupling natural product chemistry and synthetic chemistry, a semi-synthetic pathway was described in which the toxic and inactive precursor, siphonochilone **(24)**, was converted to the highly bioactive and non-toxic derivative, HLS **(25)**. This work highlights the value of utilising synthetic chemistry to overcome some of the challenges associated with natural product chemistry, like the inherent difficulty in achieving high yields and sufficient quantity of the bioactive compound required for subsequent studies.

Based on the data, HLS **(25)** was found to inhibit the viral-induced cytopathic effect of multiple variants of concern, with its mode of action hypothesised to be via the inhibition of a stable enzyme like the PLpro. Based on the cytotoxicity data, HLS **(25)** is shown to have a high selectivity index and is similarly predicted to have a wide therapeutic index. Based on *in silico* ADME predictions, HLS **(25)** shows good drug-like qualities for use as an orally administered pharmaceutical.

By utilising SCXRD, in combination with NMR and MS, the previously undescribed absolute configuration of HLS **(25)** was determined. Notably, the stereochemistry at the 4 chiral centres (C-5, C-4a, C-8a and C-9a) were found to be of the (*S*) and (*R*) configuration for positions C-5 and C-4a, respectively and similarly, (*S*) and (*R*) for stereocenters C-8a and C-9a, respectively. The incorporation of SCXRD provides a critical identification and validation step and overcomes a significant limitation of conventional NMR spectroscopy in that the absolute configuration of a molecule can be calculated. The absolute configuration is critical when incorporating drugs into biological systems. A small difference in stereochemistry could mean the difference between the molecule being biologically active or inactive, similarly, toxic or non-toxic, as demonstrated between the highly toxic compound siphonochilone **(24)** and its non-toxic, highly bioactive derivative, HLS **(25)**.

The results provide new hope for the investigation of plant-derived compounds and natural product chemistry in the probe for novel antiviral compounds against SARS-CoV-2. HLS **(25)** and the developed semi-synthetic conversion of siphonochilone to HLS **(25)**, may serve as a novel candidate for medicines against SARS-CoV-2, ready for upscale and preclinical trials.

4.7 References

1 G. Fouche, S. van Rooyen and T. Faleschini, *Siphonochilus aethiopicus*, a traditional remedy for the treatment of allergic asthma, *Tang Humanitas Med.*, 2013, **3**, 6.1-6.6.
2 C. W. Holzapfel, W. Marais, P. L. Wessels and B. E. Van Wyk, Furanoterpenoids from *Siphonochilus aethiopicus*, *Phytochemistry*, 2002, **59**, 405–407.
3 S. A. Adebayo, S. O. Amoo, S. N. Mokgehle and A. O. Aremu, Ethnomedicinal uses, biological activities, phytochemistry and conservation of African ginger (*Siphonochilus aethiopicus*): A commercially important and endangered medicinal plant, *J. Ethnopharmacol.*, 2021, **266**, 113459.
4 Threatened Species Programme | SANBI Red List of South African Plants, Threatened Species Programme | SANBI Red list of South African plants, http://redlist.sanbi.org/species.php?species=2061-1, (accessed 25 August 2022).
5 G. Fouche, N. Nieuwenhuizen, V. Maharaj, S. Van Rooyen, N. Harding, R. Nthambeleni, J. Jayakumar, F. Kirstein, B. Emedi and P. Meoni, Investigation of in vitro and in vivo anti-asthmatic properties of *Siphonochilus aethiopicus*, *J. Ethnopharmacol.*, 2011, **133**, 843–849.
6 P. Maphothoma, R. Kleynhans, G. Prinsloo, S. N. Mokgehle, I. du Plooy and H. T. Araya, Growth and yield of African ginger in response to application of organic fertiliser, *South African J. Plant Soil*, 2021, **38**, 338–342.
7 S. N. Mokgehle, S. Z. Tesfay, M. J. Makgato and H. T. Araya, Phytochemical profiling and soluble sugars of African ginger (*Siphonochilus aethiopicus*) from different growing regions in South Africa, *South African J. Plant Soil*, 2019, **36**, 157–163.
8 A. Hutchings and A. B. Scott, Alan Haxton. Lewis, Gillian. Bunningham, *Zulu medicinal plants : an inventory*, University of Natal Press, Pietermaritzburg, South Africa, 1996.
9 C. A. Lategan, W. E. Campbell, T. Seaman and P. J. Smith, The bioactivity of novel furanoterpenoids isolated from *Siphonochilus aethiopicus*, *J. Ethnopharmacol.*, 2009, **121**, 92–97.
10 J. P. Noudogbessi, H. Yedomonhan, G. A. Alitonou, P. Chalard, G. Figueredo, E. Adjalian, F. Avlessi, J. C. Chalchat and D. C. K. Sohounhloué, Physical characteristics and chemical compositions of the essential oils extracted from different parts of *Siphonochilus aethiopicus* (Schweinf.) B. L. Burtt (Zingiberaceae) harvested in Benin, *J. Chem. Pharm. Res.*, 2012, **4**, 4845–4851.
11 Y. Naudé, R. Makuwa and V. Maharaj, Investigating volatile compounds in the vapour phase of (1) a hot water infusion of rhizomes, and of (2) rhizomes of *Siphonochilus aethiopicus* using head space solid phase microextraction and gas chromatography with time of flight mass spectrometry, *South African J. Bot.*, 2016, **106**, 144–148.
12 M. E. Light, L. J. McGaw, T. Rabe, S. G. Sparg, M. B. Taylor, D. G. Erasmus, A. K. Jäger and J. Van Staden, Investigation of the biological activities of *Siphonochilus aethiopicus* and the effect of seasonal senescence, *South African J. Bot.*, 2002, **68**, 55–61.
13 L. Kruger, *Development of Siphonochilus aethiopicus as a treatment for colds and Influenza and gas chromatographic analysis of volatiles of an insect repellent*, 2020.
14 T. Chunga, S. Bareetseng, J. Senabe and E. Wadiwala, A comparison between major chemical markers of the cultivated and wild harvested *Siphonochilus aethiopicus*, African ginger, from Mpumalanga , South Africa , using Liquid Chromatography-Mass Spectrometry, *Open J. Pain Med.*, 2022, **6**, 7–11.
15 F. K. Zongwe, J. T. Muya, R. Mutimana, M. Virima, M. Mayaliwa, H. Chung and V. Maharaj, Autoxidation of siphonochilone in processed rhizomes and stored powders of *Siphonochilus aethiopicus* (Schweinf.) B.L. Burtt, *ChemistrySelect*, 2018, **3**, 8569–8574.
16 R. Bachmann, Janet; Earles, Postharvest handling of fruits and vegetables, *ATTRA*.
17 X. Su, Y. Wu, Y. Li, Y. Huang, Y. Liu, P. Luo and Z. Zhang, Effect of Different Post-Harvest processing methods on the chemical constituents of *Notopterygium franchetii*

by an UHPLC-QTOF-MS-MS metabolomics approach., *Molecules*, 2019, **24**, 3188.
18 X. Yang, M. I. Gil, Q. Yang and F. A. Tomás-Barberán, Bioactive compounds in lettuce: Highlighting the benefits to human health and impacts of preharvest and postharvest practices, *Compr. Rev. Food Sci. Food Saf.*, 2022, **21**, 4–45.
19 C. E. Ejike and M. C. Ndukwu, Pre-harvest and post-harvest factors affecting bioactive compounds from *Vernonia amygdalina* (Del.), *Res. J. Med. Plants*, 2017, **11**, 32–40.
20 N. Martins, S. Petropoulos and I. C. F. R. Ferreira, Chemical composition and bioactive compounds of garlic (*Allium sativum* L.) as affected by pre- and post-harvest conditions: A review, *Food Chem.*, 2016, **211**, 41–50.
21 G. S. Duarte, A. A. Pereira and A. Farah, Chlorogenic acids and other relevant compounds in Brazilian coffees processed by semi-dry and wet post-harvesting methods, *Food Chem.*, 2010, **118**, 851–855.
22 H. M. S. A. L. Ubeed, R. B. H. Wills and J. Chandrapala, Post-harvest operations to generate high-quality medicinal cannabis products: a systemic review, *Molecules*, 2022, **27**, 1–14.
23 D. Kusumaningrum, S.-H. Lee, W.-H. Lee, C. Mo and B.-K. Cho, A review of technologies to prolong the shelf life of fresh tropical fruits in Southeast Asia, *J. Biosyst. Eng.*, 2015, **40**, 345–358.
24 R. James Faber, C. Petrus Laubscher and M. Olaide Jimoh, The Importance of *Sceletium tortuosum* (L.) N.E. Brown and Its viability as a traditional African medicinal plant, *Nat. Drugs from Plants*, 2021, 1-12.
25 R. James Faber, C. Petrus Laubscher and M. Olaide Jimoh, The Importance of *Sceletium tortuosum* (L.) N.E. Brown and Its viability as a traditional Arican medicinal plant, *Nat. Drugs from Plants*, 2022, 1–12.
26 W. Chen and A. M. Viljoen, To ferment or not to ferment *Sceletium tortuosum* – Do our ancestors hold the answer?, *South African J. Bot.*, 2019, **122**, 543–546.
27 S. Mathur and C. Hoskins, Drug development: Lessons from nature., *Biomed. reports*, 2017, **6**, 612–614.
28 A. G. Atanasov, S. B. Zotchev, V. M. Dirsch, I. E. Orhan, M. Banach, J. M. Rollinger, D. Barreca, W. Weckwerth, R. Bauer, E. A. Bayer, M. Majeed, A. Bishayee, V. Bochkov, G. K. Bonn, N. Braidy, F. Bucar, A. Cifuentes, G. D'Onofrio, M. Bodkin, M. Diederich, A. T. Dinkova-Kostova, T. Efferth, K. El Bairi, N. Arkells, T. P. Fan, B. L. Fiebich, M. Freissmuth, M. I. Georgiev, S. Gibbons, K. M. Godfrey, C. W. Gruber, J. Heer, L. A. Huber, E. Ibanez, A. Kijjoa, A. K. Kiss, A. Lu, F. A. Macias, M. J. S. Miller, A. Mocan, R. Müller, F. Nicoletti, G. Perry, V. Pittalà, L. Rastrelli, M. Ristow, G. L. Russo, A. S. Silva, D. Schuster, H. Sheridan, K. Skalicka-Woźniak, L. Skaltsounis, E. Sobarzo-Sánchez, D. S. Bredt, H. Stuppner, A. Sureda, N. T. Tzvetkov, R. A. Vacca, B. B. Aggarwal, M. Battino, F. Giampieri, M. Wink, J. L. Wolfender, J. Xiao, A. W. K. Yeung, G. Lizard, M. A. Popp, M. Heinrich, I. Berindan-Neagoe, M. Stadler, M. Daglia, R. Verpoorte and C. T. Supuran, Natural products in drug discovery: advances and opportunities, *Nat. Rev. Drug Discov.*, 2021, **20**, 200–216.
29 D. A. Dias, S. Urban and U. Roessner, A Historical overview of natural products in drug discovery, *Metabolites*, 2012, **2**, 303–336.
30 S. McAlister, Y. Ou, E. Neff, K. Hapgood, D. Story, P. Mealey and F. McGain, The Environmental footprint of morphine: A life cycle assessment from opium poppy farming to the packaged drug, *BMJ Open*, 2016, **6**, 1–9.
31 G. Xu, L. Y. Peng, A. J. Hou, J. Yang, Q. Bin Han, H. X. Xu and Q. S. Zhao, Isolation, structural elucidation, and chemical transformation of interconvertible 8,12-hemiketal germacranolide sesquiterpenoids from *Salvia castanea* Diels f. tomentosa Stib., *Tetrahedron*, 2008, **64**, 9490–9494.
32 O. V Dolomanov, L. J. Bourhis, R. J. Gildea, J. A. K. Howard and H. Puschmann, OLEX2: a complete structure solution, refinement and analysis program, *J. Appl. Crystallogr.*, 2009, **42**, 339–341.

33 K. B. Ku, H. J. Shin, H. S. Kim, B.-T. Kim, S.-J. Kim and C. Kim, Repurposing screens of FDA-approved drugs identify 29 inhibitors of SARS-CoV-2, *J. Microbiol. Biotechnol.*, 2020, **30**, 1843–1853.

34 I. Tietjen, J. Cassel, E. T. Register, X. Y. Zhou, T. E. Messick, F. Keeney, L. D. Lu, K. D. Beattie, T. Rali, P. Tebas, H. C. J. Ertl, J. M. Salvino, R. A. Davis and L. J. Montaner, The natural stilbenoid (–)-hopeaphenol inhibits cellular entry of SARS-CoV-2 USA-WA1/2020, B.1.1.7, and B.1.351 Variants, *Antimicrob. Agents Chemother.*, 2021, **65**, e0077221.

35 L. Urda, M. H. Kreuter, J. Drewe, G. Boonen, V. Butterweck and T. Klimkait, The petasites hybridus CO2 Extract (Ze 339) blocks SARS-CoV-2 replication in vitro, *Viruses*, 2022, **14**, 106.

36 R. T. Eastman, J. S. Roth, K. R. Brimacombe, A. Simeonov, M. Shen, S. Patnaik and M. D. Hall, Remdesivir: A review of its discovery and development leading to emergency use authorization for treatment of COVID-19., *ACS Cent. Sci.*, 2020, **6**, 672–683.

37 L. Invernizzi, P. Moyo, J. Cassel, F. J. Isaacs, J. M. Salvino, L. J. Montaner, I. Tietjen and V. Maharaj, Use of hyphenated analytical techniques to identify the bioactive constituents of *Gunnera perpensa* L., a South African medicinal plant, which potently inhibit SARS-CoV-2 spike glycoprotein–host ACE2 binding, *Anal. Bioanal. Chem.*, 2022, **414**, 3971–3985.

38 J. C. Shelley, A. Cholleti, L. L. Frye, J. R. Greenwood, M. R. Timlin and M. Uchimaya, Epik: A software program for pKa prediction and protonation state generation for drug-like molecules, *J. Comput. Aided. Mol. Des.*, 2007, **21**, 681–691.

39 J. R. Greenwood, D. Calkins, A. P. Sullivan and J. C. Shelley, Towards the comprehensive, rapid, and accurate prediction of the favorable tautomeric states of drug-like molecules in aqueous solution., *J. Comput. Aided. Mol. Des.*, 2010, 24, 591–604.

40 G. Madhavi Sastry, M. Adzhigirey, T. Day, R. Annabhimoju and W. Sherman, Protein and ligand preparation: Parameters, protocols, and influence on virtual screening enrichments, *J. Comput. Aided. Mol. Des.*, 2013, **27**, 221–234.

41 M. P. Jacobson, D. L. Pincus, C. S. Rapp, T. J. F. Day, B. Honig, D. E. Shaw and R. A. Friesner, A hierarchical approach to all-atom protein loop prediction, *Proteins Struct. Funct. Genet.*, 2004, **55**, 351–367.

42 M. P. Jacobson, R. A. Friesner, Z. Xiang and B. Honig, On the role of the crystal environment in determining protein side-chain conformations, *J. Mol. Biol.*, 2002, **320**, 597–608.

43 R. A. Friesner, R. B. Murphy, M. P. Repasky, L. L. Frye, J. R. Greenwood, T. A. Halgren, P. C. Sanschagrin and D. T. Mainz, Extra precision glide: Docking and scoring incorporating a model of hydrophobic enclosure for protein-ligand complexes, *J. Med. Chem.*, 2006, **49**, 6177–6196.

44 K. J. Bowers, E. Chow, H. Xu, R. O. Dror, M. P. Eastwood, B. A. Gregersen, J. L. Klepeis, I. Kolossvary, M. A. Moraes, F. D. Sacerdoti, J. K. Salmon, Y. Shan and D. E. Shaw, in *Proceedings of the ACM/IEEE Conference on Supercomputing*, Association for Computing Machinery, Tampa, Florida, 2006.

45 W. L. Jorgensen, J. Chandrasekhar, J. D. Madura, R. W. Impey and M. L. Klein, Comparison of simple potential functions for simulating liquid water, *J. Chem. Phys.*, 1983, **79**, 926–935.

46 A. Daina, O. Michielin and V. Zoete, SwissADME: A free web tool to evaluate pharmacokinetics, drug-likeness and medicinal chemistry friendliness of small molecules, *Sci. Rep.*, 2017, **7**, 1–13.

47 H. D. Flack and G. Bernardinelli, The use of X-ray crystallography to determine absolute configuration., *Chirality*, 2008, **20**, 681–690.

48 J. R. Cossy, The importance of chirality in drugs and agrochemicals, *Comprehensive Chirality*, eds. E. M. Carreira and H. Yamamoto, Elsevier, Amsterdam, 2012, pp. 1–7.

49 M. Erasmus, L. H. du Plessis and J. M. Viljoen, In-vitro cytotoxicity of various *Siphonochilus aethiopicus* (Schweinf.) B.L. Burtt extracts in combination with selected tableting excipients., *J. Pharm. Pharmacol.*, 2019, **71**, 1714–1724.
50 D. Planas, D. Veyer, A. Baidaliuk, I. Staropoli, F. Guivel-Benhassine, M. M. Rajah, C. Planchais, F. Porrot, N. Robillard, J. Puech, M. Prot, F. Gallais, P. Gantner, A. Velay, J. Le Guen, N. Kassis-Chikhani, D. Edriss, L. Belec, A. Seve, L. Courtellemont, H. Péré, L. Hocqueloux, S. Fafi-Kremer, T. Prazuck, H. Mouquet, T. Bruel, E. Simon-Lorière, F. A. Rey and O. Schwartz, Reduced sensitivity of SARS-CoV-2 variant Delta to antibody neutralization, *Nature*, 2021, **596**, 276–280.
51 D. Tian, Y. Sun, J. Zhou and Q. Ye, The global epidemic of the SARS-CoV-2 Delta variant, key spike mutations and immune escape., *Front. Immunol.*, 2021, **12**, 751778.
52 J. Tamargo, J.-Y. Le Heuzey and P. Mabo, Narrow therapeutic index drugs: a clinical pharmacological consideration to flecainide., *Eur. J. Clin. Pharmacol.*, 2015, **71**, 549–567.
53 M. C. DeRosa and R. J. Crutchley, Photosensitized singlet oxygen and its applications, *Coord. Chem. Rev.*, 2002, **233**–**234**, 351–371.
54 A. G. Leach and K. N. Houk, Diels-Alder and ene reactions of singlet oxygen, nitroso compounds and triazolinediones: Transition states and mechanisms from contemporary theory, *Chem. Commun.*, 2002, **2**, 1243–1255.
55 A. R. Reddy and M. Bendikov, Diels-Alder reaction of acenes with singlet and triplet oxygen - Theoretical study of two-state reactivity, *Chem. Commun.*, 2006, 1179–1181.
56 F. Ronzani, A. Trivella, E. Arzoumanian, S. Blanc, M. Sarakha, C. Richard, E. Oliveros and S. Lacombe, Comparison of the photophysical properties of three phenothiazine derivatives: Transient detection and singlet oxygen production, *Photochem. Photobiol. Sci.*, 2013, **12**, 2160–2169.
57 K. Varela, H. Al Mahmud, H. D. Arman, L. R. Martinez, C. A. Wakeman and F. K. Yoshimoto, Autoxidation of a C2-olefinated dihydroartemisinic acid analogue to form an aromatic ring: application to serrulatene biosynthesis, *J. Nat. Prod.*, 2022, **85**, 951–962.
58 K. Wu, C. Fang, S. Kaur, P. Liu and T. Wang, Methylene blue-catalyzed oxidative cleavage of N-carbonylated indoles, *Synthesis (Stuttg).*, 2018, **50**, 2897–2907.
59 N. J. de Mol, J. Reisch and G. M. J. B. van Henegouwen, On the involvement of singlet oxygen in the biosynthesis of oxygenation products of the furocoumarin imperatorine, *Zeitschrift fur Naturforsch. - Sect. B J. Chem. Sci.*, 1984, **39**, 1433–1441.
60 L. K. Sy and G. D. Brown, Deoxyarteannuin B, dihydro-deoxyarteannuin B and trans-5-hydroxy-2-isopropenyl-5-methylhex-3-en-1-ol from *Artemisia anuua*, *Phytochemistry*, 2001, **58**, 1159–1166.
61 D. Kalaitzakis, A. Kouridaki, D. Noutsias, T. Montagnon and G. Vassilikogiannakis, Methylene blue as a photosensitizer and redox agent: synthesis of 5-hydroxy-1 H -pyrrol-2(5 H)-ones from furans , *Angew. Chemie*, 2015, **127**, 6381–6385.
62 T. Limpanuparb, C. Areekul, P. Montriwat and U. Rajchakit, Blue bottle experiment: learning chemistry without knowing the chemicals, *J. Chem. Educ.*, 2017, **94**, 730–737.
63 T. Limpanuparb, P. Roongruangsree and C. Areekul, A DFT investigation of the blue bottle experiment: E○half-cell analysis of autoxidation catalysed by redox indicators, *R. Soc. Open Sci.*, 2017, **4**, 170708.
64 N. Magazine, T. Zhang, Y. Wu, M. C. McGee, G. Veggiani and W. Huang, Mutations and evolution of the SARS-CoV-2 spike protein, *Viruses*, 2022, **14**, 1–11.
65 L. Lu, Y. Peng, H. Yao, Y. Wang, J. Li, Y. Yang and Z. Lin, Punicalagin as an allosteric NSP13 helicase inhibitor potently suppresses SARS-CoV-2 replication in vitro, *Antiviral Res.*, 2022, **206**, 105389.
66 C. Wu, Y. Liu, Y. Yang, P. Zhang, W. Zhong, Y. Wang, Q. Wang, Y. Xu, M. Li, X. Li, M. Zheng, L. Chen and H. Li, Analysis of therapeutic targets for SARS-CoV-2 and discovery of potential drugs by computational methods, *Acta Pharm. Sin. B*, 2020, **10**, 766-788.

67 C. Wu, Y. Liu, Y. Yang, P. Zhang, W. Zhong, Y. Wang, Q. Wang, Y. Xu, M. Li, X. Li, M. Zheng, L. Chen and H. Li, Analysis of therapeutic targets for SARS-CoV-2 and discovery of potential drugs by computational methods, *Acta Pharm. Sin. B*, 2020, **10**, 766–788.

68 J. A. Newman, A. Douangamath, S. Yadzani, Y. Yosaatmadja, A. Aimon, J. Brandão-Neto, L. Dunnett, T. Gorrie-stone, R. Skyner, D. Fearon, M. Schapira, F. von Delft and O. Gileadi, Structure, mechanism and crystallographic fragment screening of the SARS-CoV-2 NSP13 helicase, *Nat. Commun.*, 2021, **12**, 1–11.

69 E. Oh, W. Wang, K.-H. Park, C. Park, Y. Cho, J. Lee, E. Kang and H. Kang, (+)-Usnic acid and its salts, inhibitors of SARS-CoV-2, identified by using in silico methods and in vitro assay, *Sci. Rep.*, 2022, **12**, 13118.

70 D. J. Calleja, N. Kuchel, B. G. C. Lu, R. W. Birkinshaw, T. Klemm, M. Doerflinger, J. P. Cooney, L. Mackiewicz, A. E. Au, Y. Q. Yap, T. R. Blackmore, K. Katneni, E. Crighton, J. Newman, K. E. Jarman, M. J. Call, B. C. Lechtenberg, P. E. Czabotar, M. Pellegrini, S. A. Charman, K. N. Lowes, J. P. Mitchell, U. Nachbur, G. Lessene and D. Komander, Insights into drug repurposing, as well as specificity and compound properties of piperidine-based SARS-CoV-2 PLpro inhibitors, *Front. Chem.*, 2022, **10**, 1–21.

71 B. Chatterjee and S. S. Thakur, Remdesivir and its combination with repurposed drugs as COVID-19 therapeutics, *Front. Immunol.*, 2022, **13**, 1–13.

72 C. Parlak, Ö. Alver, C. N. M. Ouma, L. Rhyman and P. Ramasami, Interaction between favipiravir and hydroxychloroquine and their combined drug assessment: in silico investigations, *Chem. Pap.*, 2022, **76**, 1471–1478.

73 C. A. Lipinski, F. Lombardo, B. W. Dominy and P. J. Feeney, Experimental and computational approaches to estimate solubility and permeability in drug discovery and development settings., *Adv. Drug Deliv. Rev.*, 2001, **46**, 3–26.

74 A. K. Ghose, V. N. Viswanadhan and J. J. Wendoloski, A knowledge-based approach in designing combinatorial or medicinal chemistry libraries for drug discovery. 1. A qualitative and quantitative characterization of known drug databases, *J. Comb. Chem.*, 1999, **1**, 55–68.

75 D. F. Veber, S. R. Johnson, H.-Y. Cheng, B. R. Smith, K. W. Ward and K. D. Kopple, Molecular properties that influence the oral bioavailability of drug candidates, *J. Med. Chem.*, 2002, **45**, 2615–2623.

76 W. J. Egan, K. M. Merz and J. J. Baldwin, Prediction of drug absorption using multivariate statistics, *J. Med. Chem.*, 2000, **43**, 3867–3877.

77 I. Muegge, S. L. Heald and D. Brittelli, Simple selection criteria for drug-like chemical matter, *J. Med. Chem.*, 2001, **44**, 1841–1846.

78 D. Sun, W. Gao, H. Hu and S. Zhou, Why 90% of clinical drug development fails and how to improve it?, *Acta Pharm. Sin. B*, 2022, **12**, 3049–3062.

79 M. P. Doogue and T. M. Polasek, The ABCD of clinical pharmacokinetics., *Ther. Adv. drug Saf.*, 2013, **4**, 5–7.

80 B. Shaker, S. Ahmad, J. Lee, C. Jung and D. Na, *In silico* methods and tools for drug discovery, *Comput. Biol. Med.*, 2021, **137**, 104851.

Chapter 5

Isolation and characterisation of bioactive compounds from *Podocarpus henkelii* against SARS-CoV-2

5.1 Background on *Podocarpus henkelii*

5.1.1 Classification, geographical distribution and phytochemistry

Podocarpus henkelii forms part of the genus *Podocarpus*, derived from the Greek words 'podos' meaning 'a foot' and '*karpos'* meaning 'a fruit' referring to some species' fleshy fruit stalks (receptacle) [1]. Interestingly, *Podocarpus sp.* forms part of the ancient, most primitive seed plants, the Gymnosperms and form part of the Podocarpaceae family, which are believed to have originated in Gondwana in the late Cretaceous to early Palaeogene (63 Ma) period [2].

Research by Simpson et al. (2010) describes the family Podocarpaceae as comprising of dioecious (seldom monoecious) trees with either simple, spiral, elliptic, subulate, linear or scale-like leaves with pollen cones that are arranged terminally, solitary, axillar or clustered with many microsporophylls (Figure 5.1). Similarly, they report how the seed cones are axial, terminal, reduced, cone-like and typically fleshy, with some taxa having a peduncle which might be fused with the plant's bracts, giving rise to a receptacle. Furthermore, they describe the seeds as either erect or inverted, commonly protruding in some particular taxa with a fleshy epimatium, carpidium and receptacle with an embryo with two cotyledons (Figure 5.1) [1].

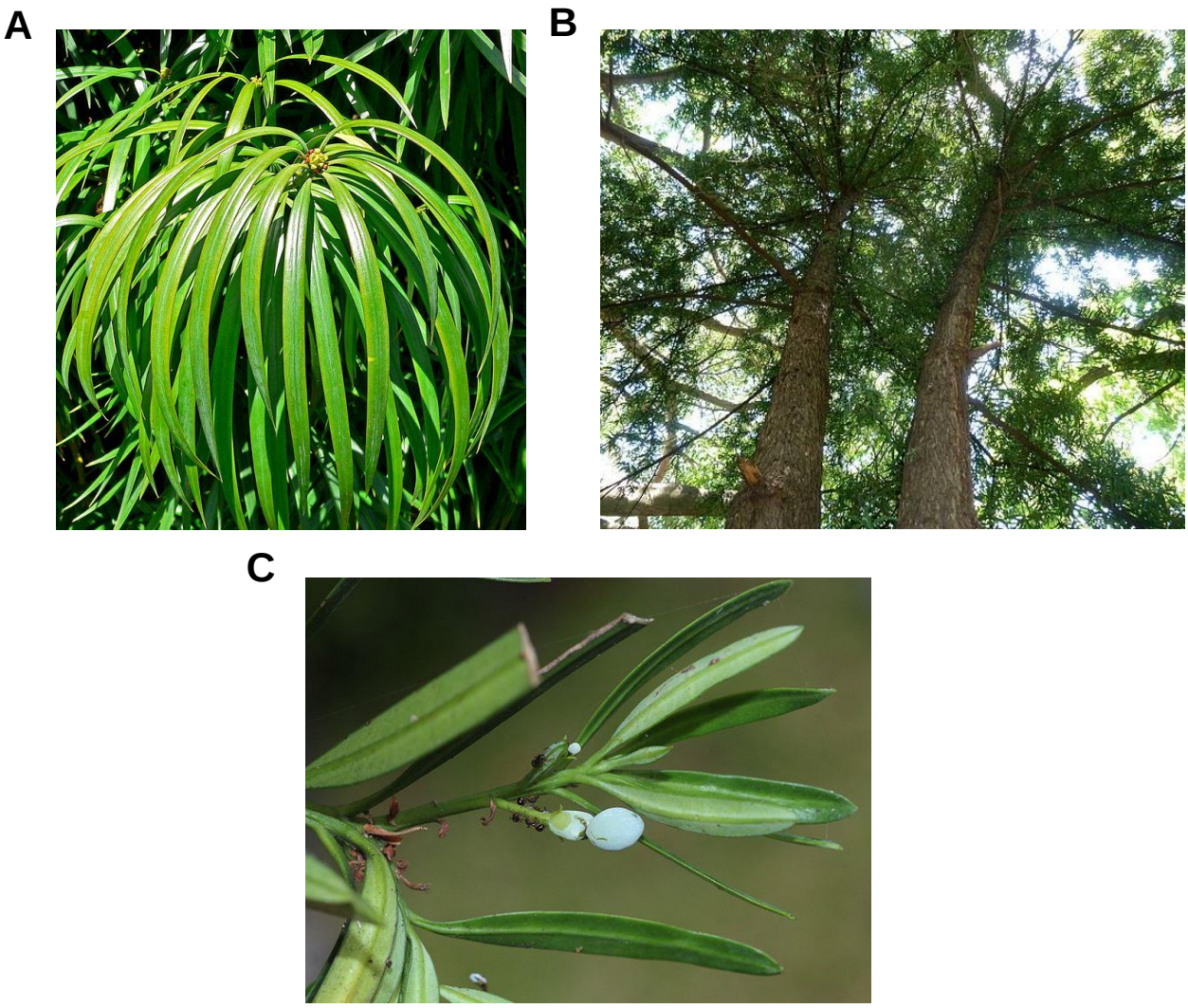

Figure 5.1: (**A**) Photograph of *P. henkelii* leaves by Stan Shebs, distributed under a CC BY-SA 3.0 license. (**B**) Photograph of a *P. henkelii* tree by JMK, distributed under a CC BY-SA 3.0 license. (**C**) Photograph of a *P. macrophyllus* seed by Alpsdake, distributed under a CC BY-SA 4.0 license.

The *Podocarpus sp.* consists of ca. 100 different species, well distributed in the southern hemisphere and parts of East Asia [3]. Of the numerous species distributed worldwide, only four occur in South Africa; these include *Podocarpus elongatus* L' Hèrit., *Podocarpus falcatus* (Thunb.) R. Br. Ex Mirb., Podocarpus *henkelii* Stapf ex Dallim. & Jacks. and *Podocarpus latifolius* (Thunb.) R. Br. Ex Mirb., all of which are used traditionally in South Africa, with *P. latifolius* renowned as South Africa's national tree [4].

P. henkelii is one of the four rare yellowwoods in South Africa and is known by different names in South Africa like 'Drooping-Leaf Yellowwood', 'Henkel-Se-Geelhout' (Afr.) and 'Umsonti' (Zulu, Xhosa). The plant grows naturally from the Eastern Cape to KwaZulu Natal [5]. Visually, *P. henkelii* closely resembles the other members of the genus in terms of the overall structure, bark, foliage, and seeds and is very popular in gardens as an ornamental tree.

The *Podocarpus sp.* have a comprehensive phytochemistry profile, with many secondary metabolites already having been isolated and characterised. A review article by Abdillahi et al. (2010) reports a large majority of those, which range from norditerpene dilactones, diterpene dilactone glycosides, monoflavonoids, bioflavonoids, flavonoid glycosides, C-glycosylflavones, flavonol 3-O-glycosides, flavonol 3-methlyether glycosides, dihydroflavonol glycoside to totarol diterpenes and sempervirol-type diterpenes [6]. A few of these are displayed in Figure 5.2.

Of the phytochemistry research conducted on *Podocarpus* sp., very little has been conducted on *P. henkelii*, with few literature outputs describing the isolation and characterisation of compounds from the plant. The most recent literature report is by Bagla (2013), who reports the isolation and characterisation of 3 compounds from the plant leaves. These being isoginkgetin **(49)**, podocarpusflavone-A **(50)** and 7', 4', 7", 4"'-tetramethoxyamentoflavone **(51)** (Figure 5.2) [7].

At the time of writing, however, no phytochemistry-type research had been conducted on the seeds of *P. henkelii*.

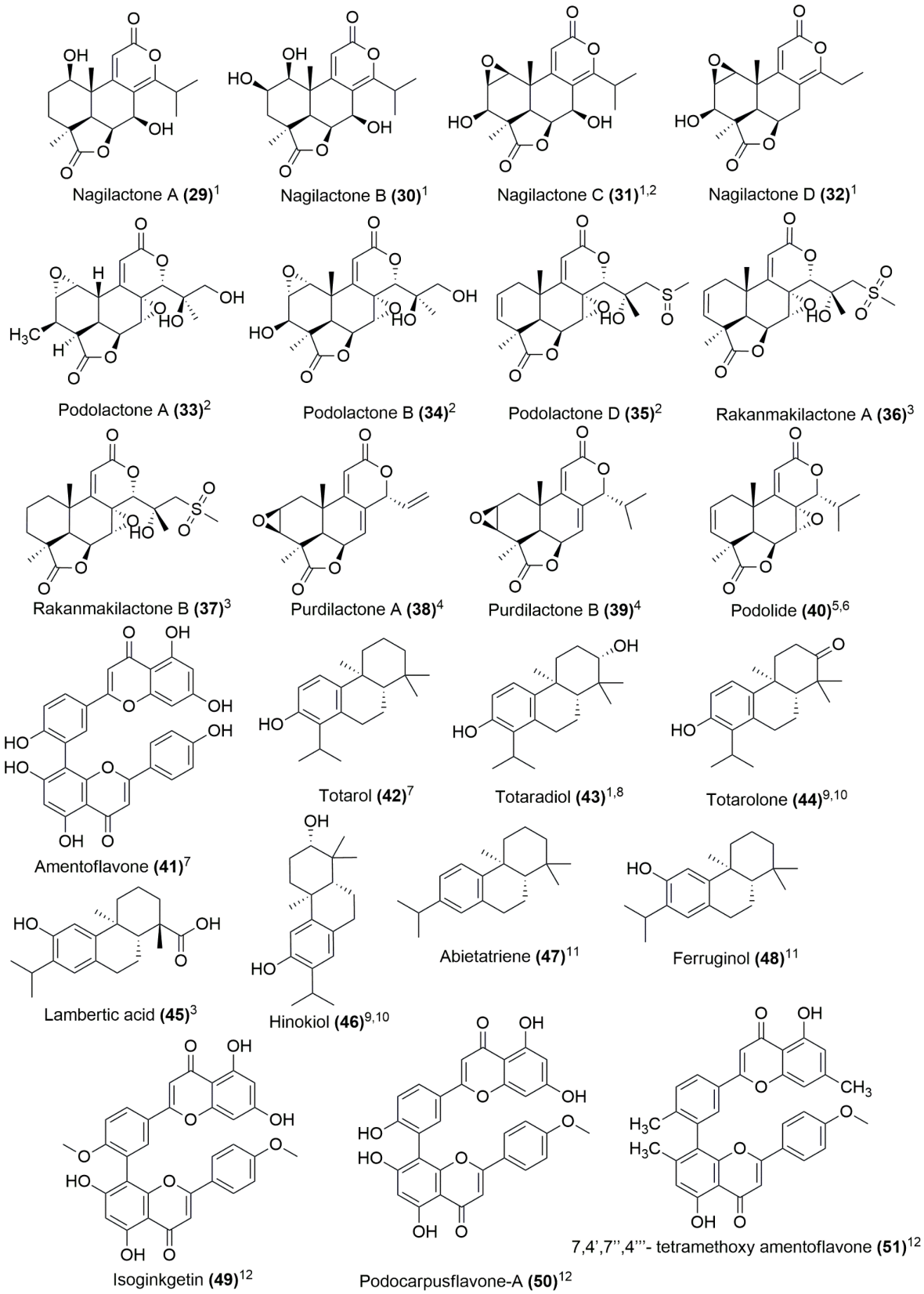

Figure 5.2: Common compounds identified in *Podocarpus sp.* as described by Abdillahi et al. (2010) and Bagla (2013) and isolated from [1]*P. nagi*, [2]*P. neriifolius*, [3]*P. macrophyllus* var. *maki*, [4]*P.purdieanus* Hook., [5]*P. gracilior*, [6]*P. falcatus*, [7]Non-selectviely in *Podocarpus sp.*, [8]*P. madagascariensis* Baker, [9]*P. nubigena* Lindl., [10]*P. saligna* D, [11]*P. ferrugineus* and [12]*P. henkelii* [6,7].

5.1.2 Traditional uses and biological assaying

The *Podocarpus* s.l. is a unique species of tree which is both used as a source of timber and, equally, used traditionally by populations in various parts of the world for the treatment of chest complaints, coughs, cholera, fever, asthma, arthritis, rheumatism, painful joints and even venereal diseases [3,4]. Another author reports that the species is used for heart, kidney, stomach and lung ailments, sweaty feet, worms, blood disorders, cholera, distemper in dogs and gall sickness in cattle [7]. In an article by Abdillahi et al. (2008), the authors highlight how the Maasai use the bark and stems of some *Podocarpus sp.* in East Africa as remedies for stomach aches and as a treatment for various cattle diseases. Similarly, decoctions of the fruit serve as a tonic for kidney, lung and stomach cleansing and the oil from the reproductive propagules, as a treatment for gonorrhoea. The authors also highlight how oil and bark from *P. falcatus* are used in Ethiopia to treat gonorrhoea and headaches, respectively [8].

In South Africa, the *Podocarpus* genus is traditionally used in KwaZulu Natal and Eastern Cape by the Zulu and woodmen working in the South African forests [4,8]. The woodmen reportedly use the sap of the four native *Podocarpus* sp. to treat chest complaints, and in the Eastern Cape, bark from *P. falcatus* and *P. latifolius* is used to treat gall sickness in cattle and canine distemper [8]. Although not widely reported, the bark of *P. henkelii* and *P. latifolius* is reportedly used by the Zulus in traditional medicine, including as a love charm, where the bark is chewed and spat into the wind while repeating the name of the person [4,6].

While other parts of the plant are traditionally used, some *Podocarpus sp.* fruits are also eaten. In literature works by Abdillahi et al. (2010), the authors detail how the fruits of *P. neriifolius*, *P. dacrydioides* A. Rich., *P. nivalis* Hook., *P. totara* and *P. salignus* are eaten in both a cooked and raw form and where *P. nagi* (Thunb.) Zoll. & Mortiz's fruits are widely sold in local markets in the Himalayas. Similarly, *P. spinulosa's* fruit is also used in Queensland in jam preserves. In Australia, the fleshy stems of *P. elatus* are eaten by the Aborigine people together with the fruit in a raw or cooked form [6].

These extensive reports of traditional uses have prompted much biological screening of the various species, many of which were found to be bioactive in various enzymatic and cellular-based assays against multiple microorganisms and diseases of interest. Some intriguing biological results were highlighted by Abdillahi et al. (2011) which include *P. latifolius*' potent antioxidant activity in DPPH assays (EC_{50} = 0.84 µg/mL), *P.elongatus* COX-1 inhibition (EC_{50} = 5.02 µg/mL) and dose-dependent tyrosinase inhibition (EC_{50} = 0.14 mg/mL). Totarol, a commercially available (produced from *Podocarpus totara*) topical anti-inflammatory drug

isolated from numerous *Podocarpus spp.,* was found to inhibit linoleic acid auto-oxidation, mitochondrial and microsomal lipid peroxidation induced by Fe (III)-ADP/NADPH [9].

The compound Nagilactone C **(31)** (*P. totara* and *P. neriifolius*) is described as having potent antiproliferative activity against human fibrosarcoma and murine colon carcinoma tumour cell lines with low ED_{50} values of 2.3 µg/mL and 1.2 µg/ml (6.0 and 3.2 µM) respectively [6,10]. Additionally, both taxol and totarol **(42)** are reported to exhibit good antitumor (antineoplastic) activity against 9 KB cell lines with totarol's ED_{50} = 4.9 µg/mL [6].

The norditerpene dilactones Rakanmakilactones A–F, isolated from *P. macrophyllus* var. *maki* Endl, are also reported to exhibit a potent cytotoxic effect against P388 murine leukaemia cells in a dose-response manner. Their IC_{50} values range from 0.31 µg/mL to 4.3 µg/mL [11]. S_R-Podolactone D **(35)** and S_S-Podolactone D **(35)** (*P. macrophyllus* var. maki) are also reported to possess cytotoxic activity against P388 murine leukemic cells with an IC_{50} value of 0.52 µg/ml and 0.23 µg/mL, respectively [12].

Some compounds isolated from *Podocarpus* spp. are also described to have antibacterial properties, with totarol **(42)** being one of the most widely reported. The compound possesses antibacterial activity against many bacteria species, including *Streptococcus mutans*, penicillin-resistant *Streptococcus pneumoniae*, Erythromycin-resistant *Streptococcus pyogenes* and even vancomycin-resistant *E. faecalis*, to name a few [6].

Four South African Podocarpus species were also investigated for antimicrobial activity, these being *P. elongatus*, *P. falcatus*, *P. henkelii* and *P. latifolius*. The four species presented a broad-spectrum antimicrobial activity against a few microorganisms, with the most following activities reported for the most potent plants, viz., *B. subtilis* (*P. henkelii*, MIC = 98 µg/mL), *Staphylococcus aureus* (*P. elongatus*, MIC = 98 µg/mL), *E. coli* (*P. henkelii, P. elongatus*, MIC = 390 µg/mL), *Klebsiella pneumoniae* (*P. elongatus*, MIC = 330 µg/mL) and *C. albicans* (*P. latifolus*, MIC = 30 µg/mL) [8].

The review article similarly describes the broad biological activity and use of some compounds and extracts of *Podocarpus* spp., which range from plant growth inhibitors, like the norditerpene dilactones and diterpene dilactones, e.g. nagilactones, podolactones and inumakilactones, to insect growth inhibitors, insecticidal activity and even insect feeding deterrent properties of the nagilactones. Other compounds, like ferruginol **(48)**, were found to possess gastroprotective activity comparable to the commercially used drug lansoprazole [6].

Totarol **(42)** also possesses potent antiplasmodial activity against the chloroquine-resistant strain of *Plasmodium falciparum*, whose IC_{50} was found to be 4.29 µM together with a larvicidal activity (LC_{50} = 0.25–0.37 µg/ml) and highlights the broad biological activity of a few essential compounds isolated form *Podocarpus spp.* [13,14].

As with the various other *Podocarpus spp.*, *P. henkelii* also possesses good biological activity in bioassays, albeit less researched. Petroleum ether and DCM extracts of the leaves and stem were found to have good COX-1 and COX-2 inhibitory activities in contrast to the 80% ethanol extract. Of particular note was the DCM extract of the leaves and stems against COX-1 enzyme, which was found to have an EC_{50} of 8.83 ± 0.11 µg/mL and 9.63 ± 0.08 µg/mL for the leaves and stem extract, respectively [4]. Crude acetone and methanol extracts of *P. henkelii* leaves are also described to have good activity against canine distemper virus (CDV) and lumpy skin disease virus (LSDV). The acetone extract was found to have an EC_{50} value of 3.76 µg/mL against CDV, with a SI of 12.01. The methanol extract was found to inhibit viral CPE of LSDV with an EC_{50} of 3.36 µg/mL and a SI of 45.61 [7].

Three bioflavonoids isolated from *P. henkelii*, i.e., isoginkgetin **(49)**, podocarpusflavone-A **(50)** and 7', 4', 7", 4"'-tetramethoxyamentoflavone **(51)** (cf. Figure 5.2) were also found to possess antimicrobial activity against a few pathogenic microorganisms. Of note, isoginkgetin **(49)** was found to be bioactive against *E. coli* (IC_{50} = 130 µg/mL), *S. aureus* (IC_{50} = 60 µg/mL), *Aspergillus fumigatus* (IC_{50} = 30 µg/mL) and *Cryptococcus neoformans* (IC_{50} = 30 µg/mL) with good selectivity indices. Podocarpusflavone-A **(50)** was also found to be active against *Enterococcus faecalis* and *Pseudomonas aeruginosa* with IC_{50} of 60 µg/mL against both microorganisms [7].

These reported and observed antimicrobial activities provide some rationale for the traditional use of some *Podocarpus spp.*

5.1.3 Use of *Podocarpus henkelii* by the Cape Parrot

P. henkelii is not one of the most widely used traditional medicines by South Africans; its importance from an ecological viewpoint, however, is far from mediocre. The tree plays an astronomically important role in the animal world, especially to the endemic Cape parrot (*Poicephalus robustus*)(Figure 5.3), where *P. henkelii* is the nesting tree of choice and an important source of food for the critically endangered bird [15–17].

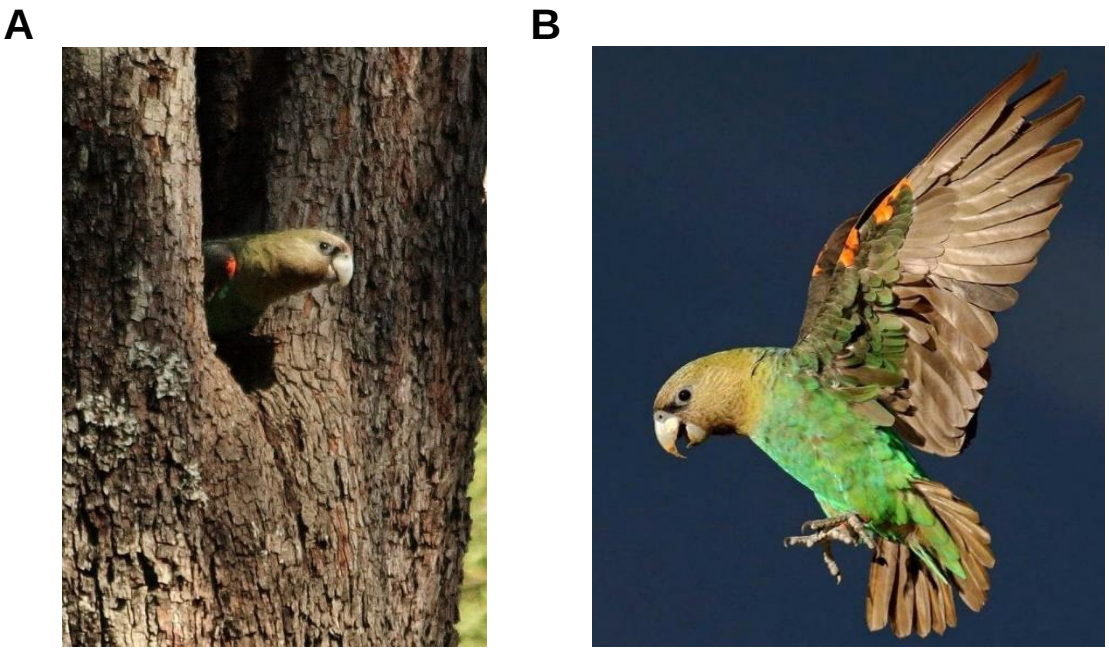

Figure 5.3: (**A**) Photograph of *Poicephalus robustus* by Alan Manson, distributed under a CC BY-SA 2.0 license. (**B**) Photograph of a *P. robustus* by Dave Brown, distributed under a CC0 1.0.

P. robustus is South Africa's only endemic parrot, with less than 1800 birds left in the wild and classified as 'Endangered' under the IUCN/Birdlife International threat criteria [17,18]. Their distribution is confined to mature Afromontane forests, which span from the Eastern Cape to the KwaZulu-Natal province (KZN). Some remnant populations of the parrot still occur in forests in the eastern Mpumalanga and southern Limpopo provinces [16]. The parrots' nest preferences are secondary cavities in forest canopy trees, with *Podocarpus* sp. being a particular favourite [17]. The parrots are food nomadics and travel locally in search of food which consists mainly of the endocarps of *Podocarpus* sp. and the occasional forest fruit [19]. The *Podocarpus* forest is a special forest habitat for the cape parrot and not only provides the parrot with nesting sites but also a source of food. *P. henkelii*, *P. falcatus* and *P. latifolius* are

key food sources for the parrot. The seeds and radicles of *P. henkelii,* being a favourite, are eaten while green and hard [17,19].

The various reasons for the low population numbers of the Cape Parrot are broad, with many possibilities. The most widely accepted reasons include habitat loss/forest degradation, exotic and commercial plantations of non-indigenous tree species, food and nest-site shortages, illegal pet bird trade and viral diseases like Psittacine Beak and Feather Disease (PBFD) (Figure 5.4) [15,20].

The fatal PBFD is caused by the *Circovirus sp.*, which spreads through contaminated water sources, nesting sites and ingestion/inhalation of the virus through feather dust. Viral infections occur in 3 forms which range in severity, these being acute, chronic and subclinical, with acute infections observed mainly in juveniles who only survive for a few months [15]. The disease leads to extreme feather loss, abnormal beak and nail growth and paralysis in the later stages of the disease (Figure 5.4) [17]. Although no extensive study has been conducted on how widespread PBFD is amongst the Cape Parrot population, reports of incidental and small-population sampling estimate that around 17% of the Eastern Cape population of parrots show clinical signs of the disease [15]. Alarmingly, in recent years, there has been an increase in the number of sightings of Cape Parrot, which present with PBFD symptoms [21].

Figure 5.4: Rose-breasted cockatoo (left) with severe feather loss and beak deformities and a sulphur-crested cockatoo (right) infected with BFDV by Shane R. Raidal, Charles Sturt University, distributed under CC BY-SA 4.0 license.

Although no direct link or correlation has been made between the Cape Parrot's consumption of *Podocarpus* sp. fruit and the incidence of PBFD in the parrot population, it would be unreasonable to assume an increased occurrence of PBFD and a decreased abundance of yellowwood species is purely coincidental. Similarly, the yellowwood's absence and parrots'

lack of favoured nesting and food source due to deforestation of the yellowwood forests, is the key contributor to the dwindling parrot population despite other trees fulfilling these needs. Could it be that the well-reported antimicrobial properties of *Podocarpus* sp. provide some protection/treatment to the birds, which rendered them less susceptible to diseases like PBFD? These sentiments were also shared in literature by Boyes RS (2010), who stated: “Perhaps the loss of the antimicrobial activity of yellowwood nuts in their diet is significant?” in reference to the widespread PBFD in the Cape Parrot population [22].

5.2 Materials and Methodology

5.2.1 Reagents and standards

The DCM, MeOH and FA analytical grade (AR) extraction solvents were purchased from Merck, South Africa (Merck, Darmstadt, Germany). The solvents used in the fractionation and HPLC purification, viz., the super purity HPLC grade MeOH and ACN, were purchased from Romil-SpS™, Microsep, South Africa (Waterbeach, Cambridge, UK) and the EtOAc from Sigma-Aldrich (Merck, Darmstadt, Germany).

5.2.2 Plant material and processing

P. henkelii fruit (green, fresh and hard) was collected from a plant in the University of Pretoria’s Hatfield campus gardens, Gauteng, South Africa. A voucher specimen was deposited at the H.G.W.J. Schweickerdt Herbarium (University of Pretoria) and was assigned a voucher specimen number: PRU 128788, where the plant’s identity was confirmed. The plant material was prepared by dissecting the seeds in quarters and airdrying them at room temperature for seven days (Figure 5.5). The dried fruit was then ground into a fine powder using a hammer mill before recording the dried weight and storing it at room temperature until extraction.

Figure 5.5: Halved *P. henkelii* seeds, collected from the University of Pretoria's Hatfield gardens.

5.2.3 Extraction

Microextraction using the solid phase extraction (SPE) was conducted as described in Chapter 2, Section 2.2.4. Thereafter, the upscale extraction was done in a batch fashion, where 45 g of the dried plant material was added to a 1L Erlenmeyer flask with 200 mL of DCM:MeOH (1:1) and stirred on a shaker bed overnight. Thereafter, the solution was filtered using a Büchner funnel and Whatman No. 1 filter paper and stored at 4 °C. A subsequent extraction cycle was done (on the same plant material) with 200 mL of 100% MeOH overnight. The solution was similarly filtered and combined with the DCM:MeOH (1:1) extract and concentrated on a rotary evaporator before drying down to completion in an SP Genevac HT6 (Genevac Ltd., Ipswich, UK), yielding a dry crude extract. The dry crude extract's yield was recorded before being stored at 4 °C before further analyses were conducted.

5.2.4 Primary fractionation

Primary fractionation for initial screening was done on a small quantity of extract as described in Chapter 2, Section 2.2.4, a method adapted from Thornburg et al. (2018) [23]. For isolation purposes, 3.6 g of extract was fractionated, as before, using a C8 SPE cartridge and a Gilson GX-241 ASPEC® liquid handler fitted with a Verity® 4060 pump controlled with TRILUTION® software. In this case, 7 different eluent systems were used in series to elute fractions rich in compounds with similar polarity. The eluent systems ranged from highly polar to moderately

non-polar in nature: 95:5 (H_2O:MeOH); 80:20 (H_2O:MeOH); 60:40 (H_2O:MeOH); 40:60 (H_2O:MeOH); 20:80 (H_2O:MeOH); 100 % MeOH and 1:1 (ACN:MeOH). Seven fractions were generated, one for each eluent system and collected in separate collection vessels on a volume-based collection method. Due to the variation in eluent systems, the fractions ranged from highly polar (Fraction 1) to moderately non-polar (Fraction 7). These fractions were dried in individually pre-weighed polytops using a Genevac HT6, their yields recorded, and samples stored at 4 °C until analysis was conducted.

5.2.5 Ultra-performance liquid chromatography-high resolution mass spectrometry (UPLC-HRMS)

The *P. henkelii*-derived samples were prepared and subsequently analysed using the same instrumentation and MS source conditions as previously described in Chapter 3, Section 3.3.5. The extract was prepared at a 1000 ppm concentration, the fractions at a 500 ppm concentration and the pure compounds at a 100 ppm concentration, respectively. The samples were analysed in both ESI-positive and ESI-negative ionisation modes. A minor modification was made in terms of the solvent system used, where solvent A consisted of H_2O (0.1% FA) and solvent B, MeOH (0.1% FA).

5.2.6 High-performance liquid chromatography (HPLC)-based fractionation of primary fraction 4 (LI-1-48E)

Due on the good bioactivity observed for primary fraction 4 (cf. Table 2.3) (labelled as LI-1-48E) (270 mg), produced from the SPE system, the fraction was prioritised for further analysed on a Waters chromatographic system equipped with a Waters photodiode array (PDA) detector (Model 2998) and ACQUITY QDa detector (Waters, Milford, MA, USA). The fraction was prepared by dissolving it in 1.5 mL H_2O:MeOH (2:3) before filtering using a 0.22 µm nylon filter. Initial analysis and method development were conducted on an analytical column (Xbridge® BEH analytical C18 OBD™ (4.6 x 150 mm, 5 µm)) before upscaling to preparative scale. A satisfactory chromatographic method was developed, which consisted of H_2O (0.1% FA), and MeOH (0.1% FA) used as solvent A and solvent B, respectively. The stepwise chromatographic method ran as follows: 8% solvent B for 1 min before a linear increase to 45 % solvent B over 4 min (1-4 min) followed by an isocratic hold at 45% solvent B for 11 min (8-15 min) before a linear increase to 100 % solvent B (15-17 min) where a column wash was incorporated for 3 min (17-20 min) followed by a linear return to starting conditions (20-21 min)

and a 4 min equilibration step (21-25 min). A flow rate of 1.1 mL/min and an injection volume of 5 µL was used.

Primary fraction 4 was subsequently fractionated using a semipreparative HPLC-PDA-MS instrument. Fractionation was done by means of a single injection (1.0 mL), on an Xbridge® Prep C18 OBD™ (19 × 250 mm, 5 µm) column. A step gradient method was developed based on the analytical work conducted. The solvent system consisted of H_2O (0.1% FA) and MeOH (0.1% FA) as solvents A and B, respectively. The chromatographic method was optimised with a flow rate of 19.0 mL/min and ran as follows: 8% solvent B for 1 min before a linear increase to 45 % solvent B over 8 min (1-8 min) followed by an isocratic hold at 45% solvent B for 17 min (8-25 min) before a linear increase to 100 % solvent B (25-29 min). A column wash was incorporated for 6 min (29-35 min) followed by a linear return to starting conditions (35-36 min) and a 7 min equilibration step (36-43 min).

For both analytical and preparatory work, the QDa (MS) was set to acquire in ESI positive mode, with data collection set at a range from 30 Da to 1250 Da. The source temperature was kept at 120 °C, with a probe temperature of 600 °C. The capillary voltage was set to 0.80 kV, and the cone voltage to 30.00 V. The PDA detector settings were optimised as follows: a sampling rate of 10 points/sec, a UV scan range of 210-400 nm and a resolution of 2.4 nm.

A time-based collection was used in which collection was done on an ongoing basis with fractions collected in 1.4 min intervals (from 1-28.8 min). The resulting fractions were dried using an SP Genevac HT6 before recording yields and storing at 4 °C prior to further analysis.

5.2.7 Mass-directed HPLC isolation of sandaracopimaric acid (53)

Sandaracopimaric acid **(53)** was purified in two chromatographic-based purification steps. The first was conducted as follows: primary fraction 6 (labelled LI-1-48G)(320 mg), produced from the SPE-based fractionation step, was further purified in the same Waters HPLC-PDA-MS chromatographic system as described in Section 5.2.6. The fraction was prepared by dissolving it in 3.5 mL MeOH (100%) before filtering using a 0.22 µm nylon filter. Analysis, method development and purification were conducted on a semi-preparative column (Xbridge® BEH analytical C18 OBD™ (10 x 150 mm, 5 µm)). A satisfactory chromatographic method was developed, which consisted of H_2O (0.1% FA), and MeOH (0.1% FA) used as solvents A and solvent B, respectively. The chromatographic method ran as follows: an isocratic hold at 65% solvent B for 1 min before a linear increase to 100% solvent B over 16 min (1-17 min) followed by an isocratic column wash at 100% solvent B for 3 min (17-20 min)

followed by a linear return to starting conditions (20-21 min) and a 3 min equilibration step (21-24 min). A flow rate of 5.0 mL/min and an injection volume of 200 µL was used.

A manually set time-based collection was used to trigger the collection of MS and UV intense peaks, of particular interest were those with *m/z* 303 $[M+H]^+$ and λ_{max} = 210 nm. The resulting fraction (Labelled LI-1-99H) was dried using an SP Genevac HT6 before recording the yield and storing at 4 °C prior to further analysis.

The second purification step was optimised as follows: LI-1-99H (132 mg) was prepared by dissolving it in 1.0 mL MeOH (100%) before filtering using a 0.22 µm nylon filter. Analysis, method development and purification were conducted on a semi-preparative column (Xbridge® BEH analytical C18 OBD™ (10 x 150 mm, 5 µm)). A satisfactory chromatographic method was developed, which consisted of H_2O (0.1% FA) and MeOH (0.1% FA) used as solvent A and solvent B, respectively. The chromatographic method ran as follows: an isocratic hold at 87% solvent B for 1 min before a linear increase to 100% solvent B over 16 min (1-17 min) followed by an isocratic column wash at 100% solvent B for 3 min (17-20 min) followed by a linear return to starting conditions (20-21 min) and a 3 min equilibration step (21-24 min). A flow rate of 5.0 mL/min and an injection volume of 200 µL was used.

A manually set time-based collection was used to trigger the collection of MS and UV intense peaks, of particular interest were those with *m/z* 303 $[M+H]^+$ and λ_{max} = 210 nm. The resulting 4 fractions (Labelled LI-1-101C to LI-1-101F) were dried using an SP Genevac HT6 before noting the yields and storing at 4 °C prior to further analysis.

For both sets of analyses, the QDa (MS) was set to acquire in ESI positive mode, with data collection set at a range from 100 Da to 1000 Da. The source temperature was kept at 120 °C, with a probe temperature of 550 °C. The capillary voltage was set to 0.80 kV, and the cone voltage to 15.00 V. The PDA detector settings were optimised as follows: a sampling rate of 10 points/sec, a UV scan range of 210-400 nm and a resolution of 2.4 nm.

5.2.8 NMR analysis of sandaracopimaric acid (53)

For compound identity confirmation, sandaracopimaric acid **(53)** was prepared and analysed using NMR spectroscopy.

Sandaracopimaric acid **(53)** was dissolved in 500 µL $CDCl_3$ and analysed in a 5 mm NMR tube. Subsequent NMR analyses were conducted at 25 °C on a Bruker 500 MHz NMR, fitted

with a BBO 500 S1 prodigy probe (cryoprobe). The operating frequency for the ^{1}H and ^{13}C was 500.0031 MHz and 125.738 MHz, respectively.

Data processing was done using ACDLabs Spectrus Processor v 2021.1.1. All chemical shifts are reported in ppm (δ-scale), with coupling constants "*J* ", reported in Hertz (Hz). Trace protons from the deuterated solvent were used to calibrate the resulting spectra, i.e., δ_H = 7.24 ppm and δ_C = 77.2 ppm for chloroform-d ($CDCl_3$).

5.2.9 Separation and Single Crystal X-ray Diffraction (SCXRD) analysis of inumakilactone B (52) and sandaracopimaric acid (53)

Purified inumakilactone B **(52)** was obtained by dissolving secondary fraction 6 (labelled LI-1-64F) in 500 µL of MeOH before placing it in a polytop with a perforated lid and leaving it undisturbed at room temperature. After 2 days, crystals appeared, which were centrifuged out of the mother liquor at 4000 rpm. As with inumakilactone B **(52)**, crystals of sandaracopimaric acid **(53)** were obtained by dissolving LI-1-101E in 500 µL of MeOH before placing it in a polytop with a perforated lid and leaving it undisturbed at room temperature. After 2 days, crystals appeared, and the polytop was sealed to avoid further solvent evaporation and dehydration of the crystals.

X-ray diffraction analysis was conducted on both inumakilactone B **(52)** and sandaracopimaric acid **(53)**.

For valid results, four single crystals, with different morphology, of inumakilactone B **(52)** and sandaracopimaric acid **(53)** were selected and analysed on a Rigaku XtaLAB Synergy-R diffractometer with diffraction measurements performed at 150 K with the use of an Oxford Cryogenics Cryostat. The instrument has a rotating-anode X-ray source (monochromated Cu Kα radiation (k = 1.54184 Å)) and a HyPix CCD detector. Absorption and data reduction were done using CrysAlis^{Pro} v. 1.171.40.39a. The analysed structures were solved using intrinsic phasing with ShelXle. Subsequent refinement was done using ShelXle-2014/7 using the ShelXle interface. For chemical accuracy, all H atoms were placed in geometrically idealised positions, additionally constrained to ride on their parent atoms. Structural elucidation of the target structures was done using Olex software [24]. Refinement and collection parameters are described in Table 5.6 and Table 5.10. The X-ray crystallographic coordinates of inumakilactone B **(52)** have been deposited at the Cambridge Crystallographic Data Centre (CCDC), with deposition numbers CCDC: 2250652

The X-ray crystallographic coordinates of sandaracopimaric acid **(53)** were previously deposited in the CCDC by Comte et al. (1995) [25] and Liu et al. (2007) [26], which correlate with deposition numbers 1315639 and 602370, respectively.

5.2.10 SARS-CoV-2 Plaque-based bioassays

P. henkelii extract, fractions and the isolated pure compounds were tested in viral plaque-based bioassays conducted personally at the University of Basel, Department of biomedicine, under Professor Thomas Klimkait. The bioassays were carried out as described in Chapter 2, Section 2.3.2. The initial samples, viz., the extract and primary fractions, were tested against the Wuhan strain of the virus (the only variant available at the time) at 25 µg/mL. Later, crystals of inumakilactone B **(52)** and sandaracopimaric acid **(53)** were sent for bioassays. The bioassays of the pure compounds were performed in a dose-dependent manner and tested against clinical isolates of the Beta and Omicron variants of the SARS-CoV-2 virus. Additionally, cytotoxicity testing was conducted on the pure compounds using healthy Vero E6 cell lines to estimate the cytotoxic concentration (CC_{50}) and calculate the selectivity index (CC_{50}/IC_{50}) of the compounds. The compounds were evaluated for response in a dose-dependent manner which ranged from 0.02-5 µg/mL for both inumakilactone B **(52)** and sandaracopimaric acid **(53)**. For valid results, remdesivir was used as a positive control, being widely reported as an antiviral against SARS-CoV-2 *in vitro*, similarly an FDA-approved drug for use in severe SARS-CoV-2 cases [27–30].

5.2.11 AlphaScreen binding assays and M^{pro} inhibition assay

The *P. henkelii*-derived samples, which included the extract, fractions and pure compounds, namely, inumakilactone B **(52)** and sandaracopimaric acid **(53)**, were tested for any antiviral activity against the spike and M^{pro} SARS-CoV-2 enzymes. The analyses were conducted by collaborators at the Wistar Institute (USA), under the supervision of Prof. Ian Tietjen, where the samples were screened in AlphaScreen spike RBD/ACE2 inhibition assays and M^{pro} inhibition assays with methodology previously described in Tietjen et al. (2021) and Invernizzi et al. (2022) and similarly described in Chapter 2, Section 2.3.1 [28,31]. For compound selectivity determination against the spike RBD/ACE2 interaction and M^{pro} enzyme, respectively, the compounds were similarly tested for activity against an unrelated PD-1/PD-L1 ligand/receptor pair and Cathepsin L. enzyme. For valid results, the extract and fractions

were screened in triplicate in a dose-dependent manner. The control-neutralising antibodies REGN10987 (imdevimab) and REGN10933 were used as positive controls for comparison.

5.3 Results and discussion

5.3.1 Extraction, fractionation and bioassaying

A sequential ultrasonicator-mediated extraction method was used to produce a small quantity of extract for the initial antiviral screening. Based on the good bioactivity and high yield obtained from the DCM:MeOH extraction method, in comparison to the ethanol-based extracts (cf. Table 2.2 and Table 2.3), the DCM:MeOH extraction method was used for subsequent analyses. The DCM:MeOH extraction of 6.8 g of plant material yielded 1.23 g (18.1% yield) of a sticky dark-yellow extract. Subsequent fractionation of a 190 mg portion of the dried extract using the SPE yielded 7 semi-pure fractions with the percentage yield ranging from 24.8% to 1.4% (Table 5.1).

Table 5.1: Mass and yield (%w/w) of the extract and primary fractions produced from the SPE fractionation of the *P. henkelii* DCM:MeOH extract.

Sample	Mass (mg)	Yield (%w/w)
Dry plant material	6 800	N/A
Extract	1 230	18.1
Fraction 1	34.2	18.0*
Fraction 2	47.1	24.8*
Fraction 3	22.3	11.7*
Fraction 4	12.5	6.6*
Fraction 5	2.7	1.4*
Fraction 6	21.2	11.2*
Fraction 7	5.4	2.8*

*Based on 190 mg of extract used

Based on the observed % yields, skewed more towards the polar fractions, one can assume a high concentration of polar compounds such as sugars are present, giving credence to the fruits' uses in jams [6]. The extract and fractions were screened in spike RBD/ACE2 interaction and M^{pro} inhibition bioassays and similarly in SARS-CoV-2 plaque-based bioassays at 25 µg/mL.

In the AlphaScreen bioassays, the *P. henkelii* extract and primary fractions (2-6) showed good activity, with their IC_{50} values found to be in the low µg/mL range, activity not observed for the method blank (Figure 5.6; Table 5.2). Of particular interest were Fractions 3 and 4, which were found to have an IC_{50} of 0.194 ± 0.214 µg/mL and 0.31 ± 0.29 µg/mL, respectively. The samples were also assessed for selective inhibition of the spike RBD/ACE2 interaction by assessing their ability to disrupt an unrelated PD-1/PD-L1 ligand/receptor pair. The selectivity index of the fractions ranged broadly between the fractions, with a selectivity index (SI) >25 noted for the two most active fractions, i.e., Fraction 3 and Fraction 4 whose SI was found to be 26.4 and >32.1, respectively (Table 5.2).

The positive control, REGN10987, was similarly found to disrupt the spike RBD/ACE2 interaction with an IC_{50} of 0.025 µg/mL.

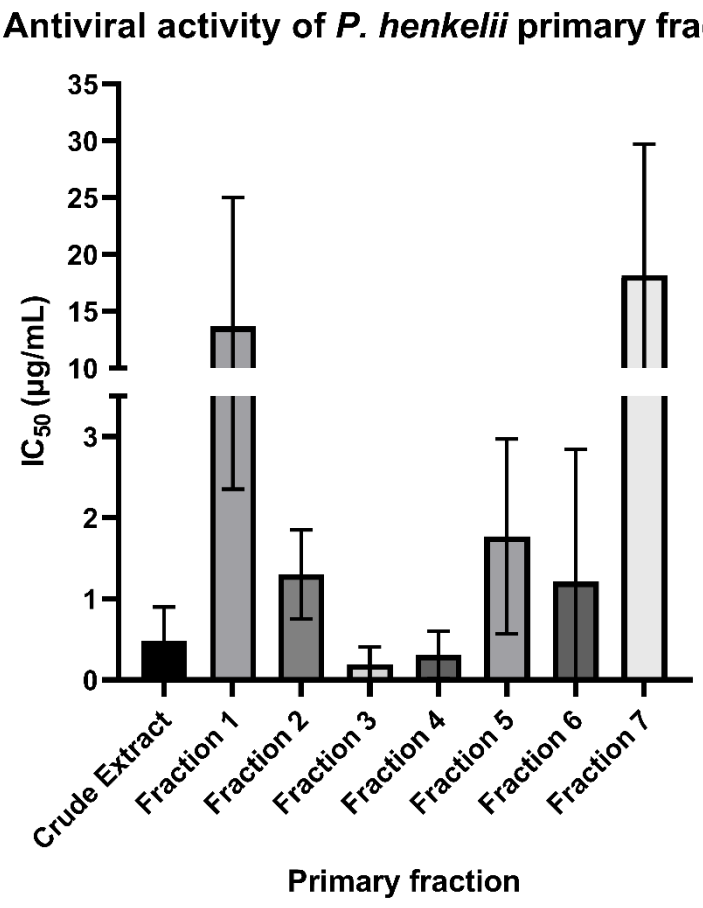

Figure 5.6: Spike RBD/ACE2 interaction inhibition (IC_{50}) of *P. henkelii* primary fractions screened in AlphaScreen bioassays against the WT(USA-WA1/2020).

In contrast to the AlphaScreen bioassays, the extract and fractions showed little to no activity against the M^{pro} SARS-CoV-2 enzyme, with their respective IC_{50} values all found to be >100 µg/mL (Table 5.2).

Table 5.2: Spike RBD/ACE2 and M^{pro} inhibition data (IC_{50}) of the *P. henkelii* extract and primary fractions.

Sample Label	**Detail**	**Spike RBD/ACE2 (IC_{50} (µg/mL))**		**PD-1/PD-L1 (IC_{50} (µg/mL))**	**Selectivity Index (SI)**	**M^{Pro} (IC_{50} (µg/mL))**
		Average	SD	Average		
LI-1-09C	Crude Extract	0.48	0.42	2.727	5.7	>100
LI-1-16A	Primary Fraction 1	13.69	11.34	5.87	0.4	>100
LI-1-16B	Primary Fraction 2	1.3	0.55	7.276	5.6	>100
LI-1-16C	Primary Fraction 3	0.194	0.214	5.114	26.4	>100
LI-1-16D	Primary Fraction 4	0.31	0.29	> 10	> 32.1	>100
LI-1-16E	Primary Fraction 5	1.77	1.2	> 10	> 5.6	>100
LI-1-16F	Primary Fraction 6	1.211	1.628	> 10	> 8.3	>100
LI-1-16G	Primary Fraction 7	18.18	11.57	> 10	> 0.5	>100

As demonstrated by the single-point plaque-based bioassays (Figure 5.7), Fraction 4 and Fraction 6/7 were found to demonstrate the greatest inhibition against the virus-induced cytopathic effect, with Fraction 4 and Fraction 6/7 presenting ca. 75% inhibition of the viral cytopathic effect imposed by the virus. Based on these results, *P. henkelii* contains compounds with good, selective antiviral activity against the SARS-CoV-2 virus, with the mode of action hypothesised to be by the disruption of the spike RBD/ACE2 interaction.

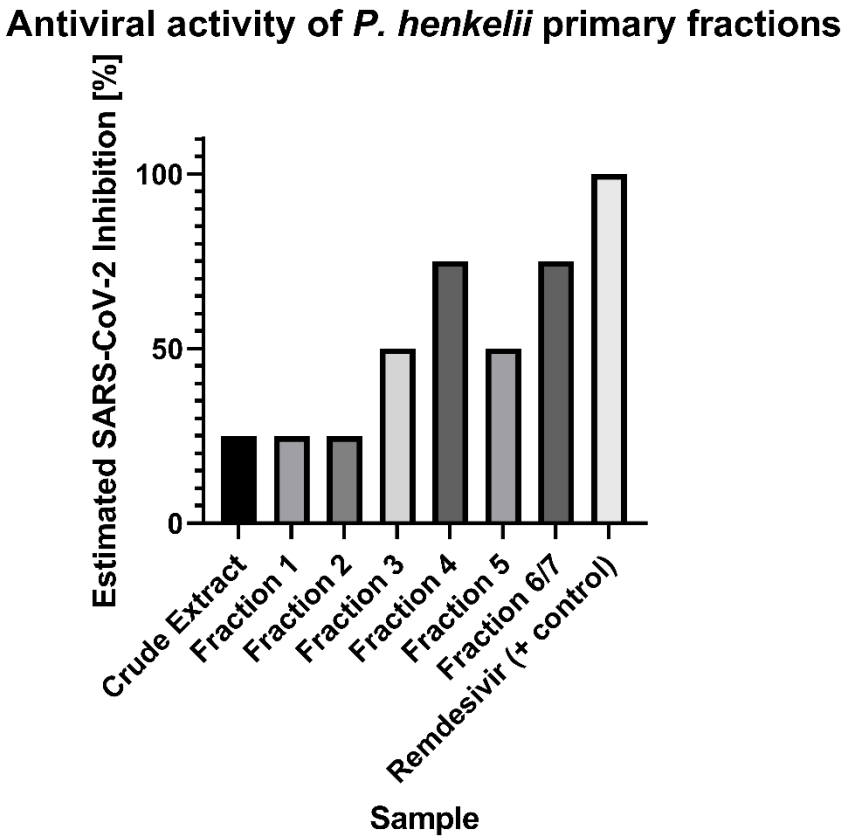

Figure 5.7: Single point bioassay results of the *P. henkelii* extract, primary fractions, and the positive control (remdesivir) to inhibit plaque formation in plaque-based bioassays against the Wuhan strain of the SARS-CoV-2 virus at 25 µg/mL.

UPLC-HRMS analysis of the DCM:MeOH extract showed the presence of a broad range of compounds, ranging from highly polar to highly non-polar (Figure 5.8). Comparison of the extract (labelled as LI-1-48A) and the bioactive primary Fraction 4 (labelled as LI-1-48E) showed similarities in a few of the more polar intense peaks (peak 1-3) (Figure 5.9), which were of interest for further purification and biological assaying.

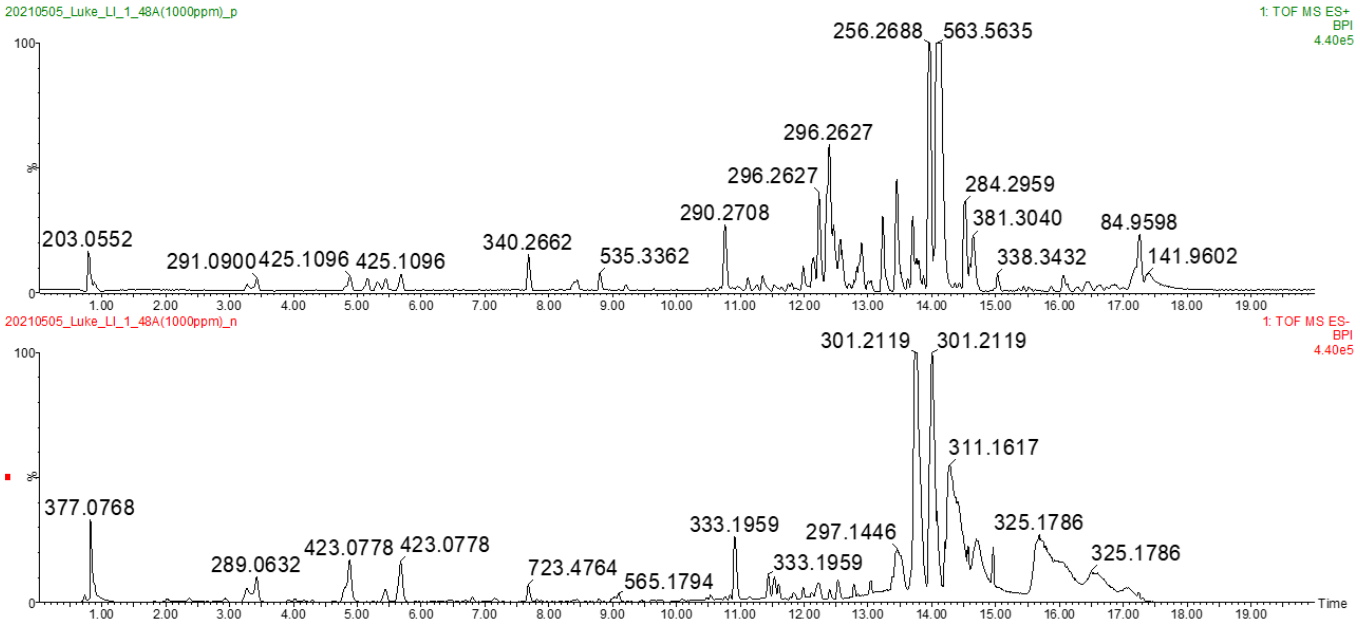

Figure 5.8: UPLC-HRMS BPI chromatogram of the crude DCM:MeOH extract of *P. henkelii* analysed in both ESI positive mode (top) and ESI negative mode (bottom).

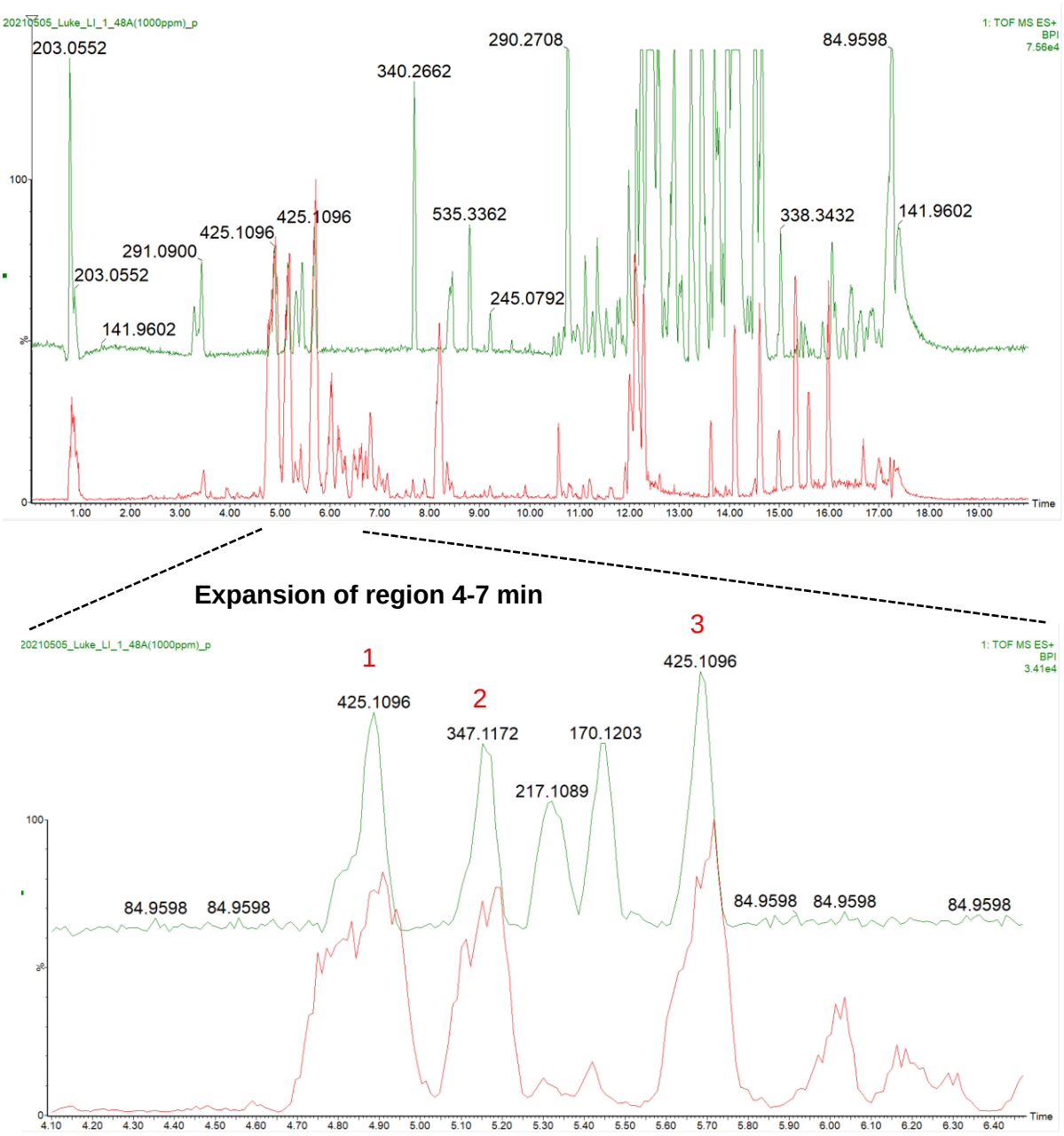

Figure 5.9: UPLC-HRMS BPI chromatogram of the crude (top) and bioactive primary Fraction 4 (bottom) of *P. henkelii* analysed in ESI positive mode. Expansion of the 4-7 min region highlights compounds common to both samples and hypothesised to be the bioactive compounds, highlighted as peak 1-3.

5.3.2 Secondary fractionation of LI-1-48E and biological assaying

In order to obtain more bioactive primary fractions for purification purposes, a batch extraction was conducted on 45.0 g of plant material, where 10.0 g of dried extract was obtained. A repeat SPE-based fractionation step was conducted on 3.60 g (22.2% yield) of the extract with similar yields obtained to those originally observed (cf. Table 5.1).

Due to the complexity of the primary fractions, a secondary fractionation step was done on Primary Fraction 4 (labelled as LI-1-48E) using the preparatory HPLC-PDA-MS and a reverse phase C18 column yielding 19 secondary fractions (labelled as LI-1-64A to LI-1-64S) with varying yields obtained (Table 5.3). Based on the observed HPLC-PDA-MS chromatogram (Figure 5.10), the fraction is presumed to consist mainly of polar compounds, with major peaks observed toward the beginning of the chromatogram, correlating with the mass yield obtained.

Table 5.3: Mass and yield (%w/w) of the secondary fractions produced by fractionation of Primary Fraction 4 (267 mg) (labelled as LI-1-48E) using a HPLC-PDA-MS.

Sample	Mass (mg)	Yield (%)*
Fraction 1 (LI-1-64A)	35.11	13.15
Fraction 2 (LI-1-64B)	33.55	12.57
Fraction 3 (LI-1-64C)	28.66	10.73
Fraction 4 (LI-1-64D)	26.86	10.06
Fraction 5 (LI-1-64E)	32.15	12.04
Fraction 6 (LI-1-64F)	15.22	5.70
Fraction 7 (LI-1-64G)	9.45	3.54
Fraction 8 (LI-1-64H)	5.63	2.11
Fraction 9 (LI-1-64I)	6.66	2.49
Fraction 10 (LI-1-64J)	4.02	1.51
Fraction 11 (LI-1-64K)	3.94	1.48
Fraction 12 (LI-1-64L)	0.84	0.31
Fraction 13 (LI-1-64M)	2.28	0.85
Fraction 14 (LI-1-64N)	5.76	2.16
Fraction 15 (LI-1-64O)	1.13	0.42
Fraction 16 (LI-1-64P)	1.12	0.42
Fraction 17 (LI-1-64Q)	3.83	1.43
Fraction 18 (LI-1-64R)	3.62	1.36
Fraction 19 (LI-1-64S)	1.09	0.41

*Based on a 267 mg injection

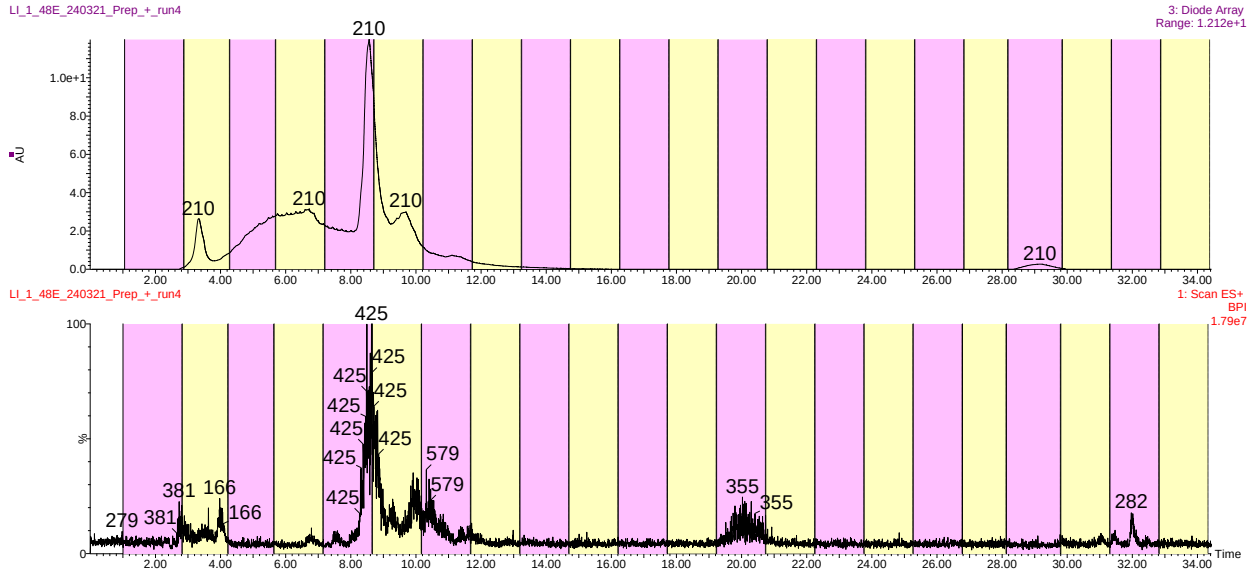

Figure 5.10: (**A**) UV chromatogram and (**B**) BPI MS chromatogram of the bioactive primary Fraction 4 (labelled as LI-1-48E) of *P. henkelii* fractionated in ESI positive mode on a Waters HPLC-PDA-MS instrument.

Samples of the secondary fractions were screened in SARS-CoV-2 plaque-based bioassays at 25 µg/mL and in spike RBD/ACE2 inhibition bioassays.

Of the various secondary fractions screened, Secondary Fraction 6 (labelled as LI-1-64F) was found to inhibit 100% of the viral cytopathic effect imposed by the SARS-CoV-2 virus, with activity equivalent to the positive control, remdesivir, at 25 µg/mL (Figure 5.11). Similarly, the fraction possessed good inhibitory activity in the spike RBD/ACE2 interaction screens (AlphaScreens) with an average IC_{50} value of 0.56 µg/mL (Figure 5.12). Although other secondary fractions were found to have good activity in AlphaScreens, based on the good corresponding data observed between the two independent biological assays, i.e., the plaque-based bioassays and the AlphaScreens only Secondary Fraction 6 (Labelled as LI-1-64F) was prioritised for further chemical investigation. Although multiple compounds seem to be contributing to the overall activity observed in the fraction and extracts, LI-1-64F was hypothesised to contain one of the major contributing compounds with selective activity against the SARS-CoV-2 virus with its MOA hypothesised to be by inhibition of viral entry.

UPLC-HRMS analysis of LI-1-64F, in ESI positive mode, showed the presence of an intense peak with a high instrument response, viz. *m/z* 347, which was observed in both the original extract and bioactive primary fraction and not in any of the method blanks (Figure 5.13).

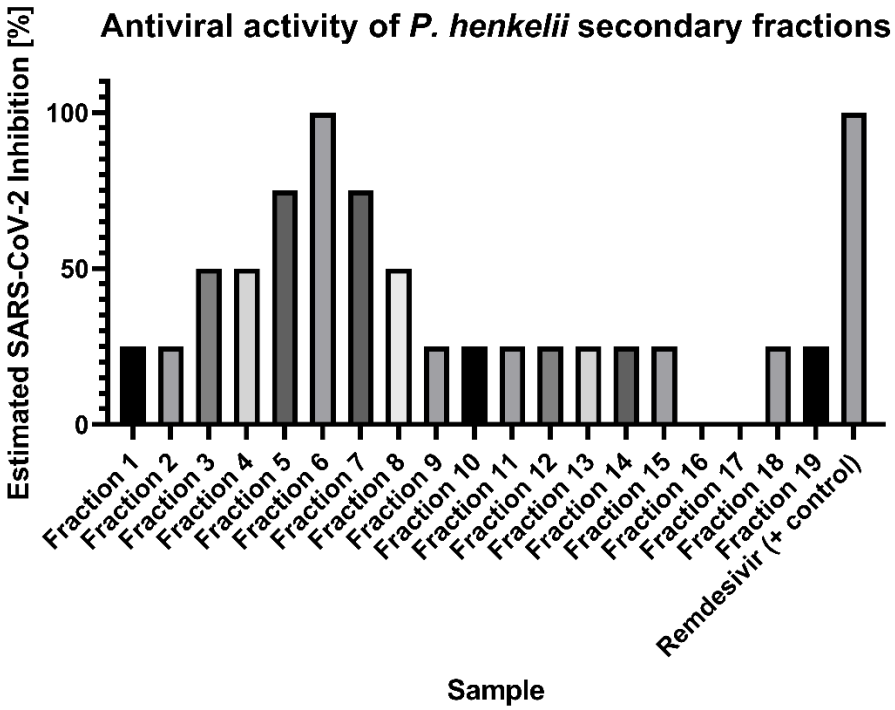

Figure 5.11: Single point bioassay results (n=1) of the *P. henkelii* secondary fractions and the positive control (remdesivir) in plaque-based bioassays against the SARS-CoV-2 Wuhan strain at 25 µg/mL.

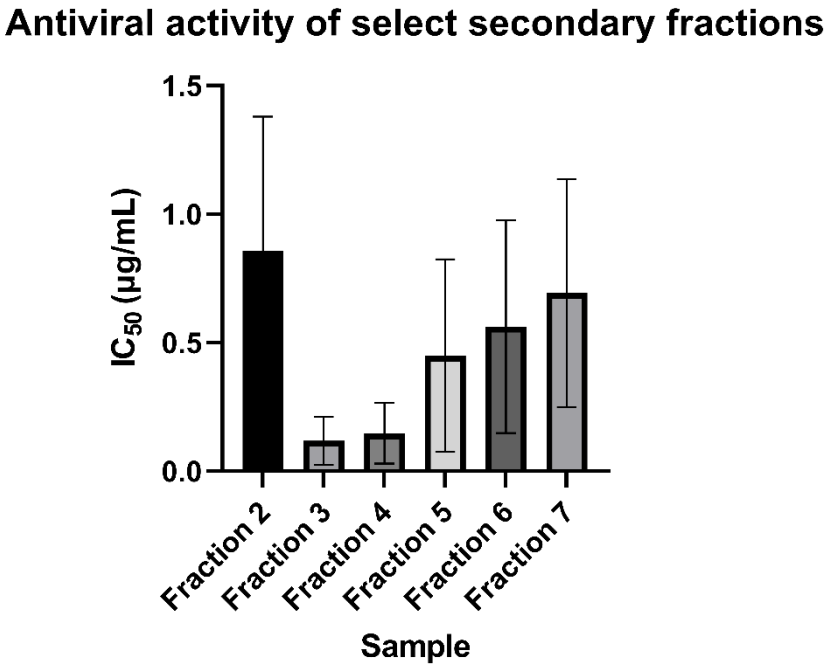

Figure 5.12: Spike RBD/ACE2 interaction inhibition (IC_{50}) of select *P. henkelii* secondary fractions screened in AlphaScreen bioassays against the WT.

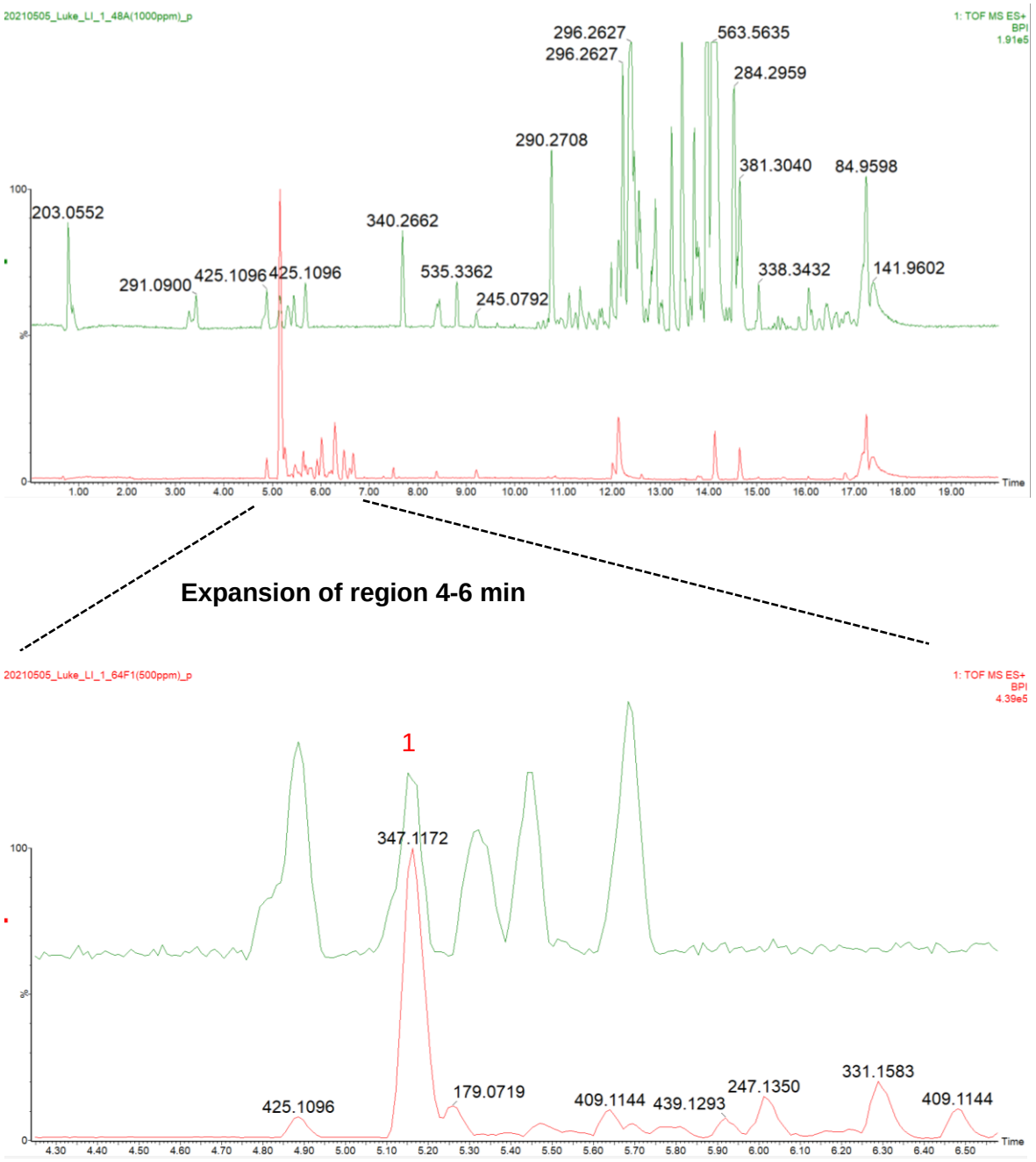

Figure 5.13: Overlay of the UPLC-HRMS BPI chromatogram of the bioactive primary Fraction 4 (top) and the bioactive secondary fraction (LI-1-64F) (bottom) of *P. henkelii* analysed in ESI positive mode. Expansion of the 4-7 min region highlight compounds common to both samples and hypothesised to be the bioactive compound, peak highlighted as '1' with *m/z* 347.

5.3.3 Compound isolation, structure elucidation and bioassays

5.3.3.1 Inumakilactone B (52)

Purification and identification of *m/z* 347.1129 $[M+H]^+$, i.e., compound **52**, was achieved by evaporative crystallisation, centrifugation to remove pelleted crystals and subsequent SCXRD and MS spectroscopic analysis in order to identify the compound and gain a better understanding of the molecule's physical and chemical characteristics.

Of the 15.2 mg of Secondary Fraction 6 (LI-1-64F), 0.7 mg of compound **52** was obtained in the form of fine, short, transparent needle-like crystals from the mother liquor.

Single crystals, suitable for X-ray diffraction, were successfully grown of compound **52**, with SCXRD analysis conducted on 5 independent crystals for validity. The compound was found to crystallise in an orthorhombic space group $P2_12_12_1$ (nr. 19) with Z=1, and was identified as inumakilactone B **(52)**, a diterpene lactone (Figure 5.14) and plant growth inhibitor originally isolated from *P. macrophyllus* seeds [32].

As expected, the compound's decalin rings took on a puckered low-energy configuration for saturated and fully substituted cycloalkanes. No abnormal bond lengths or dihedral angles were noted (Table 5.4; Supplementary Data, Table S5.1). The Flack parameter of the compound was found to be -0.14, providing reassurance that the obtained structure is the absolute configuration of the compound.

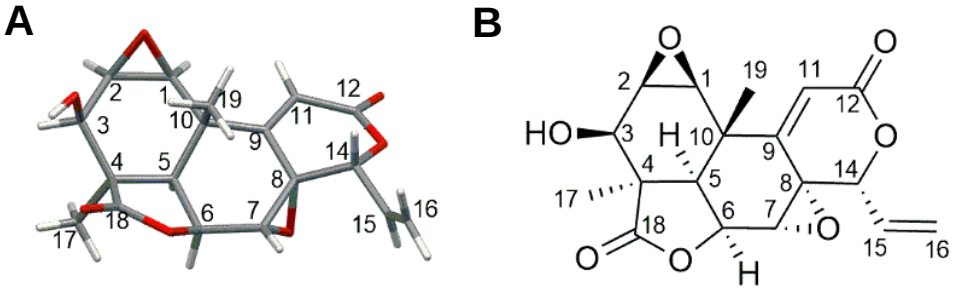

Figure 5.14: (**A**) SCXRD structure of inumakilactone B, processed with Mercury v2021.3.0 (**B**) Stick diagram illustrating the absolute configuration of inumakilactone B **(52)**.

Table 5.4: Torsions/dihedral angles of inumakilactone B **(52)**.

Atom 1	Atom 2	Atom 3	Atom 4	Torsion Angle(°)
O13	C14	C15	C16	128.129
C16	C15	C14	C8	-114.498

Crystal packing was found to be facilitated by a strong intermolecular hydrogen bond between the epoxide formed between C7/C8 (O as the hydrogen bond acceptor) and the alcohol group of C3 (H as donor) (Figure 5.15; Supplementary Data, Figure S5.1 and Figure S5.2). The hydrogen bonding information is detailed in Table 5.5. Crystal data and structure refinement parameters are presented in Table 5.6.

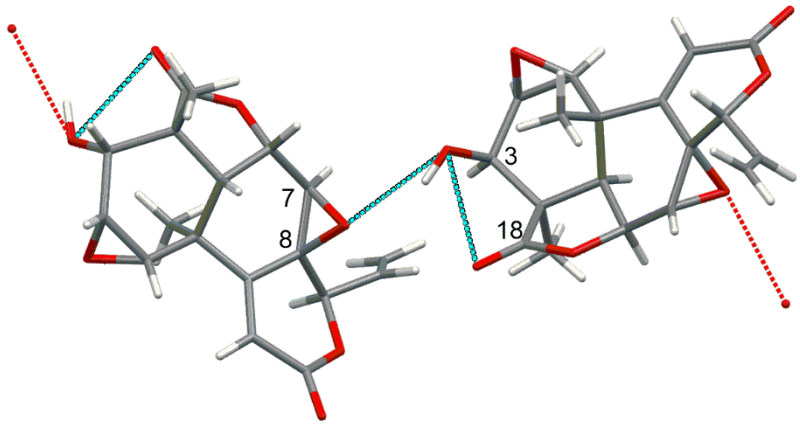

Figure 5.15: SCXRD structure of inumakilactone B **(52)**, illustrating the intermolecular hydrogen bond between the oxygen of the epoxide (C7/C8) and C3-OH. An intramolecular hydrogen bond is observed between the carbonyl group of C18 and C3-OH.

Table 5.5: Intermolecular hydrogen-bonding interactions observed within the inumakilactone B **(52)** crystal structure.

Donor	Acceptor	D-H (Å)	H...A (Å)	D...A (Å)	D-H...A (°)
C3-O-H	O7	0.84	2.100	2.854	149.2

Table 5.6: SCXRD refinement and collection parameters of inumakilactone B **(52)**.

Compound	**Inumakilactone B (52)**
Emp. Formula	$C_{18}H_{18}O_7$
CCDC Identifier	2250652
Molecular weight (g.mol^{-1})	346.32
Crystal description	Translucent needles
Crystal system	Orthorhombic
Space group	$P2_12_12_1$ (no. 19)
a (Å)	7.8300
b (Å)	11.5611
c (Å)	16.4405
α (º)	90.00
β (º)	90.00
γ (º)	90.00
Volume (Å^3)	1488.25
Z	Z: 1
F(000)	728.0
Independent refl.	2790 [R_{int} = 0.0377, R_{sigma} = 0.0362]
Completeness (%)	100
Data/Restr/Para	2790/0/234
Goodness of fit on F^2	1.131
Final R1 indexes (I > 2σ(I))	0.0332
wR2 indices (all data)	0.0801
Largest diffraction peak and hole (e.Å^{-3})	0.21/-0.23
Flack parameter	-0.14(15)

The UPLC-HRMS analysis of the inumakilactone B **(52)** chromatographic peak was observed at *m/z* 347.1129 $[M+H]^+$ (RT: 6.8 min), where the peak was found to have a monoisotopic mass of 346.1051 Da (mass error -0.2 mDa). The peak had a molecular formula of $C_{18}H_{18}O_7$ (calculated 346.1053 Da). Further analysis of the low and high-energy MS fragmentation pattern for inumakilactone B **(52)** showed the presence of multiple MS peaks. Although to date, no published ESI+ MS spectra exists for the molecule, the spectra may be of use to future research. The data provides supporting evidence for the successful identification of *m/z*

347 $[M+H]^+$, namely inumakilactone B **(52)**, with the chromatogram, retention time and accurate mass corresponding with that observed in the bioactive primary and bioactive secondary fraction. Similarly, the high energy fragmentation of the molecule observed in the mass spectrum also corresponds with those of inumakilactone B **(52)** (Table 5.7).

Table 5.7: UPLC-HRMS data of inumakilactone B **(52)**.

Compound	Observed m/z[a] (Da)(Mass error (mDa))	Observed quasi-molecular ion	Molecular formula	Calculated monoisotopic mass (Da)[b]	RT[c] (min)	Observed fragment (*m/z*)(Mass error (mDa))
Inumakilactone B (52)	347.1129 (-0.2)	$[M+H]^+$	$C_{18}H_{18}O_7$	346.1053	6.8	143.0846 (-1.5) 129.0701 (-0.3) 121.0653 (-0.5) 111.0446 (0.1) 91.0548 (0.0) 69.0340 (0.0)

[a]*m/z*, mass to charge ratio; [b]determined directly from molecular formula; [c]*RT,* retention time

The isolated inumakilactone B **(52)** was rescreened in AlphaScreen-based technology against the WT variant of concern, as well as against an unrelated PD-1/PD-L1 ligand/receptor pair, in M^{pro} inhibition bioassays and in plaque-based bioassays (Omicron and Beta variant) in a dose-response manner.

The IC_{50} of inumakilactone B **(52)** in the spike RBD/ACE2 inhibition assay (AlphaScreen) was found to be 0.572 ± 0.227 µg/mL (1.652 ± 0.656 µM) and 7.211 ± 0.293 µg/mL (4.77 ± 1.89 µM) against the WT(USA-WA1/2020) and an unrelated PD-1/PD-L1 ligand/receptor pair respectively. From this, the selectivity index (SI) of inumakilactone B **(52)** was found to be 12.6. In contrast, the compound was found to have very weak activity against the SARS-CoV-2 M^{pro} enzyme (Figure 5.16), providing evidence for the selective antagonistic activity against the spike RBD/ACE2 interaction. In the spike RBD/ACE2 inhibition screens, the positive control, REGN10987, a monoclonal antibody, was found to have an IC_{50} value of 0.18 nM.

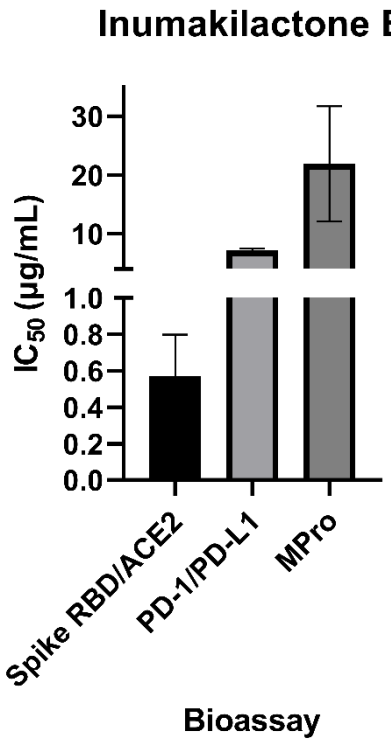

Figure 5.16: SARS-CoV-2 Spike RBD/ACE2 inhibition, PD-1/PD-L1 inhibition and M^{pro} inhibition activity of inumakilactone B **(52)**, represented as IC_{50} (µg/mL).

In the whole-cell plaque-based bioassays, inumakilactone B **(52)** was found to inhibit the formation of virus-driven cytopathic changes, specifically in a dose-dependent fashion, against the Omicron and Beta variants of SARS-CoV-2 (Figure 5.17). The IC_{50} value for inumakilactone B **(52)** was found to be 0.35 µg/mL against the Beta variant with a CC_{50} = 18.64 µg/mL with noticeable cytotoxicity observed in healthy Vero E6 cells at concentrations exceeding 16 µg/mL. The SI was found to be SI = 53 with a goodness of fit (r^2) = 0.998. Additionally, against the Omicron variant, inumakilactone B's IC_{50} value was found to be IC_{50} = 0.285 µg/mL, SI = 65 and goodness of fit (r^2) = 0.997. For comparative purposes, remdesivir was also evaluated and found to have an IC_{50} value of 0.263 µg/mL against the Beta variant with no observed cytotoxicity at any tested concentration (CC_{50} > 50 µg/mL) with a goodness of fit (r^2) = 0.999. Similarly, remdesivir was found to have an IC_{50} = 0.355 µg/mL against the Omicron variant with a goodness of fit (r^2) = 0.9884. Based on these results, inumkaliactone B **(52)** was found to be equipotent to the positive control remdesivir against both the Omicron and Beta variants of concern, although more toxic with a narrower selectivity index (Figure 5.17).

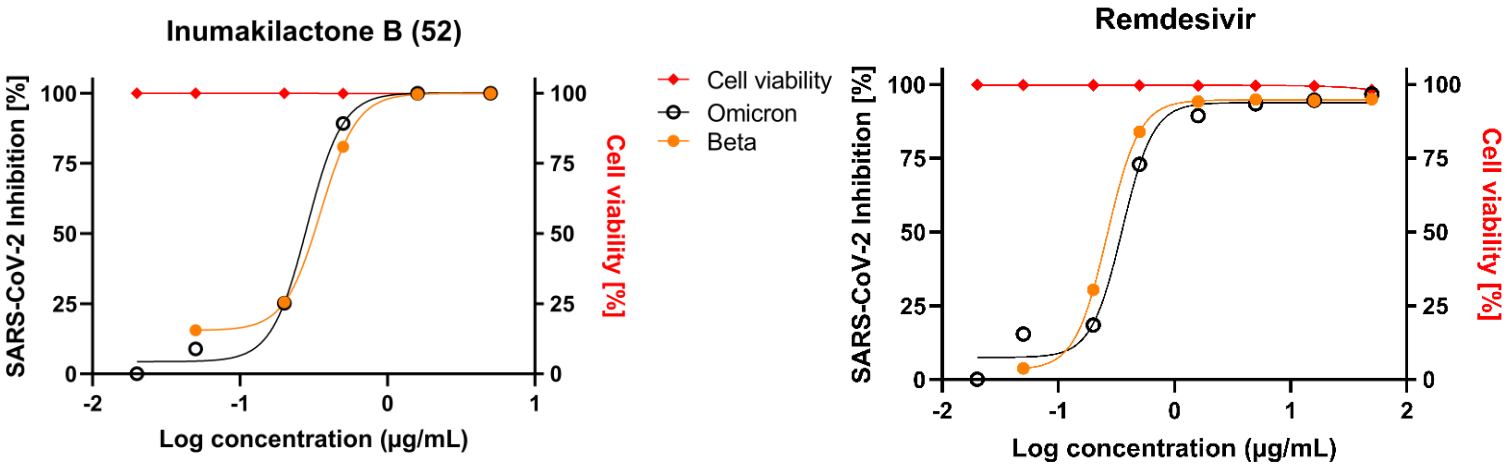

Figure 5.17: Antiviral and cytotoxic activity (▲) of inumakilactone B **(52)** and the positive control, remdesivir, against SARS-CoV-2 (Omicron (○) and Beta var. (●)) in Vero E6 cells. Inhibition of SARS-CoV-2 infection (%) is represented in the legend. Cytotoxicity data were expressed as the mean of three replicates (n=3), and results were analysed on a 95% confidence interval. Antiviral activity expressed as triplicate analysis (n=3) for the Omicron and Beta variants.

Based on these bioassay results, inumakilactone B **(52)** is hypothesised to act on a non-mutating region of the SARS-CoV-2 virus and to act through the prevention of viral entry into the cell, although it may act on other enzymes within the virus. One common question is whether epoxides remain stable *in vitro* and *in vivo* as they are typically non-selective and prone (sensitive) to non-selective chemical reactions. However, purely based on the chemical analysis performed here (with no stability testing conducted), the compound appears to be stable in a weakly acidic solution with no by-products observed when UPLC analysis was conducted (single peak), which might be due to overall stability of the molecule with no excessive strain observed in XRD analysis. The stability of the molecule to enzymatic reactions, however, cannot be predicted nor inferred.

Overall, little biological research has been conducted on the compound, with most research confined to cancer research, where the compound was found to be cytotoxic against murine P388 leukaemia cells (IC_{50} = 0.22 µg/mL) [33], and against other cancer cell lines like AGS cell lines (IC_{50} = 0.55 µM), HeLa (IC_{50} = 0.62 µM), MDA-MB-231 (IC_{50} = 0.66 µM), HepG2 (IC_{50} = 3.5 µM) and Panc-1 cells (IC_{50} = 8.5 µM) [34].

5.3.3.2 Sandaracopimaric acid (53)

Purification and identification of *m/z* 301 $[M-H]^-$, i.e., compound **53**, was achieved by targeted semi-preparatory HPLC-PDA-MS, 1D/2D NMR and subsequent SCXRD and MS spectroscopic analysis.

Of the 320 mg of primary Fraction 6 (labelled as LI-1-48G), 132 mg of the compound mixture was obtained (labelled as LI-1-99H) and used to isolate sandaracopimaric acid **(53)** (*m/z* 302 $[M+H]^+$), with an accompanying UV maximum absorbances (λ_{max}) at 210 nm (Figure 5.18). A yield of 5.1 mg of sandaracopimaric acid **(53)** was obtained in the form of a fine white powder.

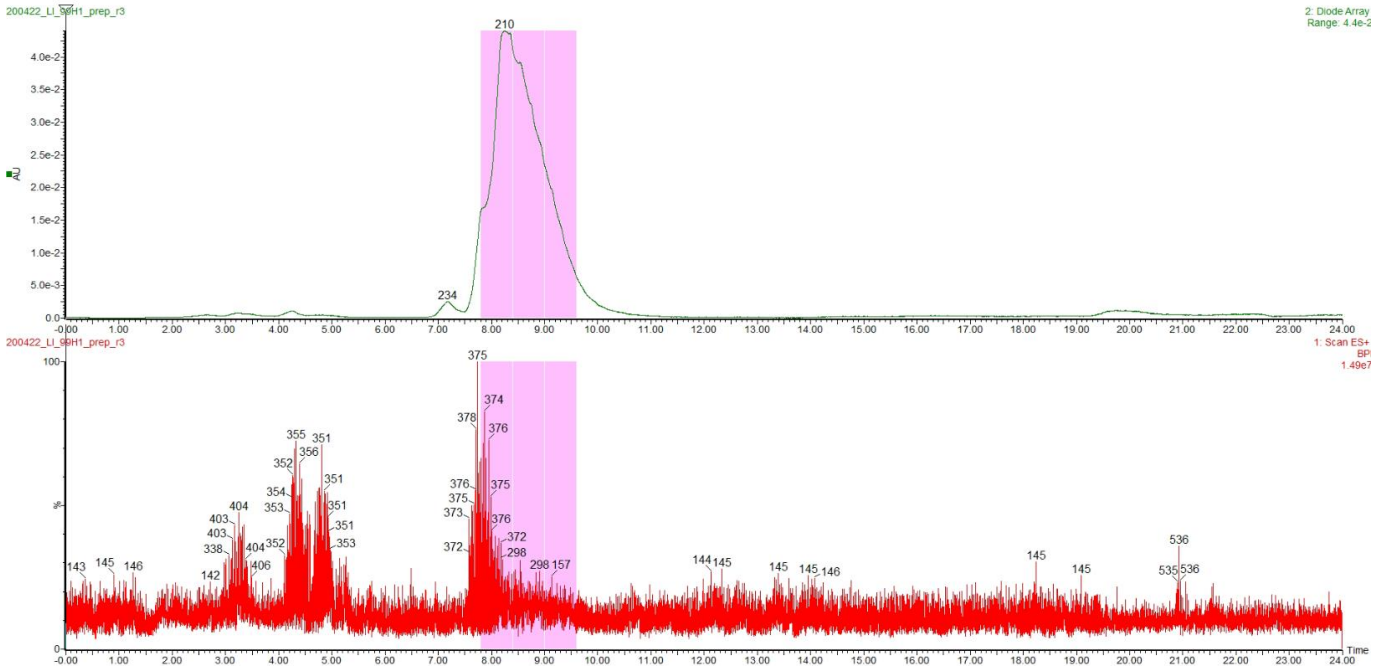

Figure 5.18: UV (top) and BPI MS chromatogram (bottom) of LI-1-99H illustrating the isolation of sandaracopimaric acid **(53),** analysed in ESI positive mode on a Waters HPLC-PDA-MS instrument.

1D and 2D NMR analyses were performed to identify compound **53** (Supplementary Data, Figure S5.3-S5.8)(Table 5.8). ^{13}C NMR (Supplementary Data, Figure S5.4) analysis confirmed the presence of one carbonyl moiety at δ_C 184.9 (C-18), methyl groups at δ_C 15.2 (C-20), δ_C 16.8 (C-19) and δ_C 26.0 (C-17); methylene groups at δ_C 18.2 (C-2), δ_C 18.6 (C-11), δ_C 24.9 (C-6), δ_C 34.4 (C-12), δ_C 35.5 (C-7), δ_C 37.0 (C-3) and δ_C 38.3 (C-1), methine group at δ_C 110.2 (C-16), δ_C 129.1 (C-14), δ_C 136.6 (C-8) and δ_C 148.9 (C-15); and quaternary carbons at δ_C 37.4 (C-13), δ_C 37.7 (C-10) and δ_C 47.3 (C-4).

The multiplicity of carbons were confirmed by HSQC-DEPT experiments (Supplementary Data, Figure S5.5) and from the ^{1}H NMR spectra (Supplementary Data, Figure S5.3). The hydrogens belonging to the olefinic hydrogens were assigned to H-14 (1H, δ_H 5.24, s), H-15 (1H, δ_H 5.79, dd, *J* = 17.4, 10.38 Hz) and H-16 (2H, δ_H 4.93, m). The OH moiety of the carboxylic acid was assigned to H-18 (1H, δ_H 11.15, br. s). The three additional methyl groups were observed at δ_H 0.86 (3H, s, 20-Me), δ_H1.06 (3H, s, 17-Me) and δ_H 1.23 (3H, s, 19-Me).

The $2J_{CH}$, $3J_{CH}$ and $4J_{CH}$ bond correlations observed in the HMBC data (Supplementary Data, Figure S5.6) confirmed the correct placement and linking of the respective moieties. One olefinic proton (δ_H 5.24) was assigned at C-14 with HMBC correlations between C-7, C-9 and C-15. A second olefinic proton (δ_H 5.79) was assigned at C-15 with HMBC correlations between C-12, C-13, C-14, C-17 and two olefinic protons (2H, δ_H 4.93) with HMBC correlations between C-13 and C-15. Positions of the three methyl groups were also deduced by the HMBC correlations, more specifically, 17-Me (3H, δ_H 1.06) presented correlations with C-8, C-12, C-14, C-15 and C-16. The 19-Me (3H, δ_H 1.23) presented correlations with C-3, C-4, C-18 and 20-Me (3H, δ_H 0.86) presented correlations with C-5, C-9 and C-10. Further confirmation of the pimarane diterpenoid structure and attachment was provided by HMBC correlations between the protons at C-11 (2H, δ_H 1.6) and C-10. Similarly, correlations between the proton at C-9 (δ_H 1.83) and C-4 and C-8 and finally the correlation of the C-5 proton (δ_H 1.95) and C-3, C-4, C-18 and C-19.

A few key COSY correlations (Supplementary Data, Figure S5.7) also provided assurance and guided in the determination of the correct structure. These are the correlation between H-5 and H-6/19-Me. Similarly, between H-6 and H-7; H-7 and H-14 and finally between H-14 and H-9.

Proton-bearing carbons were determined by HSQC analyses, with moiety arrangement determined by HMBC and COSY analyses (Figure 5.19; Table 5.8). Key NOE correlations (Supplementary Data, Figure S5.8) were observed between protons of 19-Me and 20-Me; H-5 and H-9; 17-Me and H-7 and finally, H-7 and H-6/H-14. These were used to determine the relative configuration of the hydrogens at C-6, C-14, C-17, C-20, C-19, C-9 and C-5.

Based on the NMR spectra, chemical shifts and closely corresponding literature by Muto et al. (2008) [35], compound **53** was identified as sandaracopimaric acid, a pimarane diterpenoid plant metabolite found in multiple species of plants, including the *Pinus sp.* [36] with little biological activity published in the literature.

Table 5.8: ^{1}H, ^{13}C, HMBC and COSY data of sandaracopimaric acid **(53)** analysed on a 500 MHz in $CDCl_3$

Position	$\delta^{1}H$ (ppm, *J* in Hz)	$\delta^{13}C$ (ppm)	HMBC (H→C)	COSY
1	1.77 (2H, m)	38.3	C-3	
2	1.59 (2H, m)	18.2	C-3, C-4	
3	1.67 (2H, m)	37.0	C-2	
4		47.3		
5	1.95 (1H, dd, *J* = 12.47, 2.69)	48.9	C-3, C-4, C-18, C-19	H-6, H-19
6	1.49 (2H, m)	24.9	C-3, C-5	H-5, H-7_{eq}
7_{ax}	2.25 (1H, m)	35.5	C-5, C-8, C-14	H-6, H-7_{eq}
7_{eq}	2.15 (1H, m)		C-8	H-6, H-7_{ax}, H-14
8		136.6		
9	1.83 (1H, s)	50.6	C-4, C-8	
10		37.7		
11	1.6 (2H, m)	18.6	C-10	
12		34.4		
13		37.4		
14	5.24 (1H, s)	129.1	C-7, C-9, C-15	H-7_{eq}, H-9
15	5.79 (1H, dd, *J* = 17.4, 10.38)	148.9	C-12, C-13, C-14, C-17	H-16
16	4.93 (2H, m)	110.2	C-13, C-15	H-15
17	1.06 (3H, s)	26.0	C-8, C-12, C-14, C-15, C-16	
18-OH	11.15 (1H, br s)			
18		184.9		
19	1.23 (3H, s)	16.8	C-3, C-4, C-18	H-5
20	0.86 (3H, s)	15.23	C-5, C-9, C-10	

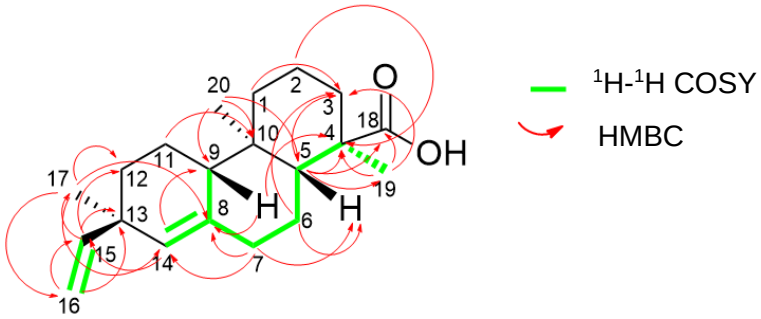

Figure 5.19: Selected COSY and HMBC correlations for sandaracopimaric acid **(53)**

Single crystals suitable for SCXRD were successfully grown of sandaracopimaric acid **(53)**, by evaporative crystallisation from methanol. Large, translucent, needle-like crystals were obtained and successfully analysed by SCXRD analysis. Crystals of sandaracopimaric acid **(53)** crystallised in an orthorhombic space group $P2_12_12_1$ (nr. 19) with Z=4. The structure of the compound was found to correlate with that obtained from NMR analysis (Figure 5.19, Figure 5.20). Complimentary to the results obtained from NMR, the absolute configuration of sandaracopimaric acid **(53)** was obtained, based on the observed Flack parameter of 0.1. SCXRD being valuable in that it is able to determine the absolute configuration of a molecule [37], and greatly compliment traditional NMR spectroscopy. The unit cell parameters obtained for sandaracopimaric acid **(53)** were found to correlate with those previously published in literature and are represented in Table 5.9 [25,26].

As with inumakilactone B **(52)**, sandaracopimaric acid's decalin rings took on a puckered low energy configuration, as expected, and can be seen in Figure 5.20. In comparison to published data [25], no abnormal bond angles or bond lengths were noted.

The bond and torsion angles and bond lengths and other data are not reported in this chapter and have been omitted for the sake of brevity; the crystallographic data of sandaracopimaric acid **(53)** being already-published and deposited in the CCDC (CCDC identifier: 602370 [26]; 1315639 [25]).

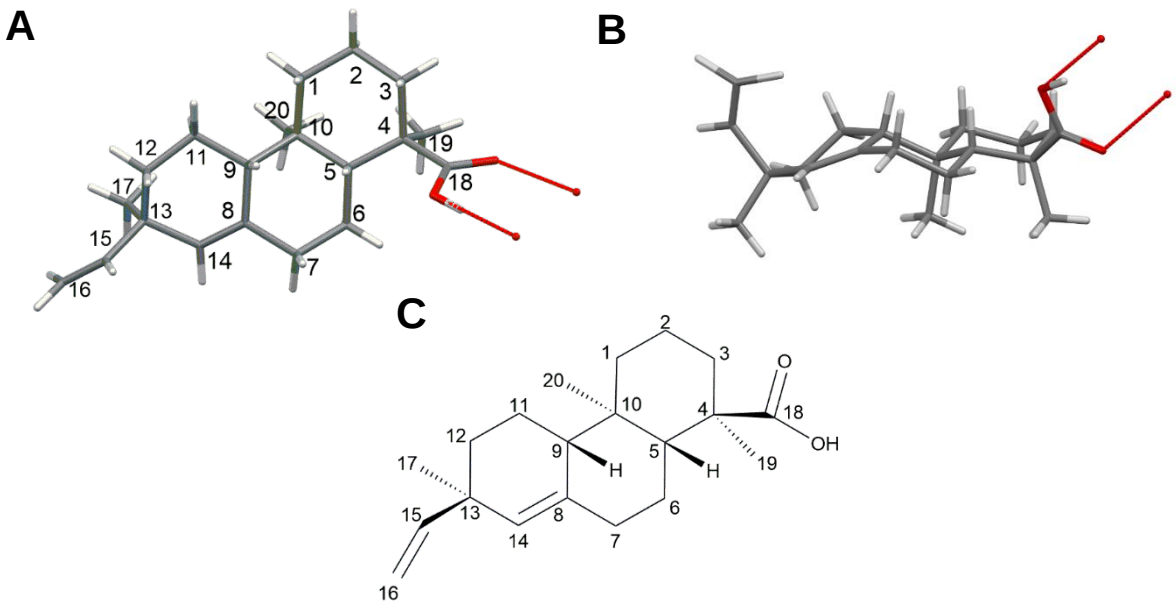

Figure 5.20: (**A**) SCXRD structure of sandaracopimaric acid, processed with Mercury v2021.3.0 (**B**). Puckered configuration of the two fused ring structures of sandaracopimaric acid. (**C**) Stick diagram illustrating the absolute configuration of sandaracopimaric acid **(53)**.

Table 5.9: SCXRD refinement and collection parameters of sandaracopimaric acid **(53)**

Compound	**Sandaracopimaric acid (53)**
Emp. Formula	$C_{20}H_{30}O_2$
CCDC Identifier	602370 [26]; 1315639 [25]
Molecular weight (g.mol^{-1})	302.44
Crystal description	Long translucent needles
Crystal system	Orthorhombic
Space group	$P2_12_12_1$ (no. 19)
a (Å)	7.3776
b (Å)	10.8827
c (Å)	43.2338
α (°)	90.00
β (°)	90.00
γ (°)	90.00
Volume (Å^3)	3471.164
Z	4
F(000)	1328.0
Independent refl.	6873 [R_{int} = 0.0617, R_{sigma} = 0.0587]
Completeness (%)	100
Data/Restr/Para	6873/0/414
Goodness of fit on F^2	1.145
Final R1 indexes (I > 2σ(I))	0.0863
wR2 indices (all data)	0.2600
Largest diffraction peak and hole (e.Å^{-3})	0.93/-0.35
Flack parameter	0.1(2)

Crystal packing was found to be facilitated by 2 strong intermolecular hydrogen bonds between C-18 (H as donor) and the carbonyl (O) attached to C-18 as the hydrogen bond acceptor (Figure 5.21; Supplementary Data Figure S5.9). The hydrogen-bonding information is detailed in Table 5.10 with the crystal data and structure refinement parameters presented in Table 5.9.

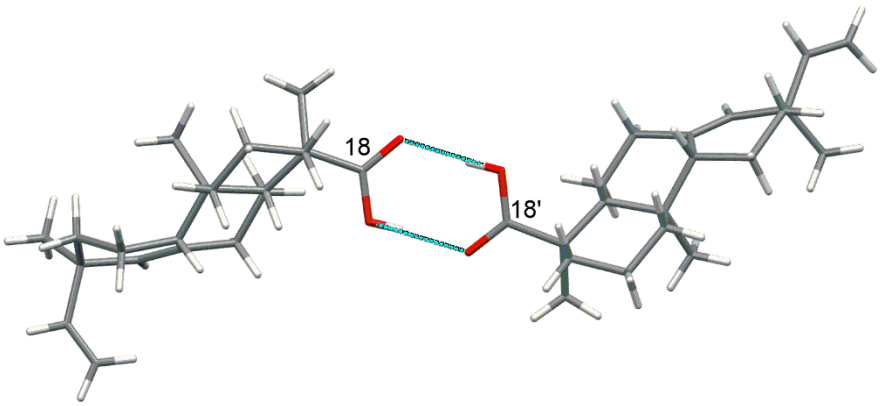

Figure 5.21: SCXRD structure of sandaracopimaric acid, illustrating the intermolecular hydrogen bond between the two carboxylic acid groups of C-18.

Table 5.10: Intermolecular hydrogen-bonding interactions observed within the sandaracopimaric acid **(53)** crystal structure.

Donor	Acceptor	D-H (Å)	H...A (Å)	D...A (Å)	D-H...A (°)
O18-H18	O18’	0.84	1.828	2.661	171.1
O18’-H18’	O18	0.84	1.833	2.625	156.7

Sandaracopimaric acid **(53)** was observed at *m/z* 301.2181 (RT: 13.75 min) (cf. Figure 5.8), where the peak was found to have a monoisotopic mass of 302.2246 Da with an accompanying mass error of 1.3 mDa, and a molecular formula of $C_{20}H_{30}O_2$ (calculated 302.2246 Da) (Table 5.11). At the time of writing, no complete ESI MS^E fragmentation pattern for sandaracopimaric acid **(53)** had been reported in literature, to our knowledge. Further analysis of the low and high-energy MS fragmentation pattern for sandaracopimaric acid **(53)** showed the presence of multiple peaks (Supplementary Data, Figure S5.10) with the high-energy fragmentation of the molecule observed in the mass spectrum corresponding to fragmentations predicted for sandaracopimaric acid **(53)** (Table 5.11). Although to date, no published ESI MS spectra exist for the molecule, the spectra may be of use to future researchers. The data provides supporting evidence to the NMR and SCXRD results for the successful identification of *m/z* 301 $[M-H]^-$ viz. sandaracopimaric acid **(53)**.

Table 5.11: UPLC-HRMS data of sandaracopimaric acid **(53)**.

Compound	Observed m/z[a] (Da)(Mass error (mDa))	Observed quasi-molecular ion	Molecular formula	Calculated monoisotopic mass (Da)[b]	RT[c] (min)	Observed fragment (*m/z*)(Mass error (mDa))
Sandaracopimaric acid (53)	301.2181 (1.3)	$[M-H]^-$	$C_{20}H_{30}O_2$	302.2246	13.75	119.0497 (2.1) 183.0141 (-0.7) 205.1243 (1.4) 220.1477 (1.4)

[a]*m/z*, mass to charge ratio; [b]determined directly from molecular formula; [c]*RT,* retention time

The isolated sandaracopimaric acid **(53)** was rescreened in AlphaScreen-based technology against the WT variant of concern, as well as against an unrelated PD-1/PD-L1 ligand/receptor pair, in M^{pro} inhibition bioassays and in plaque-based bioassays (Omicron and Beta variant) in a full-dose response manner.

The IC_{50} value of sandaracopimaric acid **(53)** in the spike RBD/ACE2 inhibition assay (AlphaScreen) was found to be 4.143 ± 0.699 µg/mL against the WT(USA-WA1/2020) and 64.164 ± 5.176 µg/mL against an unrelated PD-1/PD-L1 ligand/receptor pair (Figure 5.22). From this, sandaracopimaric acid's selectivity index (SI) against the spike RBD/ACE2 interaction was found to be 14. Interestingly, the compound was also found to have good bioactivity against the SARS-CoV-2 M^{pro} enzyme, where the compound was found to have an IC_{50} value of 5.4 ± 0.3 µg/mL and an IC_{50} value of 78.1 ± 30.9 µg/mL against Cathepsin L. The selectivity index (SI) for the compound against the M^{pro} enzyme was found to be 14.5 (Figure 5.22).

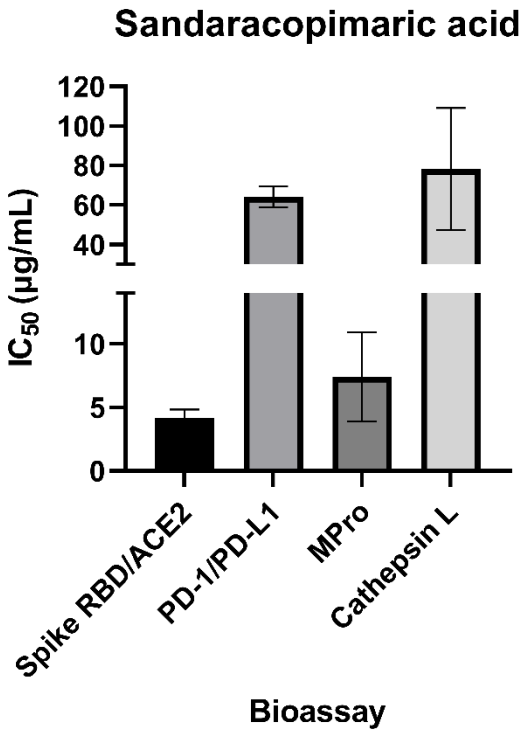

Figure 5.22: SARS-CoV-2 Spike RBD/ACE2 inhibition, PD-1/PD-L1 inhibition, MPro inhibition activity and Cathepsin L activity of sandaracopimaric acid **(53)**, represented as an IC_{50} (µg/mL).

In the whole-cell plaque-based bioassays, sandaracopimaric acid **(53)** was found to be inactive (n=3) against the Omicron and Beta variants of SARS-CoV-2, and similarly displayed no cytotoxicity in healthy Vero E6 cells. The highly non-polar nature of the compound is suspected to be a significant contributing factor to its inactivity, perhaps hindering the absorption or uptake into the cells.

5.4 Conclusion

Despite new vaccines and treatments against SARS-CoV-2, the emergence of new SARS-CoV-2 variants could present additional catastrophic problems in the world. This chapter highlights the value of focusing not only on traditionally-used medicinal plants but also on plants used extensively by other animals and observing the effect of their withdrawal. Hypotheses made in this way, *a priori* or by deductive reasoning, provide scientists with alternative ways to approach a research problem. The work presented follows a systematic screening of *P. henkelii* seed extract through to the pure bioactive compounds by incorporating various complementary analytical techniques like UPLC-HRMS, 2D NMR and SCXRD.

Amongst other possible bioactive compounds present in *P. henkelii* seeds, heavily consumed by the endogenous Cape Parrot, inumakilactone B **(52)** and sandaracopimaric acid **(53)** were found to be key compounds contributing to the observed biological activity of the plant extract and fractions. This, being the first report, to our knowledge, of the investigation of *P. henkelii* seeds and, thus, the first report of inumakilactone B **(52)** and sandaracopimaric acid **(53)** occurring in the seeds of the plant, although their presence is known to occur in other *Podocarpus* species. Additionally, this report is the first to fully describe the absolute configuration and crystal structure of inumakilactone B **(52)** and the first report of its potent antiviral activity against SARS-CoV-2.

Based on the data, inumakilactone B **(52)** was found to inhibit the viral-induced cytopathic effect of SARS-CoV-2 with its mode of action hypothesised to be via the inhibition of the spike RBD/ACE2 interaction, and hence by prevention of viral entry; although other modes of action are also possible and could explain the highly potent activity in plaque-based bioassays. The stability of the compound, particularly due to the presence of 2 epoxide moieties, is an important consideration and should be investigated when considering any *in vivo* trials. Although no absolute conclusion can be drawn on its stability in this study, perhaps the fact that no additional molecules were observed during the UPLC-HRMS analysis (which took place in an acidic pH environment) and the observations made with SCXRD where no unusual torsion angles or bond lengths were noted, might correlate with its intrinsic stability. Nonetheless, epoxides present attractive medicinal chemistry opportunities for synthetic modification, with a few being well-known antineoplastic pharmaceuticals commercially available.

The observed antiviral activity of the compounds might provide credence to the plant's current use by the Cape Parrot and why a significant increase in viral illnesses, especially PBFD, are more prevalent with the decrease of *Podocarpus sp.* forests.

The results provide new hope for investigating plant compounds and natural product chemistry in the probe for novel antiviral compounds against SARS-CoV-2. The compounds identified may serve as new antiviral drug leads against SARS-CoV-2, with future work focused on *in vivo* trials and the evaluation of the compounds against other viruses like CDV and circovirus causing PBFD.

5.5 References

1 M. G. Simpson, Evolution and diversity of woody and seed plants, *Plant Systematics (Second Edition)*, ed. M. G. Simpson, Academic Press, San Diego, 2010, pp. 129–162.

2 M. P. Quiroga, P. Mathiasen, A. Iglesias, R. R. Mill and A. C. Premoli, Molecular and fossil evidence disentangle the biogeographical history of *Podocarpus*, a key genus in plant geography, *J. Biogeogr.*, 2016, **43**, 372–383.

3 H. L. Li, H. C. Song, Y. Zhang and Y. G. Chen, Chemical constituents of the barks of *Podocarpus macrophyllus*, *Chem. Nat. Compd.*, 2016, **52**, 539–541.

4 H. S. Abdillahi, J. F. Finnie and J. Van Staden, Anti-inflammatory, antioxidant, anti-tyrosinase and phenolic contents of four Podocarpus species used in traditional medicine in South Africa, *J. Ethnopharmacol.*, 2011, **136**, 496–503.

5 A. R. A. Noel and J. van Staden, Seed coat structure and germination in *Podocarpus henkelii*, *Zeitschrift für Pflanzenphysiologie*, 1976, **77**, 174–186.

6 H. S. Abdillahi, G. I. Stafford, J. F. Finnie and J. Van Staden, Ethnobotany, phytochemistry and pharmacology of *Podocarpus sensu latissimo* (s.l.), *South African J. Bot.*, 2010, **76**, 1–24.

7 V. P. Bagla, *Isolation and characterization of compounds from Podocarpus henkelii (Podocarpaceae) with activity against bacterial, fungal and viral pathogens,* University of Pretoria, Pretoria, 2013.

8 H. S. Abdillahi, G. I. Stafford, J. F. Finnie and J. Van Staden, Antimicrobial activity of South African *Podocarpus* species, *J. Ethnopharmacol.*, 2008, **119**, 191–194.

9 H. S. Abdillahi, J. F. Finnie and J. Van Staden, Anti-inflammatory, antioxidant, anti-tyrosinase and phenolic contents of four *Podocarpus* species used in traditional medicine in South Africa, *J. Ethnopharmacol.*, 2011, **136**, 496–503.

10 K. Shrestha, A. H. Banskota, S. Kodata, S. P. Shrivastava, G. Strobel and M. B. Gewali, An antiproliferative norditerpene dilactone, Nagilactone C, from *Podocarpus neriifolius*., *Phytomedicine*, 2001, **8**, 489–491.

11 H.-S. Park, N. Yoda, H. Fukaya, Y. Aoyagi and K. Takeya, Rakanmakilactones A—F, new cytotoxic sulfur-containing norditerpene dilactones from leaves of *Podocarpus macrophyllus* var. maki., *Tetrahedron*, 2004, **60**, 171–177.

12 H.-S. Park, Y. Takahashi, H. Fukaya, Y. Aoyagi and K. Takeya, SR-Podolactone D, a new sulfoxide-containing norditerpene dilactone from *Podocarpus macrophyllus* var. maki, *J. Nat. Prod.*, 2003, **66**, 282–284.

13 C. Clarkson, C. C. Musonda, K. Chibale, W. E. Campbell and P. Smith, Synthesis of totarol amino alcohol derivatives and their antiplasmodial activity and cytotoxicity., *Bioorg. Med. Chem.*, 2003, **11**, 4417–4422.

14 S.-E. Lee, E.-K. Park and J.-G. Kim, A mosquito larvicidal diterpenoid isolated from *Podocarpus totara* D. Don ex Lambert, *J. Entomol. Sci.*, 2000, **35**, 474–477.

15 K. F. Carstens, K. Wimberger, R. O. Martin, C. T. Downs, H. Davies-Mostert, A. Young, P. Singh, C. J. Padfield, M. Howes-Whitecross, S. Wilkinson and K. Morrison, Cape Parrot and Mistbelt Forest Conservation Action Plan, 2020, 73.

16 C. Symes, M. Brown, L. Warburton, M. Perrin and C. Downs, Observations of Cape Parrot, *Poicephalus robustus*, nesting in the wild, *Ostrich*, 2004, **75**, 106–109.

17 C. Pienaar and C. T. Downs, *Cape Parrot (Poicephalus robustus) action plan stakeholder workshop report, SASOL and BirdLife South Africa*, 2002.

18 K. F. Carstens, K. Wimberger, R. Martin, D. Letsoalo and C. T. Symes, Monitoring an isolated population of Cape Parrots *Poicephalus robustus* in the Limpopo province, South Africa, *Ostrich*, 2022, **93**, 78–82.

19 J. O. Wirminghaus, C. T. Downs, C. T. Symes and M. R. Perrin, Diet of the cape parrot, *Poicephalus robustus*, in afromontane forests in Kwazulu-Natal, South Africa, *Ostrich*, 2002, **73**, 20–25.

20 C. T. Downs, Abundance of the endangered Cape parrot, *Poicephalus robustus*, in South Africa: implications for its survival, *African Zool.*, 2005, **40**, 15–24.

21 C. T. Downs, M. Brown, L. Hart and C. T. Symes, Review of documented beak and feather disease virus cases in wild Cape parrots in South Africa during the last 20 years, *J. Ornithol.*, 2015, **156**, 867–875.
22 S. Boyes, Disease decimates Cape Parrots, *Africa - Birds & Bird.*, 2010, 15(4):14-15.
23 C. C. Thornburg, J. R. Britt, J. R. Evans, R. K. Akee, J. A. Whitt, S. K. Trinh, M. J. Harris, J. R. Thompson, T. L. Ewing, S. M. Shipley, P. G. Grothaus, D. J. Newman, J. P. Schneider, T. Grkovic and B. R. O'Keefe, NCI Program for natural product discovery: a publicly-accessible library of natural product fractions for high-throughput screening, *ACS Chem. Biol.*, 2018, **13**, 2484–2497.
24 O. V Dolomanov, L. J. Bourhis, R. J. Gildea, J. A. K. Howard and H. Puschmann, OLEX2: a complete structure solution, refinement and analysis program, *J. Appl. Crystallogr.*, 2009, **42**, 339–341.
25 G. Comte, D. P. Allais, A. Simon, D. Es-Saady, A. J. Chulia, C. Delage and M. Saux, Crystal structure of sandaracopimaric acid, a lipoxygenase inhibitor from *Juniperus phoenicea*, *J. Nat. Prod.*, 1995, **58**, 239–243.
26 X.-T. Liu, Y. Shi, B. Yu, I. D. Williams, H. H.-Y. Sung, Q. Zhang, J.-Y. Liang, N. Y. Ip and Z.-D. Min, Antibacterial diterpenoids from *Sagittaria pygmaea*, *Planta Med*, 2007, **73**, 84–90.
27 K. B. Ku, H. J. Shin, H. S. Kim, B.-T. Kim, S.-J. Kim and C. Kim, Repurposing screens of FDA-approved drugs identify 29 inhibitors of SARS-CoV-2, *J. Microbiol. Biotechnol.*, 2020, **30**, 1843–1853.
28 I. Tietjen, J. Cassel, E. T. Register, X. Y. Zhou, T. E. Messick, F. Keeney, L. D. Lu, K. D. Beattie, T. Rali, P. Tebas, H. C. J. Ertl, J. M. Salvino, R. A. Davis and L. J. Montaner, The natural stilbenoid (–)-hopeaphenol inhibits cellular entry of SARS-CoV-2 USA-WA1/2020, B.1.1.7, and B.1.351 Variants, *Antimicrob. Agents Chemother.*, 2021, **65**, e0077221.
29 L. Urda, M. H. Kreuter, J. Drewe, G. Boonen, V. Butterweck and T. Klimkait, The petasites hybridus CO2 extract (Ze 339) blocks SARS-CoV-2 replication in vitro, *Viruses*, 2022, **14**, 106.
30 R. T. Eastman, J. S. Roth, K. R. Brimacombe, A. Simeonov, M. Shen, S. Patnaik and M. D. Hall, Remdesivir: A review of its discovery and development leading to emergency use authorization for treatment of COVID-19., *ACS Cent. Sci.*, 2020, **6**, 672–683.
31 L. Invernizzi, P. Moyo, J. Cassel, F. J. Isaacs, J. M. Salvino, L. J. Montaner, I. Tietjen and V. Maharaj, Use of hyphenated analytical techniques to identify the bioactive constituents of *Gunnera perpensa* L., a South African medicinal plant, which potently inhibit SARS-CoV-2 spike glycoprotein–host ACE2 binding, *Anal. Bioanal. Chem.*, 2022, **414**, 3971–3985.
32 S. Itô, M. Sunagawa, M. Kodama, H. Honma and T. Takahashi, Structures of inumakilactones B and C, lactones of diterpenoid origin, *J. Chem. Soc. D Chem. Commun.*, 1971, 91b – 93.
33 K. Sato, Y. Inaba, H.-S. Park, T. Akiyama, T. Koyama, H. Fukaya, Y. Aoyagi and K. Takeya, Cytotoxic Bisnor- and Norditerpene Dilactones Having 7α,8α-Epoxy-9,11-enolide Substructure from Podocarpus macrophyllus D. DON, *Chem. Pharm. Bull.*, 2009, **57**, 668–679.
34 Y. Ren and A. D. Kinghorn, Development of potential antitumor agents from the scaffolds of plant-derived terpenoid lactones., *J. Med. Chem.*, 2020, **63**, 15410–15448.
35 N. Muto, T. Tomokuni, M. Haramoto, H. Tatemoto, T. Nakanishi, Y. Inatomi, H. Murata and A. Inada, Isolation of apoptosis- and differentiation-inducing substances toward human promyelocytic leukemia HL-60 cells from leaves of *Juniperus taxifolia*, *Biosci. Biotechnol. Biochem.*, 2008, **72**, 477–484.
36 A. V Shpatov, S. A. Popov, O. I. Salnikova, E. N. Shmidt, S. W. Kang, S. M. Kim and B. H. Um, Lipophilic extracts from needles and defoliated twigs of *Pinus pumila* from two different populations, *Chem. Biodivers.*, 2013, **10**, 198—208.

37 H. D. Flack and G. Bernardinelli, The use of X-ray crystallography to determine absolute configuration., *Chirality*, 2008, **20**, 681–690.

Chapter 6

General Conclusion

The SARS-CoV-2 virus and, as an extension, the COVID-19 pandemic has led to unprecedented damage, economic hardship, and mental and/or physical strain on a global scale and highlighted humanity's need for adequate pandemic preparedness. Amongst this, drug development remains one of the fundamental cornerstones to conquering the challenges associated with a novel virus or disease. With more significant human infiltration into the unexplored regions of the planet, the risk of discovering novel microorganisms like pathogenic viruses with zoonotic potential remains high, considering the predicted number of undiscovered viruses in existence [1].

The SARS-CoV-2 virus relies on essential structural and non-structural proteins for the virus' successful replication and ultimate survival in the host. Theoretically, each of these proteins can be targeted by antiviral drugs to disrupt the virus' life cycle [2]. Of note, the spike protein, viral M^{pro}, helicase and PLpro are amongst the most well-reported and researched biological targets for potential therapeutics. Indeed, some current FDA-approved drugs act on these proteins [3,4].

Traditionally used medicinal plants and natural products play an essential role in treating and managing many diseases of both infectious and non-infectious origin. Diseases such as cancer, malaria, HIV-AIDS, colds/flu and even SARS have been managed with traditional medicine [5–10]. South Africa has an extensive biodiversity, amongst the top in the world, with ca. 3000 South African plants used in traditional medicine, ca. 250 of which are used for treating respiratory illnesses [11,12].

The goal of this study was to interrogate, identify, characterise, and develop new antiviral agents from South African plants for the treatment and/or management of COVID-19. Through the use of an in-depth database search and screening criteria, a subset of South African plants were selected for biological screening against the SARS-CoV-2 virus in an HTS manner. Of the 147 plant fractions screened, 37 were found to have good antiviral activity against the SARS-CoV-2 M^{pro} or spike protein. Interestingly, the bioactivity of the semi-purified fractions often differed from the parent extract, highlighting the value of a pre-fractionation step in overcoming an expected shortfall of classical bioguided fractionation where initial sole screening of extracts samples could lead to false-positive results, or worse, false-negatives.

Of the plants screened, three widely-used traditional plants, *viz*., *Gunnera perpensa*, *Siphonochilous atheopicus* and *Podocarpus henkelii* were prioritised for comprehensive chemical and biological investigation in a bid to identify their bioactive counterparts. The bioactive compounds were successfully identified through the use of hyphenated analytical techniques like UPLC-IMS-HRMS, SCXRD and NMR spectrometry. By employing *in silico* molecular docking, the bioactive compound's respective mechanisms of action were hypothesised.

Notably, the hydroxylated lactone of siphonochilone (HLS)**(25)** was found to inhibit the SARS-CoV-2 virus in a dose-dependent manner in plaque-based bioassays, where the compound was found to have an IC_{50} value which ranged between 8.0 µM and 16.0 µM against the Wuhan, Beta and Delta SARS-CoV-2 variants of concern. Importantly, the compound exhibited a high selectivity index with minimal cytotoxicity observed against healthy Vero E6 cells. Mechanism of action investigation found HLS **(25)** to likely act on the PLpro enzyme of the virus. Subsequent chemical investigations were conducted, and a semi-synthetic method was developed to produce, in a stereoselective and time-efficient fashion, HLS **(25)** from the toxic inactive primary chemical compound present in the plant, *viz*., siphonochilone **(24).** Successful proof of concept work was conducted in preparation for upscale and preclinical developments with *in silico* ADME work predicting HLS to show good druglike qualities necessary for identifying viable oral drugs.

In the investigation of *G. perpensa* L., extracts made from the aerial parts of the plant were found to potently inhibit the viral spike RBD-ACE2 interaction in enzymatic-based bioassays. Through the use of ion-mobility coupled mass spectrometry, punicalin **(23)**, α/β-punicalagin **(18)** and lespedezic acid **(17)** were identified as key bioactive compounds in the plant, with subsequent quantification and partial method validation conducted. Of particular note, the IC_{50} values of punicalin **(23)** ranged between 9.5 nM (Delta) and 35.4 nM (Lambda), with the IC_{50} values of α/β-punicalagin **(18)** ranging from 6.6 nM (Beta) to 13.3 nM (Omicron), comparable to the positive control REGN10933. The compounds similarly inhibited the SARS-CoV-2 virus in a dose-dependent manner in plaque-based bioassays. Punicalin's **(23)** IC_{50} value was found to range between 1.2 µM and 7.6 µM between the Wuhan, Beta, Delta and Omicron variant and α/β-punicalagin's **(18)** IC_{50} values was found to range between 4.0 µM and 14.8 µM amongst the various variants of concern. Importantly, both compounds exhibited a high selectivity index with minimal cytotoxicity observed against healthy Vero E6 cells. Subsequent investigations on various combinations of the 2 ellagitannins led to the observation of biological synergism where punicalin:α/β-punicalagin (10:1) and punicalin:α/β-punicalagin (3:1) combinations significantly increased the biological activity of the individual compounds.

Mechanism of action investigation found the ellagitannins to act on the spike RBD/ACE2 interaction. The results provide credence for the plant's current use in the Eastern Cape for COVID-19 treatment and management, and highlight the value of using traditional medicine as a guide for drug discovery.

Investigation of *P. henkelii*, one of South Africa's endangered yellowwood species and a tree which plays a fundamental role in the survival of the endangered Cape Parrot, led to the isolation of 2 antiviral compounds. Through the use of various analytical techniques, which included UPLC-HRMS, NMR and SCXRD analysis, the compounds were successfully characterised and identified as inumakilactone B **(52)** and sandaracopimaric acid **(53).** Of particular interest, inumakilactone B **(52)** was found to inhibit the SARS-CoV-2 virus in a dose-dependent manner in plaque-based bioassays, where the compound was found to have an IC_{50} value ranging from 0.285 µg/mL to 0.35 µg/mL against the Omicron and Beta variants respectively. The compound's bioactivity compared well with those observed for the positive control, remdesivir, for which the IC_{50} value ranged between 0.263 µg/mL to 0.355 µg/mL. Importantly, the compound exhibited a high selectivity index, with cytotoxicity observed only at high concentrations in healthy Vero E6 cells. Sandaracopimaric acid **(53)** was found to act selectively against both the spike RBD/ACE2 interaction and M^{pro} enzyme. Its IC_{50} value was found to be 4.143 ± 0.699 µg/mL in the spike RBD/ACE2 interaction screens against the WT(USA-WA1/2020) and 5.4 ± 0.3 µg/mL against the M^{pro} enzyme of the same virus. The observed bioactivity of the compounds and fruit extract may provide credence for its use by the Cape Parrot and may explain why an increase in viral infections amongst the birds has spiked in recent years with significant deforestation of the yellowwood forests [13].

Although clear conclusions can be drawn from the data, the empirical results reported in the study should be considered in light of a few limitations. These surround the biological assays where the initial screening was only conducted against two SARS-CoV-2 enzymes. Other potential antiviral compounds might have been overlooked due to their inactivity against the enzymes. Funds permitting, whole-cell bioassays should have been conducted on all samples to avoid false-negative results. Additionally, a lack of sufficient biological repeats may influence the calculated IC_{50} values. However, single repeats are common and accepted during the initial screening phases due to the sheer number of samples. Funds permitting, biological repeats in both enzyme-based and plaque-based bioassays would allow for more accurate IC_{50} values for the biological compounds. From a chemistry perspective,the semi-synthesis of HLS **(25)** was only conducted in lab-scale quantities. The success of the reaction may differ when upscaled. Although thorough research was conducted on the SARS-CoV-2

enzymes used in the *in silico* work, no biological work was conducted to verify the correct pharmacophore and biological target.

With reference to the compound isolated from *P. henkelii*, future biological work should focus on compound MOA studies, *in vivo* studies such as preclinical and clinical phases of research and testing against different viruses, where the compounds could serve as candidates for other viral infections like influenza, canine distemper virus, bird beak and feather disease and other viruses. From an upscale point of view, viable synthetic routes could be investigated to produce the bioactive compounds. Stability studies could also be conducted on the compounds to ensure their viability, inumakilatone B **(52)**, being of particular interest.

Through this work, it can be concluded that South African medicinal plants present exciting opportunities for developing new antiviral agents against the SARS-CoV-2 virus to complement ongoing vaccination efforts. Overall, the study's aims and objectives were met and demonstrate that using hyphenated analytical techniques and HTS methodology, natural product drug discovery efforts can be accelerated to produce drug candidates ready for the preclinical and clinical stages of development. Excitingly, coming from a dire situation where at the peak of the pandemic, thousands of infections were reported daily with no known antiviral agents against the virus known in South Africa, this PhD work made a significant contribution to South African drug discovery research where numerous antiviral leads were identified. Both the work conducted and conclusions drawn were novel and allowed for the filing of a patent and additionally led to the first report of *in vitro* bioactivity of South African plant constituents against the SARS-CoV-2 virus [14]. Encouragingly, the work conducted and results obtained also highlight the success of discovering a niche when it was most needed.

References

1 Z. L. Grange, T. Goldstein, C. K. Johnson, S. Anthony, K. Gilardi, P. Daszak, K. J. Olival, T. O'Rourke, S. Murray, S. H. Olson, E. Togami, G. Vidal, J. A. K. Mazet, K. Anderson, P. Auewarakul, L. Coffey, R. Corley, G. Dauphin, J. Epstein, K. Fukuda, S. Goodman, B. Han, J. Hughes, M. Jeggo, W. Karesh, R. Kazwala, T. Kelly, G. Keusch, M. Kurilla, J. Mackenzie, W. Markotter, C. Monagin, D. Morens, V. Munster, E. Muhlberger, P. Pandit, A. Peel, D. Pfeiffer, O. Restif, O. Tomori, J. Towner, S. Van Der Werf, S. VonDobschetz, S. Wacharapluesadee, M. Ward, L. Weirsma, M. Wilson, D. Wolking, K. Wongsathapornchai, L. Brierley, N. Null, C. Tambrana-Torellio, null null, A. Islam, S. Islam, Z. Raman, V. Hul, V. Duong, M. Mouiche, J. Nwobegahay, K. Coulibaly, C. Kumakamba, E. K. Syaluha, J.-P. Lukusa, D. Belay, N. Kebede, W. Ampofo, S. Bel-Nono, R. Suu-Ire, K. Douokoro, H. Dursman, I. Pamungkas, N. Rachmitasari, S. Saputro, W. Damanik, T. Kusumaningrum, M. Rambitan, B. Rey, D. Safari, A. Soebandrio, J. Triastuti, E. Abu-Basha, K. Allan, K. Joseph, M. Samson, B. Khamphaphonphane, W. Theppanga, J. Desmond, S. Samules, M. H. Lee, J. Lee, B. Damdinjav, E. Shiilegdamba, O. Aung, M. Bista, D. Karmacharya, R. Shrestha, J. Nziza, J.-C. Tumushime, M. M. Lo, A. Ndiaye, M. C. Seck, J. Bangura, E. Lavalie, G. Mwangoka, Z. Sijali, R. O. Okello, B. Ssebide, S. Wacharpluesadee, N. Nguyen, J. Epstein, E. Hagan, W. Karesh, A. Latinne, A. Laudisoit, H. Li, C. Machalaba, S. Martinez, N. Ross, A. Sullivan, C. Z. Torrelio, J. Mackenzie, R. Waldman, S. Morzaria, W. Kalpravidh, Y. Makonnen, S. Von Dubscheutz, F. Claes, K. Pelican, C. B. Behravesh, E. Mumford, J. P. Clark, T. D. Vu, K. Saylors, B. Edison, J. Euren, A. Gillis, C. Lange, M. LeBreton, D. McIver, D. O'Rourke, M. Valitutto, D. Zimmerman, J. Belkhiria, B. Bird, H. Chale, E. Preston, N. Gardner, B. Genovese, K. Gonzalez, L. Keatts, T. Kelly, E. Leasure, C. Monagin, P. Pandit, N. Randhawa, B. Smith, W. Smith, A. Tremeau-Bravard, D. Wolking, C. Churchill, S. Olson, C. Walzer and A. Fine, Ranking the risk of animal-to-human spillover for newly discovered viruses, *Proc. Natl. Acad. Sci.*, 2021, **118**, e2002324118.

2 C. Gil, T. Ginex, I. Maestro, V. Nozal, L. Barrado-Gil, M. Á. Cuesta-Geijo, J. Urquiza, D. Ramírez, C. Alonso, N. E. Campillo and A. Martinez, COVID-19: Drug targets and potential treatments, *J. Med. Chem.*, 2020, **63**, 12359–12386.

3 Coronavirus (COVID-19) | Drugs | FDA, https://www.fda.gov/drugs/emergency-preparedness-drugs/coronavirus-covid-19-drugs, (accessed 28 December 2022).

4 W. Yin, C. Mao, X. Luan, D.-D. Shen, Q. Shen, H. Su, X. Wang, F. Zhou, W. Zhao, M. Gao, S. Chang, Y.-C. Xie, G. Tian, H.-W. Jiang, S.-C. Tao, J. Shen, Y. Jiang, H. Jiang, Y. Xu, S. Zhang, Y. Zhang and H. E. Xu, Structural basis for inhibition of the RNA-dependent RNA polymerase from SARS-CoV-2 by remdesivir, *Science*, 2020, **368**, 1499-1504.

5 S. Mathur and C. Hoskins, Drug development: Lessons from nature (Review), *Biomed Rep*, 2017, **6**, 612–614.

6 E. Lautié, O. Russo, P. Ducrot and J. A. Boutin, Unraveling plant natural chemical diversity for drug discovery purposes, *Front. Pharmacol.*, 2020, **11**, 397.

7 A. O. Aremu and S. C. Pendota, Medicinal plants for mitigating pain and inflammatory-related conditions: an appraisal of ethnobotanical uses and patterns in South Africa, *Front. Pharmacol.*, 2021, **12**, 758583.

8 C. P. Kala, Medicinal plants used for the treatment of respiratory diseases in Uttarakhand state of India, *Stud. Ethno-Medicine*, 2020, **14**, 1–8.

9 Alamgeer, W. Younis, H. Asif, A. Sharif, H. Riaz, I. A. Bukhari and A. M. Assiri, Traditional medicinal plants used for respiratory disorders in Pakistan: a review of the ethno-medicinal and pharmacological evidence, *Chin. Med.*, 2018, **13**, 48.

10 B. B. Petrovska, Historical review of medicinal plants' usage, *Pharmacogn. Rev.*, 2012, **6**, 1–5.

11 D. Twilley, S. Rademan and N. Lall, A review on traditionally used South African

medicinal plants, their secondary metabolites and their potential development into anticancer agents., *J. Ethnopharmacol.*, 2020, **261**, 113101.

12 I. E. Cock and S. F. Van Vuuren, The traditional use of southern African medicinal plants in the treatment of viral respiratory diseases: A review of the ethnobotany and scientific evaluations, *J. Ethnopharmacol.*, 2020, **262**, 113194.

13 C. Pienaar and C. T. Downs, *Cape Parrot (Poicephalus robustus) action plan stakeholder workshop report, SASOL and BirdLife South Africa*, 2002.

14 L. Invernizzi, P. Moyo, J. Cassel, F. J. Isaacs, J. M. Salvino, L. J. Montaner, I. Tietjen and V. Maharaj, Use of hyphenated analytical techniques to identify the bioactive constituents of *Gunnera perpensa* L., a South African medicinal plant, which potently inhibit SARS-CoV-2 spike glycoprotein–host ACE2 binding, *Anal. Bioanal. Chem.*, 2022, **414**, 3971–3985.

Supplementary Data

Chapter 2

S2.1 Biological assays conducted at The Wistar Institute, USA

S2.1.1 Samples, cells, viruses, and reagents

All samples were carefully prepared as accurately weighed-out dry powder samples. These were prepared for bioassays by dissolving in DMSO to a known concentration before diluting to achieve the required concentration prior to screening, typically 50 µg/mL and a set of various dilutions obtained by serial dilution.

Bioassays were conducted using Vero-E6 cells, acquired from the American Tissue Culture Collection and cultivated in D10+ medium (Dulbecco's modified Eagle medium with 4.5 g/L glucose and L-glutamine [Gibco, Gaithersburg, MD], 10% FBS [Gemini Bio Products, West Sacramento, CA, USA], 100 mg of streptomycin/mL [Sigma-Aldrich, St. Louis, MO] and 100 U of penicillin/mL). Cultivation took place in a humidified incubator at 37 °C with a 5% CO_2 atmosphere. The BHK-21/WI-2 cells used in the bioassays were obtained from Kerafast (Boston, MA,USA) which were cultured in D5+ media, similar to D10+ with only 5% FBS. Reagents used as positive controls, which include Remdesivir and GC-376 were purchased from Sigma-Aldrich and Selleckchem (Houston, TX, USA), respectively. REGN10933 was obtained from Perelman School of Medicine from excess aliquot volumes which couldn't be used by patients. REGN10987 control antibody, was generously gifted by Dr. Pablo Tebas (University of Pennsylvania, School of Medicine).

Reagents, which included the virus isolates, were deposited by the Centres for Disease Control and Prevention and obtained through BEI Resources, NIH and NIAID. These reagents consisted of the following: SARS-CoV-2 related isolates *viz.* isolate USA-WA1/2022, NR52281, isolate hCoV-19/England/204820464/2020, NR-54000 (contributed by Bassam Hallis), isolate hCov-19/South Africa/KRISP-K005325/2020 and NR-54009 (contributed by Alex Sigal and Tulio de Oliveira).

S2.1.2 AlphaScreen protein-protein interaction assay

The AlphaScreen bioassays were conducted by incubating 2 nM of ACE2-Fc (Sino Biological, Chesterbrook, PA, USA) together with 5 nM His-tagged SARS-CoV-2 spike-RBD (Sino Biological) with 150 mM KCl, 0.05% CHAPS 5 mg/mL nickel chelate donor beads in a total of 10 mL of 20 mM Tris (at pH 7.4) in opaque 384-low volume plates. Samples were diluted using DMSO to 100 times the final concentration, ready for testing. To begin, 5 µL of the ACE2-

Fc/protein A acceptor beads were added to the microtiter plate, before the addition of 100 nL of the test samples and 5 µL of the CoV-Spike-RBD-HIS/nickel chelate donor beads. The test samples were transferred to each respective well with the aid of a Janus Nanohead tool (PerkinElmer, Waltham, MA, USA). The samples were incubated at room temperature for 2 h, before measuring the AlphaScreeen fluorescent signals with a ClarioStar plate reader (BMG Labtech, Cary, NC, USA). To ensure valid results, each experiment was repeated in duplicate, and data normalised to represent percentage inhibition, where 100% inhibition was equivalent to the AlphaScreen signal (absorbance) in the absence of a SARS-CoV-2-spike-RBD-His. Similarly, a 0% inhibition signal was equivalent to the AlphaScreen signal obtained from a sample containing both proteins and the DMSO (no test compounds capable of interfering with the Spike-RBD association).

To assess selectivity to the SARS-CoV-2 spike-ACE2 RBD interaction, PD-1/PD-L1, an unrelated host pair was used as comparison. This interaction too was assessed using AlphaScreen technology. This experiment was performed by incubating 0.5 nM of human PDL1-Fc (Sino Biological) with 5 nM His-tagged human PD-1 (Sino Biological), incubated together with 5 mg/mL nickel chelate donor beads and 5 mg/mL protein A AlphaScreen acceptor beads. The mixture was made up to a total volume of 10 µL of a solution containing 0.005% Tween, 20 mM HEPES (pH 7.4) and 150 mM NaCl, in opaque, 384-low volume well plates. To begin, 5 µL of the PD-L1-Fc/protein A acceptor beads were added to the plate, before the addition of 100 nL of the test samples, finally 5 µL of the PD-1-His/nickel chelate donor beads were added. The samples were incubated at room temperature for 2h, prior to data collection, which took place as described above. In this case, however, data was similarly normalised to percentage inhibition where 0% was equivalent to the AlphaScreen signal detected solely in the presence of the proteins and 0.1% DMSO solution and 100%, equivalent to the detected AlphaScreen signal in the absence of PD-1-His. To ensure repeatable results, all experiments were repeated in duplicate.

S2.1.3 Generation of M^{pro} protein and M^{pro} enzymatic assays

To generate the main protease (M^{pro}) enzyme, the specific codon-optimised gene from the BetaCoV/Wuhan/WIV04/2019 strain, which consisted of amino acids 3264-3567 (GenBank accession nr. QHD43415.1) was acquired from IDT (Coralville, IA, USA). With the use of an expression vector, specifically a HIS-SUMO expression vector (modified pETDUET; Novagen, Madison, WI, USA), the gene was cloned before transformation into BL21(DE3). Thereafter, the fusion protein *viz.* HIS-SUMO-M^{pro} was expressed by employing the autoinduction method

[35]. This was done using 500 mL cell cultures overnight, controlled at 22 °C. Thereafter, a buffer with pH 8.5 was made using 25 mM Tris, 20 mM imidazole, 5 mM β-mercaptoethanol and 200 mM NaCl and lysed by sonication and lysozyme before centrifugation. The supernatant was removed and loaded to onto a Ni-NTA (nickel-nitrilotriacetic acid) column, kept at 4°C, and washed with the resuspension buffer. The protein of interest, *viz*. the fusion protein, was eluted using a buffered eluent system consisting of 200 mM NaCl, 300 mM imidazole and 5 mM β-mercaptoethanol, before concentrating and reloading onto a gel filtration column (HiLoad 26/60 Superdex 75; Cytiva, Marlborough, MA) which was equilibrated with the resuspension buffer prior to loading. Fractions that were deemed sufficiently pure (>90% purity) were pooled and incubated with SUMO protease overnight (4 °C). Furthermore, to remove the HIS-SUMO and SUMO protease, the digested protein solution was applied twice to a 5-ml HIS-TRAP Ni-NTA column (Cytiva) after cleavage and flowthrough collected. The protein underwent a final purification step by concentrating the solution and applying it to a second gel filtration column (HiLoad 26/60 Superdex 75; Cytiva) pre-equilibrated with 150 mM NaCl, 2 mM TCEP and 25 mM HEPES, all at a pH of 7.5. Protein purity was assessed by means of an SDSPAGE gel.

The M^{pro} enzymatic assays were then performed with protease activity measured using the quenched fluorogenic substrate {DABCYL}-Lys-Thr-Ser-Ala-Val-Leu-Gln-Ser-Gly-Phe-Arg-Lys-Met-Glu-(EDANS)-NH2 (Bachem, Vista, CA, USA). Thereafter, a 5 mL aliquot of a 25 mM M^{pro} was diluted in the assay buffer consisting of 25 mM HEPES at pH 7.4, 0.005% Tween, 150 mM NaCl and 5 mM DTT before dispensing into black low-volume 384-well plates. The test samples were diluted to the required testing concentration by means of serial dilution using 100% DMSO. A 100 µL aliquot of each diluted sample was added to the assay with the use of a Janus MDT Nanohead tool (PerkinElmer). The assays were started by adding 5 mL of a 5 mM solution of the fluorogenic substrate, with fluorescence at 355 nm (excitation) and 460 nm (emission) monitored continuously every 5 min for 50 min. This was one using an Envision plate reader (PerkinElmer). To determine the rate of substrate cleavage, a linear regression model was used, and the raw data was incorporated during the time course. The gradients of the curves were normalised to percentage inhibition by setting 100% inhibition equivalent to the rate in the absence of M^{pro} (typically 0) and setting 0% inhibition equivalent to the cleavage rate in the presence of M^{pro} and 0.1% DMSO.

S2.1.4 CPE Quantitative assay

S2.1.4.1 Virus generation

SARS-CoV-2 viruses were generated by incubating 3 x 10^6 Vero E6 cells in 15 mL D10+ medium for 24 h. Thereafter, the Vero E6 cells were washed before the addition of 10 mL of D10+ medium containing viable SARS-CoV-2 (multiplicity of infection = 0.001). Incubation of the cells was then carried out for 5 to 7 days, where clear CPE was observed uniformly throughout the flash. The medium was then harvested, and 250 mL aliquots were taken and stored at 280 °C for subsequent infection. Viral titer was determined by plating Vero E6 cells (20 000 per well), in D10+ medium and incubating for a 24 h period. These healthy Vero E6 cells were then infected by incubating them in fresh D10+ medium, which contained 5-fold serial dilutions of the SARS-CoV-2 virus. Following 4 additional days of incubation, the cells were scored for any CPE. From this, the TCID50 values were calculated using the Reed-Muench method.

S2.1.4.2 Viral CPE scoring-based assays

Viral CPE scoring-based assays were conducted by plating healthy Vero E6 cells (20 000 cells per well) in D10+ media and incubating for 24 h. Thereafter, the test compounds were added to the cells at various concentrations and allowed to incubate for 2 h prior to the addition of 50x $TCID_{50}$ of the virus. As controls, each 96-well plate contained uninfected Vero E6 cells and infected cells (treated with 0.1% DMSO). Following 4 days of incubation, the wells were scored for the presence of viral CPE.

S2.1.4.3 Viral CPE quantitative assay

Cell viability restoration was assessed using viral CPE quantitative assays. This was done as described in section 2.3.1.4.2 but with the addition of 150x $TCID_{50}$ of the virus, added after the 2 h compound incubation period. As before, the cells were incubated for 4-7 days to allow the formation of CPE before treatment with resazurin for 4 h. The cells were fixed by adding paraformaldehyde to a final concentration of 4%. Subsequent incubation of the cells at room temperature for a further 30 min allowed for viral inactivation. The cells were analysed for fluorescence, and their intensity was measured using a ClarioStar plate reader. Data was normalised by subtracting the background fluorescence detected in solutions containing resazurin and D10+ medium in the absence of but no cells.

S2.1.5 Data analysis

For all studies conducted, the sample's EC_{50} was calculated using non-linear regression analysis of a one-side binding model. These calculations were performed using Prism v. 8.4.3 (GraphPad, San Diego, CA, USA), with all data presented as the mean of 6 SEM calculated from a minimum of 3 independent experiments. Statistical significance was calculated based on a ratio paired student's t-test with p-value $\alpha<0.05$ using GraphPad Prism v. 8.4.3 i.e., a p value with $\alpha>0.05$ were classified as significant.

Chapter 3

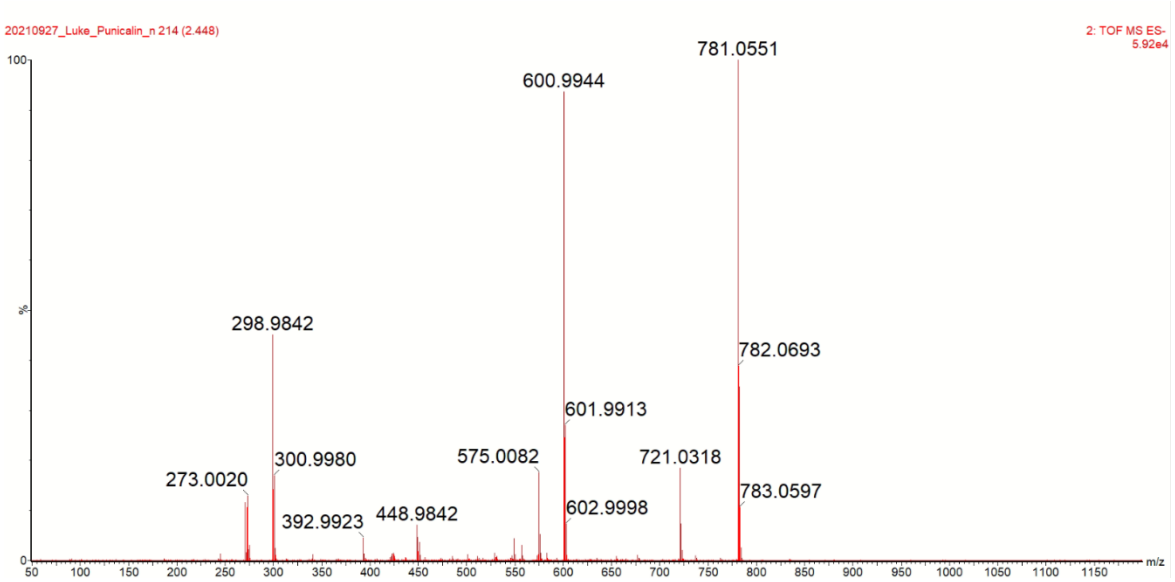

Figure S3.1: Punicalin **(23)** high energy MS fragments.

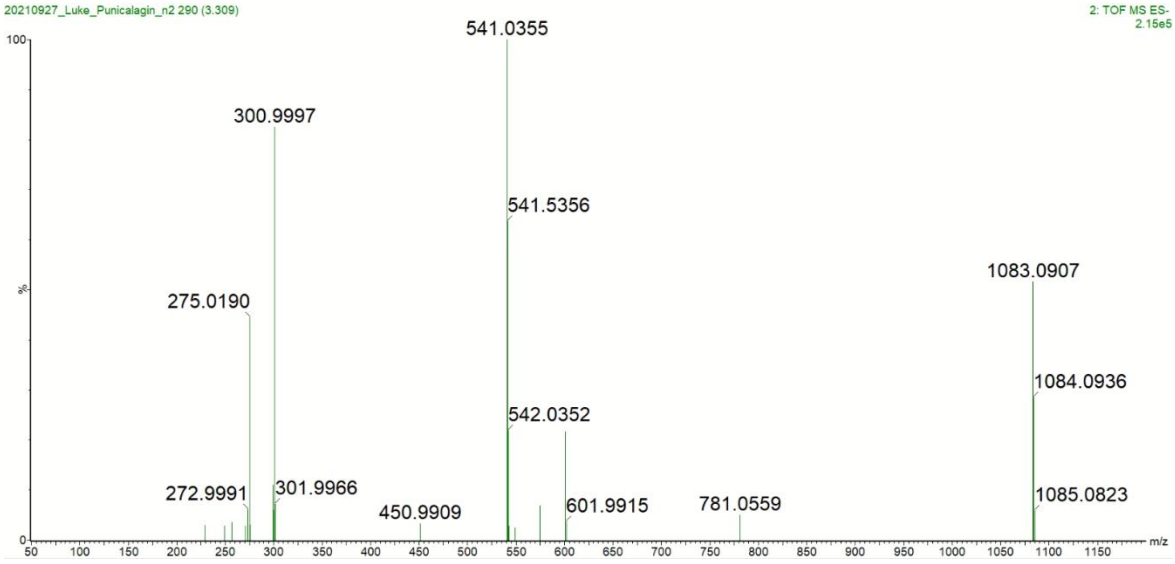

Figure S3.2: α/β-Punicalagin **(18)**, high energy MS fragmentation.

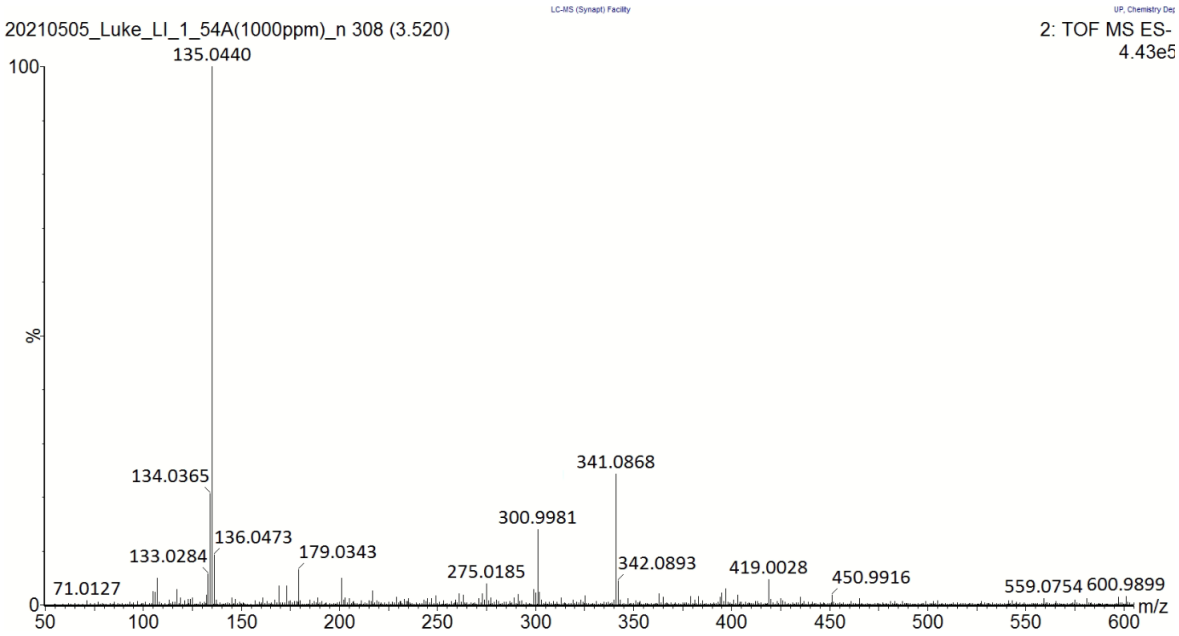

Figure S3.3: (Z)-Lespedezic acid **(17)** high energy fragments, lock mass corrected.

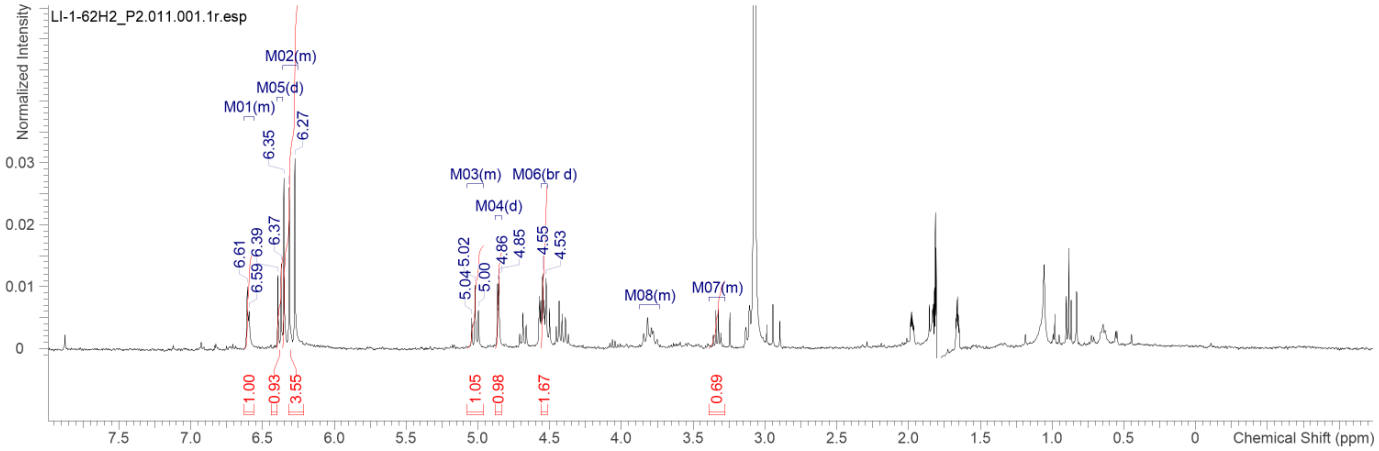

Figure S3.4: ^{1}H NMR spectra of α/β-punicalagin **(18)** in acetone-d6, analysed on a Bruker 400 MHz NMR and processed using ACD Labs.

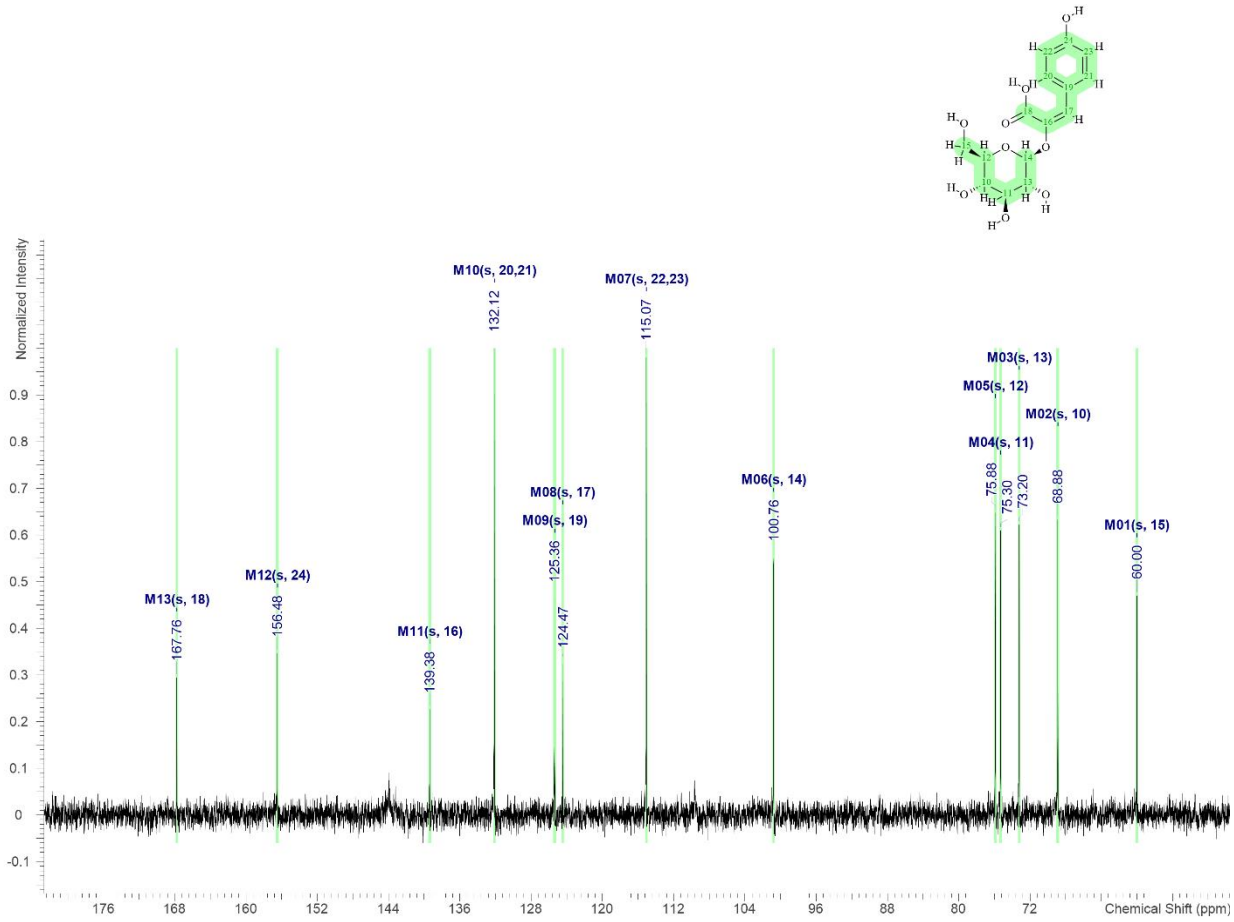

Figure S3.5: ^{13}C NMR spectra of (Z)-lespedezic acid **(17)** in D_2O, collected at 125 MHz and processed using ACD Labs.

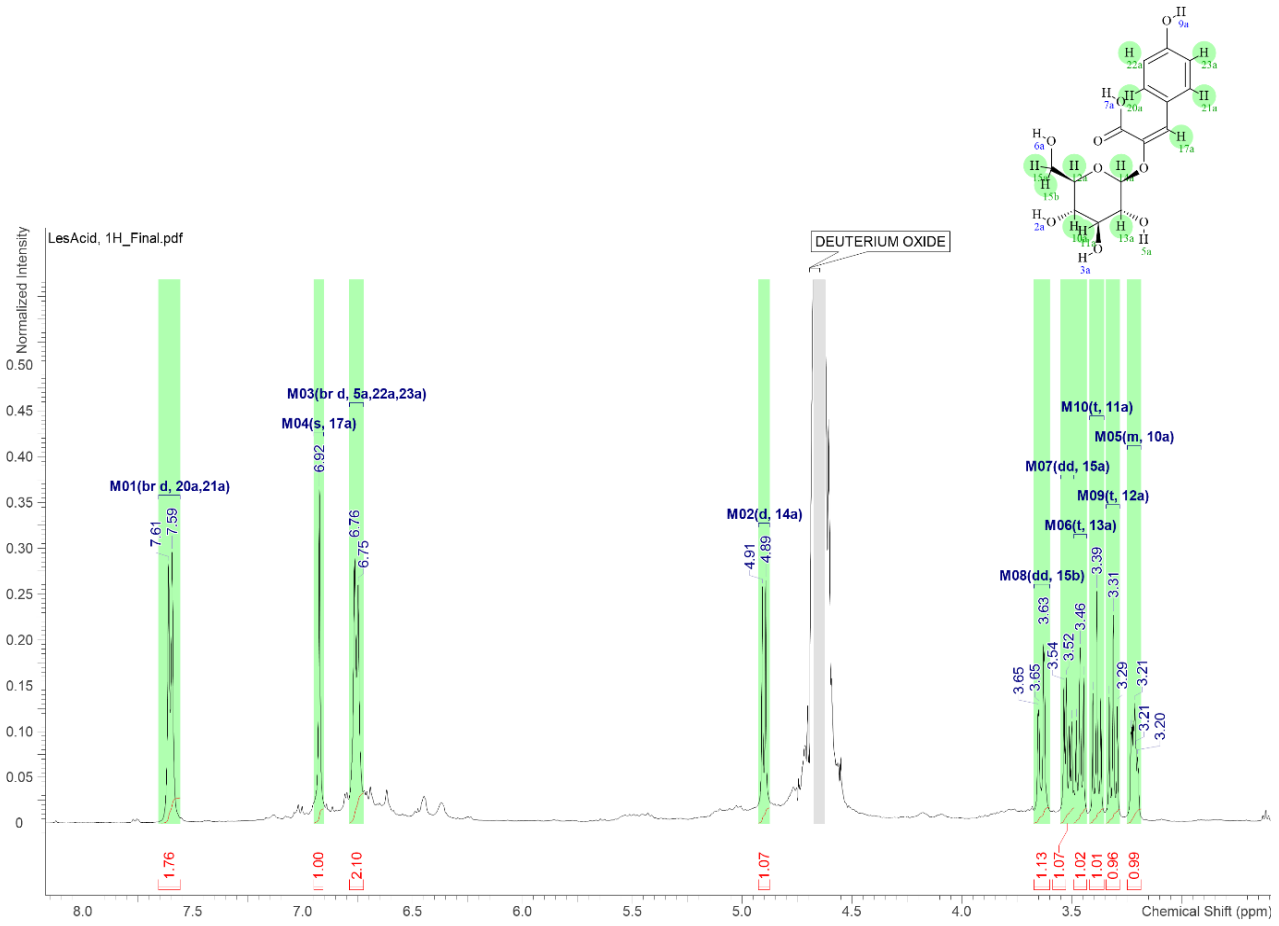

Figure S3.6: ^{1}H NMR spectra of (Z)-lespedezic acid **(17)** in D_2O, analysed on a Bruker 500 MHz NMR and processed using ACD Labs.

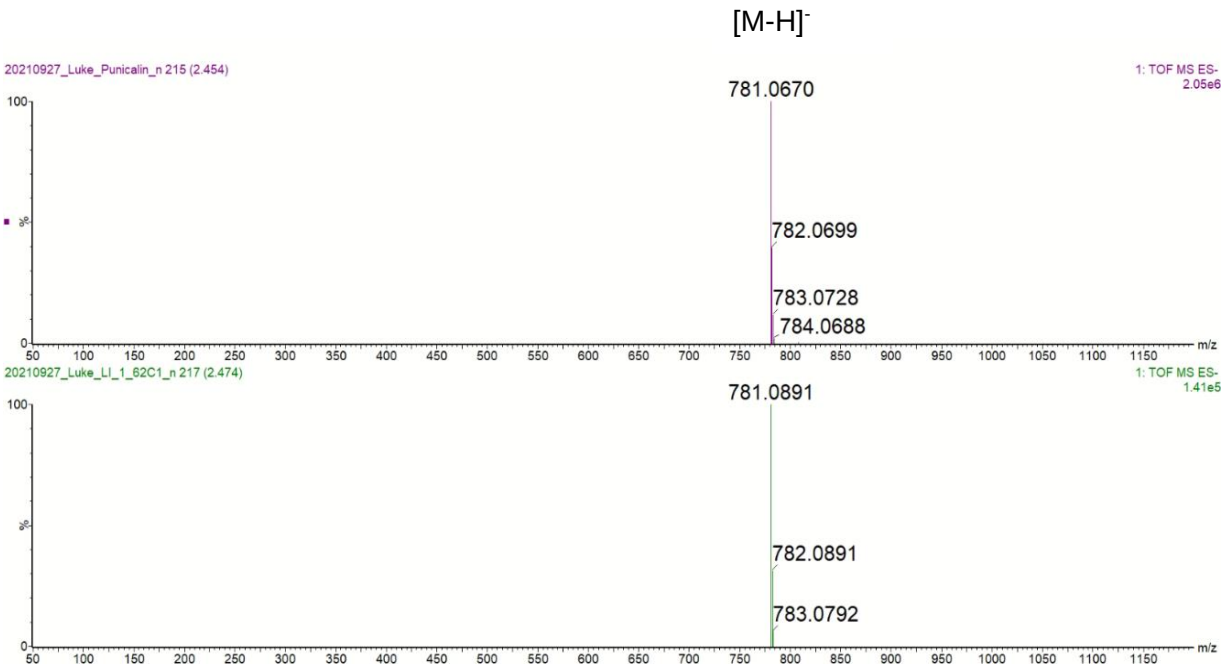

Figure S3.7: MS spectra of punicalin **(23)** in the crude *G. perpensa* extract (top) and punicalin standard (bottom) illustrating matching spectra.

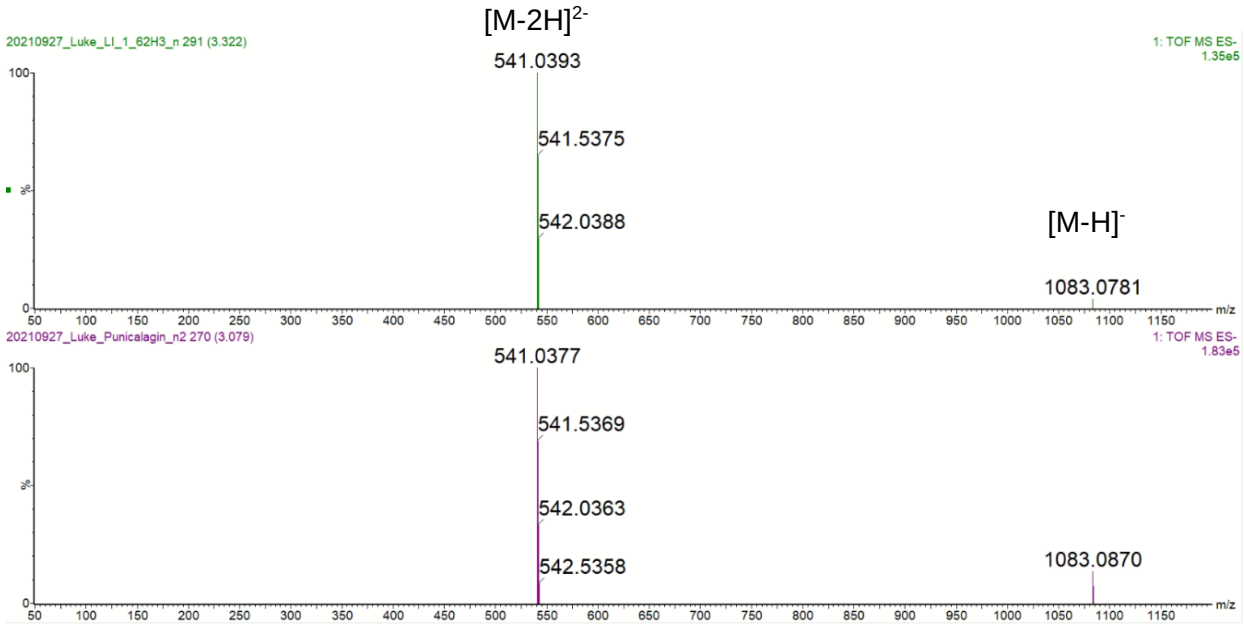

Figure S3.8: MS spectra of α/β-punicalagin **(18)** in the crude *G. perpensa* extract (top) and α/β-punicalagin standard (bottom) illustrating matching spectra.

Chapter 4

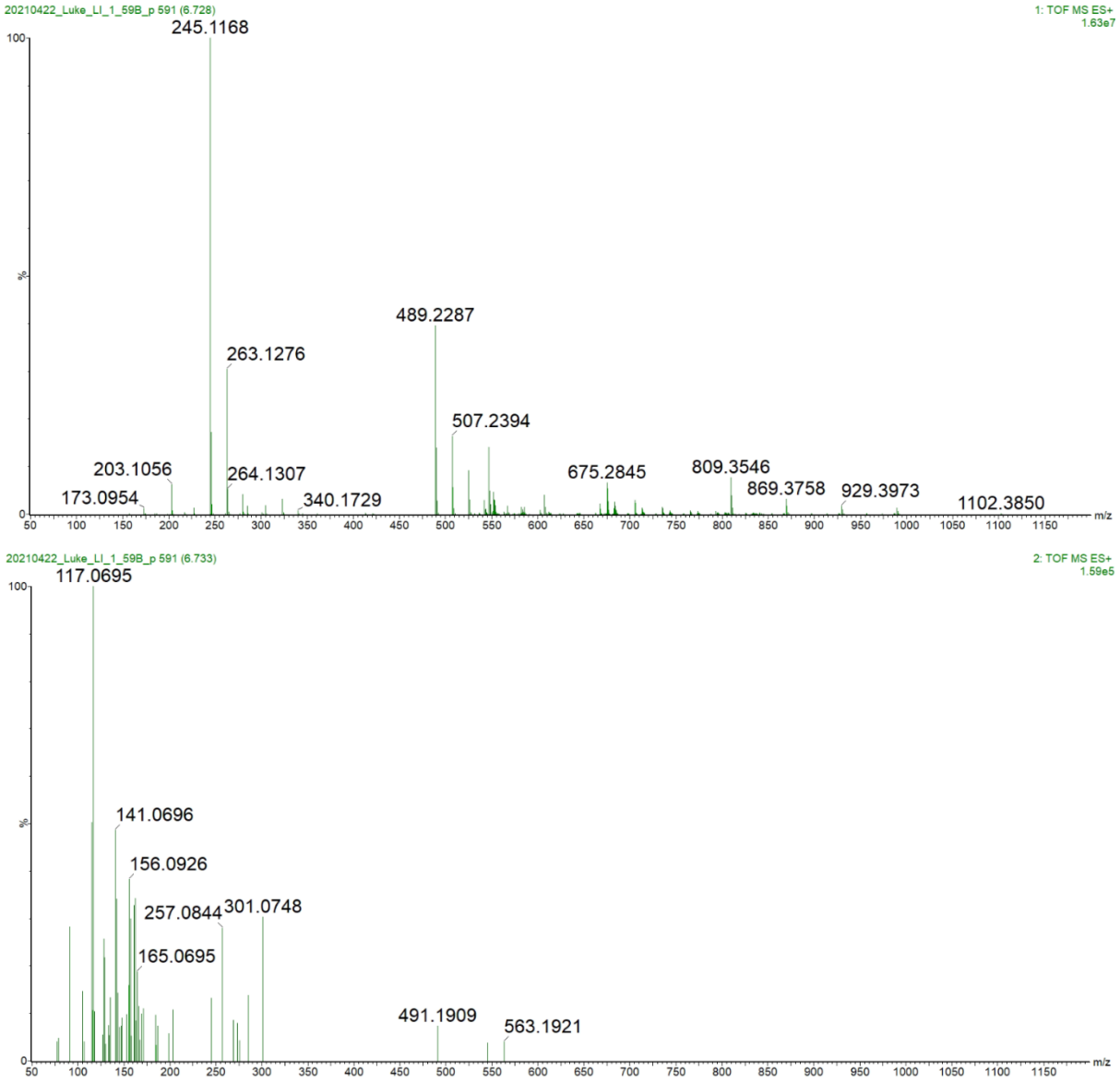

Figure S4.1: High energy (bottom) and low energy (top) MS spectra of HLS (*m/z* 245.1202 (RT: 6.8 min)) **(25)** obtained from the UPLC-HRMS.

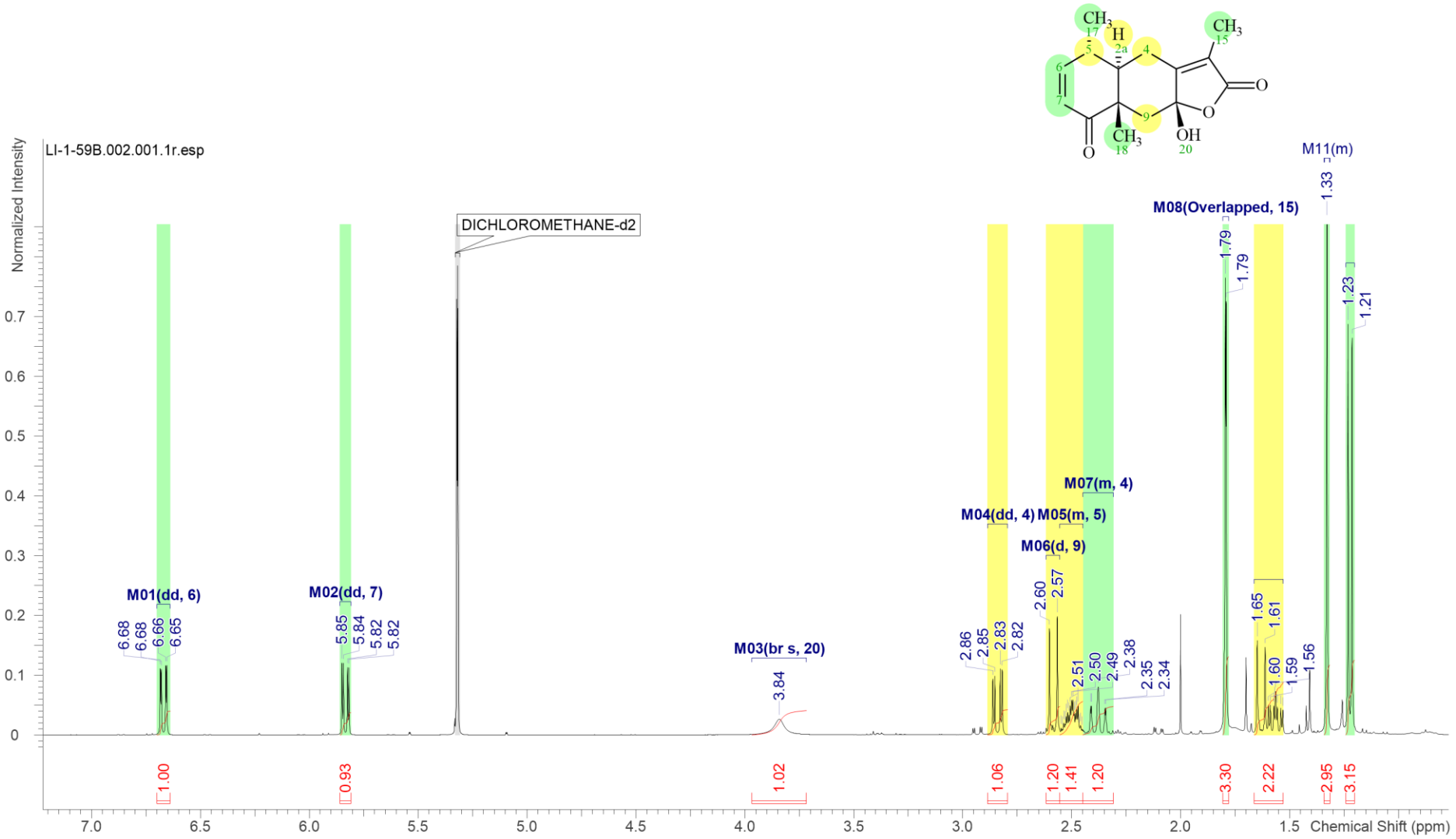

Figure S4.2: ^{1}H NMR of HLS **(24)**, processed with ACD Labs

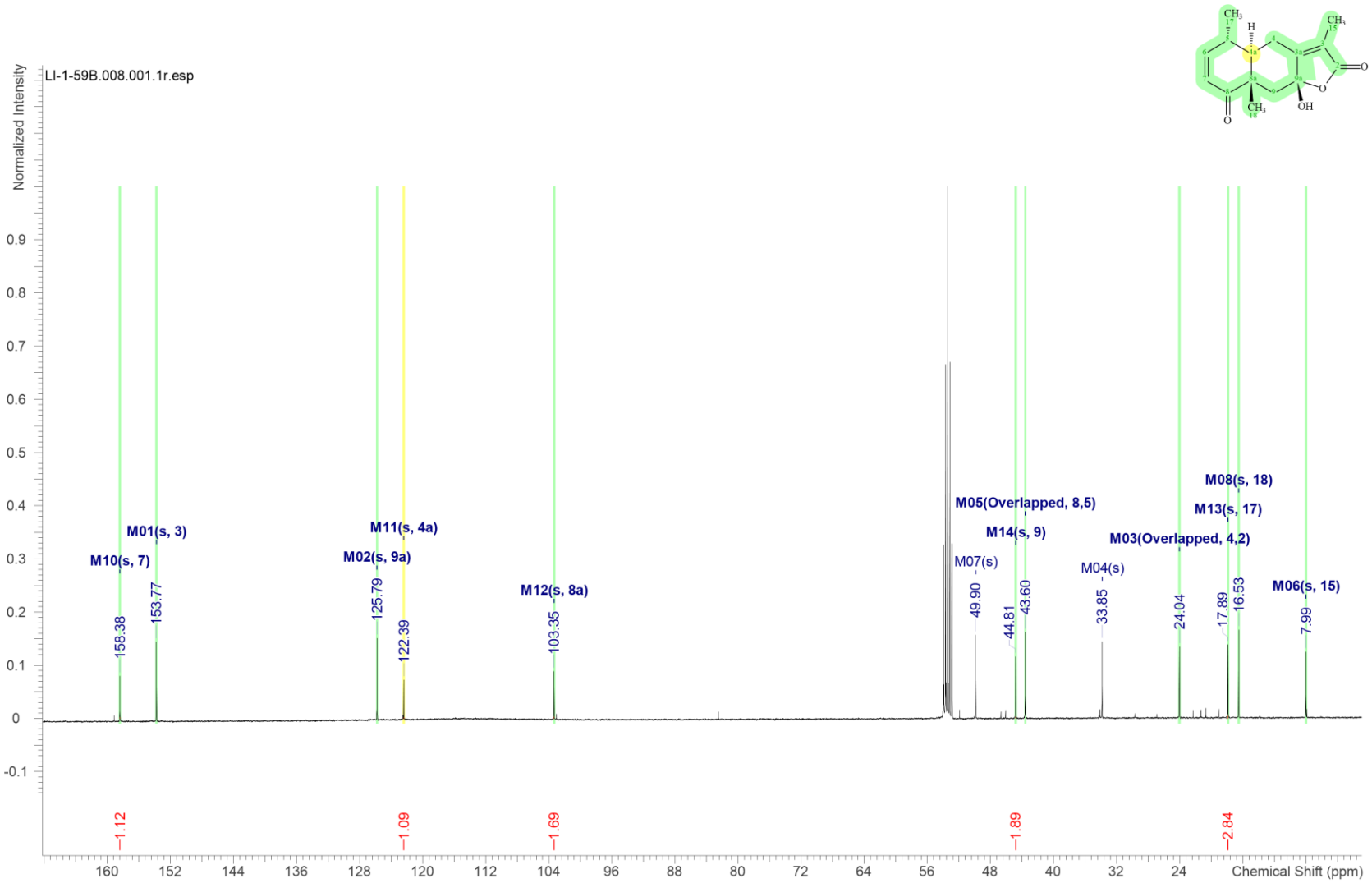

Figure S4.3: ^{13}C NMR of HLS **(24)**, collected at 125 MHz and processed with ACD Labs.

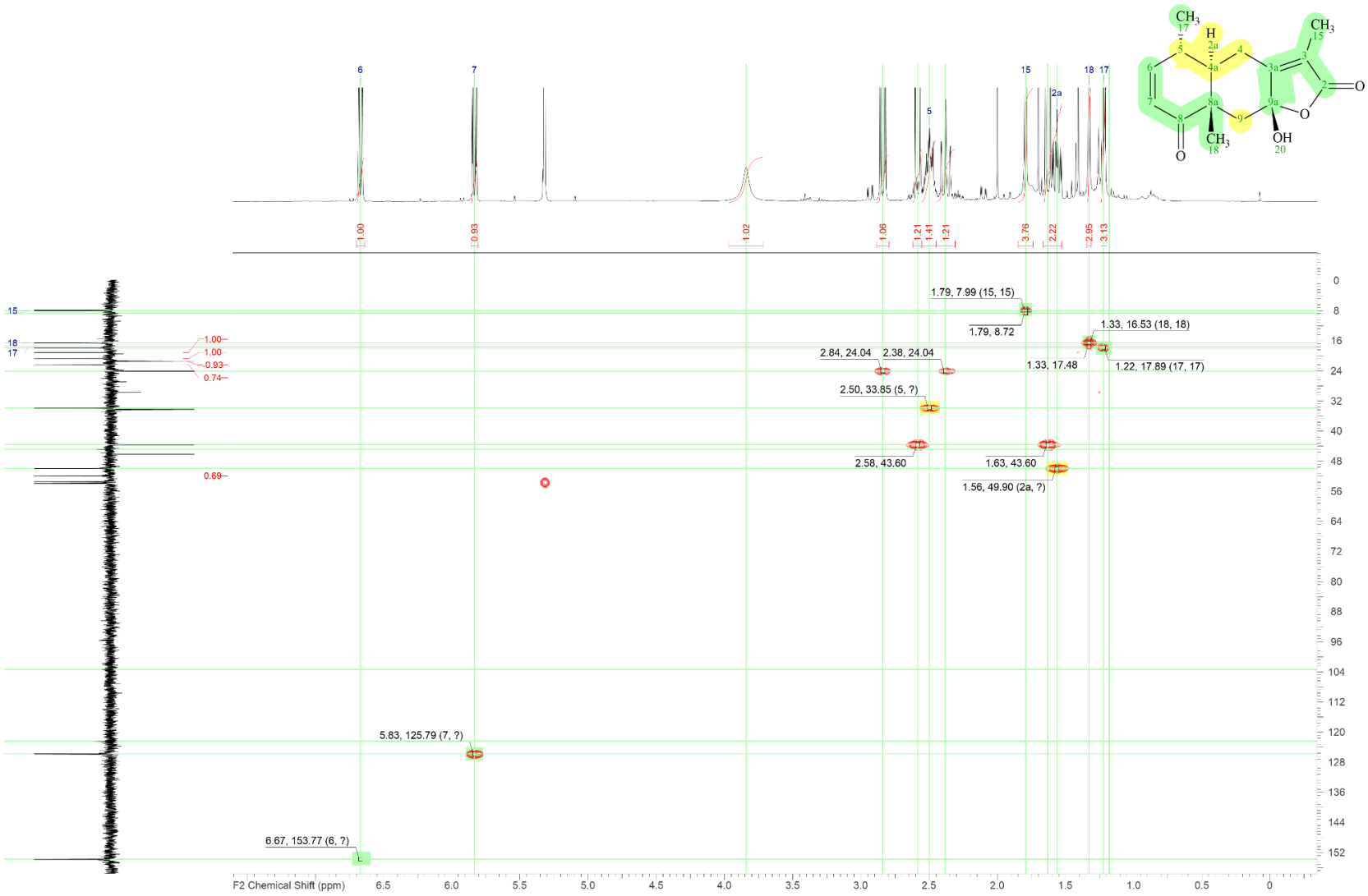

Figure S4.4: HSQC-DEPT of HLS **(24)**, processed with ACD Labs.

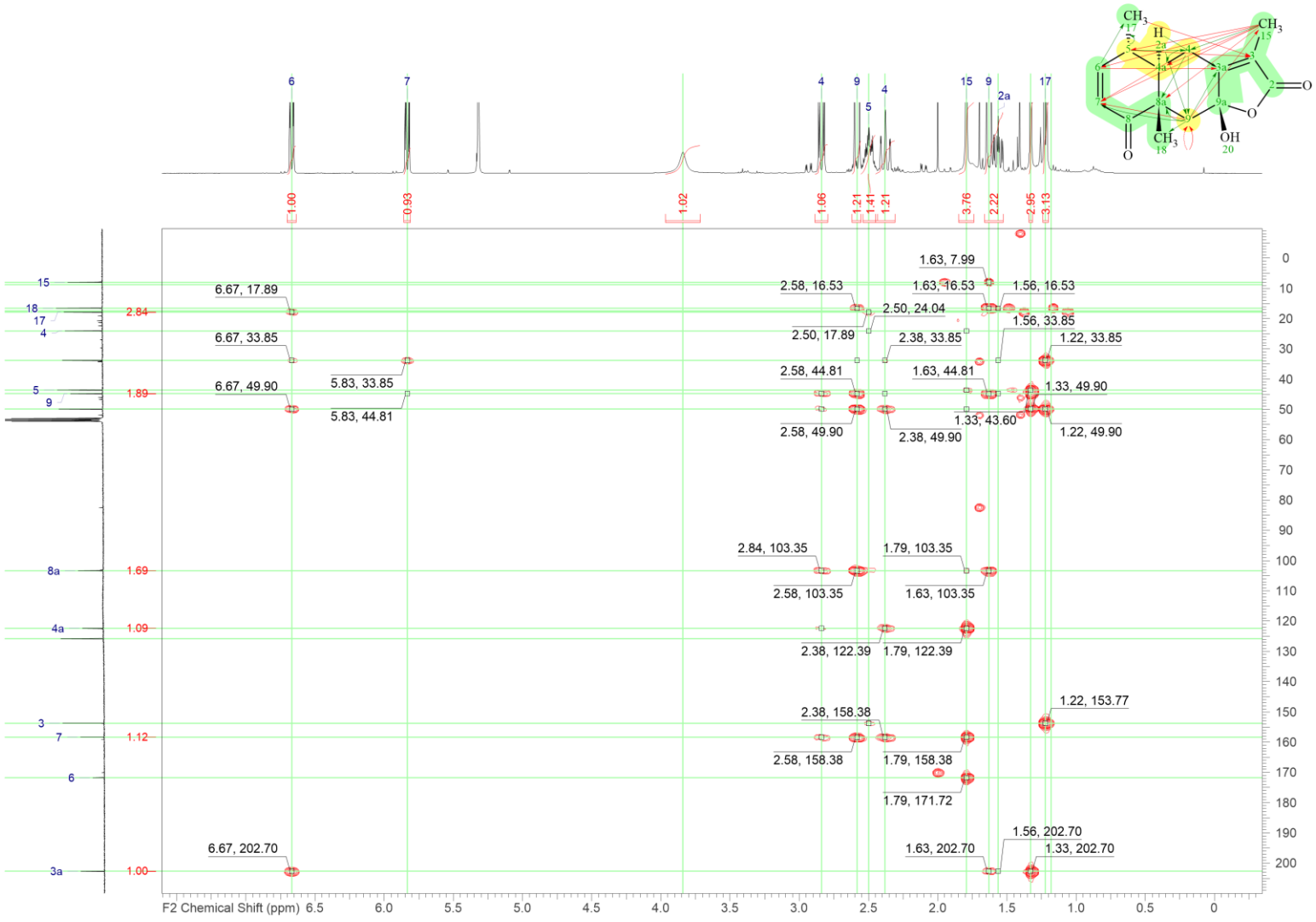

Figure S4.5: HMBC of HLS **(24)**, processed with ACD Labs.

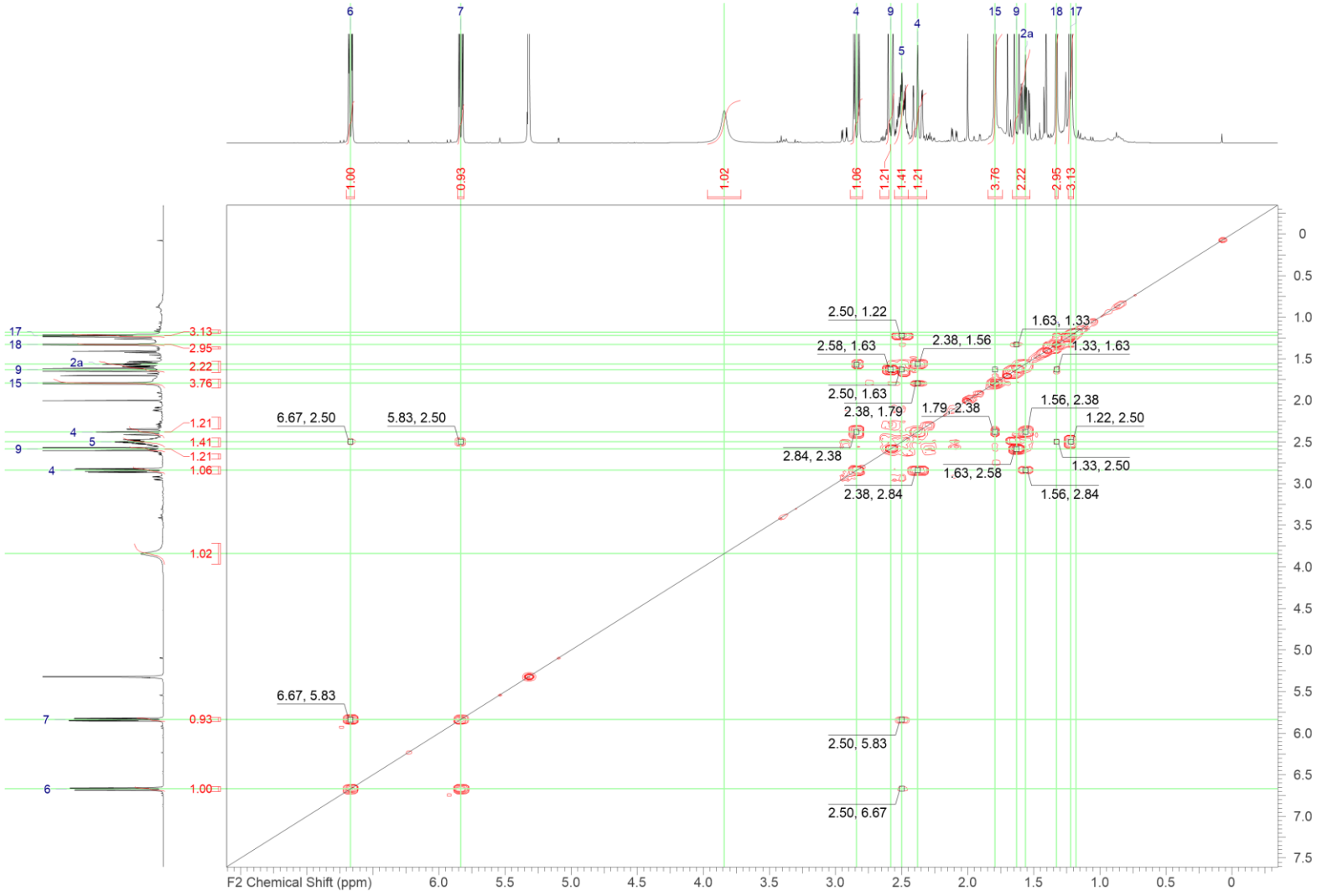

Figure S4.6: COSY of HLS **(24)**, processed with ACD Labs.

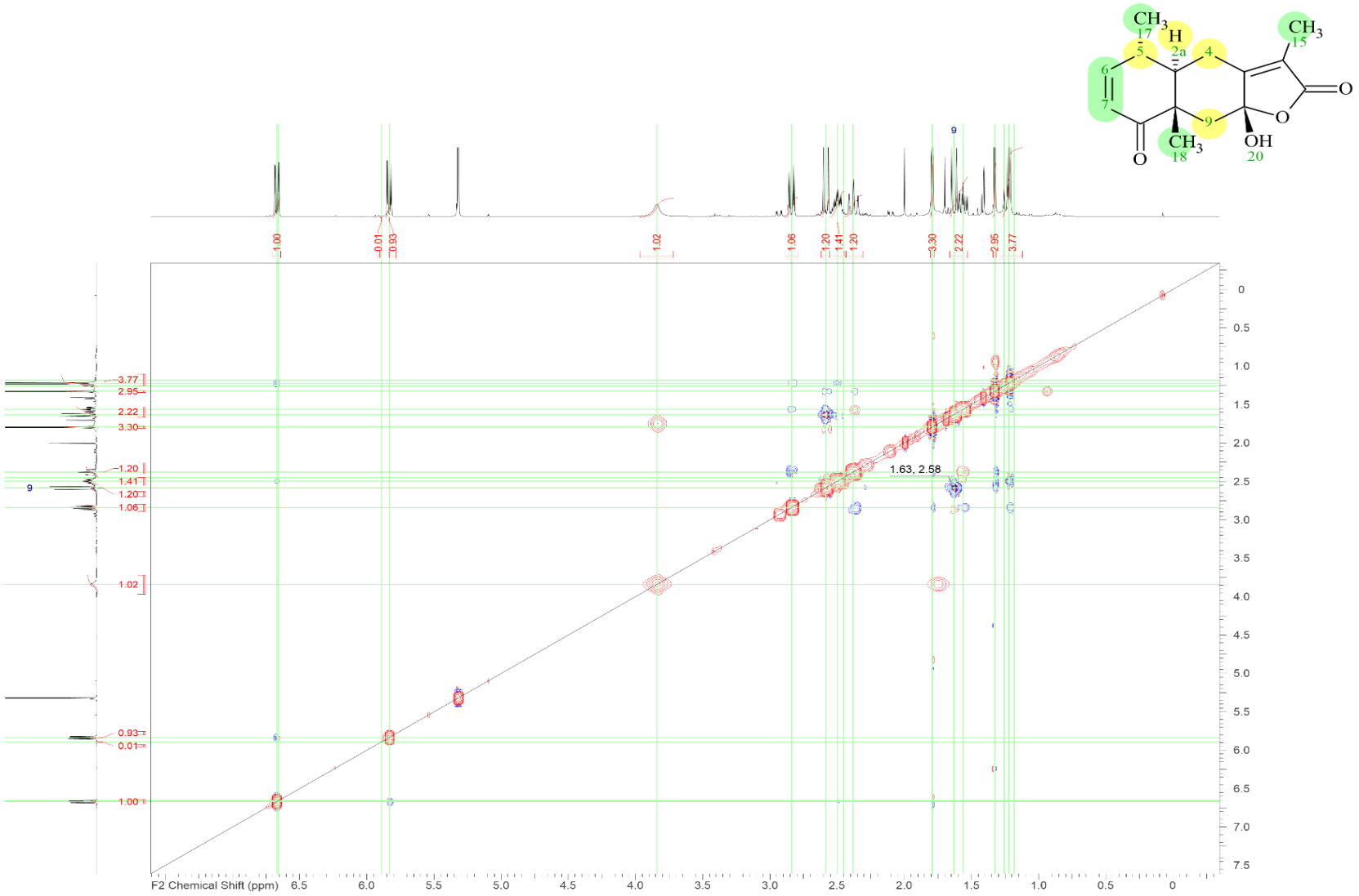

Figure S4.7: NOESY of HLS **(24)**, processed with ACD Labs.

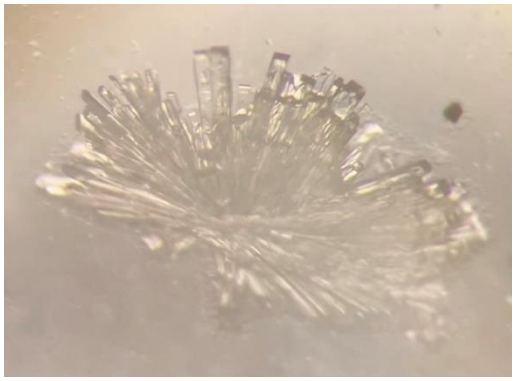

Figure S4.8: Fine needle-like crystals of HLS **(25)** viewed under a stereo microscope.

Table S4.1: Crystal data for HLS isolated from old plant material

Description	HLS (length (Å))
O14-C2	1.3971(18)
O-C9a	1.4558(17)
O-C2	1.365(25)
O=C8	1.2263(19)
O=C2	1.202(25)
C8a-C8	1.5249(19)
C8-C7	1.465(25)
C5-C4a	1.5347(19)
C4a-C8a	1.5582(19)
C4a-C4	1.5475(19)
C4-C3a	1.491(25)
C3a-C9a	1.508 (25)
C3a=C3	1.328(25)
C5-C6	1.493(25)
C5-C5Me	1.533(25)
C8a-C9	1.5446(19)
C8a-C8aMe	1.5456(19)
C9-C9a	1.5175(19)
C7=C6	1.332(25)
C3-C2	1.479(25)
C3-C3Me	1.489(25)

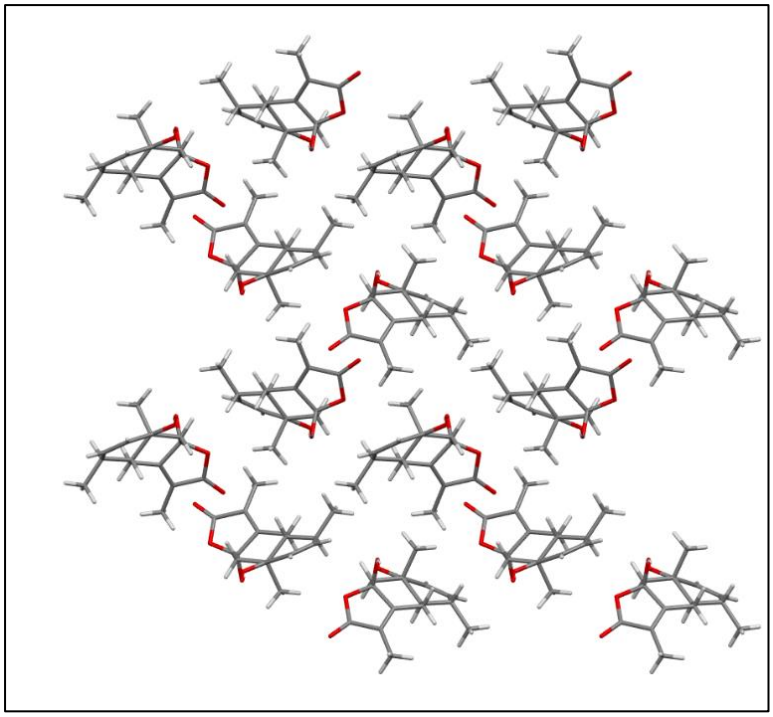

Figure S4.9: SCXRD results of HLS **(24)** illustrating the packing in the unit cell, along the **a** axis.

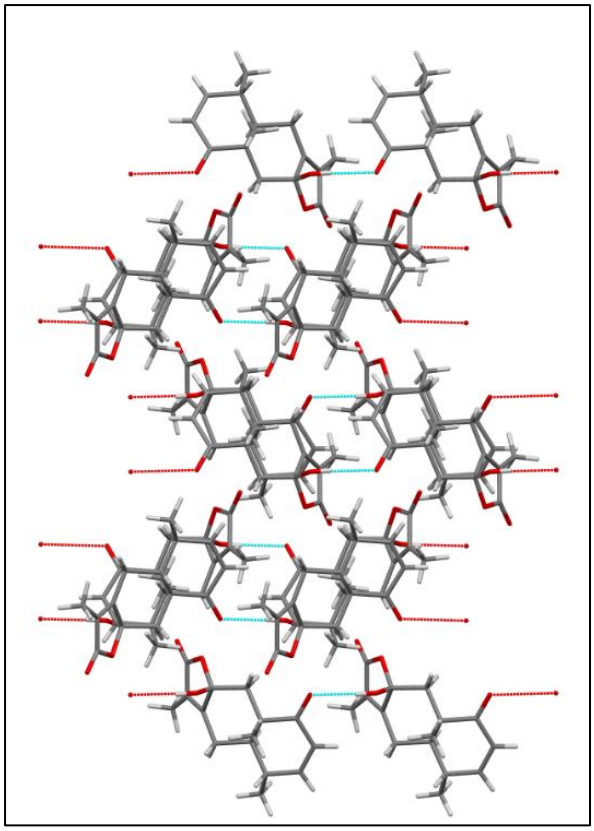

Figure S4.10: SCXRD results of HLS **(24)** illustrating the packing in the unit cell, along the **c** axis.

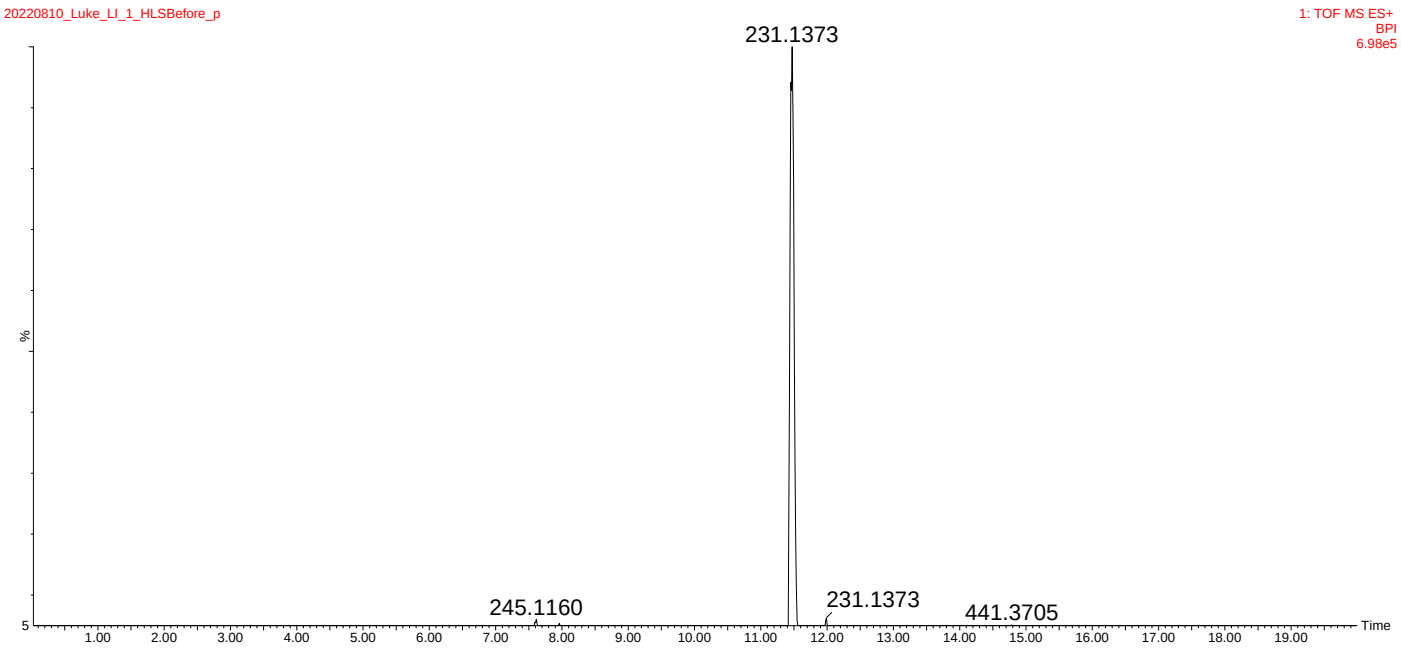

Figure S4.11: UPLC-HRMS chromatogram of siphonochilone **(24)**.

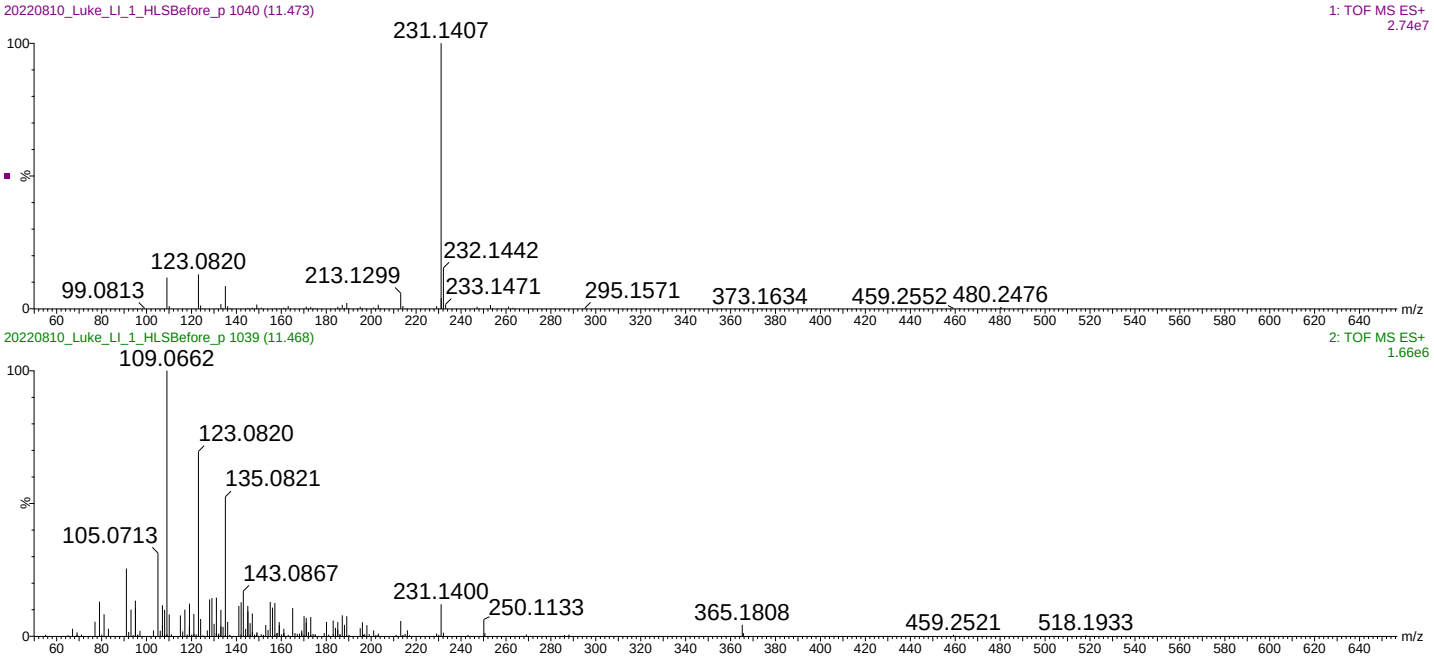

Figure S4.12: Low energy (top) and high energy (bottom) MS spectra of siphonochilone **(24)** (*m/z* 231.1407, (RT: 11.5 min)) obtained from the UPLC-HRMS.

Chapter 5

Table S5.1: Bond lengths observed in inumakilactone B **(52)** obtained by SCXRD analysis.

Description	Bond length (Å)	Description	Bond length (Å)
O18-C6	1.459	C2-C1	1.477
O18-C18	1.366	C2-C3	1.530
O2-C2	1.436	C4-C5	1.540
O2-C1	1.438	C5-C6	1.526
O13-C12	1.357	C10-C5	1.549
O13-C14	1.469	C8-C7	1.468
O8-C7	1.451	C6-C7	1.510
O8-C8	1.456	C10-C1	1.519
O12-C12	1.205	C19-C10	1.544
O3-C3	1.413	C8-C14	1.509
O18-C18	1.199	C4-C3	1.577
C11-C9	1.329	C4-C18	1.523
C8-C9	1.487	C17-C4	1.546
C10-C9	1.515	C14-C15	1.489
C11-C12	1.478	C16-C15	1.312

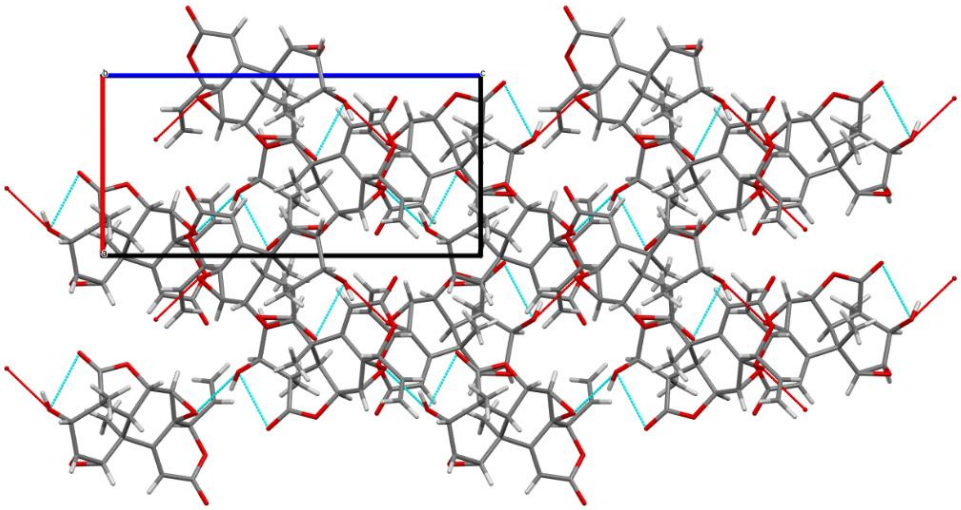

Figure S5.1: 2x2x2 Unit cell of inumakilactone B **(52)**.

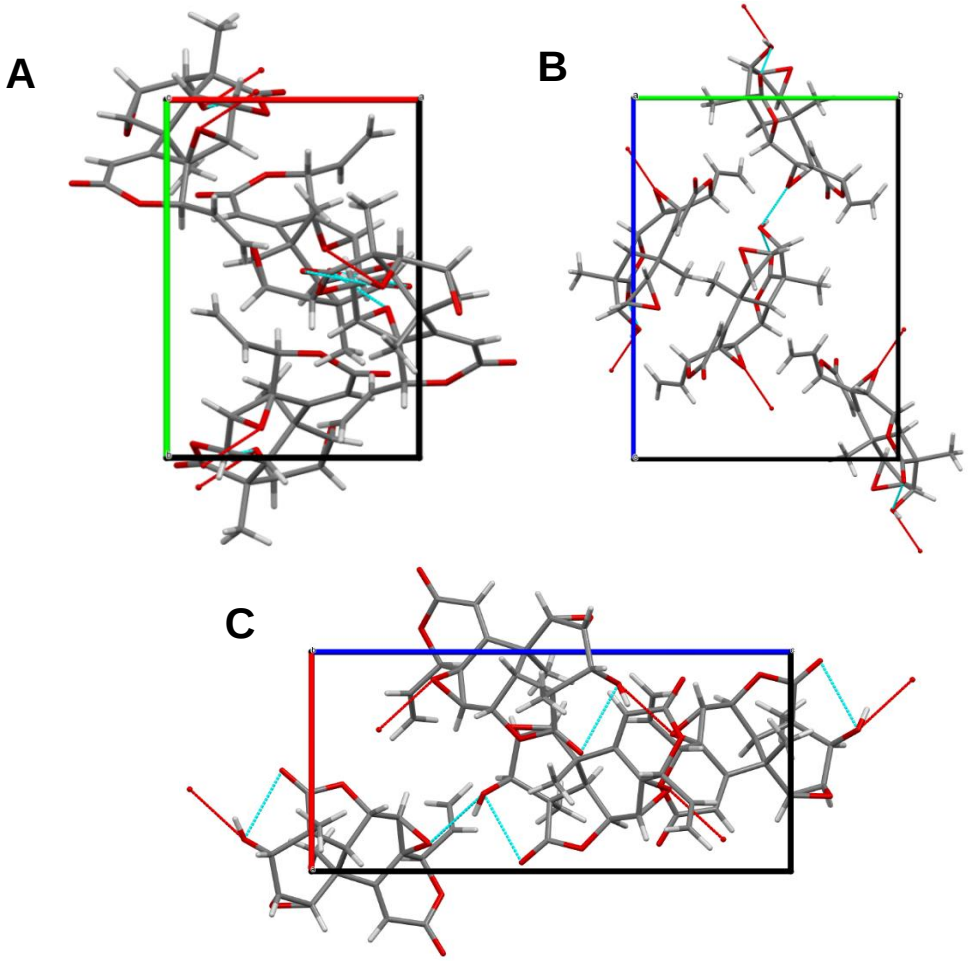

Figure S5.2: SCXRD unit cell of inumakilactone B **(52)** along the (**A**) **c** axis, (**B**) **a** axis and (**C**) **b** axis.

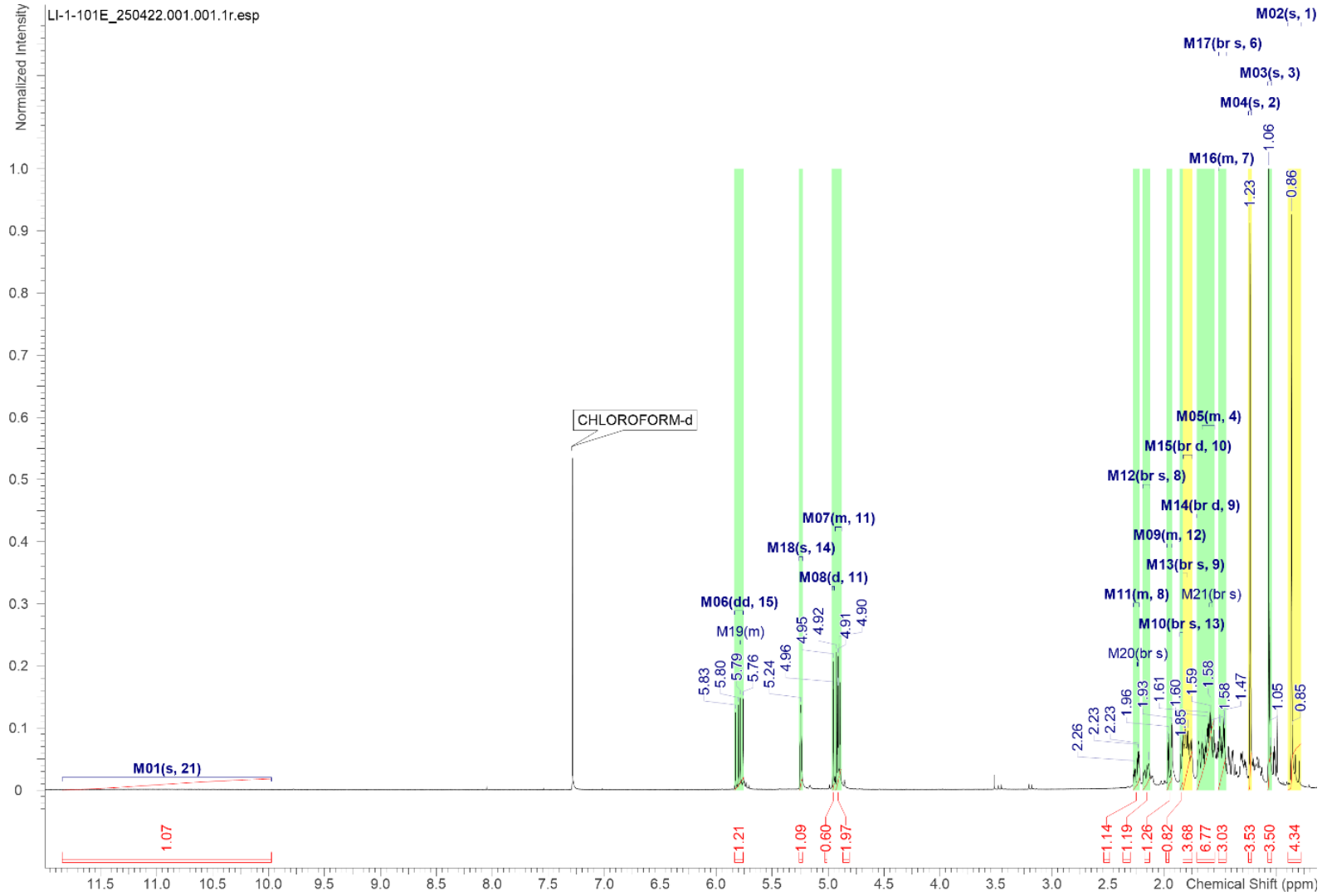

Figure S5.3: ^{1}H NMR spectra of sandaracopimaric acid **(53)**, analysed on a Bruker 500 MHz NMR and processed using ACD Labs.

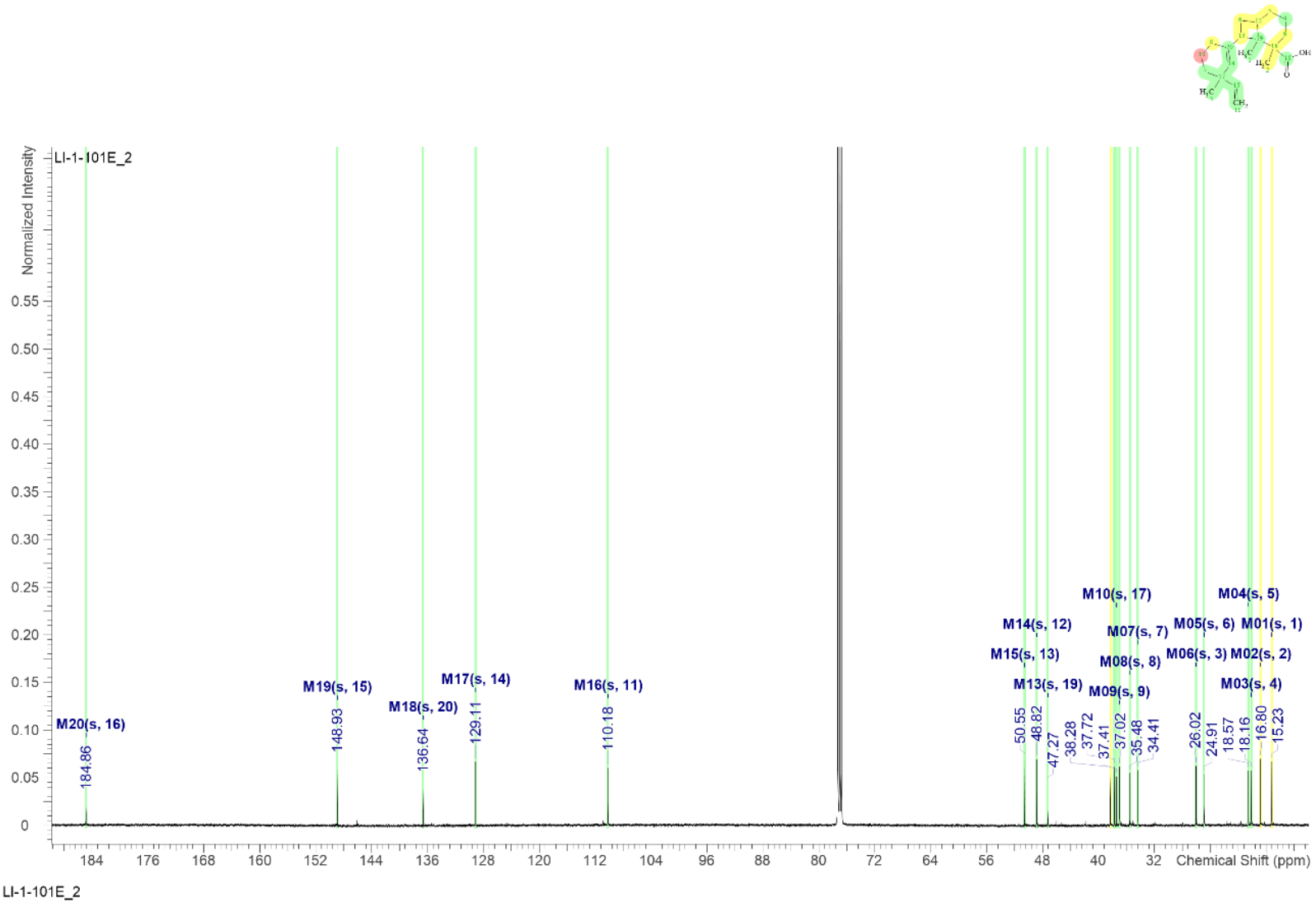

LI-1-101E_2

Figure S5.4: ^{13}C NMR spectra of sandaracopimaric acid **(53)**, collected at 125 MHz and processed using ACD Labs.

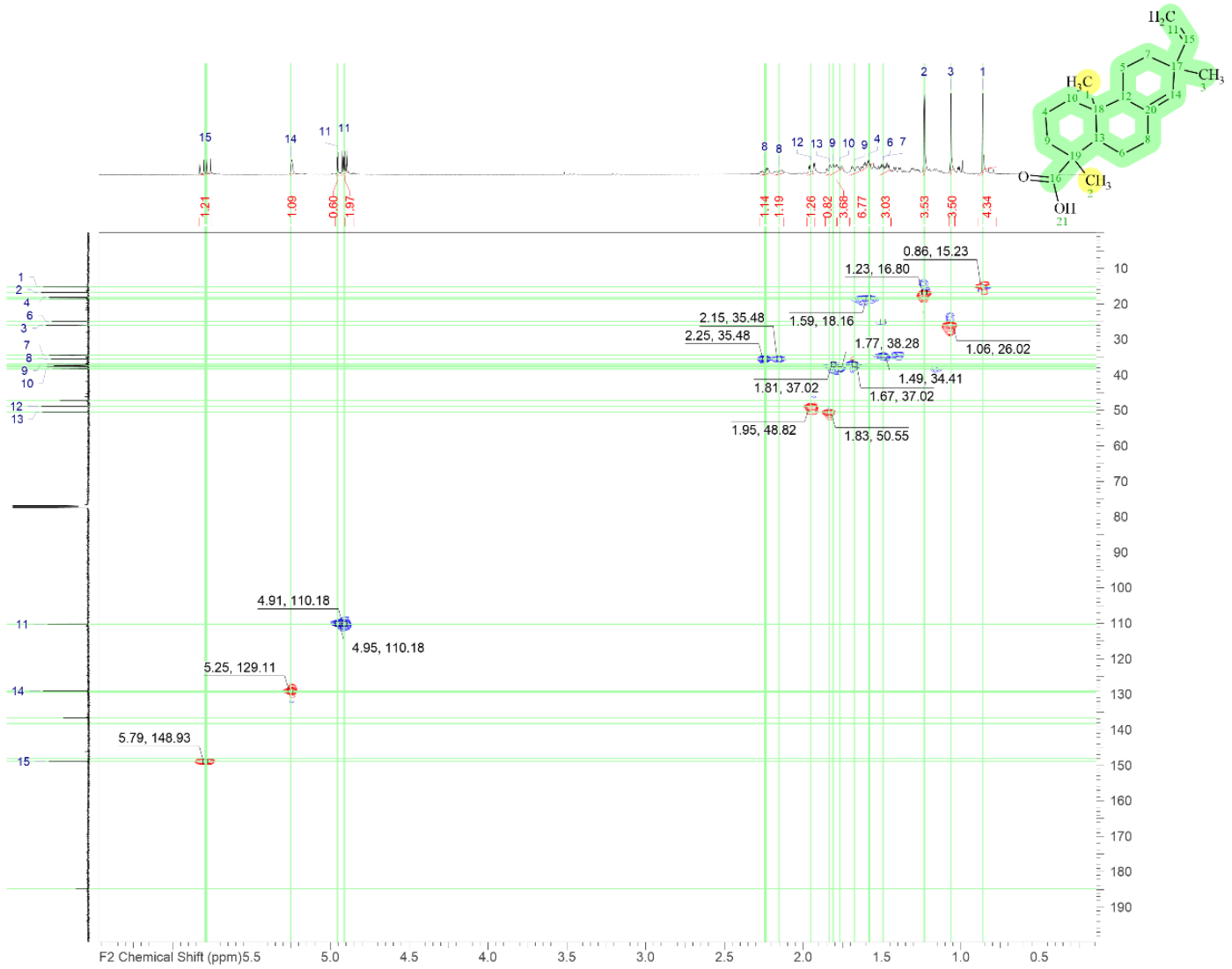

Figure S5.5: DEPT-HSQC NMR spectra of sandaracopimaric acid **(53)**, analysed on a Bruker 500 MHz NMR and processed using ACD Labs.

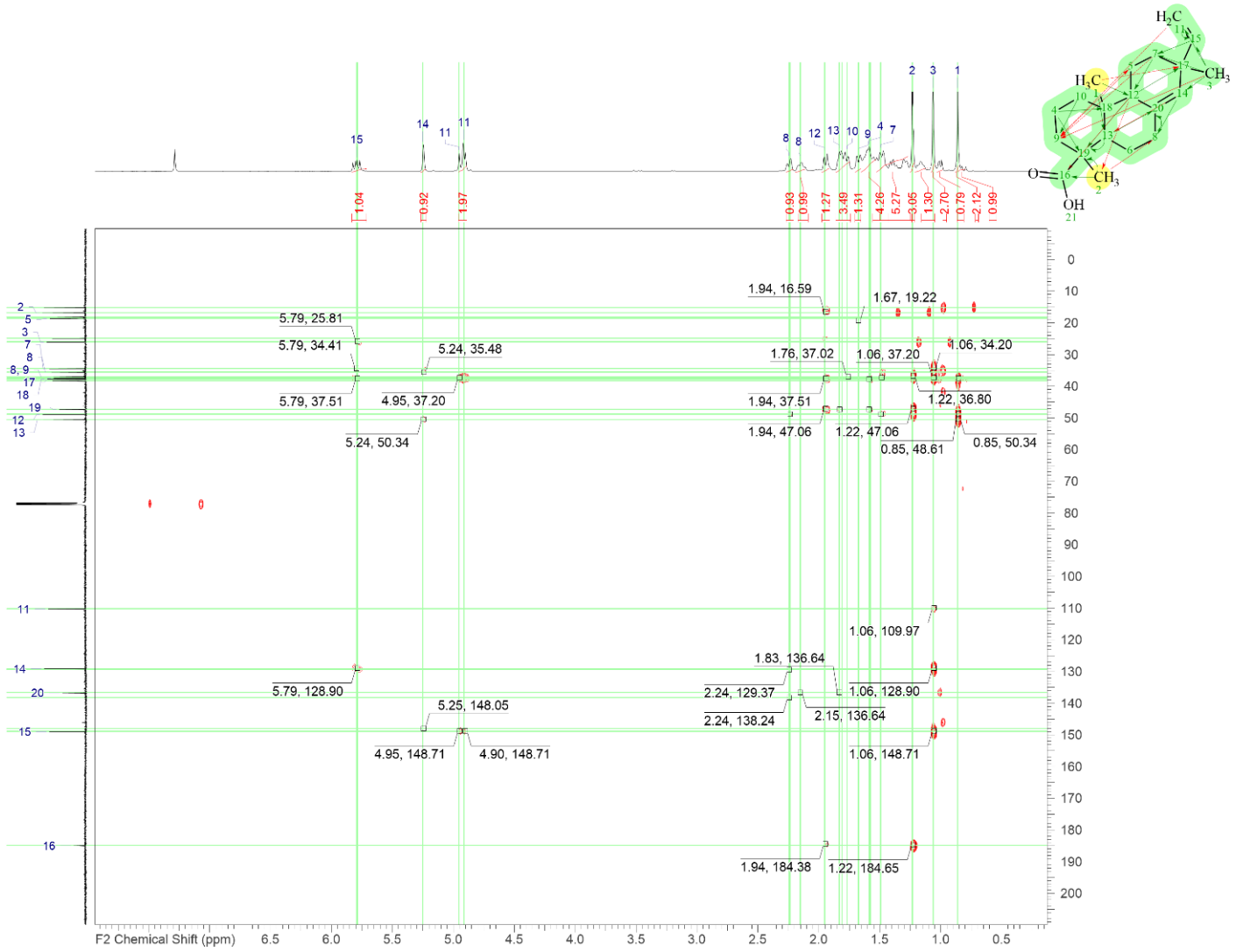

Figure S5.6: HMBC NMR spectra of sandaracopimaric acid **(53)**, analysed on a Bruker 500 MHz NMR and processed using ACD Labs.

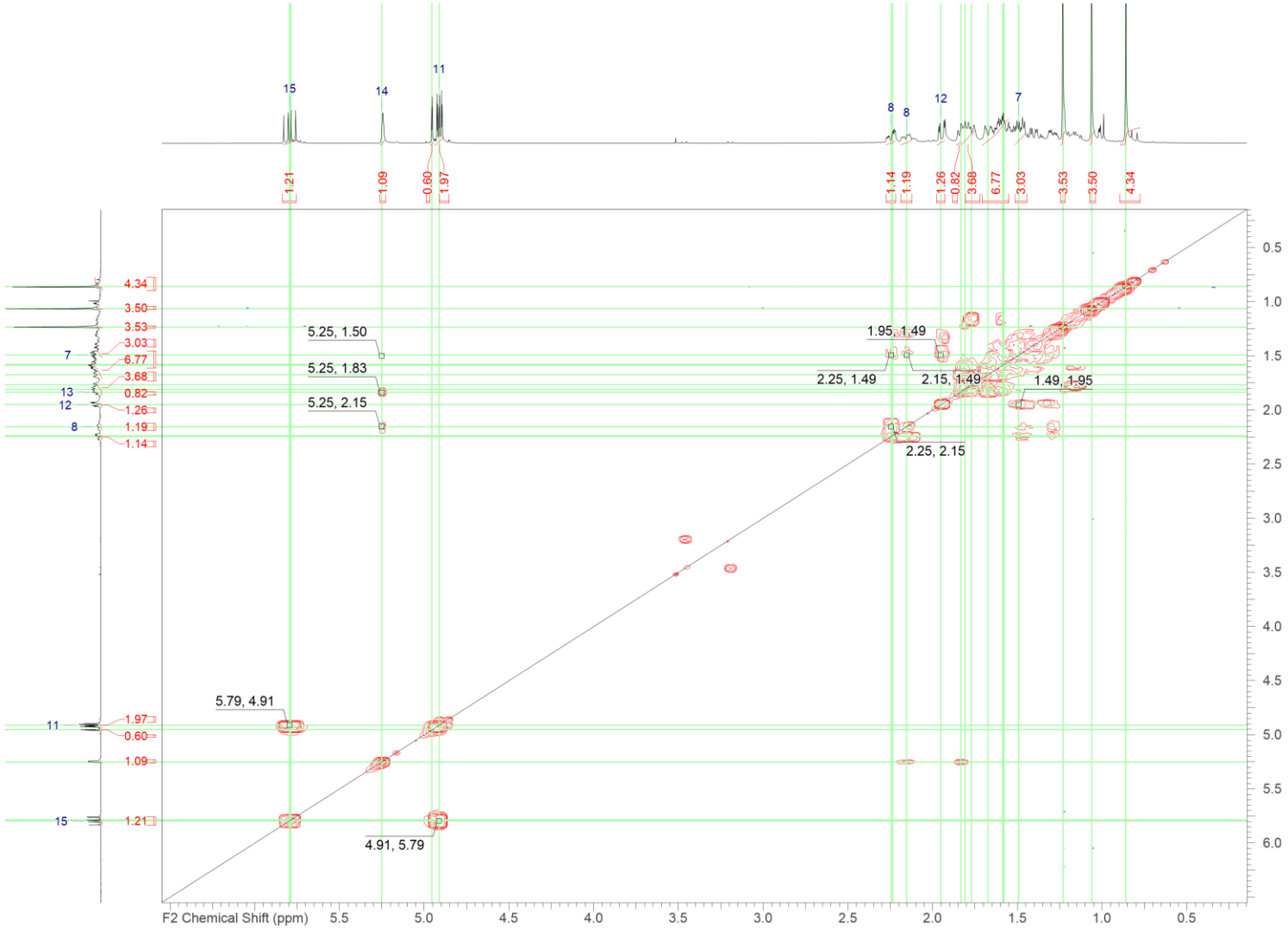

Figure S5.7: COSY NMR spectra of sandaracopimaric acid **(53)**, analysed on a Bruker 500 MHz NMR and processed using ACD Labs.

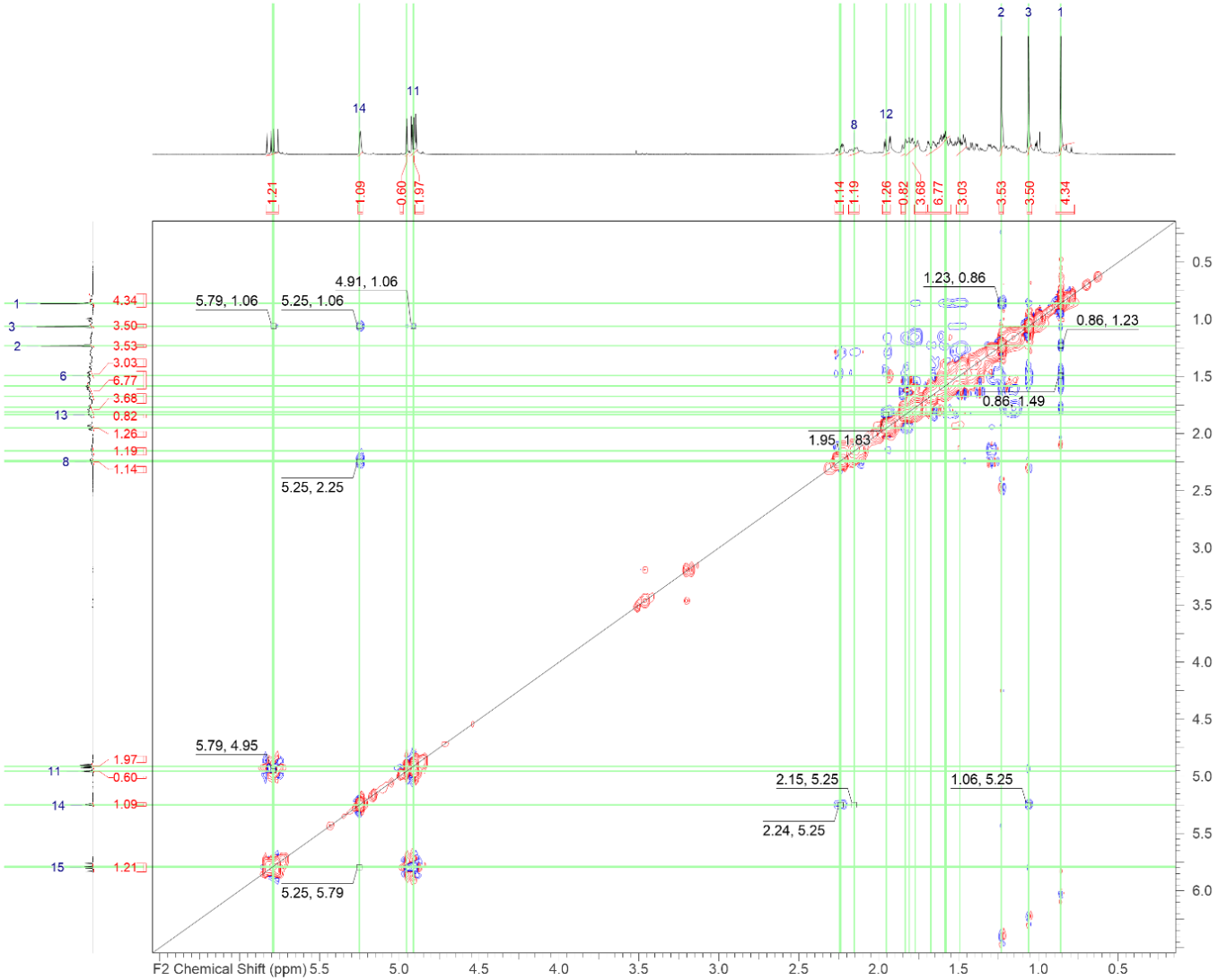

Figure S5.8: NOESY NMR spectra of sandaracopimaric acid **(53)**, analysed on a Bruker 500 MHz NMR and processed using ACD Labs.

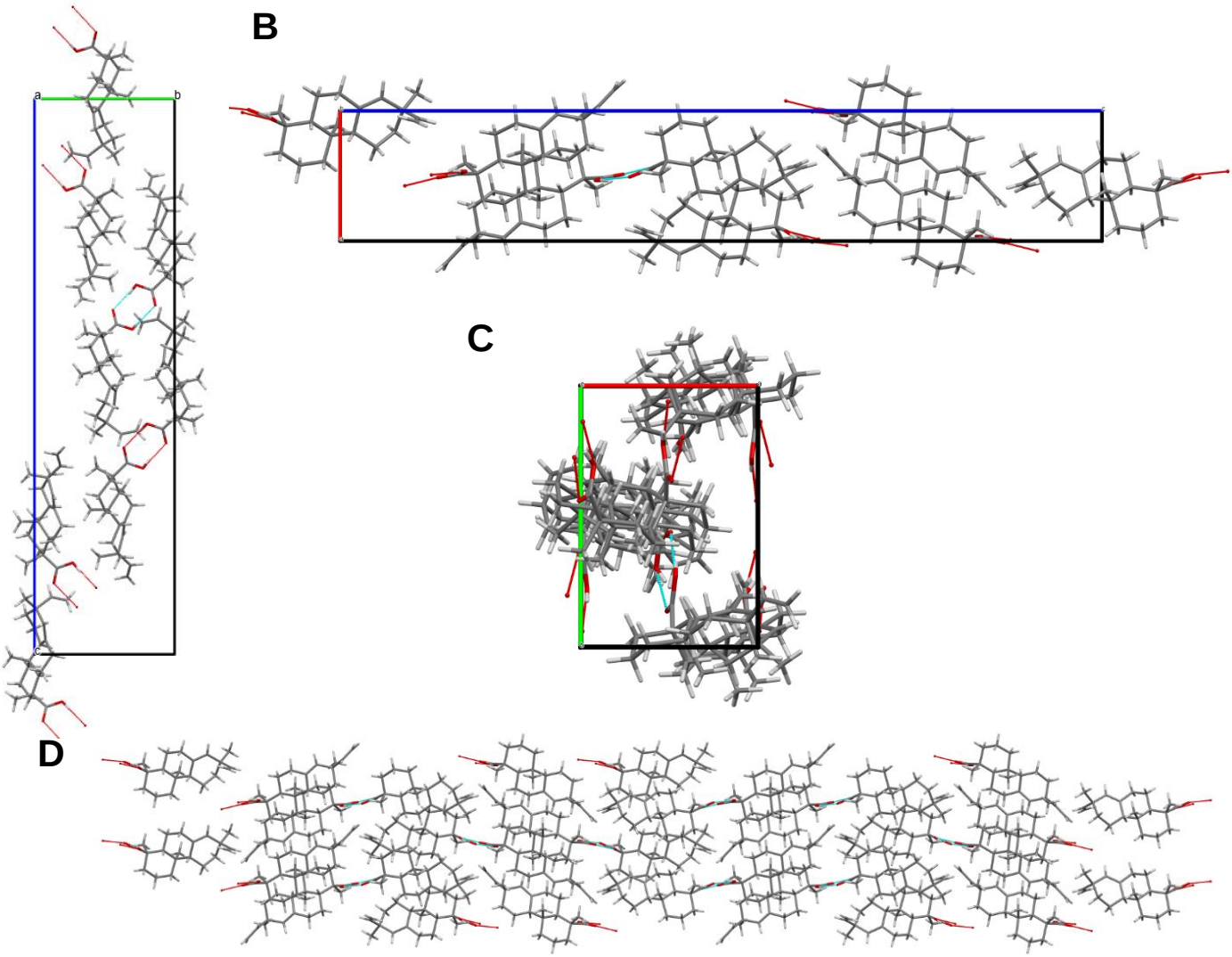

Figure S5.9: SCXRD unit cell of sandaracopimaric acid **(53)** along the (**A**) **a** axis, (**B**) **b** axis, (**C**) **c** axis and (**D**) a 2x2x2 unit cell of the compound.

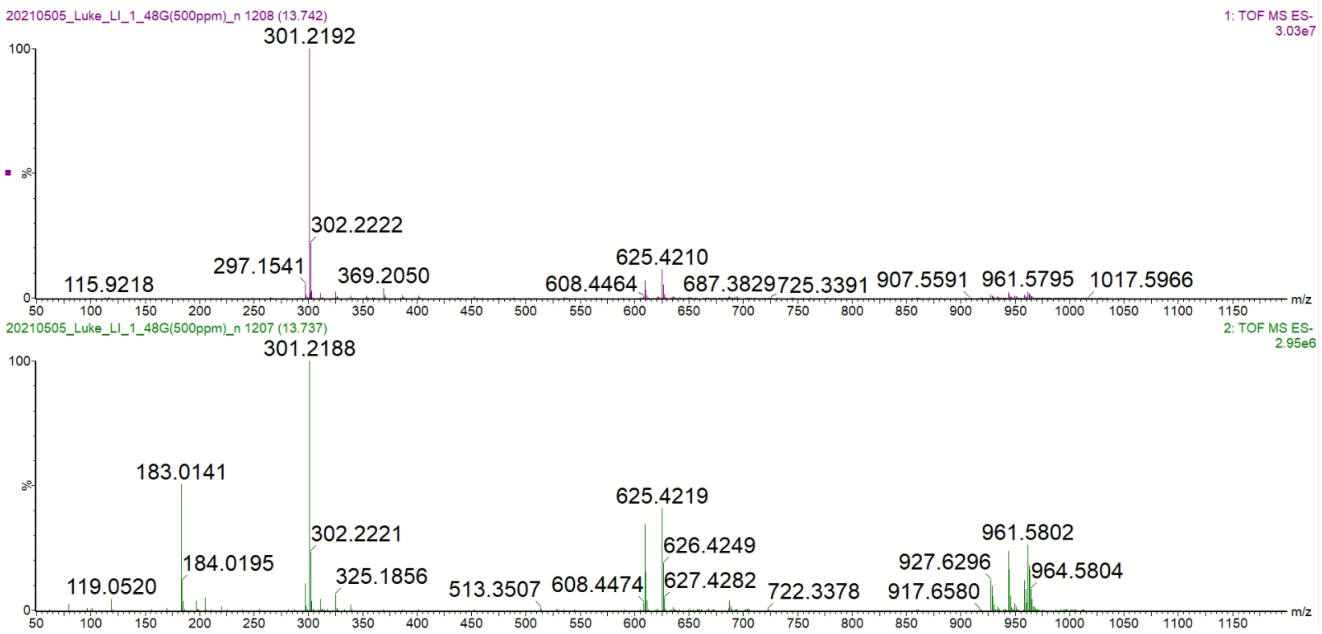

Figure S5.10: MS spectra of sandaracopimaric acid **(53)**, high (bottom) and low energy fragmentation pattern (top), lockmass corrected.